Harnessing *p*-H_2 hyperpolarisation and heteronuclear couplings in Earth's field NMR

Aminata Sakho

PhD

University of York

Chemistry

October 2022

Abstract:

The aim of this thesis was to explore the optimisation of PHIP (*para*hydrogen (p-H_2) Induced Polarisation) for detection in the zero-to-ultra-low-field (ZULF) regime, specifically the Earth's magnetic field (EF). First, I optimised the SABRE (Signal Amplification by Reversible Exchange) hyperpolarisation of three amines at 500 MHz using the pre-catalyst IrCl(IMes)(COD) (**I**) and a co-ligand, DMSO. This increased the 500 MHz polarisation level to 252-fold, which proved sufficient to enable EF detection. This was the first achievement of amines detection in the ZULF regime. In the case of 2,4,6-trifluoroamine, the heteronuclear ^{1}H-^{19}F coupling of ~5 Hz allowed differentiation between the hyperpolarised target and enhanced H_2O signals, highlighting the benefits of heteronuclear couplings in the ZULF regime for chemical differentiation.

Building on this, the potential for p-H_2 hyperpolarisation of a series of ^{31}P containing molecules with ^{1}H-^{31}P couplings ranging from ~15 – 600 Hz was investigated at high-field on reaction with **I**. Whilst several proved PHIP active, none were suitable for EF detection because of their slow p-H_2 exchange. In order to overcome this, the phosphorus compounds were changed to a series of phosphines with aromatic (PR_3) and cyclohexyl substituents. In view of earlier studies, the starting complex was changed to $IrCl(DMSO)_3$. This complex proved to react with the aromatic phosphines to form an array of orthometallation products alongside some simple substitution products, $IrCl(DMSO)y(PR_3)x$ [where y = 0, 1 and 2; x = 3, 2, 1]. Under hydrogen, these complexes react to form $[Ir(H)_2(DMSO)(PR_3)_2Cl]$ and $[Ir(H)_2(DMSO)_2(PR_3)Cl]$ according to the phosphine. In the case of PPh_3, the *bis*-phosphine product dominates and a PHIP (1 scan) in comparison to the thermal spectrum (32 scans) have signal-to-noise ratios of 5775 and 320, respectively. In contrast, when PCy_3 was examined, the *mono*-phosphine product dominates, with an estimated polarisation level enhancement of 2000-fold at 11.7 T. Significant polarisation enhancements were also observed from the *mono*-phosphine product with PPh_2PCy.

The high levels of renewable ^{1}H and ^{31}P polarisation of these three phosphine adducts, combined with their large *cis* ^{31}P – ^{1}H couplings (~20 Hz), proved to make them ideal for detection using EF NMR. This is the firstly reported direct observation of hydride hyperpolarisation in the ZULF regime and was confirmed by comparison with density matrix simulations.

Table of contents

Contents

List of Figures

Figure 2.15: depiction of Fisher or singlet carbene and Schrock or triplet carbene interacting with a metal centre.

Figure 3.1: Example of a primary amine involved in SABRE hyperpolarisation

Figure 3.2: Chemical structure of **1** benzylamine; **2** phenoxyethylamine, **3** 2,4,6-triflurobenzylamine and **I** IrCl(COD)(IMes) (where IMes stands for 1,3-bis(2,4,6-trimethylphenyl)-imidazol-2-ylidine and COD cyclooctadiene)

Figure 3.3: SABRE hyperpolarisation levels observed at 500 MHz for substrates **1**, **2** and **3** in the presence and absence of the co-ligand DMSO in chloroform-d_3. Clearly, the presence of DMSO leads to a better amine response per proton when compared to when there is no DMSO

Figure 3.4: a) ^{1}H 1D NMR spectra of a sample of 5 mM **I** and 100 mM benzylamine in chloroform-d_3 under H_2. The hydride region indicates the formation of complex **5**. b) ^{1}H 1D NMR spectrum of a sample of 5 mM of **I**, 100 mM benzylamine and 100 mM DMSO-d_6 in chloroform-d_3 with H_2. The hydride region now shows evidence for three complexes: **4** (green stars), **5** (yellow circle) and **6** (red square).

Figure 3.5: a) ^{1}H 1D NMR spectrum of a sample of 5 mM **I** and 100 mM of benzylamine in chloroform-d_3 under H_2. The hydride region shows a signal indicative of the formation of complex **5**. b) ^{1}H 1D NMR spectrum of a sample of 5 mM **I** and 100 mM of benzylamine and 100 mM of DMSO-d_6 in chloroform-d_3 under H_2. The hydride region shows signals indicative of three complexes: **7** (green stars), **8** (yellow circle) and **9** (red square).

Figure 3.6: a) Depiction of the EXSY measurement process and the dissociation of ligand L from **4** to form intermediate **4'**. b) Typical EXSY spectra of **4** at 298 K recorded successively 0.01, 0.025 and 0.05 s after selective excitation of the bound CH_2 resonance for ligand **1** *trans* to the hydride.

Figure 3.7: a) EXSY ^{1}H signal interconversion for the bound 3.33 ppm in **4** and the 3.9 ppm free benzylamine signal expressed as % abundance for a solution of 5 mM of **I**, **1** and DMSO in the ratio 1 : 20 : 20. % Abundance calculated from EXSY data (marker points) and the model (lines) for a solution of **4** at 298 K. b) An Eyring plot of $\ln\left(\frac{2k_{off}}{T}\right)$ against $\frac{1}{T}$ yields a straight line where the intercept (-9996.7x) and gradient (29.457) can be used to calculate the activation parameters for the ligand loss in **4** according to equations 3.3 and 3.4. y = -9996.7x + 29.457; R^2 = 0.9986.

Figure 3.8: a) A typical EXSY spectrum of **4** at 298 K recorded 0.05 s after selective excitation of the hydride ligand *trans* to **1**. b) Schematic representation of the exchange processes taking place in an Ir-based SABRE system in the case where **1**, Cl^-, DMSO and hydrides are ligated. In addition to the H_2 exchange in complex with k_{H2} constant association and k_{-H2} constant dissociation, there is an interchange of a ligand L, between the **4** form (k_{-i}) when L binds from the bottom and the **4''** form (k_i) occurs when ligand L binds from the top.

Figure 3.9: a) catalytic cycle of activation of SABRE catalyst **I** in presence of the amine ligand, the co-ligand DMSO and *p*-H_2. b) Comparison of the activation curves, detected in the Earth's magnetic field, of two SABRE solutions. Blue dots correspond to a solution of 5 mM of the catalyst **I**, 25 equivalents of the substrate; pink dot: 5 mM of the catalyst **I**, 25 equivalents of benzylamine and 25 equivalents of the co-ligand DMSO.

Figure 3.10: Increase in polarisation during activation as function of *p*-H_2 bubbling time same equivalence compared to 5.1 mM of **I**, **1** (**4**, green) and **2** (**7**, blue) at EF NMR (25/25 equivalents 127.5 mM of **1**/DMSO and 25/25 equivalents 127.5 mM of **2**/DMSO in 4 mL chloroform).

Figure 3.11: a) The average percent polarisation after activation as a function of concentration of **1**/DMSO measured at the Earth's magnetic field (Terranova instrument). Black dots 5/5, 10/10, 15/15, 20/20 and 25/25 benzylamine/DMSO ratio respectively. b) Average of percentage polarisation after activation as function of **1**/ DMSO ratio at 1 T (SpinSolve instrument) of the same samples.

Figure 3.12: a) The relaxation time T_1 as function of ligands excess measured at the local Earth's magnetic field. b) The relaxation time T_1 as function of ligands excess measured at the 43 MHz (1 T). c) Pulse sequence of the standard hyperpolarised T_1 at the Earth's magnetic field. VD stands for the variable delay and d) Pulse sequence for variable flip angle T_1 measurement with the (1 T) Spinsolve spectrometer.

Figure 3.13: Build-up of ^{1}H SABRE polarisation as a function of the duration of the polarisation transfer field (PTF) of the 5 samples where the field 6.5 mT has been produced by a current of 2.05 A. The samples are 5/5 purple, 10/10 green, 15/15 blue, 20/20 red and 25/25 black, **1**/DMSO ratio respectively.

Figure 3.14: a) EF NMR detection of **3**. 1D NMR spectrum centred at 2032.5 Hz which is the Larmor frequency of ^{1}H at this field, showing a splitting pattern generated by the presence of the heteroatom ^{19}F. The peak presents a positive and negative component. The sample is composed of 25 equivalence (127.5 mM) of **3** and 25 equivalence of DMSO in 4 mL chloroform. b) Increase in polarisation during activation as function of *p*-H_2 bubbling time of the same sample.

Figure 3.15: a) hyperpolarisation relaxation decay curves for solution of 127.5 mM of **3** and 127.5 mM of DMSO with 5.1 mM of the SABRE catalyst **I** in 4 mL of chloroform. a) Relaxation time T_1 as function of the variable delay τ. b) Build-up of ^{1}H SABRE polarisation as a function of the duration of the polarisation transfer field (PTF).

Figure 4.1: Chemical structure of **10** diphenyl phosphine, **11** diphenyl phosphine oxide, **12** diterbutyl phosphine oxide, **13** diterbutyl phosphite, **14** diphenyl methyl phosphine, **15** dimethyl phenyl phosphine, **16** diphenyl vinyl phosphine oxide, **17** Triphenylphosphine sulphide, **18** Trimethylphosphine sulphide. The chemical structure of the pre-catalyst IrCl(IMes)(COD) (where IMes = 1,3-bis (2,4,6-trimethylphenyl) imidazol-2-ylidene, COD = cyclooctadiene) is also added and called later **I**.

Figure 4.2: a) Reaction of 5 mM of **I** pre-catalyst, 25 mM (5 eq.) of **10** in 0.6 mL of dichloromethade-d_2 and 3 bar of *p*-H_2 leading to the formation of complexes **19**, **20**, **21**, **22** and **23**. c) First hyperpolarised spectrum recorded showing enhanced hydrides for complex **19**, **22** and **20**. b) shows still polarisation of complex **20**. a) 24hrs later, the thermal spectrum recorded show the thermodynamic products **21** and **23**.

Figure 4.3: a) 5 mM of **I** with 1.1 µL 2 eq. of **10** is mixed in dichlorometane-d_2. The rate of conversion of the complexes **20**, **21** and **23** is followed by NMR at 298K for 22hrs. b) 5 mM of **I** with 5 eq. of **10** is mixed in dichlorometane-d_2. The rate of conversion of the complexes **20**, **21** and **23** is followed by NMR at 298 K for 2hrs.

Figure 4.4: Reaction of 5 mM of **I** pre-catalyst, 1.1 µL (2 eq.) of **10** in 0.6 mL of dichloromethane-d_2 and 3 bar of *p*-H_2 observed at 500 MHz. a) 1scan PHIP NMR spectrum showing the hyperpolarised hydride signals of complexes **19** and **20**. b) The subsequent PHIP experiment now shows strong hyperpolarised hydride signal for **20** only. c) Thermally polarised spectrum recorded 20 min later with 64 scans shows **20** and **21**. Zoomed regions show the coupling patterns for **20**, where *trans* J(^{1}H-^{31}P) =

151 Hz, *cis* $J(^1H-^{31}P)$ = 18 Hz, $J(^1H-^1H)$ = 5.5 Hz. Two 18 Hz and 5.5 Hz couplings are also measured in the second pair of hydride at 23.03 ppm.

Figure 4.5: ^{31}P NMR spectra of a sample of 1 mg of **11** (a) and 0.8 µL of CH_3OH in dichloromethane-d_2 and a sample of only **11** in dichloromethane-d_2 (b).

Figure 4.6: ^1H NMR spectra recorded for a sample consisting of 5 mM of **I** pre-catalyst, 20 mM (4 eq.) benzylamine in 0.6 mL of dichloromethane-d_2, 5 mM (1 eq.) of **11** and 3 bar of *p*-H_2. a) The PHIP NMR experiment shows a strong hydride signal enhancement for **29**, which is barely visible in the thermally polarised NMR spectrum after 64 scans (b) where **27** and **28** are clearly visible.

Figure 4.7: $^1H-^{31}P$ HMQC-PHIP spectrum of a sample containing 5 mM of **I** pre-catalyst, 20 mM (4 eq.) Benzylamine in 0.6 mL of dichloromethane-d_2 was first activated with 3 bar of *p*-H_2. After complete hydrogenation of COD and total formation of $IrCl(BnNH_2)_3(H)_2(IMes)$, 5 mM (1 eq.) of **11** was added to the sample. The ^{31}P resonance of the three complexes **27**, **28** and **29** is secured by a $^1H-^{31}P$ HMQC-PHIP

Figure 4.8: $^{31}P^1$ NMR spectra of a sample of 5 mM of **I** pre-catalyst, 1.0 µL (3 eq.) of benzylamine and 2.8 mg (4 eq.) of **11** in 0.6 mL methanol-d_4. a) Before activation with H_2. b) 12 min after H_2 addition and 2hrs30min after H_2 addition.

Figure 4.9: Sample of 2 mg of **11** and 2 µL of benzylamine was mixed in 0.6 mL of dichloromethane-d_2. ^{31}P NMR spectra (a, non-decoupled ^1H) and (b, decoupled to ^1H) recorded a week after show free b and an additional signal at 19.26 ppm.

Figure 4.10: Sample of 5 mM of **I** and 10 mM (2 eq.) of **13** in 0.6 mL of dichloromethane-d_2 used to record a) ^1H NMR yielded a 17 dihydride containing species in the hydride region and b) ^1H NMR PHIP experiment that yielded a weak enhanced antiphase hydride signal for **1D**.

Figure 4.11: A sample of 5 mM of **I** and 1.0 µL (3 eq.) of benzylamine was mixed in dichloromethane-d_2 under H_2. After formation of $Ir(IMes)(H)_2(BnNH_2)_3Cl$ 0.70 mg (1 eq.) of **14** was added. a) ^1H NMR spectrum just 5min after **14** addition showing the presence of 5 species **32**, **33**, **34**, **35** and **36**. b) 24hrs after **14** addition showing evolution of the equilibrium.

Figure 4.12: 5 mM of **I** and 1.0 µL (3 eq.) of benzylamine in dichloromethane-d_2 in presence of H_2. After activation, 0.70 mg (1 eq.) of **14** was added and ^1H NMR PHIP (1 scan) showing signal enhancement for free benzylamine and antiphase enhanced signal for hydrides of various complexes.

Figure 4.13: a) $^{31}P\{^1H\}$ NMR spectrum of a sample containing **14** dissolved in dichloromethane-d_2 acquired with 64 scans. b) 5 mM of **I** and 1.0 µL (3 eq.) of benzylamine in dichloromethane-d_2 in presence of H_2. After activation, 0.70 mg (1 eq.) of **14** was added and a one scan $^{31}P\{^1H\}$ SABRE NMR spectrum recorded 24hrs later c) $^{31}P\{^1H\}$ NMR spectrum of the same sample as b) averaged 4k time.

Figure 4.14: 5 mM of **I** and 15 mM (3 eq.) of benzylamine in dichloromethane-d_2 were mixed under H_2. After complete conversion to $Ir(IMes)(H)_2(BnNH_2)_3Cl$, 0.89 µL (2 eq.) **15** was added. ^1H NMR shows three signals in the hydride region for **37**, **38** and **39**. PHIP experiment at 273 K exhibits weak antiphase signal enhancement for **37**.

Figure 4.15: a) 1 mg of (**II**), 0.32 µL (2 eq.) of acetonitrile and 7.14 mg (10 eq.) of **16** was mixed then *p*-H_2 added. Hydride region of ^1H NMR (top spectrum) at 298 K showing two complexes **40** and **41**. (bottom spectrum) After 24hrs at 298 K, **40** completely converts to **41**.

b) organic region of 1 scan PHIP ^1H NMR (top spectrum) experiment recorded in day 1, shows weakly antiphase signals of the hydrogenation product, CH_2 and CH_3 of **16'**. The strong enhanced signal at

1.52 ppm is the COA. 64 scans ^{1}H NMR (bottom spectrum) highlights the vinyl resonances of **16** at 6.73 and 6.31 ppm for CH and CH_2.

Figure 4.16: Hydrides region of NMR spectra recorded at 256 K from a sample of 5 mM solution of **I** with 4 eq. of **18** under H_2 showing signals of **42** at -21.58 and -26.46 ppm, and **43** at -23.84 and -27.14 ppm. a) 1 scan thermally polarised spectrum and b) 1 scan PHIP hyperpolarised spectrum.

Figure 5.1: Phosphines reacted with **III**. **44** tricyclohexylphosphine; **45** triphenylphosphine; **46** dicyclohexyl phenyl prosphine; **47** Tri(*p*-tolyl)phosphine; **48** Tris(4-methoxyphenyl) phosphine; **49** Tribenzylphosphine; **50** Triphenyl phosphite and; **51** methyl diphenyl phosphine

Figure 5.2: ^{1}H NMR spectrum at 298 K of a solution of $IrCl(DMSO)_3$ (**III**) (4 mg) in dichloromethane forming a bis-Ir dimer with two chlorides bridge. This data is in agreement with Milstein et al.

Figure 5.3: ^{1}H NMR spectrum at 298 K of a solution of $IrCl(DMSO)_3$ (**III**) (4 mg) in dichloromethane-d_4 in presence of *p*-H_2 where the two isomers $IrCl(H)_2(DMSO)_3$ are identified. The *cis* dihydride isomer, namely *fac*-$IrCl(H)_2(DMSO)_3$ at -16.01 ppm and two doublet peaks for the *trans* hydrides of *mer*-$IrCl(H)_2(DMSO)_3$. The spectrum recorded without *p*-H_2 also shows only the presence of these two species (not shown here).

Figure 5.4: Schematic showing products formed when 10.4 mM $IrCl(DMSO)_3$ (**III**) and 74 mM PPh_3 (**45**) equilibrate at 298 K in toluene (upper). a) ^{1}H NMR spectrum recorded 3.5 hrs after the start of reaction (298 K), revealing hydride ligand signals for **53**, **54**, **55** and **56**. b) Corresponding spectrum recorded 124 hrs later; the slow formation of **57** is indicated.

Figure 5.5: Proposed structures of the 16 electrons Ir(I) complexes formed after substitution of DMSO by PPh_3 and their respective $^{31}P\{^{1}H\}$ resonances. They reversibly undergo to the 18 electron Ir(III) C-H bond activation complexes.

Figure 5.6: 2D ^{1}H-$^{31}P\{^{1}H\}$ NMR correlation spectra recorded on a solution of $IrCl(DMSO)_3$ (**III**) 10.4 mM (3 mg) and 0.15 mL of a 74 mM solution of PPh_3 (**45**) in toluene. a) at 273 K after 24 hrs of reaction with a focus on the ligand not involved in C-H activation. b) At 273K six days later, showing the peaks for the phosphines involved in the C-H activation.

Figure 5.7: Solution of $IrCl(DMSO)_3$ (**III**) 10.4 mM (3 mg) and 0.15 mL of a 74 mM solution of PPh_3 (**45**) at 298 K in toluene. Three successive additions of 0.05 mL of a 74 mM solution of **45** where each time a ^{1}H NMR spectrum is immediately recorded corresponding to a, b and c. The singlet at -18.65 ppm is tentatively assigned as a C-H bond activation from (**III**), which very unstable and disappear as shown here.

Figure 5.8: Solution of $IrCl(DMSO)_3$ (**III**) 10.4 mM (3 mg) and 0.15 mL of a 74 mM solution of PPh_3 (**45**) at 298 K in toluene. Three successive additions of 0.05 mL of a 74 mM solution of **45** where each time a $^{31}P\{^{1}H\}$ NMR spectrum is immediately recorded corresponding to a, b and c. These spectra are zoomed on the positive region to highlight the 16 electron species.

Figure 5.9: a) reproduced from the literature figure from depicting the cleavage of sp^3 bond in methane facilitated by a transition metal. b) Depiction of a sp^2 bond activation in a phenyl facilitated by a π-back-bonding from the metal to the σ* orbital of the C-H bond and a σ-donation to the metal.

Figure 5.10: Reaction of $IrCl(DMSO)_3$ (**III**), **45** and H_2 leads to a large number of hydride ligand containing products ($Ir(H)_2Cl(DMSO)_3$ not shown). The Ir(III) products are in equilibrium with their Ir(I) precursors. The region chemistry of these reactions leans to a number of possible product isomers. Those detected by NMR are shown.

Figure 5.11: Sample of 8.6 mM of $IrCl(DMSO)_3$ (**III**) and 1 eq. of **45** in 0.6 mL of toluene-d_8 was used to record four ^1H NMR spectra at 298 K with 32 scans. a) before H_2 addition, b) 30 min after H_2 addition, c) 2 hrs after H_2 addition and d) 24 hrs after H_2 addition. These four spectra demonstrate the presence of the multiple identified species at these different stages.

Figure 5.12: Zoom on the hydride signal of **66** in the ^1H NMR spectrum at 298 K of a solution of $IrCl(DMSO)_3$ (**III**) and (3 eq.) of **45** in 0.6 mL of toluene-d_8. The coupling pattern demonstrate a *tris*-phosphine substitution

Figure 5.13: Reaction of $Ir^{I}Cl(DMSO)_3$ (**III**) with each of these phosphines in toluene trigger a C-H bond activation that give the hydride signals in the ^1H NMR spectra. In spectra a, b, c, and d the phosphines **47**, **49**, **50** and **48** was used respectively.

Figure 5.14: Reaction of $Ir^{I}Cl(DMSO)_3$ (**III**) with each of these phosphines in toluene trigger C-H bond activation and 16 electron complexes that give the numerous ^{31}P signals in the $^{31}P\{^1H\}$ NMR spectra. In a, b, c, and d the phosphines **47**, **49**, **50** and **48** was used respectively.

Figure 5.15: Sample of 17.2 mM of $IrCl(DMSO)_3$ (**III**) and 1 eq. of **48** in 0.6 mL of toluene-d_8 was used to record four ^1H NMR spectra at 298 K with 32 scans. a) before H_2 addition at 298 K, b) 5min after H_2 addition at 298 K, c) after putting the sample in a hot water bath for 10 min allows the total conversion of the C-H bond activation products and d) 24hrs after H_2 addition at 273 K. These four spectra testifies the presence of many identified species at these different stages.

Figure 5.17: Sample of 17.2 mM of $IrCl(DMSO)_3$ (**III**) and (1 eq.) of **46** in 0.6 mL of toluene-d_8 was used to record five ^1H NMR spectra at 298K with 32 scans. a) before H_2 addition at 298 K, c) 5min after H_2 addition at 298 K, c) 1hr after H_2 addition at 298 K d) 1.5hrs after H_2 addition at 273 K and e) 48hrs after H_2 addition. These five spectra testifies the presence of many identified species at these different stages.

Figure 5.18: Sample of 2 mg of $IrCl(DMSO)_3$ (**III**) with 0.60 mg (1 eq.) of Tris-benzyl phosphine (**49**) used to record three $^{31}P\{^1H\}$ NMR spectra and the speciation of different product at different stage of the reaction. a) Before H_2 addition at 298 K. b) 15 min after H_2 addition at 298 K and c) After 14hrs after H_2 addition at 313 K

Figure 5.19: Sample of 17.2 mM of $IrCl(DMSO)_3$ (**III**) and (1 eq.) of **47** in 0.6 mL of toluene-d_8 was used to record four ^1H NMR spectra with 32 scans. a) before H_2 addition at 298 K, b) 30mins after H_2 addition at 263 K, c) 24hrs after H_2 addition at 263 K d) 120hrs after H_2 addition at 253 K. These four spectra testifies the degradation of **88** over time.

Figure 5.20: Sample of (2.5 mg) 8.6 mM of $IrCl(DMSO)_3$ (**III**) and (3 eq.) 2.9 mg of **50** in 0.6 mL of toluene-d_8 was used to record three ^1H NMR spectra with 32 scans. a) before H_2 addition at 298 K, b) after putting the sample in a hot water bath for 10min and warming the probe to 333 K does not convert the C-H activation product c) 5hrs after H_2 addition at 298. These three spectra testifies the presence of many identified species at these different stages.

Figure 5.21: Sample of 2.5 mg (8.6 mM) of $IrCl(DMSO)_3$ (**III**) is reacted with 1.4 µL (2 eq.) of **51** in toluene-d_8. a) chemical structure of complex **91**. b) ^1H NMR spectrum shows in the hydride region single product **91**

Figure 5.22: Series of $^{31}P\{^1H\}$ NMR spectra showing the hydride region of a sample containing 3 mg (11.9 mM) of $IrCl(DMSO)_3$ (**III**) and 2 eq. (2.5 mg) of **44** in 0.6 mL of toluene-d_8 under H_2. a) Thermal $^{31}P\{^1H\}$ NMR spectrum recorded at 298 K before H_2 addition, showing the phosphine oxide, free **44** and the 16 electron complexes $IrCl(DMSO)_2(P_{44})$ and $IrCl(DMSO)(P_{44})_2$. b) Analogous NMR spectrum to

(a) just 10 min after H_2 addition. c) Analogous NMR spectrum, 1hr after hydrogenation at 263 K showing **92**, **93** and the presence of the starting material. d) Analogous NMR spectrum at 253 K after three days at 298 K all three ^{31}P signals of **92**, **93** and **94**.

Figure 5.23: Series of ^{1}H NMR spectra showing the hydride region of a sample containing 3 mg (11.9 mM) of $IrCl(DMSO)_3$ (**III**) and 2 eq. (2.5 mg) of **44** in 0.6 mL of toluene-d_8 under H_2. a) Thermal ^{1}H NMR spectrum recorded at 298 K showing only **92** and broad features for **93**. b) Analogous NMR spectrum to (a) but at 273 K. c) Analogous NMR spectrum at 253 K. d) Analogous 253 K NMR spectrum after two days at 298 K before cooling reveals the consumption of **92** and formation of **94** alongside **93**.

Figure 5.24: NMR spectra confirming DSMO is a requirement for the detection of **94.** 2.5mg of $IrCl(COD)PCy_3$ (**IV**) and 1.5 eq. of PCy_3 (**44**) were combined in toluene-d_8 presence of H_2. a) The ^{1}H NMR at 253 K prior to DSMO addition confirms many hydride complexes form. b) Addition of 1 µL of DMSO leads to their conversion to an equilibrium mixture **92**, **93** and **94**.

Figure 6.1: Sample of 8.6 mM of $IrCl(DMSO)_3$ (**III**) and (1 eq.) of **45** in 0.6 mL of toluene-d_8 was used to record two ^{1}H PHIP NMR spectra at 298 K with 1 scan. a) First PHIP reaction with 3 bar of *p*-H_2 showing hyperpolarised antiphase signal for **59**, **58** and **62**. b) 2nd PHIP reaction after the sample was refilled with fresh *p*-H_2 that show now hyperpolarised signals for only **58** and **62**, and free and bound DMSO. A zoom of the hydride region highlights the ^{1}H-^{1}H and ^{1}H-^{31}P coupling for **58** and **62**.

Figure 6.2: $^{31}P\{^{1}H\}$ SABRE NMR experiments on a sample of 8.6 mM of $IrCl(DMSO)_3$ (**III**) and 1 eq. of **45** in 0.6 mL of toluene-d_8 at 298 K. a) After shaking in a mu-shield for 5 s and b) at shaking in the Earth's field for 5 s.

Figure 6.3: The dihydride dissociation mechanism in $IrCl(H)_2(PPh_3)_2(DMSO)$ complex is sketched where the DMSO dissociation leading the intermediary I with a vacant site allows subsequent H_2 association.

Figure 6.4: Single scan ^{1}H NMR spectrum of a sample of $IrCl(DMSO)_3$ (**III**) with 3 eq. of **45** in toluene-d_8 under *p*-H_2 showing hyperpolarised hydride ligand signals for **62** and **66**.

Figure 6.5: HMQC-PHIP $^{31}P\{^{1}H\}$ – ^{1}H NMR correlation spectrum recorded at 298 K with two scans for a sample of $IrCl(DMSO)_3$ (**III**) and (3 eq.) of **45** in 0.6 mL of toluene-d_8 showing **66** with the two axial ^{31}P resonance is located at -3.00 whereas the equatorial ^{31}P is at 15.93 ppm. The presence of the ^{31}P resonance of **62** is also observed.

Figure 6.6: The hydride region of several PHIP enhanced single scan NMR spectra at different temperatures resulting from the reaction of 8.6 mM of $IrCl(DMSO)_3$ (**III**) and 1 eq. of **49** in 0.6 mL of toluene-d_8 with 3 bar of *p*-H_2. a) 298 K; signal for **80** only. b) 308 K; signals for **79** and **80** seen. c) 313 K; signals for **79** and **80** appear with reduced intensity relative to (b).

Figure 6.7: Enhanced PHIP ^{1}H NMR spectra from a sample of 8.6 mM of $IrCl(DMSO)_3$ (**III**) and 1 eq. **50** toluene-d_8 under *p*-H_2. a) Hydride region of a spectrum at 298 K showing weak enhancement of *mer*-$IrCl(H)_2(DMSO)_3$ and **95** hydrides. b) Hydride region of a spectrum at 333 K showing strong enhancement of *mer*-$IrCl(H)_2(DMSO)_3$, **95** and **96** hydrides. Additional weak signal enhancement of **89** is also observed in this spectrum.

Figure 6.8: Enhanced PHIP ^{1}H NMR spectrum of a sample of 6.94 mM of $IrCl(DMSO)_3$ (**III**) and 1 eq. of **N** in toluene-d_8 reacted with *p*-H_2 for a ^{1}H PHIP experiment. High antiphase hydride enhancement is observed for both **75** and **76**.

Figure 6.9: Enhanced PHIP ^{1}H NMR spectrum from a sample of 8.7 mM of IrCl(DMSO)$_3$ (**III**) and 1 eq. 1.1 mg of **47** in toluene-d_8 with 3 bar of p-H$_2$. A zoom on the hydride region shows a weak hydride signal enhancement of **88** at both 298 K and 273 K.

Figure 6.10: PHIP enhanced ^{1}H NMR spectrum obtained during the reaction of 8.6 mM of IrCl(DMSO)$_3$ (**III**) with 0.5 eq. of **44** in toluene-d_8 under 3 bar of p-H$_2$. Strong hydride ligand signals enhancements result for **92** at 298 K. The expanded regions highlight the clearly visible heteronuclear ^{1}H-^{31}P and the homonuclear ^{1}H-^{1}H couplings.

Figure 6.11: First PHIP enhanced hydride signals spectra of a series of sequential experiments recorded from a sample of a) 0.54 mM of IrCl(COD)(PCy$_3$) (**IV**) with 5 eq. of DMSO in 0.6 mL of toluene-d_8 and b) Similar sample was made in dichloromethane-d_2 showing both first spectrum have comparable signal intensity.

Figure 6.12: a) Normalised integrals of three sequential PHIP hydride signals recorded from a sample of 0.54 mM of IrCl(COD)(PCy$_3$) (**IV**) with 5 eq. of DMSO in 0.6 mL of dichloromethane showing the hyperpolarised hydride signals decaying to zero after the second scan. b) Similar sample was now made in toluene where the corresponding sequential enhanced hydride signal integrals result to hydride signals persisting after the twelves scan.

Figure 6.13: Proposed mechanism of H$_2$ dissociation in **92** IrCl(H)$_2$(DMSO)$_2$(44). The H$_2$ addition is preceded by dissociative loss of DMSO a vacant site on the intermediate I. In the intermediate, there is an interconversion between the chloride and the vacant site.

Figure 6.14: a) Hyperpolarised ^{1}H NMR spectrum recorded from a sample of 17.2 mM of IrCl(DMSO)$_3$ (**III**) and 1 eq. of **46** in 0.6 mL of toluene-d_8 under 3 bar of p-H$_2$ showing strong hydride signals enhancement for **75**, **76** and **77**. b) The second resulting PHIP ^{1}H NMR spectrum shows strong hydride signals enhancement of only **75**, **76**.

Figure 6.15: Zoom of the hydride region for a hyperpolarised ^{1}H NMR spectrum recorded from a sample of 17.2 mM of IrCl(DMSO)$_3$ (**III**) and 1 eq. of **46** in 0.6 mL of toluene-d_8 under 3 bar of p-H$_2$. It highlights the stronger hydrides signal enhancement for **75** compared **76**. The opposite behaviour was observed the phosphine **45** is employed.

Figure 6.16: Schematic description of the stable complexes that provides enhanced antiphase hydride signals after PHIP experiments

Figure 7.1: Chemical structures of the phosphines **10**, **44**, **45** and **46** used in the Earth's magnetic field studies and metal catalyst IrCl(COD)(IMes) (**I**), IrCl(DMSO)$_3$ (**III**) and IrCl(COD)(PCy$_3$) (**IV**)

Figure 7.2: In black, ^{1}H NMR spectrum of 200 mL of phosphine **10** acquired in the Earth's magnetic field after pre-polarisation for 4 s at 18.8 mT. The signal averaging was 256 scans. In blue, density matrix simulation obtained using Spinach in Matlab.

Figure 7.3: Enhanced PHIP ^{1}H NMR spectrum recorded from a sample of 8 mM of **III** with 1 eq. of **45** in toluene-d_8 under 3 bar of p-H$_2$ showing the hydride signals for **62** and **58** as well as free and bound DMSO.

Figure 7.4: a: Earth's field NMR spectrum from a sample of 10 mM of **III** was reacted with 18 mM (1.8 eq.) of **45** in 4 mL of toluene-d_8 showing two antiphase peak separated by 35 Hz. The inner separation of the antiphase peak of each peak is 6 Hz. b) Simulated spectrum using a Matlab program showing perfect match with the experimental spectrum.

Figure 7.5: Matlab simulations of the **58** spin system (^{1}H, ^{1}H and ^{31}P) where the dihydrides starting state is (a) $(I_{1z} - I_{2z})$ and (b) $2(I_{1z}I_{2z})$. Matlab simulations of the **62** spin system (^{1}H, ^{1}H, ^{31}P and ^{31}P) where the dihydrides starting state is (a) $(I_{1z} - I_{2z})$ and (b) $2(I_{1z}I_{2z})$.

Figure 7.6: EF NMR spectrum obtained from a sample of 9.26 mM of **III** with 1.8 eq. of **45** in 4 mL of proto-toluene. Higher signal intensity of the spectrum was obtained with deuterated phosphine with less signal averaging (128 scans)

Figure 7.7: ^{1}H EF NMR spectra recorded on a sample of 9.26 mM of **III** with 1.8 eq. of deuterated **45** in 4 mL of toluene under *p*-H_2. a) 8 scans with a PTF of 51.7 μT for 2 s before a π/4 pulse. b) 4 scans with a PTF of 6.5 mT for 10 s before a π/2 pulse. c) 8 scans with a PTF of 6.5 mT applied for 1.5 s before a π/4 pulse. d) 16 scans with a PTF of 51.7 μT applied for 2 s before a π/4 pulse.

Figure 7.8: Hydride region of a PHIP enhanced ^{1}H NMR spectrum recorded from a sample 2 mg of IrCl(COD)PCy_3 (**IV**) with 5 eq. of DMSO in dichloromethane-d_2 under 3 bar of *p*-H_2. The key *J* couplings involved in the **92** spin system are highlighted.

Figure 7.9: ^{1}H EF NMR spectra recorded from a sample of sample of 5.27 mM (13 mg) of **IV** with 5 eq. DMSO in 4 mL dichloromethane-d_2. a) 128 signal averaging where a PTF of 64.4 μT switched on for 3 sec before a π/4 pulse. b) 32 signal averaging where a PTF of 6.5 mT was turned on for 10 sec before a π/2 pulse applied.

Figure 7.10: a: Experimental hyperpolarised *in-situ* EF NMR spectrum from a sample of 10.5 mM (26 mg) of **IV** with 5 eq. DMSO-d_6 in 4 mL dichloromethane-d_2. The spectrum acquired with 128 scans where a PTF of 64.4 μT was applied for 3 s before a π/4 pulse, showing signal of **92** in the Earth's magnetic field. b: Simulated spectrum involving 3 spins ^{1}H, ^{1}H, ^{31}P where the starting state is $(I_{1z} - I_{2z})$.

Figure 7.11: Simulation of **92** spin systems involving 3 spins ^{1}H, ^{1}H, ^{31}P where the starting state is $2(I_{1z}I_{2z})$.

Figure 7.12: Earths field NMR spectra recorded on a sample of 13.5 mM (26 mg) of **III** with 0.7 eq. of PCy_3-D_{33} in 4 mL toluene. a) 128 scans, with a PTF of 51.7 μT for 3 sec before a π/4 pulse. c) 128 scans with a PTF of 51.7 μT applied for 3 s before a π/4 pulse. b) 32 scans with a PTF of 6.5 mT for 10 s before a π/4 pulse. d) 32 scans with a PTF of 6.5 mT applied for 10 sec before a π/4 pulse.

Figure 7.13: ^{1}H NMR FID (a) and spectrum (b) recorded with a π/2 pulse and 512 signal averaging from a sample of 10.4 mM (20 mg) of **III** mixed with 10.28 mg (0.9 eq.) of **46** in 0.4 mL of toluene in presence of *p*-H_2.

Figure 7.14: SABRE ^{1}H EF NMR spectrum of free DMSO recorded by applying a PTF of 6.5 mT for 10 sec before a π/2 pulse

Figure 7.15: Simulated ^{1}H NMR spectra of **75** spins systems (^{1}H, ^{1}H and ^{31}P). a and b, the dihydrides starting state is the $2I_{1z}I_{2z}$ term and the transverse relaxation time T_2 was respectively set to 50 and 500 ms. c and d, the dihydrides starting state is the $(I_{1z} - I_{2z})$ term and the transverse relaxation time T_2 was respectively set to 50 and 500 ms.

Figure 9.1: a) Nutation curve recorded with a 500 mL bottle of water at the Earth's magnetic field. b) One scan ^{1}H EF NMR spectrum of a sample of 500 mL of water sample acquired with a 90° pulse. A pre-polarising field of 18.8 mG was used for a duration of 4 s.

Figure 9.2: a) Reproduced from the literature. Schema of the *in situ* SABRE hyperpolarisation set-up. The reaction chamber containing the SABRE solution sits inside the EF NMR probe. *p*-H_2 from the

generator is bubbled through the solution by passing through the frit within the chamber. The pressure difference across the *p*-H_2 inlet and the exhaust is set by the user and controlled by the polariser unit. b) Pulse sequence for *in situ* SABRE hyperpolarisation with EF NMR detection which is described in detail above.

Figure 9.3: Pulse sequence used for *p*-H_2 EXSY.

Figure 9.4: Pulse sequence loop for phosphine complexes

List of Tables

List of Schemes

List of Abbreviations

ALTADENA	Adiabatic Longitudinal Transport After Dissociation Engender Nuclear Alignment
BF	Brute Force
CINDP	Chemically Induced Dynamic Nuclear Polarisation
COD	*cis*,*cis*-1,5-cyclooctadiene
COE	cyclooctene
COA	cyclooctane
CSA	Chemical Shift Anisotropy
COSY	Correlation Spectroscopy
DMSO	Dimethyl sulfoxide
DNP	Dynamic Nuclear Polarisation
EF NMR	Earth's Field Nuclear Magnetic Resonance
EXSY	Exchange Spectroscopy
Emf	electro motive force
HMQC	Heteronuclear Single Quantum Coherence
INEPT	Insensitive Nuclei Enhanced by Polarisation Transfer
NMR	Nuclear Magnetic Resonance
NOE	Nuclear Overhauser Effect
p-H_2	*para*-hydrogen
PHIP	*Para*-hydrogen Induced Polarisation
PASADENA	Parahydrogen and Synthesis Allow Dramatically Enhanced Nuclear Alignment
PTF	Polarisation Transfer Field
r.f	Radio frequency
SABRE	Signal Amplification By Reversible Exchange
SEOP	Spin-Exchange Optical pumping
SQUIDS	Superconducting Quantum Interference Devices
SNR	Signal-to-Noise Ratio
TMS	Tetra-methyl silane
TEP	Tolman Electronic Parameter
ULF	Ultra-Low Frequency
ZQ_x	Zero-Quantum-x
ZULF	Zero and Ultra-Low Field
I	IrCl(COD)(IMes)
II	$[Rh(COD)(PPh_3)_2]BF_4$
III	$IrCl(DMSO)_3$
IV	$IrCl(COD)(PCy_3)$
NHC	N-Heterocyclic Carbene
1 = $BnNH_2$	Benzylamine
2 = POEA	Phenoxyethylamine
3	2,4,6-triflurobenzylamine
4	$IrCl(H)_2$(**1**)(DMSO)(IMes)

5	$[Ir(H)_2(IMes)(\mathbf{1})_3]Cl$
6	$[Ir(H)_2(IMes)(\mathbf{1})_2(DMSO)]Cl$
7	$IrCl(H)_2(\mathbf{2})(DMSO)(IMes)$
8	$[Ir(H)_2(IMes)(\mathbf{2})_3]Cl$
9	$[Ir(H)_2(IMes)(\mathbf{2})_2(DMSO)]Cl$
10= PPh_2H	diphenyl phosphine
11= $POPh_2H$	diphenyl phosphine oxide
12	diterbutyl phosphine oxide
13	diterbutyl phosphite
14 = $PMePh_2$	diphenyl methyl phosphine
15 = PMe_2Ph	dimethyl phenyl phosphine
16	diphenyl vinyl phosphine oxide
17	Triphenylphosphine sulphide
18	Trimethylphosphine sulphide
44 = PCy_3	Tris-cyclohexyl phosphine
45 = PPh_3	Tris-phenyl phosphine
46 = PCy_2Ph	Dicyclohexyl phenyl phosphine
47	Tri(*p*-tolyl)phosphine
48	Tris(4-methoxyphenyl) phosphine
49 = PBn_3	Tris-benzyl phosphine
50 = $P(OPh)_3$	Tris-phenyl phosphite
51 = $PMePh_2$	Methyl diphenyl phosphine

بسم الله الرحمن الرحيم

لطفلي الذي غادر باكراً لينضم إلى ملائكة الفردوسي

Acknowledgments

I would like to thank my supervisors Prof. Simon Duckett and Dr Meghan Halse for giving me the opportunity to be part of the Marie Curie training network ZULF NMR. I am also indebted to Dr Aneurin Kennerley for his continual encouragement as my independent panel mentor. Their constant support, guidance and great advice throughout this PhD journey were priceless.

I would like to express my great thanks to all my friends and colleagues from the CHyM and Halse Labs. Helena: the love of my life, Vicky A., Vicky L., Alastair, Fraser, Matheus, Pete, Matt, Olga, James, Ben, Wissam, Jenny and Liz for their moral support and intellectual stimulus. Special thanks to Vicky A., Lyndsay and Denise for their technical support. Many thanks to Ana for being a great friend and support; I will miss our charity shopping and Nandos party. Callum and Paven, my procrastination friends, I am also very grateful for knowing you. I will miss the ''Thursday Coffee morning''.

I would like to express special thanks to the Marie and Kim family for hosting me in their family during all occasions and all their great support during the COVID lockdown. You made me not feel lonely in York. I am very grateful that we have crossed paths.

To my dear friend Marianna, many thanks for all your support since my first day in CHyM and for always having attentive ears. I will miss our trips to the seaside.

To my mother, I am so lucky and grateful to have you. Without your love and wisdom, none of this would have been possible. To my father, my first teacher, thank you for the unconditional love you have for your ''thiat'' and for always pushing me beyond my limits. Many thanks to all my family.

Finally I would like to express my immense gratitude to my guardian angel for keeping the ''batine'' always on and the great connection.

Declaration of Author

I declare that this thesis is a presentation of original work and I am the sole author. This work has not previously been presented for an award at this, or any other, University. All sources are acknowledged as References.

Chapter 1 : Introduction

1.1 Introduction

Standard nuclear magnetic resonance (NMR), using magnetic fields of 4.7 Tesla or above, is commonly utilised for a range of applications such as determining the structure of organic molecules in solution and exploring the chemo-physical properties of solids and crystalline materials. NMR also has a well-recognised application in medicine as an imaging tool known as magnetic resonance imaging (MRI). In solution state NMR, the key information that can be obtained includes chemical shift, which provide information on the chemical environment of the nucleus and are field dependant, and J-couplings, which are field independent and provide information on chemical bonding. Standard NMR spectrometers that use superconducting magnets are very expensive (often costing hundreds of thousands of pounds) and require expert maintenance and cryogens.

The more recent development of benchtop NMR spectrometers (between 1-2 Tesla) has seen a global effort in reducing the cost, the size and the complexity of these instruments[2, 3]. In this regime, both J-coupling and chemical shift information are present but this latter has a smaller dispersion. These new machines have found now broader applications in both academic and industry because they can be used on the workbench inside the chemistry laboratory. For example, benchtop NMR has been shown applicable to real-time monitoring of various chemical processes[4-6].

The emerging field of ZULF (Zero and Ultra Low Field) NMR also offers an alternative to standard high-field NMR. ZULF is defined as the regime in which the detection magnetic field is equal to the Earth's magnetic field or below: from tens of micro-Tesla to the nano-Tesla regime. This PhD project is part of the European training network, zero and ultra-low field nuclear magnetic resonance (ZULF NMR), funded by the European Commission under the Marie-Curie action that aims to develop and implement ZULF NMR techniques that offer some potential advantages over standard high field NMR spectrometers[7]. The potential benefits of ZULF NMR include low cost (just few thousands of pounds), and portability. At high field, the chemical shift is quoted in part per million (ppm), whereas in the Earth's field (where 1 ppm ~ 2 mHz) chemical shift differences are not observed and vanishes. Therefore, resolution relative to the magnitude of the couplings is needed, which instead is used to give information. ZULF NMR has been shown to provide a route to chemical analysis, with the potential for industrial and medical applications, including imaging, by the observation of only hetero-nuclear J-coupling interactions[8-10]. Unlike chemical shift, scalar J-couplings are field independent, allowing for their observation in the ZULF regime and direct comparison to those measured at high field. ZULF NMR therefore might offer an alternative for developing countries that cannot afford the high cost and expert maintenance required for high field NMR.

Despite being widely used, the sensitivity of NMR is often limited due to the low energy difference between nuclear spin states at ambient temperature, even in the highest available magnetic fields. The population differences across nuclear spin states are governed by Boltzmann statistics, which can be used to calculate the polarisation, *P*, for a sample. Polarisation is defined as the normalized population difference between the nuclear spin states[11]. The NMR signal intensity is proportional to the concentration of the target nuclei in the sample, *C*, and the polarisation, *P* that is the normalised population difference between the Zeeman energy levels. The polarisation, *P*, which can be calculated for a given nucleus at temperature, *T*, and field strength, B_0, using Boltzmann statistics. The intrinsic property of each nucleus is the constant gyromagnetic ratio γ.

The equation of polarisation is given in section 2.1. In some cases the polarisation, and hence the NMR sensitivity, can be artificially, albeit transiently, increased well above its low thermal equilibrium level. This possibility was demonstrated at the dawn of NMR by Carver and Slichter in 1953[12], when they increased *P* of ^{7}Li nuclei through polarisation transfer from free electrons. A method that consisted of applying a stronger magnetic field that increases *P* before detection at much weaker field was also used to tackle this sensitivity issue[13].

1.1.2 Hyperpolarisation methods

In modern NMR, hyperpolarisation is the term given to all methods that boost the sensitivity of magnetic resonance by increasing the population imbalance between nuclear energy levels. Hyperpolarisation has been used to generate MR signals enhanced by many orders of magnitude and has gone some way to address the insensitivities of NMR[14]. Large numbers of hyperpolarisation schemes have been proposed since the experiments of Carver and Slichter. The most widely used hyperpolarisation methods include: brute force (BF)[15], dynamic nuclear polarisation (DNP)[16, 17 18] spin-exchange optical pumping (SEOP)[19], and *Para*hydrogen induced polarisation (PHIP)[20, 21]. These hyperpolarisation techniques differ in both the source of their polarisation and the method of transfer to the target nuclei. In this section, are briefly described the common hyperpolarisation methods that exist. More details on PHIP are given in section 2.4, which is the hyperpolarisation method used in this thesis.

1.1.2.1 Brute Force (BF)

BF consists of generating thermal polarisation using higher fields and/or very low temperatures to generate polarisation, followed by NMR signal detection at lower fields at room temperature. The most common implementation of BF consists of integrating a Halbach permanent magnet (~2 T) to a lower magnetic field NMR instrument. Key advantages of this approach are that it does not require the Halbach magnet to have high levels of field homogeneity and which does not need superconducting magnet. Another approach is to pass a fixed amount of current to a coil to produce the necessary magnetic field to pre-polarise the magnetic moments of a sample. This is a relatively easy and cheap method; however using an electromagnet does not yield as high a level of polarisation as using a Halbach array. The main advantage of an electromagnet over a Halbach array is that the magnetic field can be changed by controlling the amount of electric current applied. However, unlike a Helbach magnet that needs no power, an electromagnet requires a continuous supply of current to maintain the magnetic field, which is limited by resistive heating of the wire. Higher polarisation levels can be reached with stronger magnetic fields and cryogenic temperatures[22, 23]. At a temperature of 15 mK the polarisation of carbon reaches 23% at 14 T[24]. In practice, this is limited by the difficulty of reaching such low temperatures. Alternatively, samples may be warmed to room temperatures after polarisation to acquire a high-resolution spectrum in the liquid state. There are, however, considerable disadvantages to low temperature Boltzmann polarisation, as the processes driving the polarisation build-up is very slow so the waiting times to build-up polarisation, which often exceed ~100 hrs, prohibit production of large hyperpolarised samples. However, long T_1 values are a consequence of this method and can be beneficial for transport. For example, frozen ^{13}C-pyruvate at 50 K and 2 T has a longitudinal relaxation time T_1(^{13}C) of ~1 h, and ~24 hrs of waiting time if dropping

to 10 K[15]. Therefore, it could be delivered to imaging in hospitals, as the hyperpolarised state is 'stored' for an hour.

1.1.2.2 Dynamic Nuclear Polarisation (DNP)

The DNP technique was built upon the theoretical work of Overhauser[16] in 1953 who predicted what is known before as Overhauser effect. Overhauser-DNP (O-DNP), is most commonly performed in the liquid state, although it has been observed in the solid state as pioneered back by Pound and Abragam[25, 26]. DNP, relies on unpaired electrons as the source of the large spin polarisation, because γ_{elec} is 660 times larger than γ_{prot}. Polarisation transfer is triggered by saturation of the electron paramagnetic resonance (EPR) transition and occurs due to cross relaxation between the hyperfine-coupled electron and adjacent nuclear spins. When the magnetic field is increased, O-DNP efficiency is expected to decrease due to the electrons Larmor frequency being larger than the frequency of modulation of the electron-nucleus hyperfine interaction, hence making magnetisation transfer much less efficient. The magnetisation transfer is expected to be smaller for magnetic fields larger than 2 T (50 GHz electron Larmor frequency, 80 MHz proton Larmor frequency)[27, 28]. However, the last 20 years have seen by Rob Griffin develop the technique such that there are now many applications of DNP in solid state MAS NMR[29]. The new experiments are typically performed at cryogenic temperatures, and commercial equipment is now readily available. Jan Henrik Ardenkjær-Larsen introduced a new method where DNP is used to sensitize liquids known as dissolution-DNP (d-DNP)[30]. d-DNP takes advantage of the very large polarisation arising from the electron, which can be close to 100% at liquid helium temperatures, by transferring polarisation in the solid state to adjacent nuclei whilst in a field of for example, 7 T. The polarised sample is rapidly dissolved in a hot solvent and transferred to the NMR spectrometer for detection. In practice, there is a difficulty in reaching 1.5 K, and polarisation build-up often takes hours. Furthermore, thawing of a hyperpolarised sample must take place on a much faster timescale than relaxation. The fact that once relaxed the sample needs to be repolarised means it reflects a very challenging technique to optimise. Additionally, the method is expensive (approx. £1 million) is a consequence of the complexity of this cryogenic instrumentation. Despite these challenges, many ^{13}C and ^{15}N enriched biomolecules have been hyperpolarised with d-DNP, including ^{13}C-pyruvic acid[31], ^{13}C-bicarbonate[31], ^{13}C-fumarate[32], ^{13}C-glutamine[33], ^{15}N-choline[34] and some of these, have found applications in medicine. These examples show that the major application of d-DNP lies currently in MRI rather than in NMR research. An alternatively, route to polarised electrons, optical DNP, involving photogenerated triplet states, which result in chemically-induced dynamic electron polarisation (CIDEP) via a radical-triplet pair mechanism (RTPM)[35] is providing excitement. Here, cross-relaxation between proton and electron generates nuclear polarisation by the Overhauser mechanism without the need of microwave irradiation.

1.1.2.3 Spin-Exchange Optical Pumping (SEOP)

SEOP of the alkali metal atoms began with Zeeman's studies of sodium vapour[36], then Kastler who established the technique as it is known today[37]. In SEOP, the vapour of an alkali metal, like rubidium, is electronically spin-polarised when placed in a magnetic field and illuminated with resonant circularly polarised light. Then, the electronic spin polarisation of the alkali metal vapour is transferred to nuclear spins of noble gas atoms like ^{3}He and ^{129}Xe during gas-phase collisions. ^{3}He has the greatest γ value of 45.42 MHz/T (and hence highest per-atom detection sensitivity), and until recently it was

the easiest to achieve the highest levels of polarisation. However, major drawbacks of ^{3}He are reflected in its low natural abundance and the fact it is not a renewable resource. In contrast, relatively inexpensive ^{129}Xe is spin-1/2 and has a γ of −11.7 MHz/T, whilst also being naturally abundant and amenable to near-unity hyperpolarisation. ^{129}Xe is almost chemically inert, has a large chemical shift range, exhibits a reasonable solubility in blood and other living tissues and is used as an anaesthetic[38]. All these properties promoted ^{129}Xe to be the most widely used gas in SEOP. SEOP is a relatively cheap and easy method that yield to high level of polarisation but is limited to ^{129}Xe nuclei and some other noble gases; however, quadrupolar isotopes such as (^{21}Ne, ^{83}Kr, and ^{131}Xe) have also been successfully hyperpolarised[39, 40-42]. However, SEOP is limited to the hyperpolarisation of noble gases, thus limiting its applications. The major application of SEOP is in *vivo*-MRI, especially for imaging airspaces such as lungs[43]. Xenon in MRI can be paired with a targeting approach by reversibly trapping xenon atoms in hydrophobic molecular cages such as cryptophanes to form so-called biosensors that include a targeting moiety for a particular analyte[44, 45]. These reversible host–guest complexes also allow for indirect detection through saturation transfer techniques without significantly impairing the relaxation behaviour of hyperpolarized xenon. In addition, xenon exhibits a large chemical shift range in various cryptophanes. This enables the simultaneous use of different cages to probe different target molecules, thereby providing a different sensors[45]. Comprehensive studies of correlated biological events can therefore be achieved.

1.1.2.4 *Para*-Hydrogen Induced Polarisation (PHIP)

Of particular interest in this thesis are PHIP and its non-hydrogenative version Signal Amplification by Reversible Exchange (SABRE). They both use *para*hydrogen (p-H_2) gas as the hyperpolarisation source[46]. The use of p-H_2 as a route of hyperpolarisation was first predicted by Bowers and Weitekamp[21] in 1986 and exemplified shortly after[47]. In 1997, Bargon and Nattanaer[46], then in 2007 Bowers, described the spin-physics underlying hyperpolarisation with p-H_2 and its production route. p-H_2 molecules are bound (reversibly in SABRE, or irreversibly in hydrogenative PHIP experiments) to a substrate molecule, to produce a ^{1}H-polarised product. This typically requires the use of a metal catalyst; however, examples of molecular tweezers that can perform PHIP without a metal catalyst have been shown[49-51]. PHIP is traditionally performed with transition metal rhodium based phosphine complexes. In contrast, the iridium-phosphine complexes, which are now replaced by the iridium-carbene complexes, catalysed SABRE. Building on the early PHIP work, Golman[52, 53] and Bargon[54, 55] demonstrated that the proton hyperpolarisation can be transferred to carboxyl ^{13}C nuclei to yield hyperpolarised ^{13}C contrast agents in seconds using either RF-based or field-cycling hyperpolarisation transfer approaches, respectively. Initial PHIP studies used a rhodium-based phosphine complex but developments since then have focused on iridium-based phosphine and subsequently iridium-based carbene complexes, due to their greater activity[56]. p-H_2 can be readily produced and then stored and used for several weeks afterwards. Furthermore p-H_2 can deliver highly hyperpolarised molecules[57] as hydrogenation products or without altering them, in a period of seconds. In its simplest form, it is therefore relatively cheap (<£1,000) and simple, excluding the spectrometer cost. It does however require an understanding of metal-catalysis. A more detailed review of PHIP method is provided in section 2.5

1.2 History of Ultra-low field NMR

Due to the very low thermal polarisation in the ZULF regime, ZULF NMR requires hyperpolarisation methods to boost its sensitivity. Therefore, hyperpolarisation is always used prior to ZULF NMR detection. The most common method used in ZULF NMR is BF as this only requires a pre-polarising magnetic field. Because *p*-H_2 methods are relatively cheap, efficient, and can be scaled to produce large quantities of highly hyperpolarised substrate in seconds, it is proposed in this thesis that they are well suited to being used in conjunction with ZULF NMR. Furthermore, as the hyperpolarised nuclear states it creates do not originate from the very small detecting magnetic field, new portable, low-cost, less confined NMR instruments can be used for detection instead of the large superconducting magnets of standard NMR.

Packard and Varian first demonstrated ZULF NMR using detection in the Earth's field (EF), in 1954 by observing the precession of proton spins in a sample of water and hydrofluoric acid[58]. Since all EF NMR experiments require a pre-polarising field that increases the polarisation beyond the Boltzmann distribution across the nuclear spin states, this pioneering experiment is in fact an early example of a hyperpolarisation experiment. A pre-polarising field of 100 G perpendicular to the Earth's magnetic field was turned-on for a sufficiently long time (seconds) for the polarisation to build-up before it was turned-off non-adiabatically and the NMR signal was detected without an excitation pulse. It corresponds to a precession frequency for ^{1}H of 2185 Hz with ^{19}F being 120 Hz less. Just two years after this, Elliott and Schumacher[59] measured the J-coupling between ^{1}H and ^{19}F from a sample of fluorobenzene in the Earth's magnetic field, verifying the field independence of the spin-spin coupling. In 1982, Callagan and LeGros[60, 61] presented the first EF NMR apparatus that measured the nuclear dipole moment and relaxation times of both ^{1}H and ^{19}F from 200 mL samples of water and perfluorodelcalin. This equipment was presented as a possible teaching tool for a laboratory environment. In 1990, J. Stepisnik and co-workers[62, 63] used the Earth's magnetic field to show the first example of EF NMR imaging. In 1994, Planinstic and co-workers[64] published their works on longitudinal relaxation time measurements T_1 and imaging of plants in an outdoor setting, avoiding any disturbance of the highly homogenous Earth's magnetic field. From 1994 to 2009, Callaghan and co-workers utilized an EF NMR apparatus in Antarctica to investigate the structure of sea ice via the ^{1}H NMR signal of liquid brine as well as diffusion measurements using pulsed gradient spin echo (PGSE) NMR[65, 66]. More recently, Fukushima and co-workers have worked on detection in Antarctica of oil spills that were trapped in the ice with an EF NMR apparatus. They have also designed and optimised strong pre-polarising coil, which needed to be significantly larger than the ice thickness of 1 to 2 m in order for the field to penetrate the ice[67-69]. Remarkably, the same team reported the first remote detection of a thin layer of oil floating on water under an 81 cm thick surrogate ice block in the Earth's magnetic field with a helicopter-borne prototype NMR instrument on the ice[70].

As these examples show, the main application of the EF NMR has been in outdoor settings rather than in a standard laboratory environment. The Callaghan group worked on the development of an apparatus to allow its indoor use, in a conventional laboratory setting. The main challenge for indoors use is the disturbance of the highly homogenous, but weak, Earth's magnetic field by the proximity with any ferrous objects. Therefore, a major improvement was the integration of a shimming coil. In 2004, Magitrek Ltd developed the commercial Terranova-MRI, a 3D MRI-capable teaching system for students and teachers in a normal laboratory environment. Since then, more recent focus has been in the domain of NMR spectroscopy[71, 72]. In these last decades, many research groups have demonstrated the usefulness of EF NMR, judged by the increasing amount of published work across the NMR community. For example, Los Alamos National Laboratory has been also developing affordable Earth's magnetic apparatus combined with sensitive detectors called Superconducting Quantum Interference Devices, (SQUIDs)[1, 73-75]. This detector is able to measure extremely small

disturbances in a magnetic field produced by structural differences located at the surface or inside a material, even in the presence of large background magnetic noise. One drawback is that SQUIDs must operate at cryogenic temperatures. They also demonstrated an affordable MRI scanner operating with the Earth's magnetic field[76]. These MRI instruments combined with magnetoencephalography (MEG) were designed for the purpose of imaging both brain structure and function with the help of the direct observation of the interaction of neural currents with the spin population and ULF relaxometry. Later on, they used the MRI instrument, which is suitable for use in a public setting, to image through non-ferrous foils and cans, for a non-invasive inspection of liquids in airports by using relaxometry to identify materials. Appelt et al.[77, 78] have demonstrated high-resolution heteronuclear J-coupling spectra for a number of organic molecules and successfully detected ^{1}H, ^{7}Li and ^{19}F nuclei in the Earth's magnetic field. They have also shown for the first time high resolution ^{129}Xe hyperpolarisation in the Earth's magnetic field that allowed a direct observation of the large chemical shift differences of ^{129}Xe gas that was dissolved in various organic liquids. In a more recent paper, they have explained the interpretation of strongly coupled spectra allowing chemical analysis in low magnetic field[79]. Halse et al.[80] have successfully recorded a 2D ^{1}H-^{19}F COSY spectrum acquired in the Earth's magnetic field with DNP hyperpolarisation. Later on, Hamans et al.[81] pioneered a method to achieve NMR using the Earth's magnetic field on a dilute sample by applying *p*-H_2 induced polarisation. Simultaneous ^{19}F and ^{1}H detection of a sub-millimolar sample was realized with just one scan during the hydrogenation of trifluoro-but-2-ynoate.

By the time of writing this thesis, most available EF NMR instruments are equipped with an inductive detection coil, like the instrument used in this thesis. This is less sensitive for lower detection frequencies and can pick-up both external and internal noises. The advantages of EF NMR spectrometers come therefore at the expense of the signal-to-noise ratio (SNR) due to the inefficiency of inductive detection at lower frequencies. In addition, the low magnetic field strength (~50 μT for Earth's field) results in a lack of chemical shift dispersion and a very small population difference between the nuclear spin states and hence very low sensitivity. That is why hyperpolarisation techniques are always used in conjunction with EF NMR in order to transiently increase the sensitivity. These developments have harnessed NMR using natural Earth's magnetic field and have set up the way toward the progression to this thesis. Let us now focus on NMR using a magnetic field smaller than the Earth's magnetic field.

When the static magnetic field is below the Earth's magnetic field in the nanoTesla regime, alternative types of detection provide improved sensitivity. To achieve nanoTesla fields, the Earth's magnetic field is passively cancelled using a μ-metal shield, which can reduce the ambient Earth's field by factor of thousands. Two common methods are SQUIDs[82] or optical detection using atomic magnetometers[83]. Before the advent of Spin exchange relaxation-free, (SERF) magnetometers, SQUIDs were the predominant tool for detection of ZULF NMR signals[84]. For now, let's focus on the atomic magnetometer. In this method, the sample is firstly pre-polarised (by one of the hyperpolarisation techniques listed above), then shuttled to the detection region close to the alkali vapour cell. The detection is based on the measurement of the magnitude of the magnetic field emanating from the NMR sample via the ground-state precession of angular momenta in vaporized alkali metal atoms like K, Rb, or Cs. The sensitivity of an atomic magnetometer is limited by relaxation due to spin exchange collisions. In this zero-field regime, the relaxation is completely prohibited and the alkali vapour become Spin-Exchange Relaxation Free (SERF)[85-87] and is then more sensitive. Currently, SERF magnetometers have surpassed SQUIDs and are the most sensitive sensors, achieving an ultrahigh sensitivity of 0.16 $fT/Hz^{1/2}$ [88]. Wietekamp and Pine pioneered the zero field NMR in 1983[89]. First, they observed that in solid-state NMR and in the absence of an external magnetic field (zero field), all spins experience only their mutual local field (from the surrounding electrons). This yields a finite number of allowed transitions thus increasing the resolution of the spectrum in a powder sample. In their

pioneering experiment, powdered barium chlorate hydrate [$Ba(ClO_3)_2.H_2O$] was observed in zero field with a resolution better than the single crystal of the same molecule observed at high field. A year after, they published similar evidence in their letter, where heteronuclear spin pairs were analysed in the absence of an external magnetic field[90]. Budker and co-workers have also contributed extensively in this field[91, 92]. In 1986 and 1987, Pine and co-workers developed the theory of pulses in the zero field regime[93, 94]. Since the 2000's a large number of works have been published harnessing the zero field NMR area[91, 95-98]. Theis et al.[99, 100] and all Appelt[79] and others[9] have analysed the J-coupling multiplets derived from zero field spectra, thus providing a general analysis tool. Blanchard et al have contributed toward the understanding of J-spectroscopy emanating from zero field NMR spectra[101]. Ledbetter et al.[102], Theis et al.[103, 104] have pioneered PHIP hyperpolarisation in conjunction with zero field NMR. More recently, Barsky et al. have analysed in 2019 for the first time chemical exchange with zero field NMR spectroscopy[8].

Using a pre-polarising field B_p of 18.8 mT will enhance the NMR signals using the BF method such that they are observable in the EF. It has to be noted that this field is limited by the resistive heating of the EF NMR coil. However, this often require large volumes (>200 mL) of neat sample in order to increase the number of spins contributing to the signal and signal averaging. When combined with hyperpolarisation techniques such as PHIP, EF NMR can be performed with sub-millimolar concentrations and minimal sample volumes (< 5 mL) whilst achieving greater SNR. In this work, optimisation of the hyperpolarisation conditions using high field NMR (9.4 T and 11.7 T) was needed prior to the EF NMR studies. In fact, the high magnetic field provides both the high resolution and chemical dispersion required to characterize the organometallic complexes investigated. Kinetics and thermodynamics studies have allowed identification of the hyperpolarisation conditions of complexes that undergo PHIP i.e., what ligand excess and temperature are optimum for a minimum consumption of material.

1.3 Aims of this work

The motivation for this PhD thesis is the identification of systems (compounds and complexes) that can react with *p*-H_2 and provide strong hyperpolarised signals. The ultimate goal is then to detect these systems in ZULF NMR regime, particularly the Earth's magnetic field. Due to travel restriction of COVID-19 pandemic from March 2020 until early 2022, this thesis does not contain any ultra-low field NMR (below Earth's magnetic field) works. Instead, EF NMR detection is the focus in this work as a test bed, which tackled many of the same challenges and gives comparable information as in the nano-Tesla regime. As a complementary analysis tool to the ultra-low field NMR, standard high-field NMR is used to characterize and determine molecular structure of these systems. The research presented within this thesis can be considered as being split into two major themes. Firstly, the characterisation of complexes formed in solution and the optimisation of their hyperpolarisation level and conditions using standard high field NMR. Secondly, the Earth's field NMR detection of the optimised systems.

This thesis starts in **Chapter 2** by describing the appropriate theoretical background of NMR and *p*-H_2 hyperpolarisation. Attention is placed upon specific aspects of relevance to experiments at both High field and the Earth's magnetic field. Key properties of the metal - carbene and metal – phosphine complexes are also explained.

Chapter 3 describes the *in situ* EF NMR hyperpolarisation and detection of three amines: benzylamine, phenoxyethylamine and 2,4,6-trifluorobenzylamine, using an EF NMR instrument. The aim was therefore to increase the substrates amenable to SABRE in the Earth's magnetic field. The catalytic activation processes of SABRE are followed *in-situ* and hyperpolarised longitudinal relaxation times, T_1, are measured in the low field regime. The hyperpolarisation level of these amines are measured in the presence of the co-ligand, dimethyl sulfoxide (DMSO). The effect of the co-ligand on the polarisation level is studied using *in situ* EF NMR and directly compared to the SABRE polarisation detected using a 43 MHz benchtop NMR spectrometer. In parallel, the chemical exchange rate of the ligands (both amines and hydrides) and the corresponding thermodynamic parameters for these complexes are explored at 11.7 T (500 MHz) to develop an understanding of the role of the co-ligand in the SABRE hyperpolarisation of amines.

Chapter 4 aims to identify *p*-H_2-based methods for the hyperpolarisation of a range of phosphorus compounds (i.e. phosphines, phosphates, phosphites and phosphine-sulfides) with a view to using ZULF NMR spectrometers (Earth's field NMR and an atomic magnetometer) for detection. ^{31}P containing molecules are interesting for ZULF NMR because they can provide the J-coupling detectable in that regime. In order to achieve this task, optimisation of *p*-H_2 hyperpolarisation conditions using high field NMR (500 MHz) is necessary in order to characterize all complexes formed in solution and to investigate their reactivity with *p*-H_2. Using this approach allows for optimisation of the hyperpolarisation conditions of complexes to achieve high PHIP or SABRE activity, e.g. what ligands excess and temperature are optimum, to be carried out with a minimum consumption of materials. The aim of this chapter was to establish routes to hyperpolarisation at high field and then to determine if any of these reactions could then be scaled up for detection with the Earth's field spectrometer.

Chapter 5 explores the reactivity of $IrCl(DMSO)_y(P)_x$ (where P_x are a list of phosphine ligands that differ in their electronic and steric properties) [y = 2, 1, 0 when x = 0, 1, 2] towards H_2 addition. The goal was then to understand the reactivity of these formed complexes before tackling their hyperpolarisation studies. Prior to hydrogenation, reaction of $IrCl(DMSO)_3$ (**III**) with eight different phosphines is monitored. This complex undergoes *mono*, *bis* and *tris* substitution of DMSO by phosphine to form the corresponding 16 electron complexes $IrCl(DMSO)_2(P_x)$, $IrCl(DMSO)_1(P_x)_2$ and $IrCl(P_x)_3$ according to the excess of phosphine added. Some of these complexes have the ability to undergo C-H bond activation of the phosphine ligand and subsequently orthometallation reactions take place. This yields 18 electron complexes, which are in equilibrium with the 16 electron precursors. The comparable reactivity of these complexes is then monitored towards H_2, where they form various 18 electron dihydride species. The similarities and differences in behaviour are highlighted. Indeed, the selected phosphines ligand are different in size and electron donation ability, which is expected to change their behaviour. The formation of a series of thermodynamic and kinetic products is indicated according to NMR measurements.

Chapter 6 investigates the reaction with *p*-H_2 of the previously formed complexes (chapter 5) from the reaction of eight phosphines with $IrCl(DMSO)_3$ (**III**). This sixth chapter is therefore a continuation of the fifth chapter where these reactions were already monitored with normal H_2 gas to determine reactivity alongside thermodynamic and kinetic products. The aim was therefore to select the complexes that provided largest hyperpolarisation level detectable in the ultra low field regime. The products that are able to hyperpolarise are then optimised with respect to parameters such as reaction temperature, solvent and ligand excess. Furthermore, the mechanism of dihydrogen dissociation is also determined because it directly correlates with the gained signal enhancement. The

hyperpolarisation level and lifetime of these products are important factors that are rationalised and used to calibrate the experiments that will subsequently be carried out at Earth's magnetic field. This optimisation of the hyperpolarisation conditions at high field is used to select the best conditions for Earth's magnetic field detection.

Chapter 7 selects the phosphine complexes from Chapter 6 that provide large hydride hyperpolarisation at room temperature at high magnetic field and then detects them using the Earth's field NMR device. Here, the aim was to demonstrate the feasibility of metal complexes detection in the Earth's magnetic field through their hydride ligands. The ^{31}P ligands break the symmetry of the di-hydride ligands in the complexes such that they become magnetically inequivalent. This process enables the detection of the hyperpolarised hydride signals in the strong coupling regime where there is no chemical shift information but where the J-couplings information between hydrides and ^{31}P ligands can be measured. This section is therefore a continuation of the two preceding chapters, where many studies were done to understand the reactivity of **III** with a number of phosphine ligands. *Mono*-phosphine or *bis*-phosphine substitution were obtained in some cases with efficient *p*-H_2 activity. In addition, the position of the phosphine ligands *trans* or *cis* to the hydride ligands yielding coupling for the former (~150 Hz) and the later (~20 Hz) provided a unique signature in the EF NMR spectra. The interpretation of the EF NMR spectra is aided by density matrix simulations.

Chapter 8 provides a general conclusion for the PhD project and discusses some ideas for future work and potential improvements to the methods developed in the thesis.

Finally, **Chapter 9** presents the experimental details and methods used throughout the thesis and the Matlab code for the density matrix simulation used in **Chapter 7** is provided in the **Appendix**.

Chapter 2 : Theory

2.1 Theory of Nuclear magnetic resonance

In this section, the theory that supports the experimental chapters is described.

Note that in this thesis, the "hat" symbol will be used for operators and vectors will be in boldface whereas scalar variables will be in italic.

Matter is composed of atoms. Each atoms possesses a nucleus. When the nucleus contains an odd number of protons or an odd number of neutrons (or both), it possesses an extra property, in addition to their charge. This extra property is a magnetic moment (**μ**) and can be described by the nuclear spin quantum number (I). The angular momentum vector $(\mathbf{I})$ and the magnetic moment are both vectors and are related through a proportionality constant called the gyromagnetic ratio, γ, as shown in Equation 2.1.

$$\boldsymbol{\mu} = \gamma \mathbf{I} \quad (2.1)$$

The angular momentum operator $\hat{\mathbf{I}}$ has three scalar Cartesian components; $\hat{I}_x$, $\hat{I}_y$ and $\hat{I}_z$.
Nuclear spin (I) is an intrinsic property of each atomic nucleus, and can take half integer or whole-integer values. Those nuclei for which $I = 0$, such as ^{12}C or ^{16}O, have no nuclear spin and do not exhibit magnetic resonance (MR) properties. For the purpose of this thesis only in spin-1/2 nuclei are of interest; specifically the proton ^{1}H, fluorine ^{19}F and phosphorus ^{31}P, which have a natural abundance of 99.99%, 100% and 100% respectively and a relatively high gyromagnetic ratios of 42.57 MHz/T, 40.08 MHz/T and 17.23 MHz/T. Quadrupolar NMR that utilises nuclei that have spin >1/2 is also possible, although this is not discussed here[105].
In the absence of an external magnetic field, the magnetic moments of an ensemble of free spins are randomly oriented. However, when they are placed in a uniform magnetic field, B_0, an interaction occurs which result in quantised energy levels as depicted in Figure 2.1 for a spin-1/2 nucleus.
The resulting two energy levels are separated by the Zeeman splitting, which depends linearly on magnetic field. These two levels are labelled α and β. The Hamiltonian, which describe the energy of this system is given in Equation 2.2, where the spin Hamiltonian is assumed to be proportional to $\hat{I}_z$ because the magnetic field B_0 is along the z-axis

$$\hat{H}_0 = \omega_0 \hat{I}_z \quad (2.2)$$

ω_0 is the Larmor frequency and defined as:

$$\omega_0 = -\gamma B_0 \qquad (2.3).$$

As energy levels are quantised, specific frequencies of radiation are required to excite transitions between them. These energies can be calculated according to Equation (2.4) and (2.5), where ΔE is the energy difference between these two energy levels, $\hbar$ is the reduced Planck's constant, and v is the radiation frequency[106]. v is the Larmor frequency in frequency units (Hz) whilst ω_0 is the Larmor frequency in angular units (rad s^{-1}) in which the factor $1/2\pi$ is not added. m is the spin quantum number that represents a projection of the angular momentum $\hat{\mathbf{I}}$ along the longitudinal (z) direction

of the system. Here, the direction is defined by the external field, B_0. m can take any of $2I + 1$ values ranging from – I to I. Each different projection, or orientation, of the spin is associated with a magnetic energy, E_m. Equation (2.4) defines these magnetic energies.

$$E_m = -m\hbar\gamma B_0 \qquad (2.4)$$

$$\Delta E = h\nu = \hbar\gamma B_0 \qquad (2.5)$$

For a spin *I* = 1/2 particle such as the ^{1}H nucleus, there are two possible eigenstate orientations: spin-up, α = ($\frac{1}{2}$) and spin-down, β = ($-\frac{1}{2}$), with corresponding energies given by $E_{-1/2} = \frac{1}{2}\hbar\gamma B_0$ $E_{1/2} = -\frac{1}{2}\hbar\gamma B_0$.

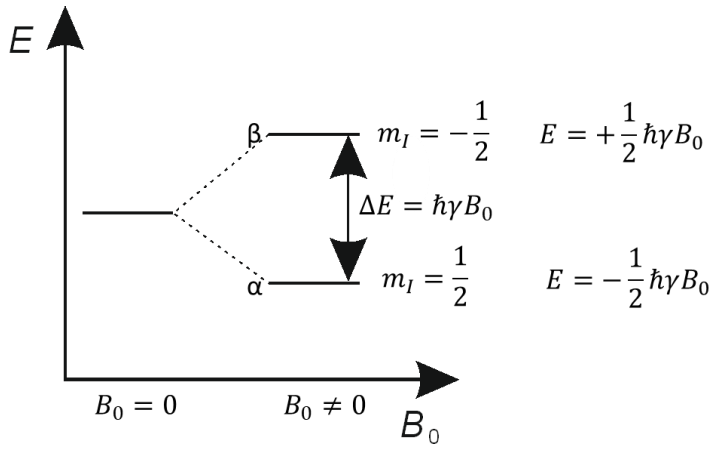

Figure 2.1: The energy levels of a spin-1/2 particle in a magnetic field.

As nuclear spin energy levels are very closely spaced in energy, only relatively low frequency (radio-frequency *r.f.*, in the MHz range) or low energy radiation is needed to match the resonance condition described in Equation (2.5).

When measuring an ensemble of spins, the nuclei have a preference to exist in the lower energy state, α. There is a difference in population for these two energy levels, $N_\alpha - N_\beta$ according the Boltzmann distribution of Equation 2.6[106], where k is the Boltzmann constant, and T is the temperature:

$$\frac{N_\beta}{N_\alpha} = e^{-\Delta E/kT} \qquad (2.6)$$

As it will be seen in section 2.4, this population difference controls NMR sensitivity. This is often defined as the polarisation level of Equation 2.7. The equation for polarisation is simplified for any temperature above few K, according to the so-called "high temperature approximation" as the energy gap is small compared with kT:

$$P = \frac{N_\alpha - N_\beta}{N_\alpha + N_\beta} = \tanh\left(\frac{\gamma\hbar B_0}{2kT}\right) \approx \frac{\gamma\hbar B_0}{2kT} \qquad (2.7)$$

At a field strength of 9.4 T and temperature of 298 K, only ~33 ^{1}H spins in a million contribute to the macroscopic NMR signal. For example, the polarisation level for ^{1}H and ^{31}P are 3.5×10^{-6} and 1.42×10^{-6} respectively. . Polarisation can be increased either by reducing the temperature or increasing the strength of the magnetic field, according to Equation (2.7).

2.2 The vector model

The detected response of an NMR experiment can be modelled as a vector that rotates that angular momentum operator in real 3D space[106]. This leads to the 'vector model' of NMR as illustrated in Figure 2.2 for an arbitrary sequence of events. At equilibrium, the magnetic moments are not aligned randomly but have a preference to align with the field in such a way that the sum of their contributions gives a net magnetic field along the direction of the applied field (B_0). This is called the bulk magnetisation of the sample and is represented by the magnetisation vector ($\mathbf{M}$ in blue). This is initially oriented along the z-axis, which corresponds to longitudinal magnetisation. It is then rotated into the xy-plane, which corresponds to transverse magnetisation, and then freely precesses around the magnetic field axis. In NMR, two concepts of "rotating frame" and "lab frame" are often used to describe the spin Hamiltonian, defined above. The spin Hamiltonian, in the presence of radio-frequency (*r.f.*) field, is time dependant. In order to make the spin Hamiltonian appears as time independent, the rotating frame is introduced. This represents a simplification that views the nuclear spins from a frame that rotates "with the (*r.f.*) field", hence avoiding rather complicated mathematics. The rotating frame spin Hamiltonian then becomes Equation 2.8:

$$\hat{H} = \Omega_0 \hat{I}_z \qquad (2.8)$$

Where the frequency $\Omega_0 = (\omega_0 - \omega_{\mathrm{ref}})$ is the difference between the Larmor frequency and that of the frame. It is called the offset frequency or resonant offset and is denoted Ω_0.

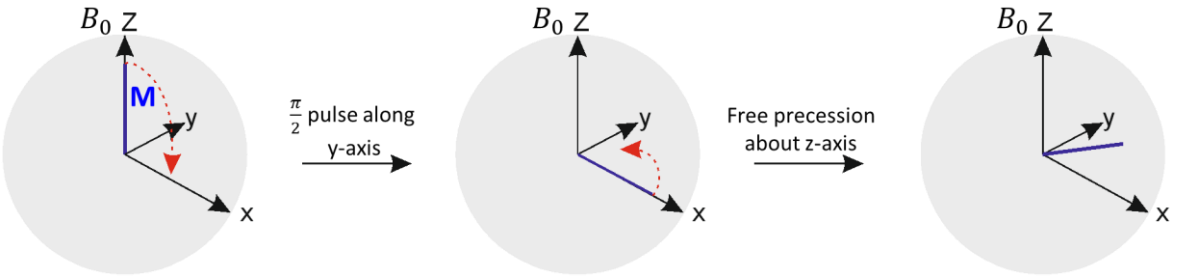

Figure 2.2: The vector model. The net magnetisation vector is shown in blue. The sequence shown is a π/2 pulse rotating the magnetisation vector around the y-axis, followed by free precession of the spins around the z-axis.

The vector can be defined by three components: $\hat{M}_z$, $\hat{M}_x$, and $\hat{M}_y$.[106] As the net magnetisation is an average over the ensemble of spins, it points along the direction of the applied magnetic field is labelled $\hat{\boldsymbol{M}}_{\boldsymbol{z}}$. therefore, depends on the number of spins and the polarisation. Under thermal conditions net magnetisation is orientated along the direction of B_0 while contributions from $\hat{M}_x$ and

$\widehat{M}_y$ are 0 as nuclear spins lose their phase coherence due to random precession in the transverse (xy) plane. This is depicted in Figure 2.2 in which the vectors $\mathbf{M}$ and B_0 are parallel. Upon the application of an (*r.f.*) pulse B_1 which is termed here as nutation frequency ω_{nut}, $\mathbf{M}$ is rotated away from the direction of B_0 and the two are no longer parallel.[106] The magnetisation vector will now experience a twisting force resulting in the precession of $\mathbf{M}$ around B_0 as shown in Figure 2.2. This precession will occur at the Larmor Frequency, $\omega_0 = -\gamma B_0$.[106]

In term of energy, the spin Hamiltonian in the presence of a pulse of frequency ω_{nut} and an angle θ, has now an x and y component[105]. Equation 2.9 describes it.

$$\widehat{H} = \Omega_0 \hat{I}_z + \omega_{nut}(\hat{I}_x \cos\theta + \hat{I}_y \sin\theta) \quad (2.9)$$

The flip angle is defined as $\theta = \omega_{nut}\tau_p = \gamma B_1 \tau_p$, where B_1 is the strength of the (*r.f.*) field, ω_{nut} is the nutation frequency and τ_p is the pulse duration. Hence, by varying the time for which the pulse is applied, the angle through which the magnetisation is rotated can be varied. As the magnetisation precesses around the magnetic field B_0 it maps out a circle on the transverse plane which is largest when $\mathbf{M}$ is perpendicular to B_0. At this point $\widehat{M}_x$ and $\widehat{M}_y$ make a contribution to $\mathbf{M}$ while the longitudinal magnetisation, $\widehat{M}_z$ is 0[106]. NMR signals are detected in the transverse plane from precessing xy magnetisation. This will be most intense when $\mathbf{M}$ is rotated 90° from $\widehat{M}_z$ to $\widehat{M}_{xy}$ and is the reason why $\pi/2$ pulses are used in NMR to excite the nuclear spins. It is therefore important to choose (*r.f.*) pulses of appropriate duration and amplitude such that $\mathbf{M}$ is rotated into the transverse plane.

Here, the concepts of populations and coherence are briefly introduced by avoiding rather complicated equations. As described above using the vector picture the $\pi/2$ pulse has two effects. Firstly, the pulse equalizes the populations of the two states and hence the longitudinal magnetisation, $\widehat{M}_z$ is reduced to 0. Simultaneously, it converts the population differences into coherences. Coherences arise from spins in states that are a superposition α and β and that have transverse polarisation vectors. Immediately following the pulse, these transverse spin polarisation vectors precess in the *xy* plane with the same frequency and phase, giving rise to a net magnetization in the *xy* plane, $\widehat{M}_{xy}$. The coherence can have orders, which are the difference in z-angular momentum of the connected states. For an ensemble of non-interacting spins ½ at equilibrium, there are only two states, with z-angular momentum quantum numbers ±1/2 and a coherence order 0. Once the pulse is applied, two coherence orders, (+1)-quantum and (-1)-quantum are created. Only the (-1)-quantum coherence is detected and gives rise to the NMR signal.

2.2.2 Relaxation

The initial net magnetisation is a result of thermal equilibration in the presence of the static field B_0 and governed by the Boltzmann equation as defined above (Equations 2.6 and 2.7). The $\pi/2$ pulse B_1 equalises the population difference created by the static field B_0 and generate coherences. Relaxation naturally occurs when the system is out of equilibrium. Relaxation in NMR is the process by which a nuclear spin system returns to its thermal equilibrium state. It is assumed that at the end of the pulse, the (*r.f.*) field is turned off and an interval τ is allowed. Two major changes are observed experimentally:

Firstly, thermal equilibrium values are gradually reached by the spin state populations and hence are time dependant. The (*r.f.*) pulse causes the state of the spin system to depart from thermal equilibrium. Over a sufficiently long time, the fluctuating molecular surroundings cause the thermal equilibrium state to be gradually re-established. Secondly, the coherence gradually decays to zero and thus has a lifetime. Hence, the spins lose their synchronisation. These deviations are a consequence of relaxation.

Bloch[106] has introduced two relaxation time constants. The time constant T_1 (longitudinal relaxation time or spin-lattice relaxation time constant) and the time constant T_2 (transverse relaxation time or spin-spin relaxation time constant).

The time taken for the longitudinal magnetisation to reach equilibrium is characterised by the time constant, T_1.[106] This time constant describes the relaxation of $\mathbf{M}$ from $\widehat{M}_{xy}$ toward $\widehat{M}_z$ and is given in Equation (2.10). The (*r.f.*) pulse equalizes the populations and then they relax back to their different equilibrium values. Longitudinal relaxation involves an exchange of energy between the spin system and the molecular surroundings. Note that $\boldsymbol{M_0}$ is the magnetisation vector at equilibrium.

$$M_z(t) = M_0 \left(1 - e^{\frac{-\tau}{T_1}}\right) \qquad (2.10)$$

The decay of magnetisation in the transverse plane is characterised by a time constant, T_2, as described by Equation (2.11). This behaviour is due to random dephasing of magnetic moments whilst interacting with other spins. T_2 is typically shorter than T_1.[106] In many case the spins execute hundreds of millions of precession circuits before losing synchronisation. The decay of coherence does not necessarily involve any exchange of energy with surroundings. However, coherence decay does increase the entropy of the spin ensemble. The decay of coherence is therefore an irreversible process.

$$M_{xy}(t) = M_0 \left(e^{\frac{-\tau}{T_2}}\right) \qquad (2.11)$$

An additional relaxation rate constant T_2* can also be introduced. T_2* describes the rate at which precessing nuclear spins dephase in the xy-plane. If a spin system is subject to a magnetic field gradient, the spins in different regions of the sample will see different B_0_fields and precess at different frequencies. This can lead to rapid dephasing of transverse magnetisation due to magnetic field inhomogeneity. Dephasing due to field inhomogeneity is different to T_2 because it is a coherent dephasing of spins, and a spin echo[106] can be used to rephase the spins to recover the transverse magnetisation, but T_2 relaxation is an incoherent process and cannot be reversed. T_2* includes both effects and therefore is always less than or equal to T_2.
The spin echo sequence consists of a π pulse, which is sandwiched by the equivalent time τ before the signal is recorded. By the end of the second τ any dephasing due to inhomogeneity is refocused, meaning that at the end of the second delay τ, the magnetisation is along the same axis of origin, regardless of the value of τ and the offset Ω_0.

2.2.3 NMR spectrum: chemical shift and *J*-coupling

2.2.3.1 Chemical shift

The precessing transverse nuclear magnetisation induces a signal (an electric current) in the coil surrounding the sample. The resulting signal is referred to as a free induction decay (FID) and is typically an exponentially decaying sinusoidal function. The current is amplified and subjected to

quadrature detection. The two outputs of the quadrature detector are digitized and stored in the computer as a set of complex numbers. The NMR signal is then Fourier transformed to obtain the NMR spectrum.

Two pieces of chemical information are obtained in a standard NMR spectrum: chemical shift and indirect dipole-dipole couplings, which comprise heteronuclear and homonuclear couplings. In order to introduce the concept of chemical shift, the atomic level of a sample need to be considered. Now suppose that the magnetic field is highly homogenous across the sample, then all spins in a molecule experience the same magnetic field and have the same Larmor frequency. On the microscopic scale, this is not true. The precise Larmor frequency of a given nucleus depends on the atomic environment. In fact, the cloud of electrons surrounding the nuclear spins are magnetic and act on those spins. These electronic effects can "shield" or "de-shield" the effect of external field B_0 on the nuclear spins thus changing slightly the Larmor frequency of each nucleus according their local environment. A chemical shielding factor σ can then be defined, which shifts the resonance frequency of a nuclear spin. This factor is included in Equation 2.12.

$$\omega_j = -\gamma_j B_0(1-\sigma) \qquad (2.12)$$

Where ω_j and γ_j define the Larmor frequency and the gyromagnetic ratio for a given nucleus *j*.
It is however possible those two nuclei have the same shielding factor, which make them chemically equivalent. The shielding factor is in the order of 10^{-6} for ^{1}H and 10^{-5} for ^{31}P [107]. In NMR, the equation of the chemical shift, δ, is then introduced as relative frequency scale that does not depend on the magnetic field and the instrument. It is a ratio that removes the dependence of the magnetic field used on the chemical shift, which now depends only on the sample. Equation 2.13 therefore gives the magnetic field independence of the chemical shift.

$$\delta = \frac{\omega_j - \omega_j^{ref}}{\omega_j^{ref}} \times 10^6 \qquad (2.13)$$

Where ω_j^{ref} is the frequency of the reference compound, which is typically tetramethyl silane (TMS) for ^{1}H, ^{13}C and ^{29}Si.
While the value of chemical shift in ppm is designed to be field independent, the observed separation between peaks in Hz and hence the chemical shift dispersion, in Hz, is field dependent. In the Earth's field (where 1 ppm ~ 2 mHz) chemical shift differences are not observed.
It is possible that two nuclei in in the same chemical environment have the chemical shift. They are then called chemically equivalent.

2.2.3.2 Spin-spin coupling

Spin-spin couplings are among the most informative of nuclear spin interactions as they lead to visible splitting of the detected NMR signals. These interactions are not magnetic field dependant, and therefore active in ZULF NMR spectroscopy when the chemical shift term is negated. The nuclear spins feel the magnetic field emanating from their neighbours through the electrons located in chemical bonds that connect them. This type of interaction is called "indirect" and therefore differs from "direct" dipole-dipole couplings which, are not considered in this thesis.

The homonuclear *J*-coupling are on the order of 1-100 Hz whereas heteronuclear J-couplings are on the order of 1-1000 Hz. At high magnetic field, where first order coupling governs the splitting, it is possible to observe both homonuclear and heteronuclear *J*-couplings. However, only the heteronuclear *J*-couplings are commonly observed in the low field that are classified as second order couplings. In some case, when the symmetry is broken with heteronuclear couplings then homonuclear couplings are also revealed at low field.
Two nuclei are called magnetically equivalent if they are chemically equivalent in addition of having the same J-coupling to all other nuclei in the molecule.

- **First order *J*-coupling**

The NMR signal for a nucleus having n equivalent spin 1/2 neighbours is split into $n+1$ line. This is called the $n+1$ rule and is common at high magnetic field or in the weak coupling regime that will be described in Equation 2.16.
As B_0 increases, the difference in Larmor frequency between two coupled spins increase and the spectra becomes first order. According to Pople notation[108], Spin systems for first order spectra will use letters far in the alphabet (AM, AX), to indicate difference in frequencies.

- **Second order *J*-coupling**

Complex splitting patterns are observed as the $n+1$ rule is not obeyed at weaker magnetic fields or in the strong coupling regime that will be also described in Equation 2.18. As B_0 decreases, the deference in Larmor frequency between two coupled spin decrease and the spectra become second order. Spin systems for second order spectra will use letters close in the alphabet (AB, ABC), to indicate similarity in frequencies. The eigenstates of the system are now a mix of Zeeman and singlet-triplet states. Predicting and analysing the NMR spectra is therefore much more difficult and the only practical approach of understanding these strongly-coupled spectra is by computer simulation.

2.2.4 Theory for EF NMR simulation

As already stated, the interpretation of EF NMR spectra are not straightforward due to the lack of chemical shift. However, the presence of heteronuclear spin-spin coupling allows the identification of chemical identities. The EF NMR spectra exhibit second order couplings, therefore a computer simulation allows for their interpretation. This section is the theoretical description needed for EF NMR and builds from the spin Hamiltonian, its density operator evolution and observation operators. The tasks are listed as follow. Firstly, spin systems are constructed and required operators are detailed. Secondly, required evolution and rotation operators are generated alongside with the density matrix at equilibrium. Relaxation might be accounted in the system with another type of operator. Then, the density matrix is manipulated by the required evolution/rotation operators. Finally, the observation operator is applied and a spectrum is generated.

As a tool of comparison and interpretation, the Spinach simulation package[109] run in the Matlab software package and a Matlab script (Written by Dr M. Halse) were used here to simulate Earth's field NMR (EF NMR) spectra. For the most part, Spinach simulates the NMR spectrum automatically and requires little coding experience of the user. As a user, just a few inputs must be edited according

to the simulation need. Firstly, the molecule is constructed with the number and type of nuclei involved along with the detection magnetic field. Followed by the matrix construction that defines the basis set in which all couplings involved in the molecule are defined. Then, the processing parameters that include where the magnetisation start and how it will be observed, the number of points, the centre frequency spectrum, the nuclei being decoupled, the spectral width as well as zero-filling factor are all set. Finally, the section of the evolution and observation of the system of the simulation as well as the Fourier transformation and the plotting are also edited by the user.

In order to understand how the simulation works, the quantum description of NMR must be taken in account. Let us first introduce the matrix representation of the three angular momentum operators in the Zeeman eigenbasis $\{|\alpha\rangle, |\beta\rangle\}$ given in equation 2.14:

$$\hat{I}_x = \frac{1}{2}\begin{pmatrix} 0 & 1 \\ 1 & 0 \end{pmatrix} \quad \hat{I}_y = \frac{1}{2i}\begin{pmatrix} 0 & 1 \\ -1 & 0 \end{pmatrix} \quad \hat{I}_z = \frac{1}{2}\begin{pmatrix} 1 & 0 \\ 0 & -1 \end{pmatrix} \quad (2.14)$$

2.2.4.1 Spin Hamiltonian

The system is described by the spin Hamiltonian operator $\hat{H}$, which provides information about the energies of states in a spin system. The spin Hamiltonian of a system in the presence of a strong magnetic field is given in Equation (2.15) which contains the Zeeman and scalar coupling interactions, where ω_I and ω_S are the Larmor frequencies for the two heteronuclear spins operators $\hat{\boldsymbol{I}}$ and $\hat{\boldsymbol{S}}$, and J_{IS} is the scalar coupling between them.

$$\hat{H} = \omega_I \hat{I}_z + \omega_S \hat{S}_z + 2\pi J(\hat{\boldsymbol{I}} \cdot \hat{\boldsymbol{S}}) \quad (2.15)$$

where $\hat{\boldsymbol{I}} \cdot \hat{\boldsymbol{S}} = \hat{I}_x\hat{S}_x + \hat{I}_y\hat{S}_y + \hat{I}_z\hat{S}_z$

High field NMR satisfies the weak coupling regime, where the frequency separation of the two heteronuclear coupled spins is much larger in magnitude than the magnitude of the scalar coupling between the two spins. This is the case when $\hat{\boldsymbol{I}}$ and $\hat{\boldsymbol{S}}$ precess at different Larmor frequencies, which are in the order of 10^8 Hz, compared to J_{IS}, which typically has a magnitude on the order of 1-1000Hz. The magnetic field is therefore approaching infinity and satisfies Equation (2.16).

$$\xi = \frac{\omega_I - \omega_S}{J_{IS}} \gg 10 \quad (2.16)$$

Under these weak coupling conditions, it is permissible to apply what is known as the secular approximation to the Hamiltonian[105], which states that the indirect spin-spin coupling terms are small compared to the Zeeman terms and so only, the $\hat{I}_z\hat{S}_z$ components of the indirect spin-spin coupling interaction need to be considered. However, in the low field regime, the secular approximation cannot be used anymore, as the weak coupling regime is no longer satisfied. The full Hamiltonian must be used that has a consequence of increasing the numerical simulation.

In an ultra-low magnetic field, such as the Earth's magnetic field, the Hamiltonian that describes a system of $n + m = N$ interacting spins, including both heteronuclear and homonuclear indirect spin-spin coupling but neglecting the small effects of chemical shift that vanishes is described in Equation (2.17).

$$\hat{H} = \sum_{j=1}^{n}\sum_{k=1}^{m} 2\pi J(\hat{\boldsymbol{I}}_j \cdot \hat{\boldsymbol{S}}_k) \quad (2.17)$$

EF NMR is in the strong coupling regime where the frequency separation of the resonance from two heteronuclear coupled spins operators $\hat{I}$ and $\hat{S}$, is comparable with the coupling constant between them. At hypothetical low field, the condition in Equation (2.18) is therefore satisfied.

$$\xi = \frac{\omega_I - \omega_S}{J_{IS}} = 0 \quad (2.18)$$

2.2.4.2 Density Operator

The density operator $\hat{\rho}$ provides information regarding the state of an ensemble of spins in a system and is therefore a simplification of the spin ensemble[105]. Any macroscopic observation may be deduced from two spin operators, with one representing the observable that is being measured and the other representing the state of the entire spin ensemble, independent of the number of spins it contains. Instead of specifying the individual microscopic states of ~10^{22} spins, the value of a single operator, i.e. the spin density operator $\hat{\rho}$ can be specified.

The matrix representation of the density operator, for an ensemble of non-interacting spin ½ is given in Equation (2.19).

$$\hat{\rho} = \begin{pmatrix} \rho_{\alpha\alpha} & \rho_{\alpha\beta} \\ \rho_{\beta\alpha} & \rho_{\beta\beta} \end{pmatrix} = \begin{pmatrix} \overline{c_\alpha c_\alpha^*} & \overline{c_\alpha c_\beta^*} \\ \overline{c_\beta c_\alpha^*} & \overline{c_\beta c_\beta^*} \end{pmatrix} \quad (2.19)$$

The overbar indicate an average over the ensemble. The right-hand-side of this equation is called the density matrix. Where c_α and c_β are complex numbers called superposition coefficients.

The diagonal elements of the spin density operator $\rho_{\alpha\alpha}$ and $\rho_{\beta\beta}$ are called populations of the states $|\alpha\rangle$ and $|\beta\rangle$, respectively. The off-diagonal elements $\rho_{\alpha\beta}$ and $\rho_{\beta\alpha}$ are called coherences between states $|\alpha\rangle$ and $|\beta\rangle$. Numerical simulations of EF NMR spectra typically start with an initial density matrix, $\hat{\rho}^{eq}$, which corresponds to the statistical state of the spin ensemble at thermal equilibrium. The ensemble average of a group of spins at thermal equilibrium at a given magnetic field is given by Equation (2.20)

$$\hat{\rho}^{eq} = \frac{1}{2}\hat{1} + \frac{1}{2}\mathbb{B}\hat{I}_z \quad (2.20)$$

Where $\hat{1}$ is the unity operator that corresponds to an equal number of spins in the $|\alpha\rangle$ and $|\beta\rangle$ state, and $\hat{I}_z$ corresponds to a population difference between the $|\alpha\rangle$ and $|\beta\rangle$ state. The Boltzmann factor $\mathbb{B}$ is given by Equation (2.21):

$$\mathbb{B} = \frac{\hbar\gamma B_0}{k_B T} \quad (2.21)$$

In a sample containing ^{1}H spins in a magnetic field of 50 µT at room temperature, $\mathbb{B}$ is therefore $\mathbb{B} = 1.66 \times 10^{-10}$. $\hat{\rho}^{eq}$ can therefore be rewritten as in Equation (2.22):

$$\hat{\rho}^{eq} = \frac{1}{2}\hat{1} + 1.66 \times 10^{-10}\hat{I}_z \quad (2.22)$$

This equation therefore testify the very weak polarisation at Earth's magnetic field.

2.2.4.3 Rotating-Frame or Lab-Frame Density Operator

Then, the perturbation of the spin ensemble from equilibrium, the evolution of the system and determination of the observable magnetisation at various points of the experiment need to be included. The excitation phase of a basic NMR experiment is equivalent to a rotation. Therefore, the action of (*r.f.*) pulses (ULF pulses in the case of EF NMR) can be included in a density matrix calculation with rotation operators. The spin ½ representation of the rotation operators of an angle θ are listed in Equation (2.23):

$$\hat{R}_x(\theta) = \begin{pmatrix} \cos\frac{1}{2}\theta & -\boldsymbol{i}\sin\frac{1}{2}\theta \\ -\boldsymbol{i}\sin\frac{1}{2}\theta & \cos\frac{1}{2}\theta \end{pmatrix} \qquad \hat{R}_y(\theta) = \begin{pmatrix} \cos\frac{1}{2}\theta & -\boldsymbol{i}\sin\frac{1}{2}\theta \\ \boldsymbol{i}\sin\frac{1}{2}\theta & \cos\frac{1}{2}\theta \end{pmatrix}$$

$$\hat{R}_z(\theta) = \begin{pmatrix} \exp\{-\boldsymbol{i}\frac{1}{2}\theta\} & 0 \\ 0 & \exp\{+\boldsymbol{i}\frac{1}{2}\theta\} \end{pmatrix} \quad (2.23)$$

2.2.4.4 Evolution operators

Now, the system must evolve with time under the influence of the time-independent spin Hamiltonian. These evolutions are included in the density matrix calculation through the use of the evolution operator $\widehat{U}(t)$, defined in Equation (2.24). If the secular approximation is used, the Hamiltonian is diagonal in this representation and so the evaluation of Equation (2.24) is relatively straightforward. However, it was already noted that the secular approximation cannot be used in the context of ultra-low field NMR. The Spinach software is aware of it and therefore in the EF NMR simulation, the option 'lab-frame' instead of 'rotating frame' was chosen.

$$\widehat{U}(t) = \exp(-i\widehat{H}t) \quad (2.24)$$

To evolve a density matrix, it must be sandwiched between rotation operators as below. Commutation between the operator and density matrix will result in no change to the system. The influence of the application of the rotation operator on the density matrix at a given time *t* are listed in Equation (2.25). This means that a pulse $\theta = \pi/2$ is applied in the y direction which rotate the $\hat{I}_z$ operator towards $\hat{I}_x$.

$$\hat{\rho}_t = \hat{R}_y^{\dagger}\hat{I}_z\hat{R}_y = \frac{1}{2}\begin{pmatrix} \cos\left(\frac{\pi}{4}\right) & \sin\left(\frac{\pi}{4}\right) \\ -\sin\left(\frac{\pi}{4}\right) & \cos\left(\frac{\pi}{4}\right) \end{pmatrix}\begin{bmatrix} 1 & 0 \\ 0 & -1 \end{bmatrix}\begin{pmatrix} \cos\left(\frac{\pi}{4}\right) & -\sin\left(\frac{\pi}{4}\right) \\ \sin\left(\frac{\pi}{4}\right) & \cos\left(\frac{\pi}{4}\right) \end{pmatrix}$$

$$\hat{\rho}_t = \hat{R}_y^{\dagger}\hat{I}_z\hat{R}_y = \frac{1}{2}\begin{pmatrix} \frac{1}{\sqrt{2}} & \frac{1}{\sqrt{2}} \\ -\frac{1}{\sqrt{2}} & \frac{1}{\sqrt{2}} \end{pmatrix}\begin{bmatrix} 1 & 0 \\ 0 & -1 \end{bmatrix}\begin{pmatrix} \frac{1}{\sqrt{2}} & -\frac{1}{\sqrt{2}} \\ \frac{1}{\sqrt{2}} & \frac{1}{\sqrt{2}} \end{pmatrix}$$

$$\hat{\rho}_t = \hat{R}_y^{\dagger}\hat{I}_z\hat{R}_y = \frac{1}{2}\begin{bmatrix} 0 & 1 \\ 1 & 0 \end{bmatrix} = \hat{I}_x \quad \text{Since,} \quad \sin\left(\frac{\pi}{4}\right) = \frac{1}{\sqrt{2}} \text{ and } \cos\left(\frac{\pi}{4}\right) = \frac{1}{\sqrt{2}} \quad (2.25)$$

The solution is therefore $\hat{I}_x$. Note that $\hat{R}_y^{\dagger}$ is the conjugate transpose rotation operator.

2.2.4.5 Observation operators

Finally, the NMR signal (Equation 2.27), is generated through the observation operators given in Equation (2.26), which can measure at any point of the time the density matrix by taking the trace of the result.

$$\hat{I}_{obs} = \sum_{n=1}^{N}(\hat{I}_{nx} + i\hat{I}_{ny}) \quad (2.26)$$

Where $\hat{I}_{nx}$ and $\hat{I}_{ny}$ are respectively the real and imaginary part of the spectrum and *N* is the number of observed spin groups.

The signal at time *t* (Equation 2.27) is given by the *trace* of the observation operator timed by the density matrix. The sum of the diagonal matrix elements is called the *trace* of an operator.

$$S(t) = tr(\hat{I}_{obs} * \rho(t)) \quad (2.27)$$

The signal is recorded as free induction decay (FID) which is typically an exponential decay of a sinusoidal function. It is then Fourier transformed, which converts the NMR signal from time domain to frequency domain.

2.3 Practical Aspects of Earth's field NMR detection

2.3.1 Methodology of EF NMR

Standard EF NMR measurements are performed on the Terranova Earth's field NMR system (Magitrek, Germany) using the core apparatus, a 500 ml sample, and a PC running the Prospa and Terranova software package. The system is quite similar to the NMR description in section 2.2. In conventional NMR applications, where the static field B_0 is large, the Larmor frequency is in the radio-frequency range (according to $\omega = \gamma B_0$ in rad/sec) and it is therefore referred to as an (*r.f.*) pulse. In the Earth's magnetic field applications, this pulse is in the ultra-low frequency (ULF) (300 – 30 kHz) and so is properly called a ULF pulse.

In the common picture of NMR as described in section 2.1, the magnetisation at equilibrium of a sample placed in an external static magnetic field lies along the longitudinal or z-axis of the rotating frame shown in Figure 2.2. In the case of EF NMR, this external magnetic field is B_E, the Earth's magnetic field. The direction of B_E defines the direction of z. The flip angle θ is created by the ULF pulse or excitation pulse that disturbs the bulk magnetisation vector M_z, from equilibrium and rotates it into the transverse plane M_{xy}. This excited magnetisation vector M_{xy} precesses about the Earth's magnetic field vector which is in the z direction, at the ULF frequency. The B_1 coil detects this precessing magnetisation. The precessing bulk magnetisation vector induces an electro motive force (*emf*) or a current in the detection coil according to Faraday's law given in Equation (2.28), which states that the induced *emf* is equal to the time rate of change of the magnetic flux.

$$emf = N\frac{d\emptyset}{dt} \quad (2.28)$$

When connected to the spectrometer the B_1 coil forms a parallel LCR circuit. It is connected in parallel to a fixed capacitance C within the spectrometer and is an inductor with an inductance L, and an

internal resistance R. Equation (2.29) describes this resonant circuit, which is used to detect the EF NMR signal that resonates at a frequency ω_0.

$$\omega_0 = \frac{1}{\sqrt{LC}} \qquad (2.29)$$

As it is already know, the NMR signal arises from the phase coherence of an ensemble of precessing nuclear spins. It has been also seen that the exponential decay of the signal is a consequence of the loss of phase coherence between spin. In practice, the magnetic field is not entirely homogenous and therefore, the loss of phase coherence is not entirely due to T_2 but is rather combined effect T_2 relaxation and magnetic field inhomogeneity. In order to ensure a high degree of field homogeneity, it is important to place the apparatus on a timber table where it is free of ferrous materials and to remove to a distance of 1 – 2 m any objects likely to disturb the Earth's field homogeneity.

Three main coils constitute the apparatus, which is shown in Figure 2.4.

The inner component coil also called B_1 (transmit and receive) coil is used to excite and detect the precessing magnetisation. By changing the capacitance, the B_1 coil is tuned to the Larmor frequency of the sample. This coil has a tuning capacitance in the range of nano-Farads (nF) to tune the Larmor frequency of ^{1}H and ^{31}P frequency of about 2200 Hz and 1200 Hz respectively.

In a later improvement to the system, the Terranova spectrometer has been fitted with a set of Helmholtz coils in the three Cartesian directions x, y and z. These coils produce magnetic fields when a current is applied, which correct the direction of the Earth's natural magnetic field (B_E) in (Figure 2.3). A current of 70 mA in the y-axis allows pushes the B_E vector from xy-plane toward the z-direction. B_0 is then the effective magnetic field summing B_E and the additional field correction. The B_0 vector is then adjusted according to the experimental needs. For example, a current of 90 mA generated by the z-coil increase the Larmor frequency up to 2700 Hz. The B_0 correction to align in the z-direction, produces an accurate nutation curve, which allows an accurate pulse length calibration. It therefore yields a better signal to noise ratio (SNR) spectrum.

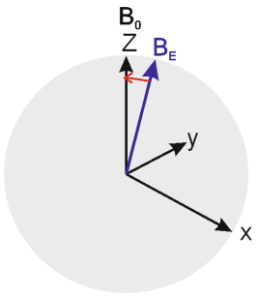

Figure 2.3: Correction of the direction of the natural Earth's field using a set of Helmotz coil where the B_E vector is aligned to z-axis.

The middle or gradient coil can provide linear magnetic field gradients across the sample. The gradient coil produces the current necessary for shimming in the three Cartesian directions, multidimensional MRI encoding and pulse and gradient spin echo (PGSE) experiments.

The outer, or polarising coil, provides an initial polarising field B_p through application of a large current, generating a nuclear magnetisation in a sample placed inside the apparatus. This method is similar to brute-force. It enables the enhancement of the sensitivity of Earth's field NMR via pre-polarising the sample with a maximum field of 18.8 mT provided by the pre-polarisation coil before excitation and detection in the very weak Earth's magnetic field. In order to obtain a good SNR of the NMR signal, the polarising coil should be placed in a good orientation because it acts as a shield to the

external ULF noise sources. The stronger the polarising magnetic field, the stronger the brute force EF NMR signals and the better the SNR. In the SABRE experiment, which will be described later, this coil is also used to generate the necessary magnetic field that triggers the polarisation transfer from *p*-H_2 to the substrates.

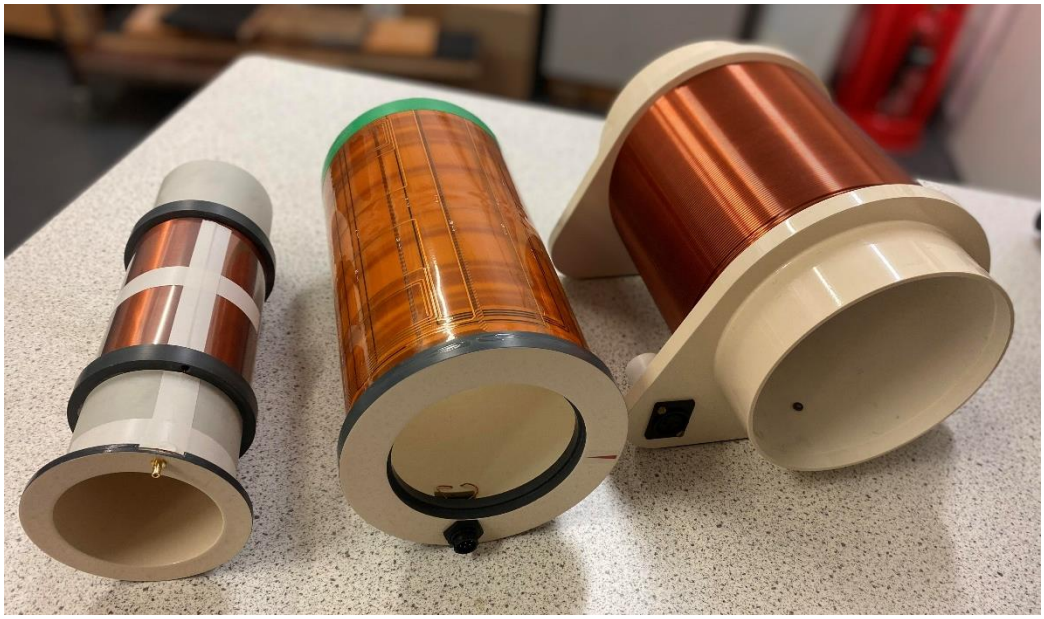

Figure 2.4: A picture of the three coils of the Earth's Field NMR probe. From left to right: the B_1 coil, the gradient coil and the polarisation coil.

One challenge of Earth's field NMR is to achieve a good quality of signal. In fact, the Earth's magnetic field is naturally highly homogenous but the field is so weak (~ 50 μT) that its homogeneity is easily disrupted by the proximity of ferrous objects or any other sources of small magnetic and electric fields. The shimming and the relative orientation of the apparatus to the Earth's magnetic field are important. Shimming is the process of iteratively applying weak magnetic fields dependent on the position across the sample until the applied fields cancel the underlying inhomogeneity of the static field. This is achieved by passing small currents through a collection of coils, in this case the gradient coils designated to generate magnetic field of specific geometries such as a magnetic field that changes linearly along one axis. It is possible to automate the process of shimming with the Terranova apparatus with the input 'autoshim'.

2.4 Hyperpolarisation

Over the last decades, many hyperpolarisation techniques have been developed to create NMR signals enhanced by many orders of magnitude[42]. Those methods were already discussed in chapter 1. However, this section describes only the hyperpolarisation method used in this thesis, which use *para*-hydrogen.

2.4.1 Spin isomers of Dihydrogen

Dihydrogen exists as two spin isomeric forms, *o*-H_2 and *p*-H_2, with the differences in the two forms being identified through the analysis of the diatomic wave-function components. This is a consequence of the antisymmetric nature of fermionic wavefunctions; hydrogen is a fermionic particle. The total wavefunction (φ_{tot}) can be separated into independent contributions according to the Born-Oppenheimer equation shown in Equation (2.30),[46] where φ_{el}, φ_{vib}, φ_{rot}, φ_{trs}, φ_{ns} are the electronic, vibrational, rotational, translational, and nuclear spin contributions, respectively.

$$\varphi_{tot} = \varphi_{el} \times \varphi_{vib} \times \varphi_{rot} \times \varphi_{trs} \times \varphi_{ns} \qquad (2.30)$$

The diatomic wave-function φ_{tot}, all combine, for H_2, to give a wave-function that is anti-symmetric with respect to exchange of the two nuclei. Since φ_{trs}, φ_{vib} and φ_{el} are all symmetric the combination of φ_{rot} and φ_{ns} spin wave-functions must be anti-symmetric. There are two combinations where this is true, when the symmetric rotational states are combined with the anti-symmetric nuclear spin state and when the anti-symmetric φ_{rot} are combined with the symmetric φ_{ns}. The terms *ortho* and *para* are associated with the symmetric and anti-symmetric nuclear spin states respectively[46].

There are four allowed spin configurations of H_2, the three which are symmetric with respect to the particle interchange are $\alpha\alpha$, $\frac{1}{\sqrt{2}}(\alpha\beta + \beta\alpha)$, $\beta\beta$ and one which is anti-symmetric, $\frac{1}{\sqrt{2}}(\alpha\beta - \beta\alpha)$. The rotational quantum number is *J*, when the value of *J* is even the rotational state is symmetric whereas when *J* has an odd value it is anti-symmetric. This means that *o*-H_2 has odd values of *J*, whereas *p*-H_2 has even values of *J* and as such occupies the lowest energy rotational states and is more stable of the two isomers. The two isomers have different spin symmetries. This means that the interconversion between the isomers is symmetry forbidden and therefore slow. This offers the opportunity to enrich and store hydrogen gas in the *para* isomer.

There is a temperature dependence associated with the relative proportions of the two isomers. At room temperature the ratio of *o*-H_2 : *p*-H_2 is 3 : 1 at thermal equilibrium; however at cryogenic temperatures in the presence of suitable paramagnetic catalyst the ratio switches in favour of the *para* isomer. Flowing H_2 gas over a silica/$FeCl_3$ catalyst at 28 K gives hydrogen gas that is 99 % *p*-H_2. As a consequence of the interconversion between the two isomers being slow, this enriched gas can be stored and used at room temperature provided there is no paramagnetic material also present[46].

The energy diagram of the two isomers of the dihydrogen molecule in the presence of a magnetic field B_0 are illustrated in Figure 2.5. Note that, in the absence of an external magnetic field, the ortho-states are degenerate.

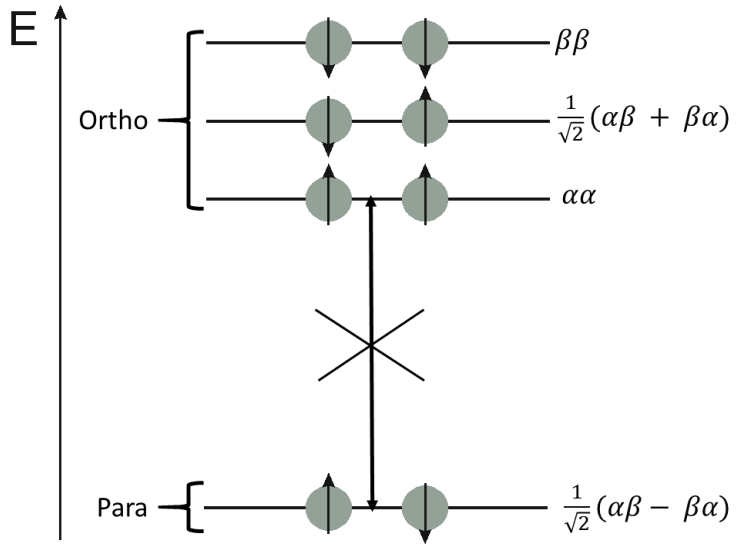

Figure 2.5: Energy level diagram of the dihydrogen molecule under the influence of a magnetic field. Upper or triplet state is *o*-H_2 and the lower or singlet state is *p*-H_2. Transitions between the ortho and para states are symmetry forbidden.

It has to be noted that in free *p*-H_2, there is magnetic equivalence between the two protons and coherent spin mixing between the singlet state and triplet states is symmetry forbidden. However, when *p*-H_2 is bound to a metal catalyst magnetic equivalence is broken. Specifically, when the two protons originating from *p*-H_2 occupy a chemically and/or magnetically inequivalent position in the complex. Consequently, the difference in their Zeeman interactions with the external field triggers the singlet-triplet spin mixing which is the *ortho-para* conversion. Figure 2.6 depicts the nuclear spin state diagram of *p*-H_2 molecule in an equivalent and inequivalent environment.

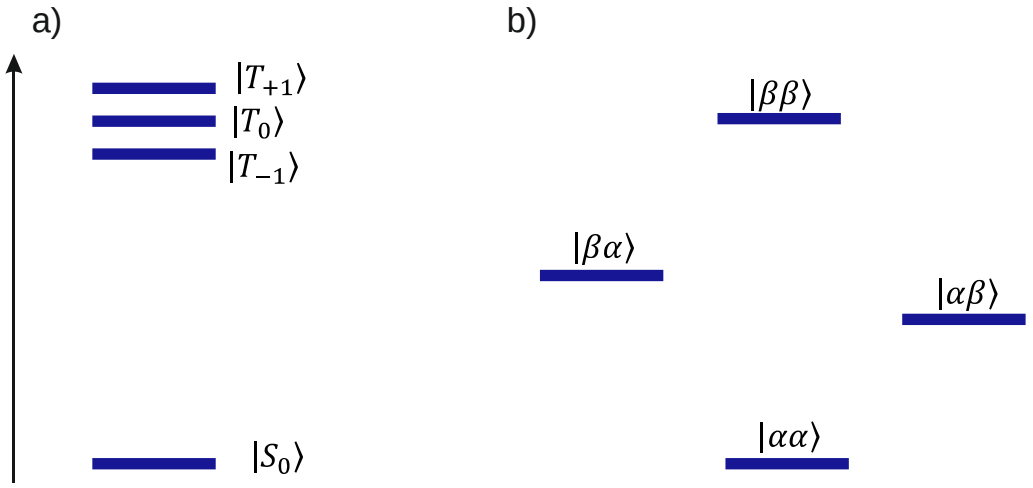

Figure 2.6: Energy level diagram for the nuclear spin states of *p*-H_2 a) before and b) after undergoing a pairwise hydrogenation reaction, which leads to a chemical or magnetic inequivalence between the two nuclei.

2.4.2 Polarisation transfer mechanism

Since *p*-H_2 itself is in the singlet state, it is NMR silent. Therefore, it needs to chemically react to be observed. Experiments with *p*-H_2 are generally performed to take advantage of either or both of the Adiabatic Longitudinal Transport After Dissociation Engender Nuclear Alignment (ALTADENA) or Parahydrogen and Synthesis Allow Dramatically Enhanced Nuclear Alignment (PASADENA) effects[46, 110].

Let us consider the case where *p*-H_2 binds to a metal catalyst to become two chemically ($\delta\omega \gg 2\pi J_{AX}$) and magnetically ($J_{AX} \neq 0$) inequivalent hydride ligands as in Figure 2.7. Then the density matrix of *p*-H_2 is defined as in Equation 2.31:

$$\hat{\rho}_{pH_2} = \frac{1}{2}\left(2\hat{I}_z\hat{I}_z + 2\hat{I}_y\hat{I}_y + 2\hat{I}_x\hat{I}_x\right) \quad (2.31)$$

Where the longitudinal term is $\frac{1}{2}(2\hat{I}_z\hat{I}_z)$ and ZQ_x is the zero-quantum-x term defined as $ZQ_x = \frac{1}{2}(2\hat{I}_y\hat{I}_y + 2\hat{I}_x\hat{I}_x)$ also called the transverse term.

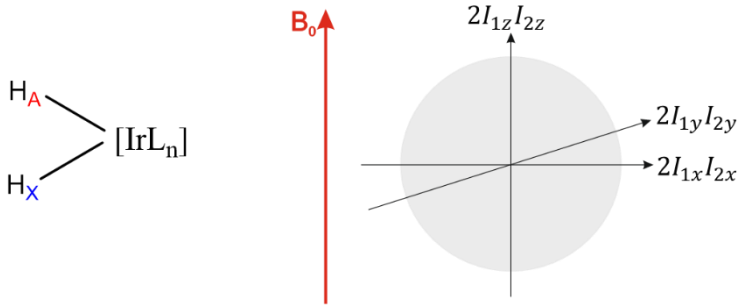

Figure 2.7: Inequivalent hydride ligands in an iridium metal catalyst

The internal Hamiltonian of the two hydrides are then given in Equation 2.32:

$$\hat{H} = -\omega_1\hat{I}_{1z} - \omega_2\hat{I}_{2z} + \pi J_{AX}\left(2\hat{I}_{1z}\hat{I}_{2z} + 2\hat{I}_{1x}\hat{I}_{2x} + 2\hat{I}_{1y}\hat{I}_{2y}\right) \quad (2.32)$$

The Hamiltonian can be split in two terms, the commuting part (H_0) and the non-commuting parts ($\hat{H}_1$) that are both given in Equation 2.33 and 2.34:

$$\hat{H}_0 = -\tfrac{1}{2}(\omega_1 + \omega_2)\left(\hat{I}_{1z} + \hat{I}_{2z}\right) + \pi J_{AX} 2\hat{I}_{1z}\hat{I}_{2z} \quad (2.33)$$

$$\hat{H}_1 = -\tfrac{1}{2}(\omega_1 - \omega_2)\left(\hat{I}_{1z} - \hat{I}_{1z}\right) + \pi J_{AX}\left(2\hat{I}_{1x}\hat{I}_{2x} + 2\hat{I}_{1y}\hat{I}_{2y}\right) \quad (2.34)$$

To produce the PASADENA enhancement effect, the sample containing the metal catalyst and the substrate that is hyperpolarised, is first pressurised with *p*-H_2, then shaken in the Earth's magnetic field for *p*-H_2 dissolution. The reaction is then performed inside the magnet in the weak coupling regime as defined in Equation (2.16).

When the limit of the magnetic field approaching infinity, where $\xi \gg 1$, as explained by Natterer and Bargon (in 1997)[46] and Bowers (in 2007)[110], the term responsible for the actual dynamics of the spin system is the scalar term $2\hat{I}_{1z}\hat{I}_{2z}$. The operators $\hat{I}_{1z}$ and $\hat{I}_{2z}$ represent the z-components of the spin angular momentum operators (with associated Cartesian components x, y and z) for spins 1 and 2,

respectively of the two ^{1}H nuclei in *p*-H_2. In this case, the initial state approached by the density operator, $\hat{\rho}_{PAS}$, can be approximated in Equation (2.35):

$$\hat{\rho}_{PAS} = \frac{1}{2}(2\hat{I}_{1z}\hat{I}_{2z}) \qquad (2.35)$$

For the case where the two ^{1}H atoms resulting from addition of a molecule of *p*-H_2 form an AX spin system in the product, the density matrix will evolve according to Equation (2.36), following a single (*r.f.*) pulse with a rotation angle θ. Upon rotations of the spins, the operators of interest are transformed as follows:

$$2\hat{I}_{1z}\hat{I}_{2z} \overset{\theta^0}{\rightarrow} \left(\hat{I}_{1z}\cos(\theta) + \hat{I}_{1x}\sin(\theta)\right)\left(\hat{I}_{2z}\cos(\theta) + \hat{I}_{2x}\sin(\theta)\right) \quad (2.36)$$

$$\cos^2(\theta)\hat{I}_{1z}\hat{I}_{2z} + \cos(\theta)\sin(\theta)(\hat{I}_{1z}\hat{I}_{2x} + \hat{I}_{1x}\hat{I}_{2z}) + \sin^2(\theta)\hat{I}_{1x}\hat{I}_{2x} \quad (2.37)$$

The flip angle is defined as $\theta = \omega_1\tau_p = \gamma B_1\tau_p$, where B_1 is the strength of the (*r.f.*) field, γ is the gyromagnetic ratio, ω_1 is the nutation frequency and τ_p is the pulse duration. When considering this evolution during the FID, it is sufficient to consider only the part, which gives rise to observable magnetisation given by $\hat{I}_x = \hat{I}_{1x} + \hat{I}_{2x}$ and$\hat{I}_y = \hat{I}_{1y} + \hat{I}_{2y}$. The only terms that thus become important are $(2\hat{I}_{1z}\hat{I}_{2x} + 2\hat{I}_{1x}I_{2z})$ presented in Equation (2.36) and highlighted in red, since the identities $\cos^2(\theta) + \sin^2(\theta) = 1$. Hence, the signal intensity is directly proportional to $\sin(2\theta)$ which, is optimal at $\theta = \pi/4$ and is zero at $\theta = \pi/2$ due to $2\sin(\theta)\cos(\theta) = 2\sin(2\theta)$. Consequently, two antiphase doublets, centred at the resonance frequencies of the two nuclei are obtained (Figure 2.8)[111, 112].

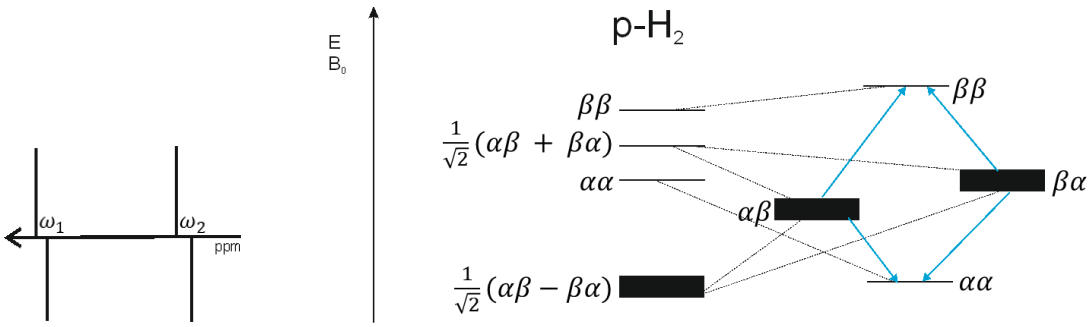

Figure 2.8: The transitions shown in blue give rise to the Anti-phase doublet characteristic of a PASSADENA experiment encoded by a $\theta = \pi/4$ and originated from the singlet state, $\frac{1}{\sqrt{2}}(\alpha\beta - \beta\alpha)$ of *p*-H_2 which populate the $\alpha\beta$ and $\beta\alpha$ states of the substrate**.**

In order to conduct an ALTADENA-type experiment, the sample that contains the metal catalyst and the substrate that is hyperpolarised, is first pressurised with *p*-H_2, then, shaken in a weak magnetic field. The reaction occurs in the strong coupling regime of Equation (2.18) which allows the polarisation transfer. Subsequently, it is introduced into the detection magnet. However, as the reaction still proceeds inside the magnet, the hyperpolarisation route changes from ALTADENA to PASADENA for any species formed at high field. The ALTADENA signals will remain detectable until depleted by longitudinal relaxation or observation[111, 112].

The *p*-H_2 derived state that results under ALTADENA conditions does not fall out of the expression quite so easily. Natterer and Bargon's explanation is presented in terms of an adapted population

model[46]. At zero field, $\xi = 0$ and the density operator produces the singlet state. Note the Earth's field and other local fields are neglected in ALTADENA experiments. At small fields, the *p*-H_2 nuclei exist in states which are mixtures of $1/2(2\hat{I}_{1z}\hat{I}_{2z})$, ZQ_x and $1/2(\hat{I}_{1z} - \hat{I}_{2z})$ states.

At higher mixing fields, the zero quantum term begins to die out leaving the $1/2(2\hat{I}_{1z}\hat{I}_{2z})$ and $1/2(\hat{I}_{1z} - \hat{I}_{2z})$ states, the latter of which persists asymptotically, even when placed for measurement into the high field of the spectrometer magnet. Given that ξ may be either positive or negative, the density operator $\hat{\rho}_{ALT}$ may be rewritten as in Equation (2.38)[46]:

$$\hat{\rho}_{ALT} = \frac{1}{2}(2\hat{I}_{1z}\hat{I}_{2z}) \pm \frac{1}{2}(\hat{I}_{1z} - \hat{I}_{2z}) \quad (2.38)$$

Signals in ALTADENA-type experiments can be viewed after a $\pi/2$ pulse since it is the effect on both the $2\hat{I}_{1z}\hat{I}_{2z} \pm (\hat{I}_{1z} - \hat{I}_{2z})$ terms with the single spin terms contributing to the observed spectrum. For a flip angle of $\pi/2$, the antiphase originating from the terms $(2\hat{I}_{1z}\hat{I}_{2x} + 2\hat{I}_{1x}\hat{I}_{2z})$ disappears, and only the inphase doublets stemming from $(\hat{I}_{1x} - \hat{I}_{2x})$ with opposite signs for each spin survive (Figure 2.9). Consequently, the appearance of the resultant NMR spectra depends strongly on the nutation angle used.

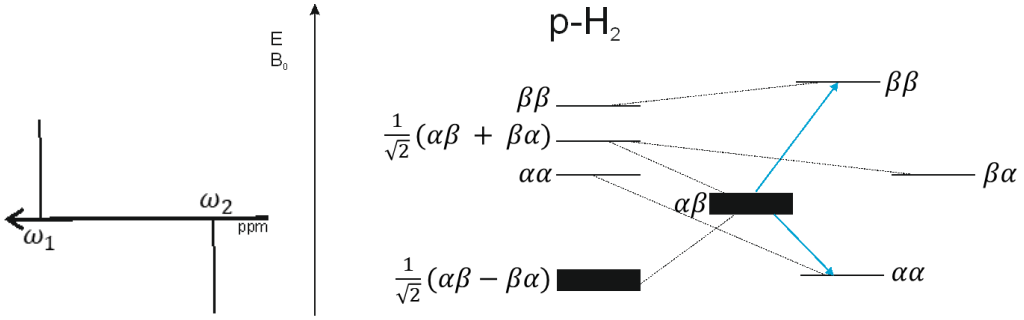

Figure 2.9: The transitions shown in blue give rise to the in phase doublet characteristic of an ALTADENA experiment encoded by a $\theta = \pi/2$ originated from the singlet state, $\frac{1}{\sqrt{2}}(\alpha\beta - \beta\alpha)$ of *p*-H_2 which populate the $\alpha\beta$ state of the substrate

In this thesis, the data presented use both the ALTADENA condition generated by a π/2 pulse and the PASADENA condition generated by a $\pi/4$ pulse to detect enhanced NMR signal of target substrates and dihydrides complexes resulting from *p*-H_2 addition.

2.4.3 Signal Amplification by Reversible Exchange (SABRE)

SABRE, which takes advantage of the ALTADENA route described above, is a non-hydrogenative technique, used to transfer polarisation from *p*-H_2 to a molecule of interest without chemically altering the molecule. This requires a magnetisation transfer catalyst, which is typically an octahedral iridium complex, to which both the molecule of interest and *p*-H_2 are able to reversibly bind. Once bound, the symmetry of the *p*-H_2 derived hydrides is broken by chemical and/or magnetic inequivalence and polarisation transfers from the *p*-H_2 to the substrate at low magnetic fields *via* long-range *J*-coupling. A simplified overview of this is shown in Figure 2.10.

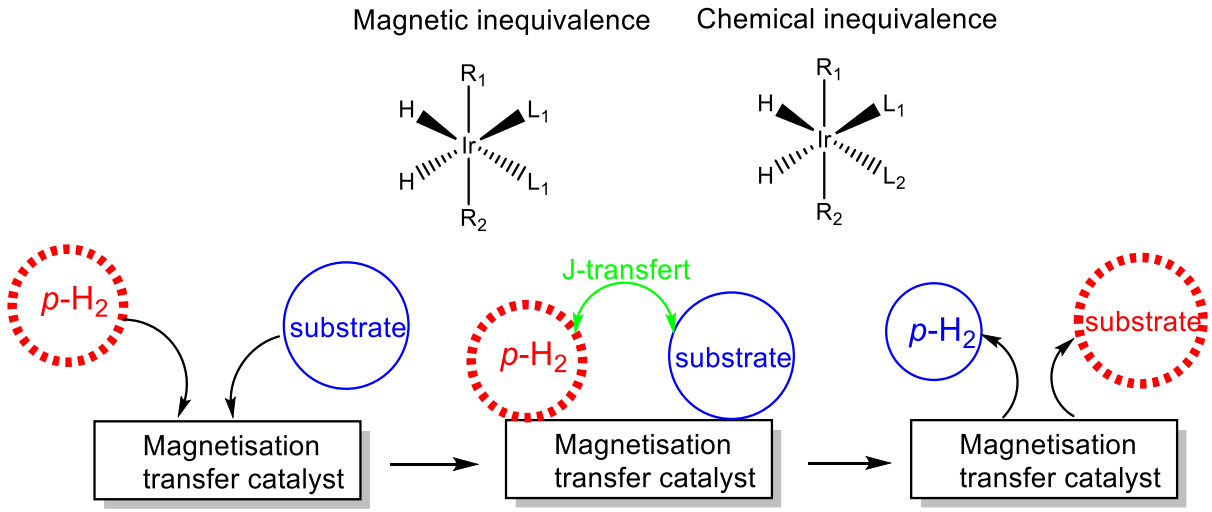

Figure 2.10 Schematic showing polarisation (red) transfer from *p*-H_2 to a substrate of interest because of the SABRE process. (Above) polarisation transfer across a metal exchange catalyst as a result of magnetic or chemical inequivalence in SABRE.

The SABRE process is a catalytic process described as follow (Figure 2.11). Prior to a SABRE experiment, a 16 electron pre-catalyst Ir(I) [IrCl(COD)(NHC)] where COD = *cis*,*cis*-1,5-cyclooctadiene and NHC is N-heterocyclic carbene is reacted with the target substrate (sub) where sub is an appropriate ligand for example pyridine, to form the complex [Ir(COD)(NHC)(Sub)]Cl. This complex undergoes an oxidative addition reaction with hydrogen to form an 18 electrons Ir(III) complex of the type $[Ir(H)_2(COD)(NHC)(Sub)]Cl$. At this stage, the COD ligand is hydrogenated to form successively cyclooctene (COE) then cyclooctane (COA) which can no longer ligate to the iridium and lead to the active SABRE catalyst $[Ir(H)_2(NHC)(Sub)_3]Cl$ formation. This active SABRE complex reversibly binds both *p*-H_2 and the substrate.

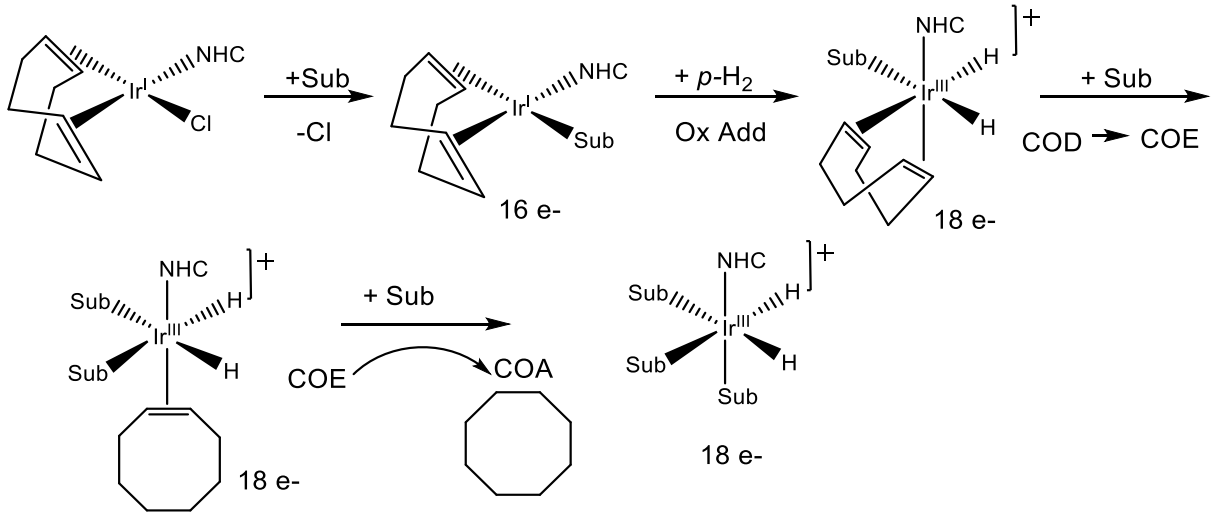

Figure 2.11: Catalytic cycle of activation of SABRE catalyst **I** in presence of an excess of substrate (Sub), for example pyridine and *p*-H_2.

In this section, coherent polarisation transfer among "strongly coupled" spins is discussed. This feature is essential in SABRE as it explains the polarisation transfer field (PTF). Recall that a two-spin system is defined as strongly coupled when the difference in their chemical shift is much smaller than their J-coupling $|\nu_A - \nu_B| \ll J^{AB}$, such a mechanism is efficient at low and ultralow magnetic fields, leading to "spontaneous" polarisation transfer, which does not require application of any (*r.f.*) fields[113]. This can be understood using the concept of Level of Anti Crossings (LACs)[114, 115]. Consider the quantum states $|S\alpha\rangle$ and $|T_k\beta\rangle$, in which S and T_k stand for the singlet S and triplet (T_{+1}, T_0 or T_{-1}) states of the hydrides H_a and H_b, whereas $|\alpha\rangle$ and $|\beta\rangle$ denote the state of other nuclei in the complex, including the ligand. A LAC arises at a magnetic field where two energy levels, corresponding to quantum states $|S\alpha\rangle$ and $|T_k\beta\rangle$ tend to cross, but due to spin-spin coupling the degeneracy is lifted and the crossing is avoided. In the SABRE case, the nuclear spin LACs in the complex will enable efficient mixing between spin states $|S\alpha\rangle$ and $|T_k\beta\rangle$. At the LAC field, the eigenstates of the system are combinations of $|S\alpha\rangle$ and $|T_k\beta\rangle$, and consequently an efficient exchange of populations of the $|S\alpha\rangle$ and $|T_k\beta\rangle$ states can occur. LAC points provide distinct field positions, at which the ligand's protons are efficiently polarised. Initially, H_a and H_b are in the singlet state; therefore, this mixing will result in transitions between $|S\alpha\rangle$ and $|T_k\beta\rangle$, depleting the $|S\alpha\rangle$ (due to the fact *p*-H_2 is used) state and enriching the $|T_k\beta\rangle$ state (initially depleted in SABRE experiment). This will lead to spin polarisation of the ligand protons which is predominantly in the spin-down state, i.e., it becomes negatively polarised[116, 117].

In the absence of the non-secular part of the scalar spin-spin interaction, a two-spin system contains a crossing of the Zero Quantum (ZQ) $|\alpha\beta\rangle$ and $|\beta\alpha\rangle$ levels at $B_0 = 0$, which is turned into an LAC by the non-secular terms. At the LAC the Zeeman states are mixed, forming the eigenstates $|S\rangle$ and $|T_0\rangle$.

The case of AA'B or AA'BB' system are used in most of my experiments, like in SABRE hyperpolarisation of amines (chapter 3), as shown below in Figure 2.12. In the interest of brevity, this is highly simplified. More complicated coupling patterns are often encountered in SABRE as was previously discussed by R. W. Adams et al. in 2009[113].

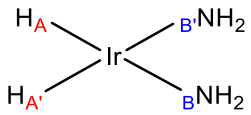

Figure 2.12: Coupling pattern in SABRE active complex where in equatorial position, amine B and B' and hydride A and A'

In this situation, there are three or four nuclei in the spin system grouped in two pairs of chemically equivalent but magnetically non-equivalent nuclei. Two pairs of spins have NMR frequencies ν_A and ν_B, and the *J*-couplings are assumed to be pairwise equal, $J_{AB} = J_{A'B'}$, $J_{A'B} = J_{AB'}$. When there is a hierarchy of spin–spin interactions, i.e., $J_{AA'}$, $J_{BB'} \gg J_{AB}$, $J_{A'B}$, $J_{AB'}$, $J_{A'B'}$, perturbation theory can be applied. In this situation, it yields two sets of matching conditions:

$\pm\nu_A - \nu_B = J_{AA'} - J_{BB'}$, crossing of $|ST_\pm\rangle$ and $|T_\pm S\rangle$,

$\pm\nu_A + \nu_B = J_{AA'} - J_{BB'} - \frac{1}{2}(J_{AB} + J_{AB'})$, crossing of $|SS\rangle$ and $|T_\pm T_\mp\rangle$.

The small couplings between AA' and BB' become active at the level of crossing resulting from these matching conditions. Hence, they transform the level crossings into LACs when a difference in couplings $J_{AB} \neq J_{A'B}$ exists. This condition is equivalent to that of magnetic non-equivalence of the AA' and BB' spins, which is necessary to drive singlet-triplet transitions for each pair of spins. Figure 2.12 shows that the LAC region occurs at 6 mT, ~60 G, which is the polarisation transfer field (PTF) that

I have used in most of my ^{1}H SABRE experiments[115, 118]. For brevity, the states $|T_{\pm}S\rangle$, $|ST_{\pm}\rangle$, $|SS\rangle$ and $|T_{\pm}T_{\mp}\rangle$ are omitted in Figure 2.13 because they remain unaffected.

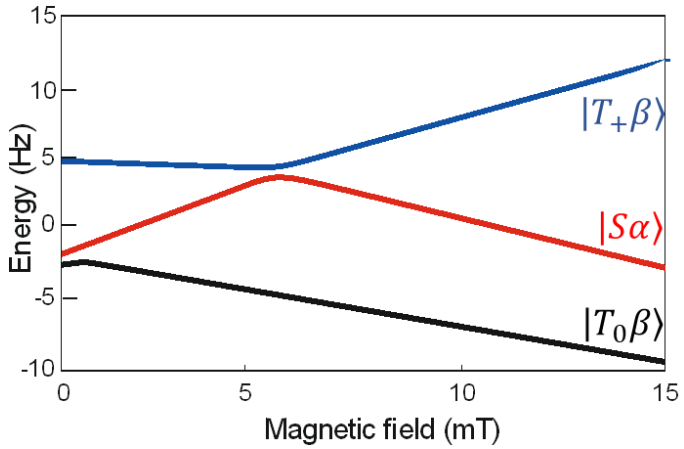

Figure 2.13: Energies level diagram in a AA'B spin system and its assignment of LACs in SABRE features dependences. The mixing states between $|S\alpha\rangle$ and $|T_k\beta\rangle$, states occurs at a magnetic field equal to 6 mT. When all spins are assumed to be protons, two spins A and A' (hydrides) have the same chemical shift of -23 ppm) and the interaction between them is $J^{AA'}$ = 7 Hz, and spin B has a chemical shift of 7~8 ppm. The difference correspond to the magnetic field of the mixing states at the LAC position[115].

2.5 Metal phosphines and metal carbenes in PHIP and SABRE reactions

In this section, the chemistry of metal-carbene and metal-phosphine that catalyse PHIP and SABRE hyperpolarisation reactions are emphasised. A brief literature review on the evolution and the various discoveries in PHIP that leaded to its modern applications are also discussed.

Hydrogenation reactions by Wilkinson's catalyst, $RhCl(PPh_3)_3$, have been examined many times. In addition to facilitating efficient hydrogenation under ambient conditions, $RhCl(PPh_3)_3$ is capable of promoting selective hydrogenation of alkene or alkyne groups in the presence of other easily reducible functionalities such NO_2 or CHO[119]. Hydrogenation with *p*-H_2 was used either for the direct detection of metal based intermediates, or to probe the hydrogenation products. In addition, the interest in $RhCl(PPh_3)_3$ is not solely limited to hydrogenation since hydrosilation, decarboxylation, and transfer dehydrogenation reactions can also be initiated[120].

In 1986, Bowers and Wietekamp predicted that the use of *p*-H_2 would result in spin-hyperpolarisation during hydrogenation reactions[20]. Nine months later they presented proof of their prediction by the addition of *p*-H_2 to form a metal di-hydride with $RhCl(PPh_3)_3$ during the hydrogenation of acrylonitrile to propionitrile[21]. At the same time, Eisenberg[121] wrongly attributed polarisation seen during the hydrogenation of phenylacetylene by the binuclear $Rh_2H_2(CO)_2(dppm)_2$ to chemically induced dynamic nuclear polarization (CINDP)[122] which was in fact the *p*-H_2 hyperpolarisation effect. The spectrum obtained when the complex $Rh(H)_2(Cl)(PMe_3)_3$ is formed via the reaction of *p*-H_2 with $Rh(Cl)(PMe_3)_3$, was found to contain substantially enhanced hydride signals. This observation was taken further by Duckett and co-workers in 1993 when Ir(Br)(CO)(dppe) was reacted with *p*-H_2 at 342 K[123]. The hydride resonances due to $Ir(H)_2(Br)(CO)(dppe)$ were shown to be 95 times more intense than those normally

obtained. Significantly, the naturally abundant ^{13}C signal for the carbonyl ligand of $Ir(H)_2(Br)(CO)(dppe)$ was detected using an insensitive nuclei enhanced by polarisation transfer (INEPT) based sequence after only 32 scans. With normal thermal conditions, this measurement would have taken weeks. In 1997, Natterer and Bargon[46] provided to the NMR community a complete description of *p*-H_2 inducing hyperpolarisation effect in their review, alongside the first description of the ALTADENA and PASSADENA routes. In 2004, the Levitt group[124, 125] took further the *p*-H_2 development and created long-lived singlet states more generally, that leads to the storage of nuclear spin order in a liquid for a time much longer than T_1 defined as T_s. This later development has brought increasing attention to this field since it promises *in-vivo* application by 'storing' and 'releasing' hyperpolarisation on demand[125]. At the same time, PHIP has found successful application in heterogeneous catalysis in addition to well-developed homogenous catalysis[126]. In 2007, Koptyug and co-workers reported the first heterogeneous PHIP catalyst, which consisted of Wilkinson's catalyst immobilised on modified silica gel or polymer beads[127]. These initials pioneering studies stimulated the interest of several groups and led to the establishment of a rapidly expanding field within NMR spectroscopy where *p*-H_2 is applied to the study of dihydrides transition metal complexes, the detection of previously unseen intermediates, and the probing of dihydrogen addition to unsaturated organic functionalities[128, 129]. Since its invention in 2009, SABRE method has allowed the observation of low concentration of analytes where *p*-H_2 transfers its nuclear spin polarisation without altering the chemical structure.

2.5.1 Choice of phosphine

In this thesis, the interest in using phosphorus-containing molecules is driven by the fact that they possess strong one bond ^1H-^{31}P couplings of hundreds of Hz, which can be harnessed for ZULF NMR detection[9]. Furthermore, transition metal phosphine complexes exhibit large *trans* hydride-phosphorus couplings of 150 Hz and *cis* hydride-phosphorus couplings of ~20 Hz[130, 131], hence making them suitable for ZULF NMR studies. The chemistry of metal-phosphine is described briefly here.

The chemistry of phosphine ligands have been widely studied since they are able to stabilise a broad range of oxidation states. Consequently, they are also able to promote many catalytic reactions where redox cycling occurs during the reaction[132]. Phosphines often donate their P lone pair to the metal centre M to give *mono*-dentate terminal M-PR_3 group. As an analogy, in M-CO, CO π* orbitals accept back bonding from M, but while PR_3 lacks the necessary π* levels, it possesses P-R σ* orbitals of the right symmetry to play this role. This is important especially for the more electronegative R groups where overlap between metal and P-R σ* orbitals increases due to the bigger size of the σ* lobe that points toward the metal. Back donation from the metal is therefore favoured by the improved accessibility of the empty σ* orbital. These orbital interactions are illustrated Figure2.14[132].

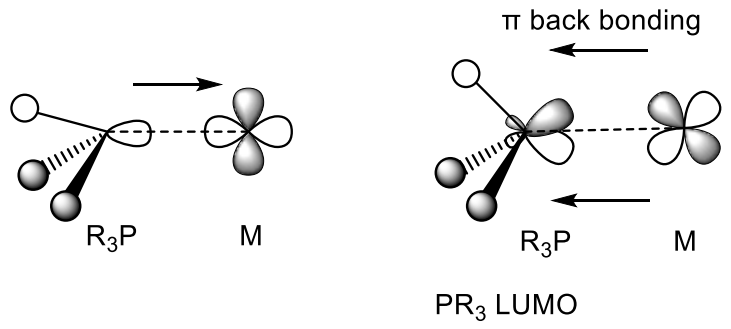

Figure 2.14: Depiction of metal (Mdπ) and phosphine (PR_3σ) bond with orbitals overlapping

Many hydrogenations catalysts that contain a phosphine ligand have been designed and used for PHIP and SABRE hyperpolarisation. In 1989 Eisenberg and co-workers[133] demonstrated polarisation transfer from *p*-H_2 to ^{31}P using the chelating Ir(Br)(CO)(dppe) catalyst with an INEPT pulse sequence[134]. The Duckett group then discovered the SABRE method in 2009 and demonstrated that PHIP could happen without incorporation *p*-H_2 into the substrate molecule[135]. This was first achieved with the cationic Crabtree catalyst [Ir(COD)(PCy_3)(pyr)]BF_4[136] which, reacted with *p*-H_2 in presence of pyridine to yield signal enhancement of the free pyridine NMR response. They also demonstrated that the presence of electronically rich and sterically encumbered phosphine ligands such as PCy_3, PCy_2Ph, or P^iPr_3 increased the signal gain seen for the signals of free pyridine. The initial development of SABRE showed that the signal enhancement was linked to the electron richness of the phosphine, but the most popular SABRE catalysts currently in use no longer contain phosphine ligands. In the case of this thesis though, transition metal complexes containing phosphine ligands that exchange *p*-H_2 are useful because they introduce a heteronuclear spin-spin coupling from the ^{31}P nucleus of the ligand to the hydride ligands, which breaks the spin systems symmetry such that measurements are possible in the ultra-low field regime where chemical shift differences are quenched. Consequently, a prediction was made that it would be possible to directly monitor these metal complexes at ultra-low field. This is a key aim of this thesis. Here, a brief description and early literature review of C-H bond activation and orthometallation that often arises with phosphine ligands is given. Phosphine complexes, assisted by transition metals, often undergo C-H activation and subsequently orthometallation. The observation of C-H bond activation assisted by a transition metal complex is well established in the literature[137, 138]. It was first observed in 1965, when Chatt reported the example of arene C-H bond activation assisted by a transition metal complex of Ru(0) to functionalize naphthalene[139]. During such C-H bond activations, the metal complex undergoes an oxidative addition (Figure 2.15) where its oxidation state goes from n to $n+2$. Since then, many such C-H bond activation products have been seen[140] so such outcome is not unexpected for the complexes described in chapter 5, section 5.2.1. The process by which the C-H bond of methane sp^3 is cleaved is illustrated in Figure 2.15.a. A similar process is depicted for an sp^2 carbon of an arene in Figure 2.15.b. Back donation in the antibonding orbital of the interacting C-H bond is critical for bond breakage and favoured when the metal is electron rich. Replacement of DMSO by phosphine in the complexes presented in section 5.2.1 achieves this outcome. Crabtree has used such a process in these types of complexes to facilitate the hydrogen isotope exchange reaction[141]. Such types of outcome are also observed in complexes containing unsymmetrically substituted carbenes[142-144]

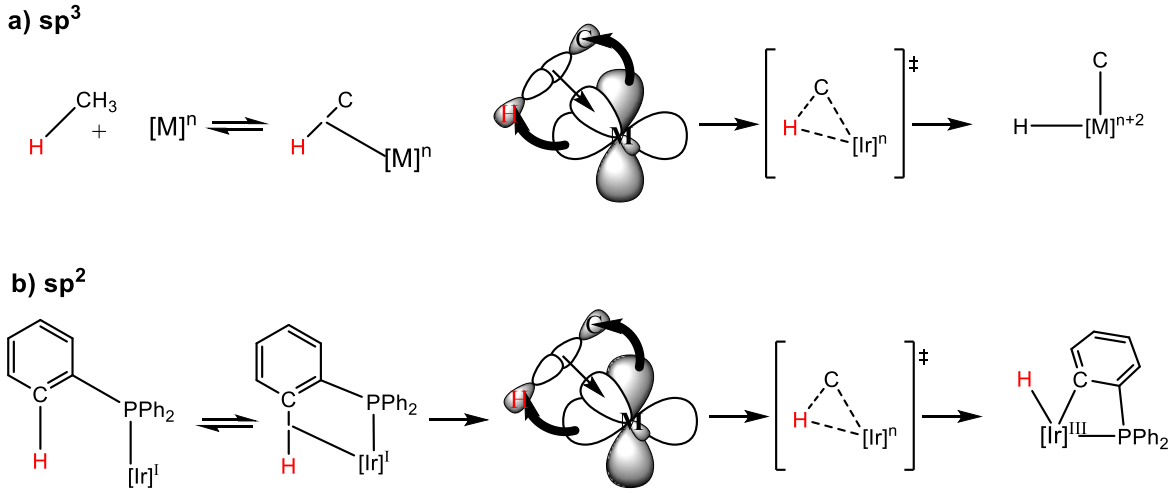

Figure 2.15: a) Reproduced from figure from reference[138] depicting the cleavage of the sp^3 C-H bond in methane by a transition metal. b) Depiction of the sp^2 C-H bond activation of a phenyl group, facilitated by a π-back-bonding from the metal into the σ* orbital of the C-H bond alongside σ-bond donation into a vacant metal orbital.

Bergman and co-workers demonstrated in 1981[147] the intramolecular C-H bond activation of a saturated hydrocarbon by an iridium complex at room temperature with a good yield. Then in 1982, Graham[148] reported an example of an iridium(I) complex that undergoes the photochemically driven oxidative addition of an sp^3 hybridised C-H bond. A year later, Feher[149] published a report on the activation of an alkane C-H bond by a rhodium complex. These pioneering results presented the first reports of C-H bond activation through oxidative addition, which proved to be thermodynamically favoured[150, 151].However, the selective functionalisation of a non-biased sp^2 or sp^3 C–H bond is inherently difficult and thus uncontrolled and random attack can take place. However, the reactivity of C-H bonds can be increased by introducing heteroatoms into heterocyclic compounds such as furan, indoles, and pyridines where the heteroatom introduces regioselectivity to the C–H bond functionalisation step. The best and most reliable procedures utilising C-H bond activation therefore involve the use of directing groups, which allow the catalyst to select certain C–H bonds whilst leaving the others alone[157 145]. Such processes are now ubiquitous to inorganic chemistry and find use in organic synthesis[140, 145, 152-156].

C-H bond activation therefore reflects a route to produce higher value products through cross-coupling reactions without the need for prefunctionalisation of the associated synthons. Consequently, opportunities exist to simplify reaction pathways and thereby increase atom efficiency. However, the use of high precious metal loadings in achieving this is inherently undesirable. Consequently, there is substantial current research into producing low cost, highly active catalysts that operate under mild conditions. Manganese, iron and cobalt derived complexes feature heavily in this research[158].

In 1969, A. Bennett and D. L. Milner reported the first orthometallation reaction by a transition metal complex [159]. In the original paper, they described the formation of a metal-carbon σ bond at the *ortho* position of a phenyl that arises by transfer of one hydrogen atom from the *ortho* position of the aromatic ring of the coordinated ligand to the metal. This process leads to a four membered ring. By using a series of PPh_3 ligands with various substituents, they established that the rate of orthometallation depends on the substituent *para* to phosphine, in the order F < < OCH_3 < CH_3. In 1963, similar observations were made on the reaction of aromatic azo compounds with $Ni(C_5H_5)_2$[160]. In 1965, the formation of covalent bonds between platinum and palladium and the *ortho* carbon atom of a azo-benzene was reported by Cope and Siekman[161]. Just three years later P. L. Pauson et al.[162] published on the analogous reaction of azo-benzene with carbonyls of iron to give *mono-*, *di-*, and *tris-* iron carbonyl derivatives containing aryl σ-bonds. Since then, such types of reaction were extensively studied and their mechanisms are now well understood.[163, 164].

Similar reaction outcomes are observed with many of the phosphines studied in Chapter 5 section 5.2.1.

2.5.2 Choice of carbene

Carbenes bind to metals via a double bond as in $M=CR_2$. In an N-Heterocycle carbene (NHC), the corresponding R groups strongly stabilizes the carbene. When compared with phosphines, most NHCs seem to be much stronger donors but modest π acceptors. P. Sutra and A. Igau compared the Tolman Electronic Parameter (TEP) of phosphines to those of carbenes[165]. The former led to a range of nickel complexes where the CO stretch lies in the region 2060 - 2100 cm^{-1}, while the latter more electron rich donors resulted in a further reduction to bring them into the range 2040 - 2050 cm^{-1}. There are two main types of carbene named after their discoverers: Fisher and Schrock[166, 167]. Work on Schrock carbenes led to the award of the Nobel Prize in 2005[166]. Fisher carbenes are electron deficient and receive π donation from the lone pair of a stabilising π-donor substituent. Consequently, carbenes of the type $L_nM=CR_2$ that have Fisher character favour low oxidation states, late transition metals, π-acceptor ligands on the metal, and π-donors substituents R such as –OMe or $–NMe_2$ on the carbene carbon. They receive limited back donation from the metal and are therefore electrophilic. As an L-type ligand, they counted as a 2e donor with electrons coming from the filled lone pair of the singlet carbene. In contrast, Schrock carbenes $L_nM=CR_2$ are associated with higher oxidation states, early transition metals, and lack both strong-π-acceptor ligands on the metal and strong-π-donor on the substituents on the carbon. Schrock carbene complexes have a nucleophilic carbon centre and are often counted as anionic four electron donors with triplet character. These differences are illustrated in Figure 2.16.

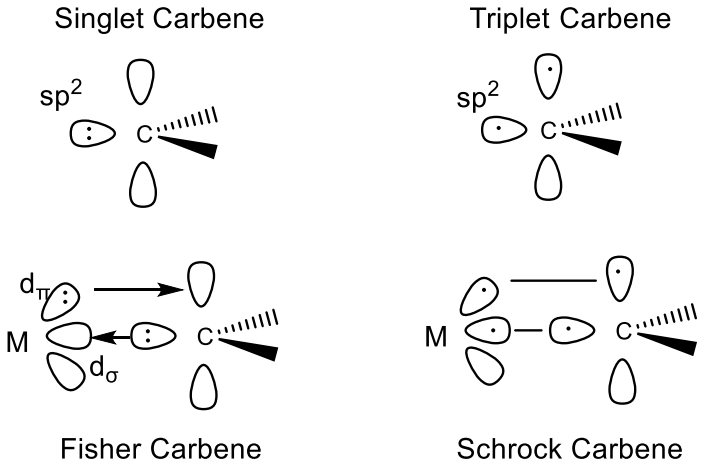

Figure 2.16: Depiction of Fisher or singlet carbene and Schrock or triplet carbene interacting with a metal centre.

The first application of a carbene as ligand for a metal complex was reported in 1968 by Wanslick[168]. The same author had investigated and synthetized themselves carbenes in the early 60's[169]. Later studies by Huang and co-workers[170] showed that NHCs often have stronger M-C bonds than comparable M-P bonds and therefore form more stable metal complexes. In addition, earlier experimental studies demonstrated that sterically bulky electron-donating phosphines, such as PCy_3, deliver the highest levels of transferred electron density. Even greater efficiencies might therefore be expected with a strongly electron-donating N-heterocyclic carbene (NHC) ligand[171], which are classified as Fisher carbenes. Thus, the utilisation of the carbene was a logical progression. A. J. Arduengo first produced one of the highly stable NHCs in 1991, hence these are sometimes referred to as Arduengo carbenes[172]. The first carbene complex to be used in conjunction with SABRE was published in 2011[56]. This work showed that IrCl(COD)(IMes), is a much better SABRE catalyst than any of the phosphine complexes reported previously. In 2013, N-Heterocycle carbene (NHC) and phosphine mixed ligand complexes were shown to be useful as catalysts for hydrogenation and magnetisation transfer reaction[173] where the required symmetry breaking that underpins SABRE is

provided for by the use of chemical inequivalence rather than the previously reported magnetic inequivalence. Rayner and co-workers[174] have synthesised over 30 NHC containing complexes, where their steric and electronic properties were varied to obtain efficient SABRE catalysts. These were then used with appropriate catalyst-substrate combinations to quantify the substrate's NMR detectability. Many other types of water-soluble catalyst have also been reported during the last decade where the choice was driven by biocompatible applications[175]. In these studies, the NHCs have been attached to hydrophilic groups, which allows the catalyst to become soluble. Immobilized catalysts have also been reported where the hydrogenation of propylene and propyne was monitored by PHIP[176]. The effect of nanoparticle size on the intensity of the PHIP signals generated on *p*-H_2 of methyl propiolate to methyl acrylate have been investigated Duckett and co-worker[177]. Zhou and co-workers have also shown supported platinum and iridium nanoparticles to catalyse pairwise replacement producing intense PHIP NMR signals on the alkene[178]. In this thesis, iridium complexes containing carbenes are used in Chapter 3 to optimise the hyperpolarisation of amines for detection in the Earth's magnetic field. However, as discussed above, for direct detection of the hydrides of the metal complex itself in the ultra-low-field regime, heteronuclear couplings are required. Therefore, in the bulk of the thesis phosphine containing complexes, where the associated ^{1}H-^{31}P couplings break the symmetry of the hydride spins, are used so they can be observed directly in the Earth's field.

Chapter 3: *In-situ* EF NMR hyperpolarisation and detection of Amines

3.1 Introduction

As shown in chapter 1 and 2, *para*-hydrogen (*p*-H_2) has been successfully used to hyperpolarise molecules through Para-Hydrogen Induced Polarisation (PHIP), a hydrogenative approach. More recently, Signal Amplification by Reversible Exchange (SABRE) has been introduced to overcome some of the limitations associated with the need for hydrogen acceptors.

SABRE, pioneered in 2009 by Duckett and co-workers[135, 179], is able to enhance the NMR signal of various nuclei such as ^{1}H, ^{31}P, ^{15}N, ^{13}C, ^{19}F, ^{29}Si, ^{119}Sn without altering the chemical identity of the target molecule[180-185]. In SABRE, *p*-H_2 and the target molecule reversibly binds to an iridium metal complex and *p*-H_2 then transfers its spin order to the target molecule through the *J*-coupling network. A weak magnetic field of around 6.5 mT for ^{1}H enables this transfer to become spontaneous. It is through this process that SABRE harnesses *p*-H_2 to produce continuously a non-Boltzmann nuclear spin distribution in the target nucleus. One great advantage of the SABRE method, when compared to other hyperpolarisation techniques,[15, 16, 19] is that there are no underlying chemical changes and the process is reversible. Hence, the polarisation process can be repeated multiple times by flushing fresh *p*-H_2 into the solution. The first paper targeting SABRE hyperpolarisation focussed on targeting protons directly, although ^{19}F and ^{15}N results were illustrated. In this case, the magnetisation from those ^{1}H nuclei was transferred to the heteronuclei present in the same molecule.

The original SABRE experiment targeted ^{1}H nuclei in pyridine, which were directly hyperpolarised when SABRE operated at 6 mT. Hyperpolarised hydride protons can relay their hyperpolarisation directly to other nuclei in the same molecule in a smaller magnetic field (μT). This was exemplified in 2014 by Theis and co-workers[186, 187] who demonstrated the feasibility of direct SABRE polarisation transfer from *p*-H_2 to ^{15}N or other heteronuclei, using a method they call SABRE-SHEATH (SABRE in shield enables alignment transfer to heteronuclei). In contrast to the original SABRE therefore, SABRE-SHEATH requires a smaller polarisation transfer field of 0.2–0.4 μT.

In the same year, Warren et al. achieved successfully Low-Irradiation Generation of High Tesla SABRE (LIGHT-SABRE)[188]. In this approach, low power pulses are used to transfer high order coherent polarisation from *p*-H_2 to bound substrate at any polarisation transfer field with the only requirement of chemical equivalence and magnetic inequivalence of the hydride ligands. For example, for a pyridine molecule as the substrate, the directly bound ^{15}N nuclei and the *ortho*-protons can be hyperpolarised using this low power method.

The first SABRE experiments used the cationic pre-catalyst $[Ir(COD)(PR_3)_2]BF_4$ and pyridine as the substrate, although the substrate range was rapidly expanded to derivatives of pyridine, purine, diazirines, nicotinamide, and pyrazine[174, 189, 190]. The common feature of these chemical groups is they are all heterocycles that contain an electron-donating nitrogen centre. In terms of the catalyst, its optimisation led to carbene-type pre-catalysts, IrCl(COD)(NHC), achieving higher polarisation levels than the phosphine-type catalysts. To widen the SABRE substrates to encompass more chemical groups that no longer need to bear a nitrogen donor atom, new methods such as SABRE-Relay were introduced.

SABRE-Relay[191-193], demonstrated in 2017 by the group of Professor Duckett, significantly extended the classes of molecule amenable to *p*-H_2 hyperpolarisation via SABRE. This method utilizes chemical exchange of hyperpolarised protons from the main SABRE-active substrate, which is then called the carrier. The carrier protons then exchange in solution with those of a second substrate, called the target, which allows hyperpolarisation transfer to take place within the target. Another way to relay polarisation involves a second adduct. It binds an already polarised carrier, and intramolecular spin-spin couplings (J-couplings) within it lead to its hyperpolarisation. These SABRE-Relay approaches can thus polarise substrates that are not able to bind to the more usual Ir-based complexes associated with SABRE. The result is that a wider range of molecules, that now include alcohols, carboxylic acids, esters, and phosphates, can be polarised. Amines are the most common SABRE-Relay hyperpolarisation carrier. For example, 1-propanol has been hyperpolarised by exchange of a hydroxyl proton $HOCH_2CH_2CH_3$ with protons of either d_7-$BnNH_2$ or NH_3, which was polarised by SABRE. At 70 G, the hyperpolarised hydroxyl proton relays the polarisation to protons and ^{13}C in the alkyl chain. 2168

and 751 folds enhancement was achieved with this method for ^{1}H and ^{13}C sites respectively[194]. Although many classes of amines have been tested for SABRE-Relay performance, ammonia (NH_3) proved to yield the best signal enhancements and hence provides the highest level of polarisation relayed to the nuclei of the target[191].

Amines contain a basic nitrogen with a lone pair. The lone pair can be involved in hydrogen bonding or can act as a nucleophile in organic reactions. They are also an important class of organic molecule that are involved in alkylations[195, 196], acylations[197] or sulfonations[198]. In addition, most primary amines are good ligands for organometallic complexes[199]. Consequently, amines react with IrCl(COD)(IMes) (where IMes stands for 1,3-bis(2,4,6-trimethylphenyl)-imidazol-2-ylidine and COD cyclooctadiene) and H_2 to form stable, but labile complexes, of the type $[Ir(H)_2(IMes)(amine)_3]Cl$[191, 193]. It is these complexes that allow *p*-H_2 to relay its polarisation into the free amine as shown in Figure 3.1.

Besides amines, others *N*-functionalities such as those of nitriles[200] are amenable to hyperpolarisation via SABRE.

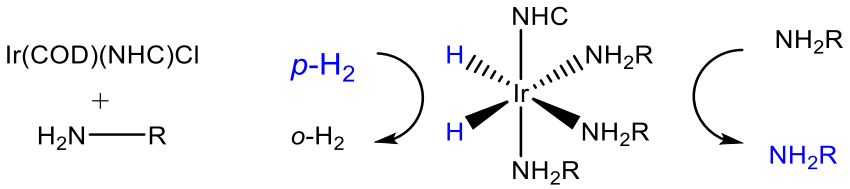

Figure 3.1: Example of a primary amine involved in SABRE hyperpolarisation

Given the complexities of ligand binding, co-ligands have proven necessary to maximise SABRE signal enhancements. The first examples of SABRE co-ligands include acetonitrile or methyl triazol[173, 201]. The co-ligand achieves a beneficial effect by either blocking coordination sites, or by reducing steric crowding around the iridium centre such that more sterically demanding substrates can be polarised [202,203, 204]. For example a 50% polarisation level was achieved on the H-2 site of 4,6-d_2-nicotinate when the co-ligand methyl-2,4,5,6-d_4-nicotinate was employed. More recently, employment of a co-ligand in SABRE has been shown to increase the target substrate affinity to the metal and therefore the hyperpolarisation gained on the substrate[205, 206]. In this pioneering work, a sulfoxide co-ligand was used to overcome the poor ligation of pyruvate that previously prevented α-keto acids from benefiting from SABRE.

As stated in chapter 1, the low strength of the Earth's magnetic field (typically around 50 μT) means that chemical shift differences, which are a key component of structural elucidation by NMR spectroscopy, are not observed. In addition, the low field strength results in a very small population difference between the nuclear spin states and hence very low sensitivity. Unlike chemical shift, scalar couplings are field independent, allowing for their observation in the Earth's magnetic field and direct comparison to those measured at high-field[77, 78]. EF NMR spectroscopy experiments are made possible by the high homogeneity of the Earth's field[60, 61], which means large sample volumes, can be used to overcome the sensitivity issue (e.g. 500 mL). Brute force hyperpolarisation can be achieved with a pre-polarisation field of 18.8 mT, by applying it for several seconds to increase net magnetisation prior to detection in the Earth's magnetic field. As seen in chapter 1, this method is relatively simple and is often used to teach NMR principles in undergraduate labs. Much higher polarisation levels can be achieved with *p*-H_2 methods using PHIP and SABRE for detection with the EF NMR system[128] as outlined in the chapter 1. In this case, more sophisticated implementations are needed such as *p*-H_2 production and storage in a paramagnetic free environment to avoid its interconversion. This approach is well

developed and now used in some research laboratories such as the Levitt group in Southampton, the Warren Group in California and the Duckett group here in York.

When studying the SABRE process and exploring the hyperpolarisation of new classes of molecule, HF detection provides both advantages and challenges. High-field (HF) instruments are excellent for the chemical structure characterisation of complexes and ligand kinetic studies. However, a drawback of HF-detected SABRE is that the polarisation transfer process occurs outside of the spectrometer and the sample must be transferred into the detector for signal acquisition. By contrast, ultra-low-field detection using an EF NMR spectrometer uses *in situ* detection, thereby allowing for the direct observation of processes such as the formation of the active SABRE catalyst[207].

The aim of this chapter is to expand the range of substrates amenable to EF NMR detection with SABRE hyperpolarisation, with a particular focus on amines. Heterocycles containing nitrogen such as pyridine, pyrazine and nicotinamide were already hyperpolarised and detected at EF NMR using methanol as the solvent[207]. The challenge here is to optimise the amine hyperpolarisation so that it can be detected in the Earth's magnetic field in a suitable solvent system. To achieve this, DMSO will be used as a co-substrate. HF NMR will be used as a complementary tool to characterise and study the kinetic and thermodynamic properties of the formed complexes in the presence of the co-substrate in the chosen solvents in order to understand their role in the hyperpolarisation process.

Here the study of the hyperpolarisation of three amines is considered: benzylamine (**1**), phenoxyethylamine (**2**) and 2,4,6-trifluorobenzylamine (**3**) (Figure 3.2) using an EF NMR instrument, where the catalytic activation processes of SABRE can be followed *in situ* and hyperpolarised longitudinal relaxation times, T_1, can be measured directly in the low field regime. The hyperpolarisation level of these amines are measured in the presence of the co-ligand, dimethyl sulfoxide (DMSO). The effect of the co-ligand on the polarisation level is studied using *in situ* EF NMR and directly compared to the SABRE polarisation detected using a 43 MHz benchtop NMR spectrometer. In parallel, the chemical exchange rate of the ligands (both amines and hydrides) and the corresponding thermodynamic parameters for these complexes are explored at 11.7 T (500 MHz) to develop an understanding of the role of the co-ligand in the SABRE hyperpolarisation of amines.

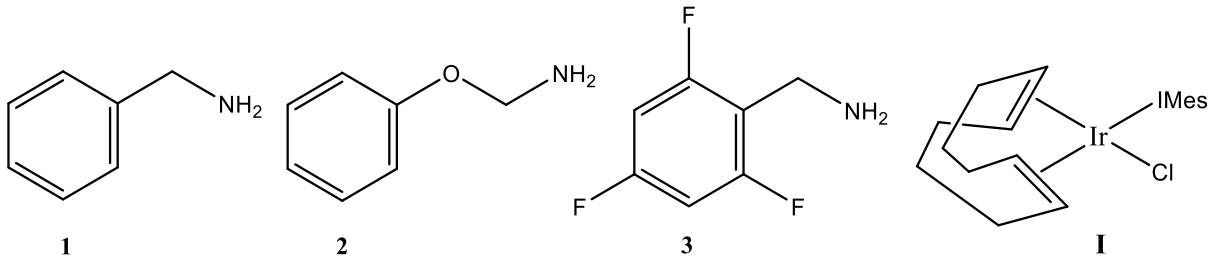

Figure 3.2: Chemical structure of **1** benzylamine; **2** phenoxyethylamine, **3** 2,4,6-triflurobenzylamine and **I** IrCl(COD)(IMes) (where IMes stands for 1,3-bis(2,4,6-trimethylphenyl)-imidazol-2-ylidine and COD cyclooctadiene)

3.2 High field studies

The role that the co-ligand DMSO plays on the hyperpolarisation of amines **1**, **2** and **3** was examined by reference to the pre-catalyst IrCl(COD)(IMes) (**I**). Because the aims is to complete EF NMR studies, the solvent should have a relatively high boiling point. This is a necessary precaution to avoid solvent evaporation when *p*-H_2 is bubbled repeatedly through the solution. It has previously been reported that methanol can be successfully used as a solvent in *in-situ* EF NMR studies, which has a boiling point of 62° C[207]. The reason why methanol cannot be used in these experiments is that it does not favour the formation of the neutral complexes of interest and rather favours the charged complex. The experiments reported here used chloroform as the solvent, where the substrate (**1**, **2** and **3**) and DMSO were present in equimolar concentrations (25 mM) such that each was in a 5-fold excess relative to **I** (5 mM). Chloroform was chosen because it has a boiling point of 62° C and favours the formation of charged species. For context, it has been reported that amines yield higher SABRE responses in lower boiling-point dichloromethane-d_2 (42° C) when compared to chlroform-d_3 (62°C)[208]. For example, d_7-$BnNH_2$ exhibits a signal enhancement of 916-fold in dichlromethane-d_2[191] and 412-fold in chlroform-d_3. The change in solvent therefore reduces the SABRE hyperpolarisation efficiency in a single experiment but allows for a larger number of experiment repetitions on a single same sample.

Three individual samples composed of 5 mM of **I** and the substrates **1**, **2** and **3**, in the ratio 1 : 20, were examined for SABRE in conjunction with 3 bar of *p*-H_2. It was observed that the SABRE response of substrate **1** was almost twice as large as that for substrate **2**. In addition, the signal enhancements for **1** in presence of DMSO was 5.7 time bigger than without the co-ligand, as shown in Figure 3.3. This first result is consistent with the hypothesized benefits of the co-ligand DMSO. For **2**, the specific signal enhancement were 31-(NH_2), 41-(CH_2), 56-(CH_2), and as expected just 3-fold per proton for the -OPh group due to these protons' spin isolation created by the ether linkage. When **3** was tested, the enhancement improved by a factor of 2.9 in the presence of DMSO when compared to the results in the absence of the co-ligand. Therefore, the presence of DMSO improves the SABRE effect for these amines considerably in all cases.

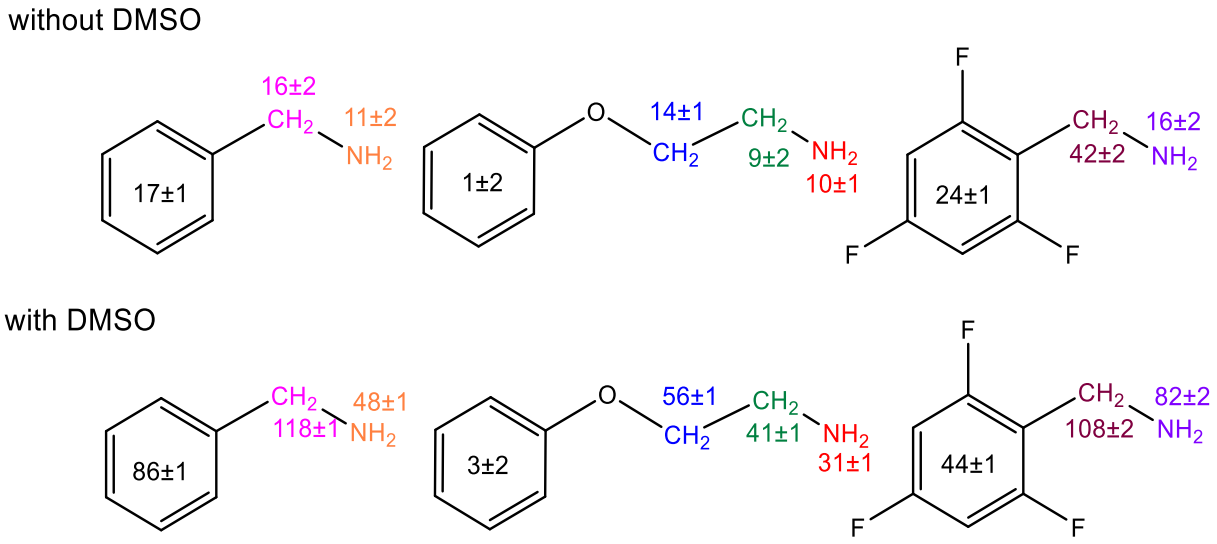

Figure 3.3: SABRE hyperpolarisation levels observed at 500 MHz for substrates **1**, **2** and **3** in the presence and absence of the co-ligand DMSO in chloroform-d_3. Clearly, the presence of DMSO leads to a increase amine NMR signals per proton when compared to when there is no DMSO. The lifetime of these hyperpolarised signals are similar (few seconds) and driven by relaxation. The errors are calculated with five repeats.

3.2.1 Complexes formed with or without co-ligands DMSO

A typical SABRE reaction in methanol-d_4 starts with a suitable pre-catalyst such as IrCl(COD)(IMes) **I**, and after reaction with a substrate (sub) and H_2 forms $[Ir(H)_2(IMes)(sub)_3]Cl$. In contrast, in other solvents, including dichloromethane-d_2 or chlroform-d_3, the neutral complex $IrCl(H)_2(IMes)(sub)_2$ is often favoured. Both types of complex undergo both H_2 and substrate exchange when *p*-H_2 is used, so SABRE hyperpolarisation of the free substrate is achieved in both cases.

First, without hyperpolarisation, NMR studies are used to determine the role of the co-ligand in the formation of the active SABRE catalyst. These studies took place at high field (11.7 T, 500 MHz) where the resolution and the sensitivity gain allows precise monitoring unlike in EF NMR. In order to complete these evaluations, a series of samples were prepared in chlroform-d_3.

As a control, a sample composed of 5 mM of **I** and **1** in the ratio 1 : 20 was interrogated and the formation of $[Ir(H)_2(IMes)(\mathbf{1})_3]Cl$ (**5**), which is known in the literature[191], was confirmed (Figure 3.4.a). This complex yields a single resonance in the hydride region at -23.96 ppm due to the two ligands **1** being *trans* to the hydrides. Next, a sample containing 5 mM of **I**, **1** and DMSO in an initial ratio of 1 : 20 : 20 was prepared. High field monitoring now showed the formation of three complexes, **4**, **5** and **6** in proportions of 94%, 6% and <0.1 % respectively (Figure 3.4.b). The neutral complex **4**, $IrCl(H)_2(\mathbf{1})(DMSO)(IMes)$,and defined by two inequivalent hydride resonances at -23.25 *trans* to **1** and -23.78 ppm *trans* to Cl^- with a mutual $J(^1H\text{-}^1H)$ of 6 Hz, in the ^1H NMR spectrum (Figure 3.4.b) and this dominates in solution. The third complex **6**, is the least prevalent of the products and is defined by a single hydride ligand signal at -22.17 ppm that is also indicative of it being *trans* to **1**.

4

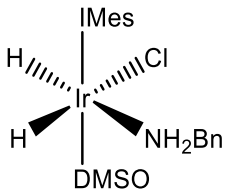

5

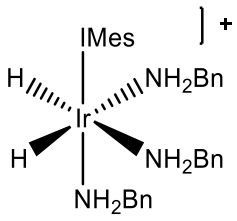

6

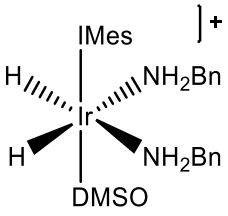

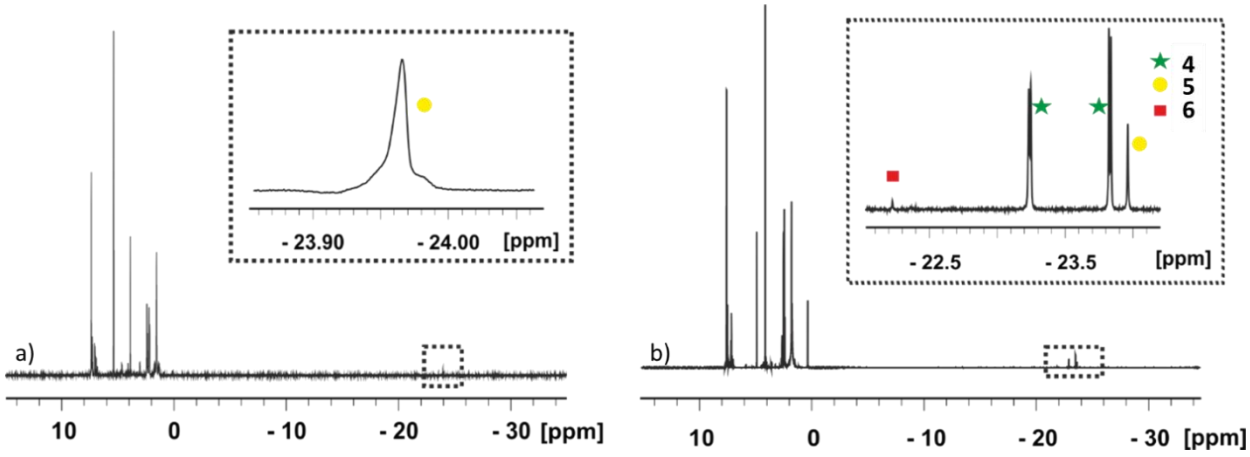

Figure 3.4: a) ^{1}H 32 scans NMR spectrum of a sample of 5 mM **I** and 100 mM benzylamine in chloroform-d_3 under H_2. The hydride region indicates the formation of complex **5**. b) ^{1}H 1D NMR spectrum of 8 scans of a sample of 5 mM of **I**, 100 mM benzylamine and 100 mM DMSO-d_6 in chloroform-d_3 with H_2. The hydride region now shows evidence for three complexes: **4** (green stars), **5** (yellow circle) and **6** (red square).

Next, a sample composed of 5 mM of **I** and **2** in a ratio of 1 : 20 (100 mM) under H_2 was interrogated and the formation of $[Ir(H)_2(IMes)(\mathbf{2})_3]Cl$ (**8**) confirmed (Figure 3.5.a). This complex yields a single hydride ligand resonance at -24.3 ppm. A second sample containing 5 mM of **I**, alongside **2** and DMSO in the initial ratio 1 : 20 : 20 with an excess of H_2 was found to form the three complexes **7**, **8** and **9** in the ratio 92 %, 6 %, and 3 % respectively (Figure 3.5.b).

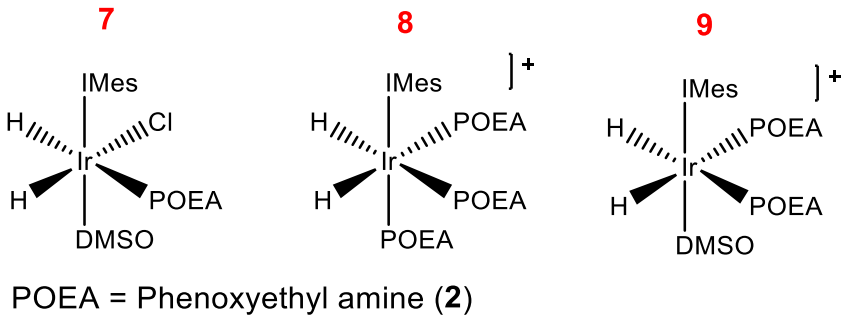

POEA = Phenoxyethyl amine (**2**)

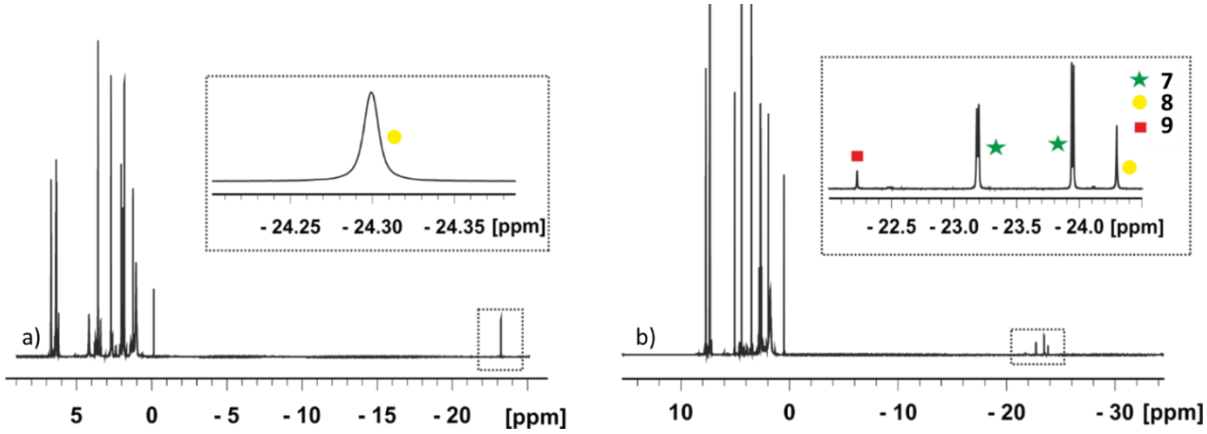

Figure 3.5: a) ^{1}H 1D NMR spectrum of a sample of 5 mM **I** and 100 mM of benzylamine in chloroform-d_3 under H_2. The hydride region shows a signal indicative of the formation of complex **8**. b) ^{1}H 1D NMR spectrum of a sample of 5 mM **I** and 100 mM of benzylamine and 100 mM of DMSO-d_6 in chloroform-d_3 under H_2. The hydride region shows signals indicative of three complexes: **7** (green stars), **8** (yellow circle) and **9** (red square).

3.2.2 Thermodynamic and kinetic studies

In the previous section, it was shown that addition of the co-ligand DMSO during the hyperpolarisation of an amine with **I** leads to two analogous species as the dominant product, neutral $IrCl(H)_2$(**x**)(DMSO)(IMes) (where **x** = **1** or **2**). In contrast, when an amine reacts with **I** and H_2 alone, the complex $[Ir(H)_2(IMes)$(**x**)$_3]Cl$ forms. In order for these complexes to exhibit SABRE, they must undergo ligand exchange on a suitable timescale. Mechanistic insights into the ligand exchange processes and the thermodynamic stability of these complexes can be obtained by analysis of EXSY data.

To develop this understanding, the substrates and H_2 exchange processes were explored using HF NMR. Selective excitation of the resonance of a bound ligand and the subsequent acquisition of a ^{1}H NMR spectrum following a reaction time, *t*, is performed. Ligand exchange is observed via the creation of a signal at the corresponding resonance of the free form. The resulting measurements consist therefore of a series of data arrays, such that *t* is increased over 12 values. The precise values are varied with temperature to suit the speed of the exchange processes. Integrals of the interchanging peaks in the associated ^{1}H EXSY spectra were obtained and converted to a percentage of the total detected signal. These data were then analysed as a function of the mixing time according to the relevant kinetic model for each reaction.

3.2.2.1 Benzylamine ligand exchange assessment in complex 4

Starting with the sample containing 5 mM of **I**, **1** and DMSO in the initial ratio of 1 : 20 : 20, the bound CH_2 of benzylamine yielding a signal at 3.33 ppm in complex **4** (Figure 3.6.b) was found to exchange with that of the free material which yields a CH_2 resonance at 3.9 ppm. This EXSY procedure was used to determine the rates of benzylamine exchange, k_{on} and k_{off}, in **4**. A differential kinetic model was used based on Equations 3.1 and 3.2. A fit is achieved by minimising the root-mean-square deviation (RMSD) difference between simulated and experimental data.

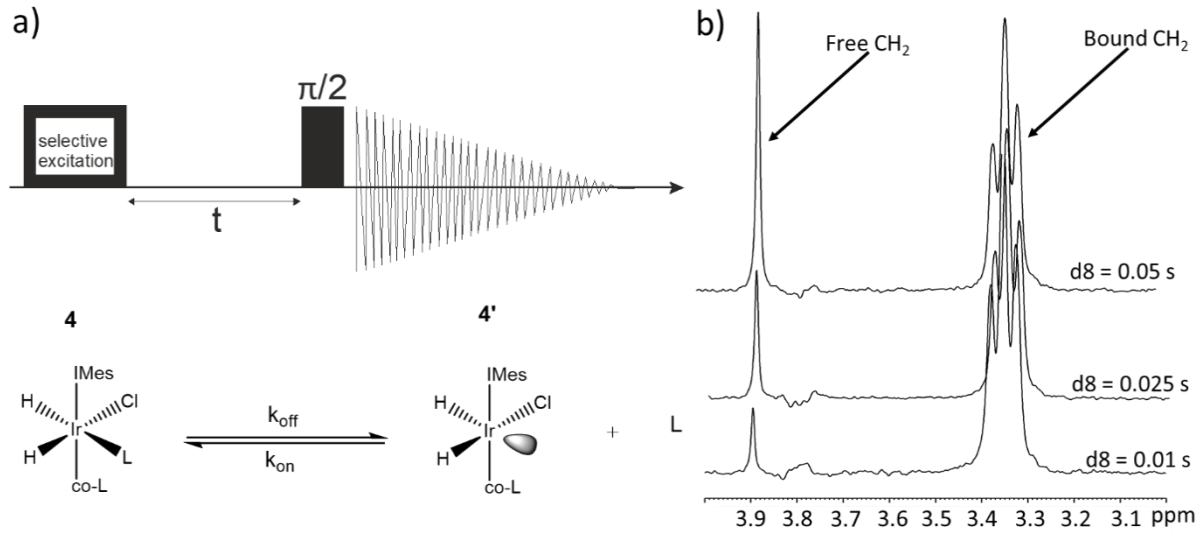

Figure 3.6: a) Depiction of the EXSY measurement process and the dissociation of ligand L from **4** to form intermediate **4'**. b) Typical EXSY spectra of **4** at 298 K recorded successively 0.01, 0.025 and 0.05 s after selective excitation of the bound CH_2 resonance for bound **1** *trans* to the hydride.

$$\frac{d[4]}{dt} = -k_{off}[4] + k_{on}[4']L \qquad (3.1)$$

$$\frac{d[4']}{dt} = k_{off}[4] - k_{on}[4']L \qquad (3.2)$$

Time delays were calculated at time t where ∂t is an incremental time difference, k_{off} the rate of dissociation and k_{on} is the rate of ligand binding.

The observed rates of benzylamine exchange, k_{off} and k_{on}, were determined by achieving the lowest sum of the least squares fit between the EXSY determined abundance and those predicted by the kinetic model described in Equations 3.1 and 3.2. A series of such data are shown in Figure 3.7.a. Transition state barriers for these processes can be calculated by recording measurements at a range of different temperatures. This can be achieved by using Equation 3.3 to determine the activation enthalpy ($\Delta H^{\ddagger}$) and activation entropy ($\Delta S^{\ddagger}$) of benzylamine exchange where T is temperature, k_B is Boltzmann's constant, h is Planck's constant, and R is the ideal gas constant. The value of k is multiplied by two as the measured rate corresponds to the crossing of the barrier, which, if symmetrical, means there is an equally probability of falling back. An example is presented in Figure 3.7.b. Errors were calculated according to established procedures using the student's t value. The Gibbs free energy of activation ($\Delta G^{\ddagger}$) can be calculated using Equation 3.4.

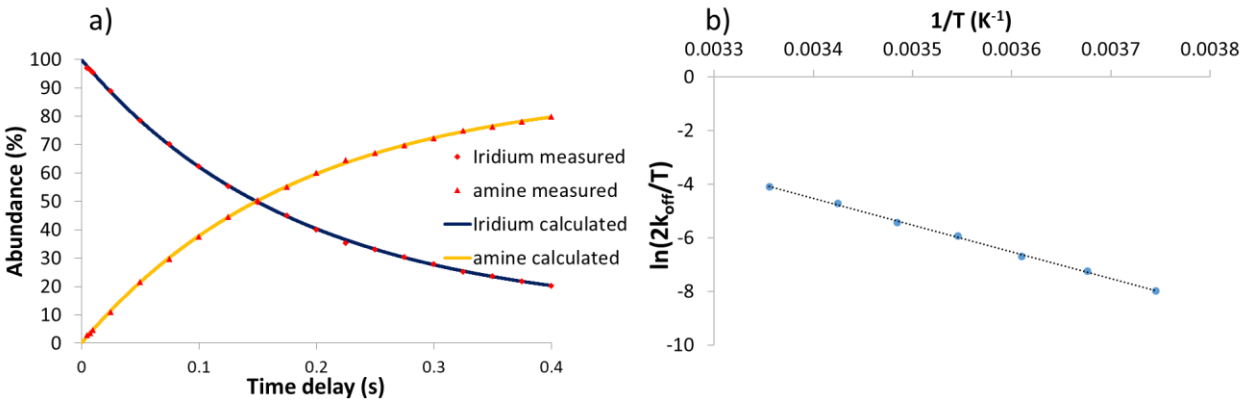

Figure 3.7: a) EXSY ^{1}H signal interconversion for the bound 3.33 ppm in **4** and the 3.9 ppm free benzylamine signal expressed as % abundance for a solution of 5 mM of **I**, **1** and DMSO in the ratio 1 : 20 : 20. % Abundance calculated from EXSY data (marker points) and the model (lines) for a solution of **4** at 298 K. b) An Eyring plot of $\ln\left(\frac{2k_{off}}{T}\right)$ against $\frac{1}{T}$ yields a straight line where the intercept (-9996.7x) and gradient (29.457) can be used to calculate the activation parameters for the ligand loss in **4** according to equations 3.3 and 3.4. y = -9996.7x + 29.457; R^2 = 0.9986.

$$\ln\left(\frac{2k_{off}}{T}\right) = \ln\left(\frac{k_B}{h}\right) + \frac{\Delta S}{R} - \frac{\Delta H}{RT} \qquad (3.3)$$

$$\Delta G^{\ddagger} = \Delta H^{\ddagger} - T\Delta S^{\ddagger} \qquad (3.4)$$

Using the EXSY data, the rate of dissociation of benzylamine at 298 K was estimated to be $k_{off} = 4.91 \pm 0.11$ s^{-1} and rate of the reverse reaction to be $k_{on} = 0.56 \pm 0.11$ s^{-1}. The former is a precise first order rate constant while the latter reflects k_{obs} as the process is second order and the concentration of **4'** not known**.** The transition state barriers $\Delta H^{\ddagger}$ and $\Delta S^{\ddagger}$ for the forward reaction were estimated to be 83.1 ± 2.0 kJ mol^{-1} and 53.1 ± 7.0 J K^{-1} mol^{-1}, respectively. The resulting free Gibbs energy $\Delta G^{\ddagger}$ at 298 K was calculated to be 67.3 ± 0.5 kJ mol^{-1}. A confidence interval of 95% was used to calculate the errors. $\Delta G^{\ddagger}$ refers to the difference in energy between the reactants and the transition state whereas $\Delta H^{\ddagger}$ informs of the stability of product formed and is the energy difference between reactant and product. $\Delta S^{\ddagger}$ measures the disorders created by the reaction. The error in $\Delta G^{\ddagger}$ is notably lower than might first be expected. This is reflective of the fact that there is real data in the region around 298 K. Consequently, two lines are drawn to describe the lower and upper confidence limits of the Erying plot. These two lines intersect with 298 K, and the corresponding difference in their y values reflects the error in $\Delta G^{\ddagger}$.

3.2.2.2 H_2 loss rate for complex 4

A similar analysis was carried out for the hydride ligands in the same complex **4** of the sample containing 5 mM of **I**, **1** and DMSO in the initial ratio 1 : 20 : 20. In this complex, the hydride ligands are chemically inequivalent. In addition to simple exchange with free H_2, there is evidence for interconversion of the inequivalent hydride ligands, due to the process illustrated in Figure 3.8.b.

Integrals of the excited peak **4**, the interchanging peak defined as **4''** and the exchanging peak to free H_2 were measured as shown in (Figure 3.8.a) in the associated ^{1}H EXSY spectra as a function of *t* and converted to a percentage of the total detected signal. These data were then analysed as a function of the *t* according to the differential kinetic model given in Equations 3.5, 3.6 and 3.7. It is expected that hydrogen exchange follows a pathway similar to that of Figure 3.7.b, in which hydrogen exchange is preceded by dissociation of the amine from the 18 electron **4** or **4'** to form a 16 electron five coordinate intermediate. This assumption is on the basis of hydrogen exchange processes reported for similar Ir(III) systems[56]. The obtained rate constant of reductive elimination of H_2 and the rate constant of the interchange of hydride sites at 298 K are $k_{H2} = 2.66 \pm 0.61$ s^{-1} $k_{Hi} = 1.22 \pm 0.60$ s^{-1} respectively. The transition state barriers $\Delta H^{\ddagger}$ and $\Delta S^{\ddagger}$ were then calculated to be 91.0 ± 2.2 kJ mol^{-1} and 74.7 ± 7.8 J K^{-1} mol^{-1} respectively for the H_2 loss process. The resulting Gibbs free energy change $\Delta G^{\ddagger}$ at 298 K was calculated to be $\Delta G^{\ddagger} = 68.8 \pm 0.3$ kJ mol^{-1}.

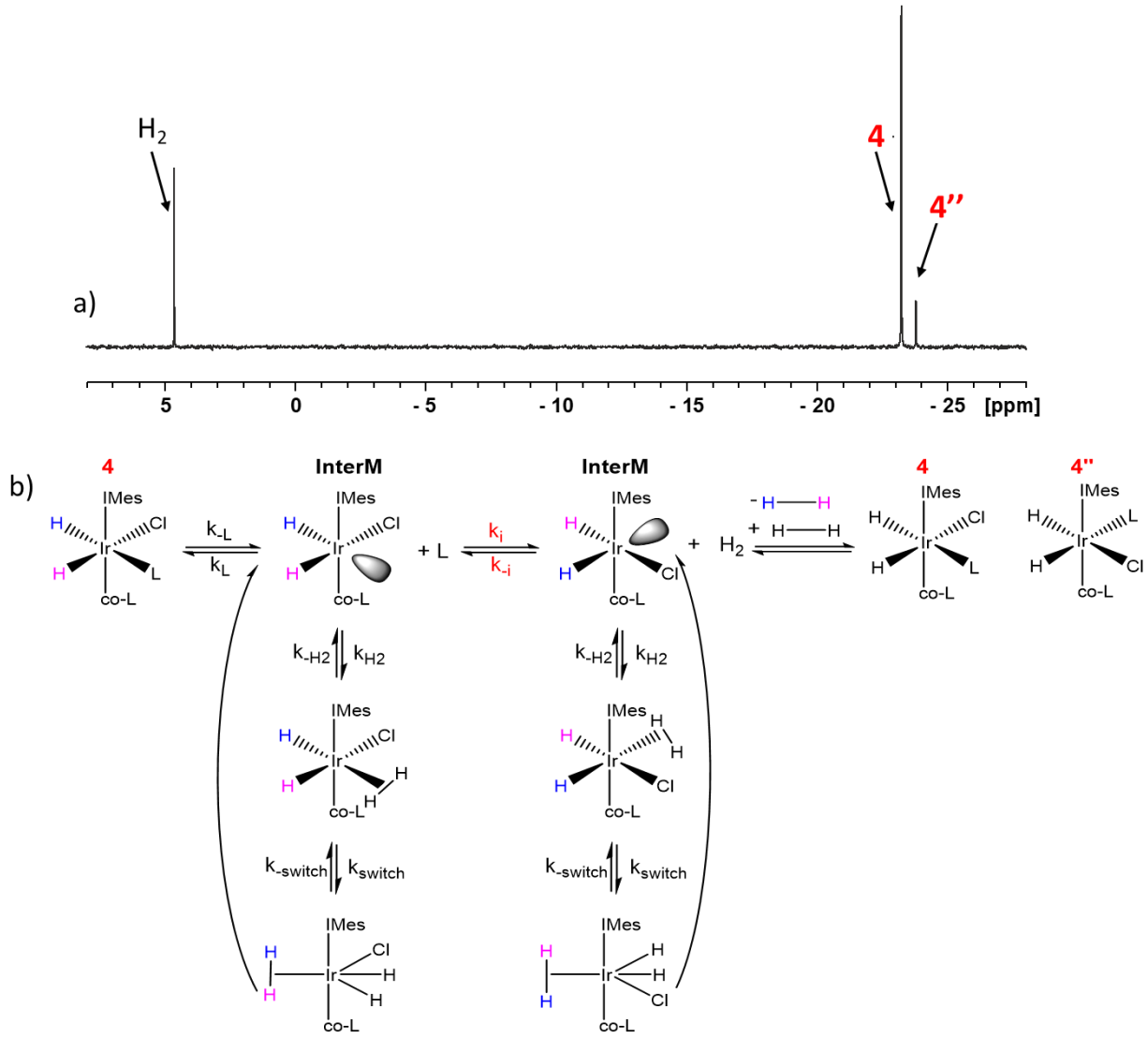

Figure 3.8: a) A typical EXSY spectrum of **4** at 298 K recorded 0.05 s after selective excitation of the hydride ligand *trans* to **1**. b) Schematic representation of the exchange processes taking place in an Ir-based SABRE system in the case where **1**, Cl^-, DMSO and hydrides are ligated. In addition to the H_2 exchange in complex with k_{H2} constant association and k_{-H2} constant dissociation, there is an

interchange of a ligand L, between the **4** form (k_{-i}) when L binds from the bottom and the **4** form (k_i) occurs when ligand L binds from the top.

$$\frac{\partial[4]}{\partial t} = (-k_{H_2}[4] + k_{-H_2}[H_2][InterM]) \quad (3.5)$$

$$\frac{\partial[4'']}{\partial t} = +(k_i[InterM] - k_{-i}[4'']) \quad (3.6)$$

$$\frac{\partial[H_2]}{\partial t} = +(k_{H_2}[4''] - k_{-H_2}[H_2]) \quad (3.7)$$

3.2.2.3 Comparative description of all fours complexes

In this section, a comparative description of all four complexes **4**, **5, 7** and **8** is given where in presence of DMSO, **4** and **7** dominate whilst in absence of DMSO, **5** and **8** are the major products (**x** = **1** or **2**). In order to rationalize the differences in behaviour raw ligand loss rates, the activation enthalpy $\Delta H^{\ddagger}$ and activation entropy $\Delta S^{\ddagger}$ and the Gibbs free energy of activation $\Delta G^{\ddagger}$ values at 298 K have been calculated. The results are presented in Tables 3.1 and 3.2.

Table 3.1: Dissociation constant k_{off} for **1** and the corresponding H_2 loss rate (**H**) in complexes **4** and **5**. Activation enthalpy ($\Delta H^{\ddagger}$), activation entropy ($\Delta S^{\ddagger}$) and Gibbs free energy of activation($\Delta G^{\ddagger}$) at 298 K.

4 , 298K	***k* (s^{-1})**	***$k_{H\ interchange}$* (s^{-1})**	**$\Delta G^{\ddagger}$ kJ mol^{-1}**	**$\Delta H^{\ddagger}$ kJ mol^{-1}**	**$\Delta S^{\ddagger}$ J K^{-1} mol^{-1}**
Loss of 1	4.91 ± 0.10	NA	67.3 ± 0.5	83.1 ± 2.0	53.1 ± 7.0
Formation of H_2	2.66 ± 0.60	1.22 ± 0.60	68.8 ± 0.3	91.0 ± 2.0	74.7 ± 8.0
5, 298 K	***k* (s^{-1})**	***k_{int}* (s^{-1})**	**$\Delta G^{\ddagger}$ (kJ mol^{-1})**	**$\Delta H^{\ddagger}$ kJ mol^{-1}**	**$\Delta S^{\ddagger}$ J K^{-1} mol^{-1}**
Loss of 1	2.66 ± 0.20	NA	69.1 ± 0.4	77.7 ± 4.0	29.1 ± 13.0
Formation of H_2	2.09 ± 0.10	NA	69.3 ± 0.2	97.2 ± 2.0	93.9 ± 8.0

Table 3.2: Dissociation constant k_{off} of **2** and the corresponding H_2 loss rate **(H)** in complexes **7** and **8**, with and without DMSO respectively. Activation enthalpy ($\Delta H^{\ddagger}$), activation entropy ($\Delta S^{\ddagger}$) and Gibbs free energy of activation ($\Delta G^{\ddagger}$) for substrate **2**.

7, 298 K	***k* (s^{-1})**	***$k_{H\ interchange}$* (s^{-1})**	**$\Delta G^{\ddagger}$ kJ mol^{-1}**	**$\Delta H^{\ddagger}$ kJ mol^{-1}**	**$\Delta S^{\ddagger}$ J K^{-1} mol^{-1}**
Loss of 2	7.85 ± 0.10	NA	66.3 ± 1.6	77.7 ± 3.6	38.3 ± 13.0
Formation of H_2	1.54 ± 0.20	2.71 ± 0.2	70.3 ± 0.2	84.6 ± 3.2	48.1 ± 11.5

8, 298 K	k (s^{-1})	k_{int} (s^{-1})	$\Delta G^{\ddagger}$ kJ mol^{-1}	$\Delta H^{\ddagger}$ kJ mol^{-1}	$\Delta S^{\ddagger}$ J K^{-1} mol^{-1}
Loss of 2	4.25 ± 0.10	NA	68.1 ± 0.4	74.6 ± 3	21.6 ± 10.0
Formation of H_2	2.33 ± 0.30	NA	69.3 ± 0.3	82.7 ± 4	44.8 ± 14.0

In order to assess which complexes are responsible for SABRE activity and to probe the differences in SABRE efficiency for **1** and **2**, the ligand dissociation rates, the activation enthalpy $\Delta H^{\ddagger}$, the activation entropy $\Delta S^{\ddagger}$ and the Gibbs free energy of activation $\Delta G^{\ddagger}$were measured and compared. In the case of **1** (Table 3.1), DMSO substituted **4** exhibits a higher ligand loss rate for **1** of 4.91 s^{-1} when compared to that of unsubstituted **5** whose value is 2.66 s^{-1}. The optimum ligand exchange rate has been suggested by Bartsky to be ~4.5 s^{-1} for pyridyl type species[115], where the transfer coupling between the hydride ligand and the substrate is around 1.2 Hz[201]. A dissociation rate of 4.91 s^{-1} is therefore predicted to be close to optimal for polarisation transfer provided the transfer coupling is similar[115]. This rate is consistent with the SABRE signal enhancement calculated (in Figure 3.3) for DMSO substituted **4,** which is higher than for **5.**

At 298 K (Table 3.2), DMSO substituted **7** exhibits a higher rate of loss of **2** (7.85 s^{-1}) when compared to unsubstituted **8** (4.25 s^{-1}). Excessively short lifetimes (fast exchange rates) will only provide enough time for significant polarisation transfer to take place if the transfer coupling is higher than 1.2 Hz[113]. The fact that the dissociation rate of 7.85 s^{-1} gives higher polarisation levels suggests the transfer coupling is higher than of pyridine. In fact, Barstky prediction was on a 5 bonds coupling of ~1.2 Hz whereas here, the hydride and amine protons are separated by 4 bonds. A bigger coupling is therefore expected and consistent with more efficient SABRE at the faster exchange rate. Other factors such as relaxation rates (which were not measured in these samples) may also impact on this deduction.

The barriers to ligand loss in these neutral DMSO substituted complexes, $[Ir(H)_2(IMes)(DMSO)(x)Cl]$, provides important information. The ligand loss rate for **4** is 4.91 ± 0.10 s^{-1} while in **7** it is 7.85 ± 0.09 s^{-1}. This is reflected in $\Delta H^{\ddagger}$ falling from 83.1 ± 2.0 (**4**) to 77.7 ± 4.0 kJ mol^{-1} (**7**) whilst $\Delta S^{\ddagger}$ decreases from 53.1 ± 7.0 to 38.3 ± 13.0 J K^{-1} mol^{-1}. Both, these terms combine at 298 K to make, $\Delta G^{\ddagger}$ for ligand loss, 67.3 ± 0.5 versus 66.3 ± 2.0 kJ mol^{-1} respectively. Due to the errors, these $\Delta G^{\ddagger}$ values are indistinguishable. However, as the pk$_a$ of the two ligands are predicted to be 9.33 and 4.70 respectively, there should be an impact on the iridium-ligand bond energy which will be reflected in $\Delta H^{\ddagger}$, which is higher for the better donor **1**. The larger bond energy might be expected to be associated with a shorter bond and consequently a greater release in entropy on reaching the transition state. This hypothesis is consistent with these data.

The H_2 loss rates in these two complexes have also been measured (Table 3.1 and 3.2), and decrease from 2.66 s^{-1} in **4** to 1.54 s^{-1} in **7**. This is surprising as H_2 exchange takes place after dissociative loss of L. The measured barrier for H_2 loss therefore includes the impact of loss of amine and any associated solvation changes prior to the slow step, which is H_2 loss. Consequently, it is clear that reducing the electron density on the metal makes the process of H_2 exchange slower even though the barrier $\Delta H^{\ddagger}$ falls from 91.0 ± 2.0 kJ mol^{-1} in **4** to 84.6 ± 3.0 kJ mol^{-1} in **7**. This change in rate is a consequence of the entropy term, which goes from, 74.7 ± 8.0 J K^{-1} mol^{-1} to 48.1 ± 12.0 J K^{-1} mol^{-1}.

Data for the corresponding $[Ir(H)_2(IMes)(x)_3]Cl$ species, **5** and **8**, are also presented. The rate of loss of **1** in **5** is 2.66 ± 0.20 s^{-1} while in **8** loss of **2** proceeds with a rate of 4.25 ± 0.10 s^{-1}. Both bond strengths now appear to be similar as $\Delta H^{\ddagger}$ are 77.7 ± 3.8 and 74.6 ± 2.9 whilst $\Delta S^{\ddagger}$ again are almost identical at 29.1 ± 13.0 and 21.6 ± 10.1 J K^{-1} mol^{-1} on going from **5** to **8**. However the H_2 loss is again indistinguishable for **8** compared to **5** (2.33 ± 0.20 s^{-1} vs 2.09 ± 0.30 s^{-1}). Similar trends are again seen for the entropy and enthalpy changes to those for **4** and **7**. Hence, it appears that both **5** and **8** undergo relatively similar kinetic behaviour.

In conclusion, the co-ligand DMSO in $[Ir(H)_2(IMes)(DMSO)(x)Cl]$ acts to lower the barrier for amine ligand loss when compared to that of the parent complex $[Ir(H)_2(IMes)(x)_3]Cl$. This proved to be beneficial for SABRE. Examination of the enthalpy and entropy revealed that the better donor **1** has stronger bonds to iridium but these are offset by the release in entropy associated with the dissociative nature of ligand exchange. For H_2 exchange, more complex behaviour is indicated which results in broadly similar rates for all species.

3.3 *In-situ* Earth's field NMR studies

According to the high field data presented above, the presence of DMSO favours better polarisation transfer for **4** rather than **5**. This is now verified experimentally using *in situ* SABRE hyperpolarisation with Earth's field NMR detection.

3.3.1 Earth's field NMR of amine 1

3.3.1.1 Comparative polarisation level of 1 in 4 and 5 complexes

The conversion of **I** into $[Ir(H)_2(IMes)(\mathbf{1})_3]Cl$ **5** (Figure 3.9.b blue) and **I** into $[Ir(H)_2(IMes)(DMSO)(1)(Cl)]$ **4** (Figure 3.9.b pink) was tracked by following the growth in SABRE response as a function of *p*-H_2 bubbling time using the *in-situ* EF NMR probe. Continuous SABRE polarisation can be recorded using this approach without the need to manually transfer the sample.

Two samples were used to monitor this conversion, one containing 204 mM (40 equivalents) of **1** and the second 127.5 mM (25 equivalents) of **1** and 51.2 mM (25 equivalents) of DMSO in 4 mL of chloroform. No NMR signal is observed from the protons in the solvent chloroform due to the extremely low sensitivity of EF NMR detection. Therefore, unlike for high-field NMR, there is no need to use deuterated solvents. Figure 3.9.b presents the growth in SABRE signal (percentage polarisation) as a function of reaction time for the two samples. The percentage polarisation values were obtained by comparison to a calibration plot derived for water. This reference plot demonstrated that the signal increases linearly with increase in volume of H_2O and hence number of ^1H nuclei. The result, P_{SABRE} is given by equations 3.9 and 3.10 where C_{REF} derives from the water calibration reference[209].

$$\frac{P_{SABRE}}{P_{REF}} = \frac{S_{SABRE}}{S_{REF}} \qquad (3.9)$$

$$P_{SABRE} = \frac{S_{SABRE}}{S_{REF}} \times P_{REF} = C_{REF} \times S_{SABRE} \qquad (3.10)$$

S_{SABRE} is the signal per mol of ^{1}H for the SABRE spectrum, S_{REF} is the signal per mol of ^{1}H for a reference, P_{REF} is the polarisation level of the reference, and C_{REF} is the calibration constant that relates the SABRE signal to the polarisation level. Further information relating to this calibration methodology is found in this paper[209].

The benefit of the *in-situ* Earth's field NMR setup is that the activation cycle of the SABRE catalyst **I** can be followed over a timescale of seconds to minutes. If a standard high field NMR was used, refilling and outgassing manually between each shake and drop would lead to fewer data points during the activation cycle. The catalytic cycle of the activation reaction is shown in Figure 3.9.a. Prior to the *in situ* SABRE reaction, a 16 electron pre-catalyst **I** = Ir(I) [IrCl(COD)(IMes)]was reacted with the target ligand (L) and the co-ligand (co-L) to form the complex [Ir(COD)(IMes)(Sub)]Cl. This complex undergoes an oxidative addition reaction with hydrogen to form an 18 electron Ir(III) complex of the type $[Ir(H)_2(COD)(IMes)(L)]Cl$. At this stage, the cyclooctadiene (COD) ligand is hydrogenated to form cyclooctene (COE) and subsequently cyclooctane (COA), which cannot ligate anymore. This last step lead to the active SABRE catalyst $IrCl(H)_2(IMes)(L)(co\text{-}L)$ formation. Upon completion of this cycle, the active SABRE complex reversibly binds both H_2 and the ligands that reach the maximum hyperpolarisation.

For the sample containing just **1** (**5**), the intensity of the detected signal increased up to the twentieth experiment, which corresponded to the point where 500 s of bubbling of *p*-H_2 had taken place. After this point, the signal reached a steady state, meaning the sample was fully activated (Figure 3.9.b, blue points). The maximum polarisation level obtained at this point was 0.005%. In contrast, the signal seen for the 25/25 **1**/DMSO sample the major isomer (**4**) (pink dots, in Figure 3.9.b) continued to increase up to 2000 s of continuous bubbling. An estimated polarisation level of 0.014% was achieved, which is approximately three times higher than that seen for the sample containing 40 equivalents of **1**. These data confirm there is improved SABRE efficiency of **1** resulting from the added sulfoxide co-ligand.

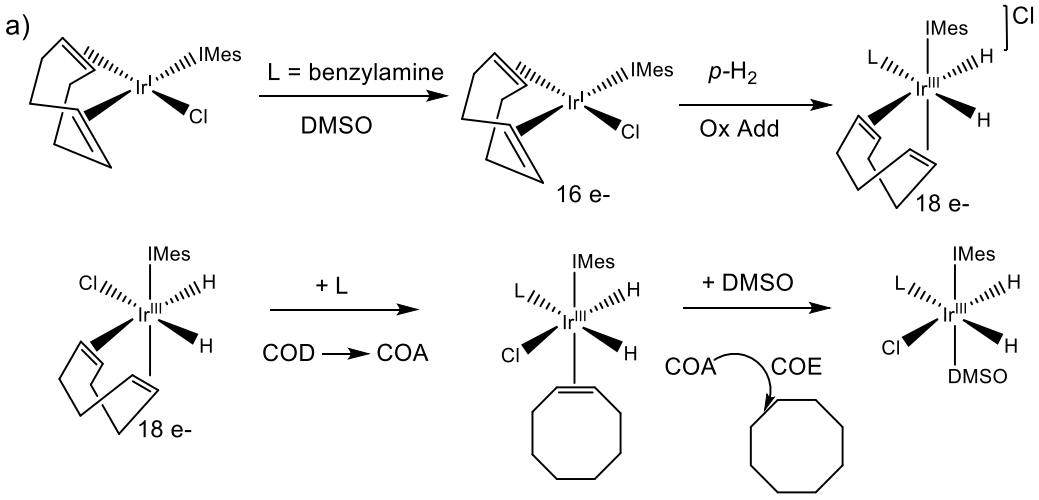

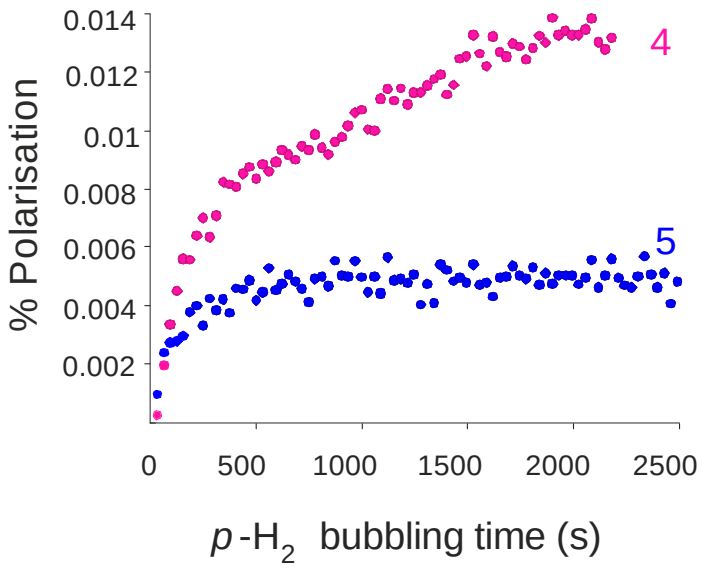

Figure 3.9: a) catalytic cycle of activation of SABRE catalyst **I** in presence of the amine ligand, the co-ligand DMSO and *p*-H_2. b) Comparison of the activation curves, detected in the Earth's magnetic field, of two SABRE solutions. Blue dots correspond to a solution of 5 mM of the catalyst **I**, 25 equivalents of the substrate; pink dot: 5 mM of the catalyst **I**, 25 equivalents of benzylamine and 25 equivalents of the co-ligand DMSO.

3.3.2 Comparative polarisation level of 1 and 2 in 4 and 7 complexes

In this section, hyperpolarisation of **2** is studied and compared to **1**. **2** was chosen because there is an oxygen atom between the phenyl ring and the rest of the molecule. By introducing an ether linkage, the result is expected to be the isolation of the phenyl group. As reported in section 3.2, Figure 3.3, high-field NMR showed that the polarisation transfer across the oxygen linker is inefficient at the usual Polarisation Transfer Field (PTF) and so the hyperpolarisation is concentrated on the aliphatic protons[191] (see Figure 3.2). This would mean that in the Earth's field case, only the aliphatic protons will contribute to the signal and the contribution of the phenyl protons could be neglected.

Figure 3.10 presents the polarisation levels achieved for similar samples of the two amines **1** and **2** and DMSO with pre-catalyst **I** (5.1 mM) (25/25 equivalents 127.5 mM of **1**/DMSO and 25/25 equivalents (127.5 mM) of **2**/DMSO). It can be seen that the presence of DMSO favours the detection of a hyperpolarised signal for both **1** and **2** in the Earth's magnetic field, with the level of signal enhancement seen to be far higher for **1**. At 298 K, complex **7** exhibits a dissociation rate of 7.85 s^{-1} compared to **4** whose value is 4.91 s^{-1}, which is predicted being optimal for a 5-bonds coupling transfer of 1.2 Hz in pyridine[115]. However, a faster dissociation rate as seen for **2** is also consistent with a larger 4-bonds coupling transfer between the hydrides and amines. Although these kinetic values seem good for the detection of **1** and **2** in the EF NMR, they might not be optimal. Variable temperature studies might give a more accurate ligand dissociation rate that provides the best signal enhancement. Unfortunately, this is not possible with the current EFNMR setup where no temperature control exist.

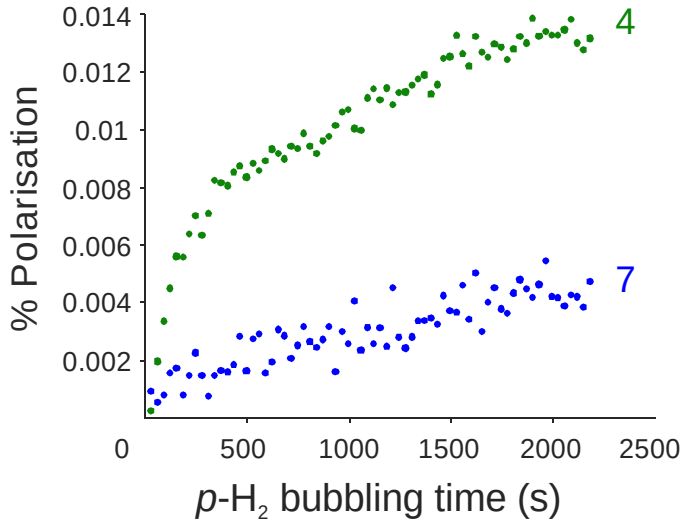

Figure 3.10: Increase in polarisation during activation as function of *p*-H_2 bubbling time same equivalence compared to 5.1 mM of **I**, **1** (**4**, green) and **2** (**7**, blue) at EF NMR (25/25 equivalents 127.5 mM of **1**/DMSO and 25/25 equivalents 127.5 mM of **2**/DMSO in 4 mL chloroform).

3.3.2.1 Effect of ligands concentration on polarisation level of 1

In this section, a 1 T (43 MHz) detection field was used in addition to the Earth's NMR detection to provide parallel confirmation of the observed polarisation level trends. At this higher magnetic field, the chemical shift differences allow for separation of resonances and an independent control measurement for the EF NMR sample. A 1 T instrument was used instead of a standard high-field NMR spectrometer because it is able to lock and measure samples in protonated solvents. In order to carry out equivalent measurements at 1 T and EF, a 4.6 mL volume of 5.1 mM of **I** and the target concentration of **1**/DMSO was prepared in chloroform and shared between EF NMR (4 mL) and 1 T (0.6 mL) samples. This dual-spectrometer approach allows for the direct comparison between these two detection fields and route to validate the EF NMR results.

A series of samples of **1** were prepared and analysed where the ratio of benzylamine to DMSO was kept constant at 1 : 1 while the concentration of the amine was decreased relative to a fixed initial concentration of **I** of 5.1 mM. The relative loading of 1/1 for the ligand and co-substrate is maintained in all samples in order to maintain the three formed complexes in the same proportion as characterised in section 3.2.1. The samples contained 20/20, 15/15, 10/10 and 5/5 equivalents of **1**/sulfoxide relative to iridium. The resulting average hyperpolarised signal data is plotted in Figure 3.11.a, where polarisation level is plotted as function of sample concentration. Analysis of these data reveals that the 5 : 5 loading yields the highest polarisation level of 0.032 % despite having the lowest concentration. The polarisation level decreases with increase in concentration to 0.0035% for 25/25 of **1**/DMSO. Such behaviour has been seen at high field[185, 210-212]. This is mainly explained by the fact that only a limited amount of substrate is hyperpolarised by the SABRE complex per unit time. Consequently, as the concentration of free substrate increases, large numbers of substrate molecules do not interact with the catalyst and therefore do not contribute to the hyperpolarised signal. Hence the net signal enhancement falls.

The method to collect data on the 1 T benchtop NMR spectrometer consisted of filling a 5 mm Young's tap NMR tube with 0.6 mL of the sample mixture. 3 bar of *p*-H_2 was added into the head-space of the tube before it was shaken vigorously in a PTF of 6.2 mT, supplied by a handheld permanent magnet array[213]. This was followed by the introduction of the tube into the NMR spectrometer and the acquisition that yielded an enhanced NMR spectrum. Figure 3.11.b presents the resulting average polarisation levels obtained after activation as a function of **1**/DMSO ratio relative to **I**. In the measurements at 1 T, the SABRE polarisation level, P_{SABRE}, is determined from the enhancement factor, ε, which is equal to the integral of the hyperpolarised SABRE signal relative to that of the thermally polarised control spectrum. As in the case of EF NMR, there is a strong inverse correlation between the substrate excess and hence concentration of the ligand and the SABRE polarisation level. In fact, the overall intensity trend matches closely with that of the EF measurements. However, the sample with a 5/5 ratio yields a polarisation level of 0.014% is significantly lower than the level detected in the EFs study. Furthermore, it decreases essentially linearly with increase in concentration to 0.008 for 25/25 **1**/DMSO ratio.

In principle, the polarisation level resulting from SABRE is not dependent on the magnetic field used for detection[5, 211]. However, the NMR tubes used for the 1 T measurements are filled with 3-bar *p*-H_2 of 99% purity (from a home-build system) while that used in the EF NMR study is 90% pure (from a commercial Bruker *p*-H_2 generator) which, to a first approximation would lead a 13% reduction in efficiency which is opposite to the effect seen. In addition, the calibration of the polarisation in EF NMR has the cumulative error of 12.2% calculated from the propagation of the uncertainties associated with the measurements of S_{REF}, T_{1,B_p}, and T_{1,B_E} as calculated in the paper[209]. The build-up of the polarisation in the pre-polarisation field, B_p, is driven by longitudinal (T_1) relaxation which is given by T_{1,B_p}. The decay of the polarisation during the delay, d_2, between the switching of the pre-polarisation field and the application of the *r.f.* pulse stand for T_{1,B_E}. These two relaxation times T_{1,B_E} and T_{1,B_p} are taken in account in P_{REF} calculation given in Equation 3.10. In fact, these two relaxation time parameters contribute to lower the polarisation measured in the reference P_{REF}. Furthermore, several factors are causing daily variations in the response of the Earth's field NMR spectrometer. Earth's magnetic field fluctuations, the variation of noise levels and the differences in field homogeneity are potential sources of signal disruption that might affect the polarisation obtained with EF NMR, contributing to the cumulative error.

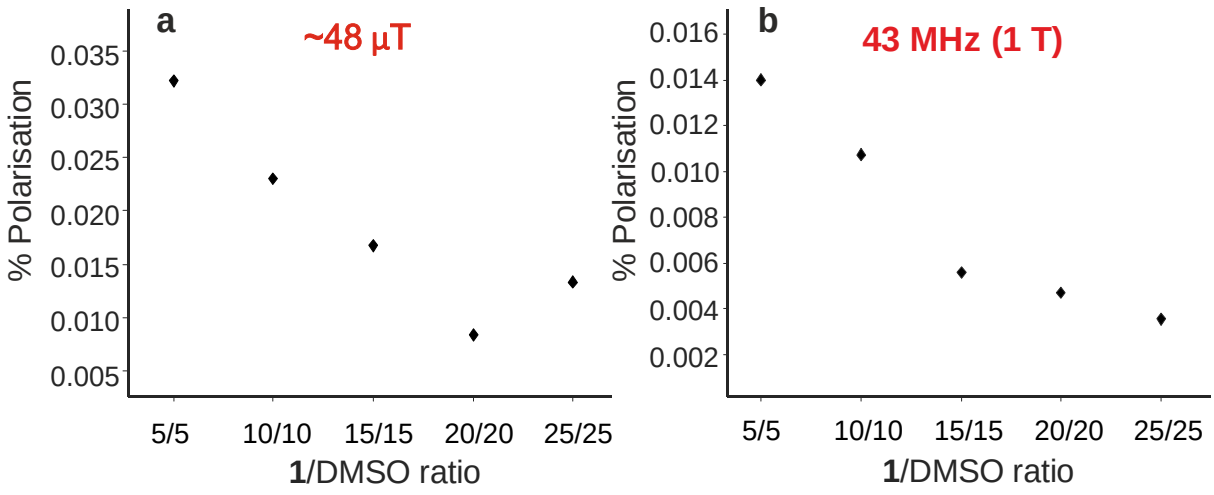

Figure 3.11: a) The average percent polarisation after activation as a function of concentration of **1**/DMSO measured at the Earth's magnetic field (Terranova instrument). Black dots 5/5, 10/10, 15/15,

20/20 and 25/25 benzylamine/DMSO ratio respectively. b) Average of percentage polarisation after activation as function of **1**/ DMSO ratio at 1 T (SpinSolve instrument) of the same samples.

3.3.2.2 Effect of ligands concentration on Relaxation time T_1 level of 1

Relaxation is the process by which nuclear spins return to equilibrium after excitation. It is caused by random transverse fields that are generated within the sample, often due to interactions of spins with one another or with their environment. A method for measuring the hyperpolarised signals longitudinal relaxation time T_1 within the Earth's magnetic field is presented in Figure 3.12.c. It is designed as follows: Firstly, the bubbling of the *p*-H_2 is switched on during the whole experiment. Then the PTF current, which creates a 6.5 mT magnetic field to transfer polarisation from *p*-H_2 to the substrate through the J-coupling network of the catalyst is then turned on for a limited duration to enable polarisation build-up. This field is then turned off adiabatically to allow the created magnetisation to reorient with Earth's magnetic field. Subsequently, a variable delay τ is sampled, followed by a 90° pulse. This sequence is repeated several times whilst incrementing the delay τ. Consequently, relaxation of the NMR signal is encoded as an exponential decay, which can be modelled as detailed in Equation 3.11, where I_0 and I are the relative intensities of the signals seen in the first and subsequent data-points respectively. The duration of the hyperpolarised signal in the low field regime was measured.

$$\frac{I}{I_0} = e^{\frac{-\tau}{T_1}} \qquad (3.11)$$

The method used to measure T_1, with the (1 T) Spinsolve spectrometer involved a variable flip angle sequence (Figure 3.12.d). In this method, a number n of FID separated by a time δt_n are recorded sequentially where each FID is associated with a unique pulse angle θ_n. In this way, the first FID recorded has an amplitude proportional to the initial hyperpolarised magnetisation and will decay again to encode the hyperpolarisation lifetime. A more detailed explanation for this process can be found in the literature[5].

The hyperpolarised relaxation times, T_1, in the Earth's field and at 1 T are plotted in Figure 3.12.a and b respectively. An increase in EF T_1 value, starting from 4.5 to 9.5 s is observed with increase in ligand loading in Figure 3.12.a. In this case, the errors bar, calculated from the fitting, are very big due to the noisy EF NMR spectra. A similar trend is observed in the corresponding 1 T data in Figure 3.12.b but the relaxation time is much shorter in this field. It has to be noted that in this plot, the errors bar, calculated from the fitting errors are too small to be visible. The observed relaxation time is a weighted average of the relaxation times of the bound and free ligand. The metal complex reduces the relaxation time of the bound ligand. Therefore, as ligand concentration is increased, the free pool dominates and the average T_1 that is measured increases. This agrees with other studies[190, 214, 215].

Experimental conditions such as temperature and magnetic field affect also the relaxation time. T_1 is temperature dependent because of random field fluctuations that originate in the molecular environment and the correlation time, which is also temperature dependant. The temperature of the (1 T) Spinsolve probe is 28 °C whereas the (50 µT) Terranova spectrometer operates at lower temperature ~ 20 °C (ambient temperature in the laboratory). Hence, the effects of ligand exchange will differ. The relaxation time is also magnetic field dependent so the relaxation time measured on

the 1 T NMR instrument is again different from that measured on the 50 µT instrument. As field strength is increased, the resonant frequency of the measured protons also increases and becomes less matched to the molecular motion frequencies.

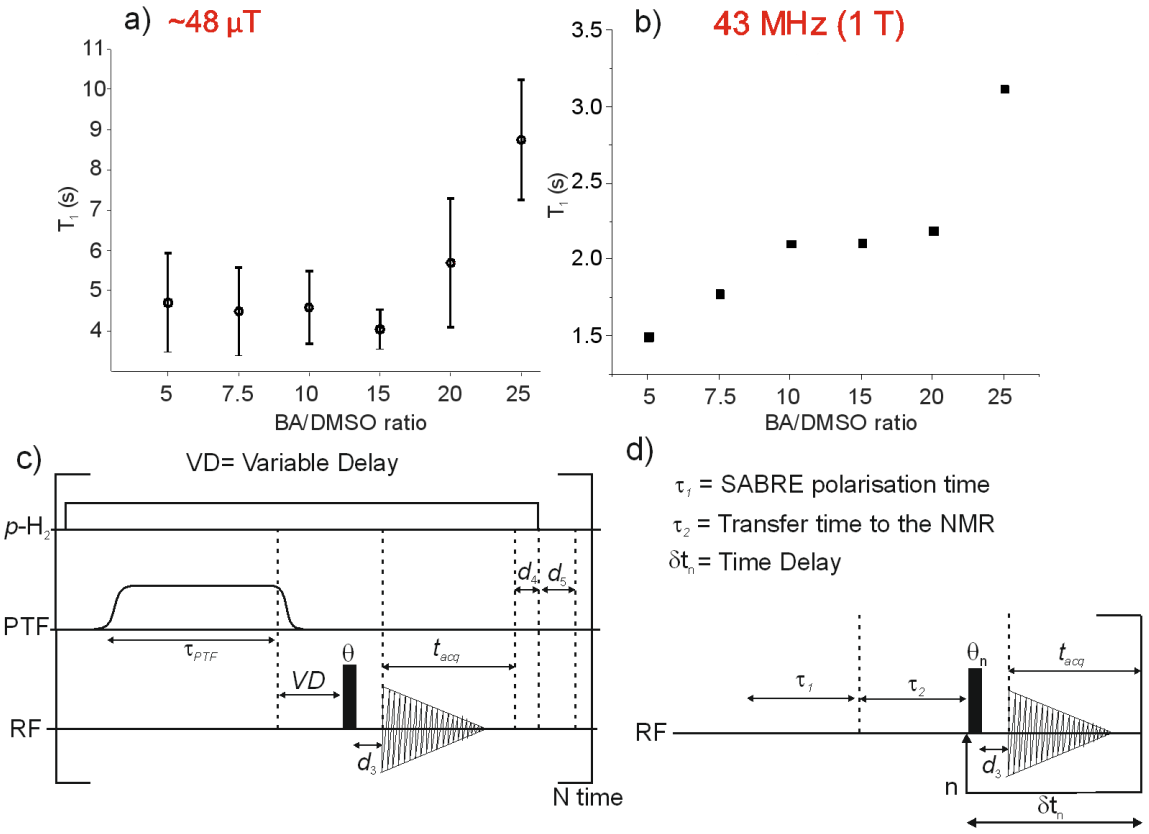

Figure 3.12: a) The relaxation time T_1 as function of ligands excess measured at the local Earth's magnetic field. b) The relaxation time T_1 as function of ligands excess measured at the 43 MHz (1 T). c) Pulse sequence of the standard hyperpolarised T_1 at the Earth's magnetic field. VD stands for the variable delay and d) Pulse sequence for variable flip angle T_1 measurement with the (1 T) Spinsolve spectrometer.

3.3.2.3 Polarisation transfer field (PTF) duration at EF NMR

The *in situ* SABRE approach also allows for the observation of the build-up of the hyperpolarisation in the PTF. As stated in chapter 2 section 2.4.3, the optimal PTF is a direct consequence of the Level Anti-Crossing (LACs) and is usually ~6.5 mT for protons. However, the duration for which this field is applied also has an importance and varies according to the sample and its exchange rate. Figure 3.13 presents the build-up of ^{1}H SABRE hyperpolarisation for samples where a 5/5, 10/10, 15/15, 20/20 and 25/25 **1**/DMSO ratio respectively (with 5.1 mM catalyst) is used in PTF of 6.5 mT as a function of the PTF duration. This required field is produced by a current of 2.05 A in the outer coil. Due to the extremely low sensitivity of EF NMR detection, these build-up curves are noisy but clearly show that a plateau is reached in all samples about 10 sec after the current is turned on. Slower build-up curves are obtained at higher concentration of ligands (20/20 and 25/25) where the plateau seems to be reached at 15 sec of bubbling. Similar effects have been previously seen at high field during the optimum SABRE

polarisation build-up of protons[56]. Furthermore, they confirm that higher polarisation is achieved in lower concentration samples. These results of PTF duration can also be correlated to T_1 values where samples with longer hyperpolarised signal lifetime have build-up a slower PTF duration maximum and inversely.

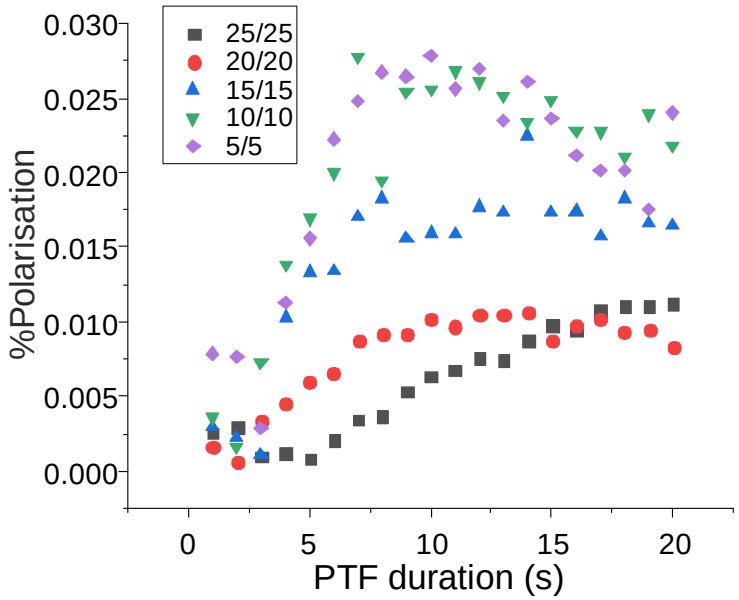

Figure 3.13: Build-up of ^{1}H SABRE polarisation as a function of the duration of the polarisation transfer field (PTF) of the 5 samples where the field 6.5 mT has been produced by a current of 2.05 A. The samples are 5/5 purple, 10/10 green, 15/15 blue, 20/20 red and 25/25 black, **1**/DMSO ratio respectively.

3.3.3 Earth's field NMR detection of 3

The final compound that was explored using the *in situ* SABRE approach is 2,4,6-triflurobenzylamine. The sample used to record the EF NMR data in Figure 3.14 contained 5.1 mM of **I**, 25 equivalents (127.5 mM) of **3** and 25 equivalents of DMSO in 4 mL chloroform. Figure 3.14.a presents the spectrum of the ^{1}H 1D NMR acquired with a single scan. In contrast to **1** and **2**, the EF NMR spectrum of **3** is not a singlet. Instead, a signal of approximately 5 Hz width is observed with a broad positive component split by a sharp negative component. The broad positive component with a width of ~5 Hz originates from **3** hyperpolarisation, can be attributed to ^{3}J (^{1}H-^{19}F) coupling between two adjacent fluorine and proton in the ring. Then, the sharp opposite signal can be attributed to water polarisation. In the absence of heteronuclear couplings, all the proton resonances will collapse into a singlet. This is mainly due to the weak magnetic field, which means that the differences in Larmor frequency between protons due to chemical shift are so small that their signals all appear at the same frequency and no homonuclear coupling is observed. In **3** the amine contains three fluorine atoms on the benzene ring at the *ortho* and *para* positions. The ^{19}F heteroatom is spin ½ and 100% abundant and couples to the aromatic and aliphatic protons of the amine. As described earlier, this coupling introduces the inequivalence in the spin system needed to see an enhanced signal in the Earth's field NMR spectrum.

The presence of the heteronuclei therefore offers a route to signal differentiation at low magnetic field. It was assumed that the samples were not anhydrous and the small fraction of H_2O present is polarised by protons exchanging with the amine. The amine and H_2O polarisation are known from HF

experiments to have opposite polarisation signs[194, 216]. Due to the lack of chemical shift in the Earth's field regime, these two peaks overlap and the bigger component cancels the smaller one. It is therefore assumed that this H_2O contamination is reducing the total polarisation observed in this experiment.

The activation of the complex in the Earth's magnetic field was also monitored. In these data (Figure 3.14.b), the integral over a 30 Hz region was used. No phase correction was applied, these result therefore includes some cancellation due to the water signal. The plateau, which reflects the point where full activation of the complex is reached occurs at around 1000 sec of bubbling where the maximum polarisation level of 0.03% is reached. When the positive and negative components of the signal were integrated separately, no significant difference was observed in the associated data when compared to that obtained from the first method. The polarisation level measured for **3** is almost double the maximum value measured for substrate **1**; however the EF NMR spectra of **3** have much lower SNR because of the broad peak.

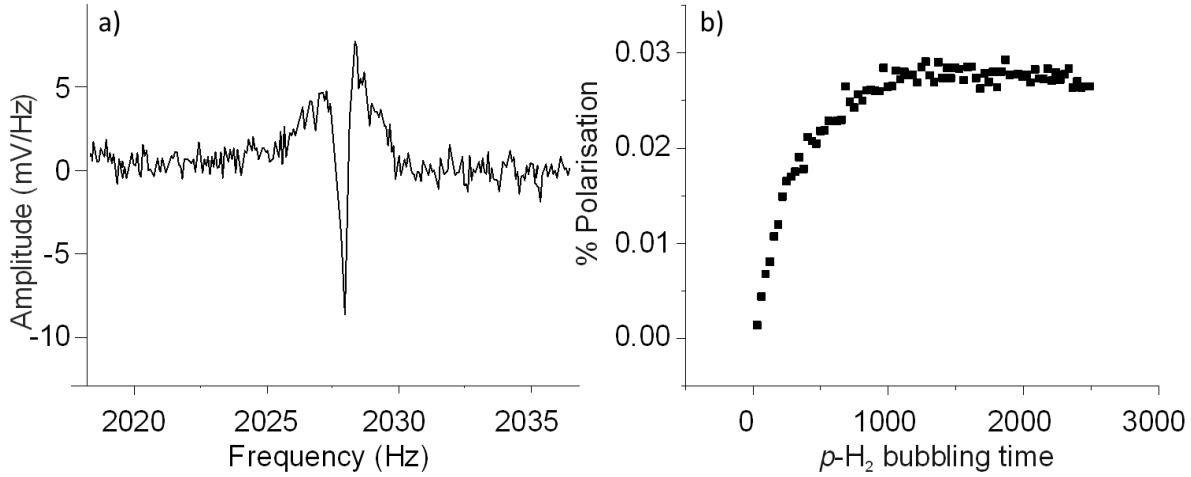

Figure 3.14: a) EF NMR detection of **3**. 1D NMR spectrum centred at 2028 Hz which is the Larmor frequency of ^1H at this field, showing a splitting pattern generated by the presence of the heteroatom ^{19}F. The peak presents a positive and negative component. The sample is composed of 25 equivalence (127.5 mM) of **3** and 25 equivalence of DMSO in 4 mL chloroform. b) Increase in polarisation during activation as function of *p*-H_2 bubbling time of the same sample.

3.3.3.1. SABRE Polarisation build-up and decay of 3 in the Earth's magnetic field

The build-up of the hyperpolarisation in the PTF and the subsequent relaxation decay in the ultra-low-field regime for **3** was also measured. Figure 3.15.a shows the decay of the hyperpolarisation as a function of the variable delay τ (VD in Figure 3.12.c) between the PTF pulse and NMR detection for a sample of 127.5 mM of **3** and 127.5 mM of DMSO with 5.1 mM of **I** in 4 mL of chloroform. The relaxation time for **3** is T_1 = 2.05 ± 0.20 s, while the relaxation time of **1** at the same concentration of ligands was 8.75 ± 1.51 s. The presence of heteronuclei ^{19}F reduces the T_1 and confirms the sensitivity of relaxation to chemical environment[183, 217]. For spin ½ nuclei many factors that include dipole-dipole relaxation, chemical shift anisotropy (CSA) and spin-rotation can influence the relaxation in the Earth's field regime. A similar observation was made at low field where the relaxation process is dominated by CSA rather than dipolar relaxation and can, therefore, be expected to scale with B_0[183]. The small T_1 value measured might also be attributed to interactions with ^{14}N (i.e. within the NH_2), acting as an

efficient quadrupolar relaxation centre in the micro-Tesla regime, probably via scalar relaxation. Figure 3.15.b presents the build-up of ^{1}H SABRE hyperpolarisation in PTF = 6.5 mT (2.05 A) as a function of the PTF duration. The same difference is observed for the build-up of polarisation. **3** reaches the plateau at 6 s of bubbling time while **1** was at 17 s of bubbling time. This effect also might be attributed to the presence of the heteronuclei in the molecule, which trigger relaxation of the hyperpolarised states. The fast build-up polarisation is also in agreement with the rapid decay of the hyperpolarised signal. In addition, this figure is a single exponential but due to the evaporation of the solvent with more experiment repetition, the sample get more concentrated and the SABRE response is different.

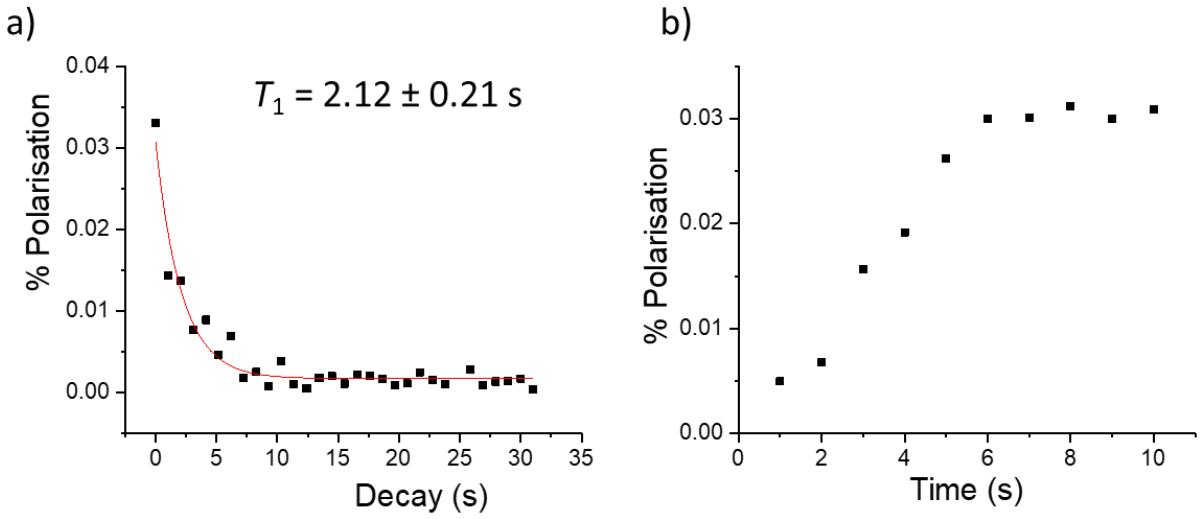

Figure 3.15: a) hyperpolarisation relaxation decay curves for solution of 127.5 mM of **3** and 127.5 mM of DMSO with 5.1 mM of the SABRE catalyst **I** in 4 mL of chloroform. a) Relaxation time T_1 as function of the variable delay τ. b) Build-up of ^{1}H SABRE polarisation as a function of the duration of the polarisation transfer field (PTF).

3.4 Conclusions

This chapter describes the hyperpolarisation of three amines in the Earth's magnetic field. This work was possible due to optimisation of the hyperpolarisation conditions of these molecules through the employment of a suitable co-ligand, dimethyl sulfoxide. The co-ligand was shown to favour faster exchange rate of ligands and therefore shorter complex lifetimes involved in the hyperpolarisation transfer for substrates **1** and **2**. These parameters were not measured for **3** but same outcomes are expected. In addition, the co-ligand seems to lower the Gibbs activation energy barrier of these complexes thus allowing efficient polarisation transfer. In all complexes probed, the entropy $\Delta S^{\ddagger}$ is positive in agreement with the dissociation mechanism. In the presence of the DMSO, the enthalpy $\Delta H^{\ddagger}$ increases slightly leading to a tighter **Ir**-**L** bond, which is directly related to the lifetime of the complex for efficient polarisation transfer.

Substrate **2** however presents similar reactivity in presence of the co-ligand. When measuring the hyperpolarisation level in the ultra-low field regime, less efficiency was observed compared to substrate **1**. DMSO addition increases the exchange rate in a way that polarisation transfer is no longer optimal for Barstky predicted model, in which the 5-bonds coupling between the hydrides and the ortho-protons of pyridine is ~1.2 Hz. The fast dissociation rate of 7.85 s^{-1} is therefore consistent with

a bigger 4-bonds coupling (~7 Hz) between the hydrides and the amine protons. The activation enthalpy $\Delta H^{\ddagger}$ and activation entropy $\Delta S^{\ddagger}$ are higher for both **Ir-1** and **Ir-H** bonds when **1** is employed than in **2**. This is in agreement with a more stable Ir-ligand bond when **1** is employed whereas **2** promote less stable complex. It was shown that the co-ligand clearly increases the signal enhancement of **2** at high field and allows **2** to be detected in the week Earth's magnetic field. In fact, in the absence of DMSO, no signal could not be detected for **2** at the Earth's magnetic field. Although the presence of DMSO in hyperpolarisation of **2** is not as optimum as for **1**, it therefore helps to increase the signal enhancement of **2** to a detectable level in the Earth's magnetic field.

In contrast to **1** and **2**, substrate **3** exhibits a EF NMR spectrum with a multiplet structure, a consequence of ^{1}H coupled to the ^{19}F nuclei. The maximum percentage polarisation of 0.03% achieved with this molecule is far higher than in all amines tested in the EF NMR. Contrary to the results obtained at high field similar signal enhancement level were obtained for both **1** and **3** (section 3.2). Two approaches was used to calculate the polarisation level of **3** in the EF NMR. Firstly, in these presented data (Figure 3.14.a.b), the integral was measured from a 30 Hz width, hence the total signal was used. No phase correction was applied, thus, a cancellation in some part of the total signal occurred. In the second approach, integration of the negative component (water signal) and the total signal were undertaken. Subsequently, a subtraction of the opposite sign signals was undertaken and yielded the real contribution of the amine **3** signal. There was no significant difference in the results between these two approaches and the maximum polarisation measured was 0.03%; hence, the first data was kept. Even the hyperpolarised signal has a shorter build-up and relaxation time, the *in-situ* EF NMR setup allowed their direct measurement avoiding hyperpolarisation loss during manual transfer (high field case). Indeed, relaxation of the hyperpolarised signal occurs during this manual transfer leading to signal loss. These measurements would have been more challenging at high field where significant signal loss occurs also due to the similarity between T_1 and the transfer time.

The potential water contamination highlighted in section 3.3.3 may reduce the overall signal for **1** and **2**. In fact, water polarisation has an opposite sign compared to amines polarisation. In the absence of heteronuclear couplings, a unique signal is recorded for all protons, which is the Larmor Frequency. When these two signals are summed up, a cancellation of the opposite component occurs, hence a decrease of the total signal.

The optimisation of the solvent used was also key to the *in-situ* detection of SABRE-enhanced amines in the Earth's field regime. The bubbling of the *p*-H_2 through the sample solution evaporates the solvent, thus making the solution more concentrated and less favourable for SABRE reaction as the number of repeat experiments increases. Therefore, choosing a high boiling point solvent that allows more experiment repetitions is essential. Previous amine hyperpolarisation was demonstrated in dichloromethane-d_2 solvent, which has low boiling point of 42°C. To adapt to EF NMR detection, here the reactions were performed in chloroform, which has higher boiling point of 6262°C. Although the hyperpolarisation level achieved with this solvent is less than in dichloromethane, more NMR experiment repetitions are possible with the same sample. In addition, the use of DMSO as a co-substrate increased the polarisation efficiency in chloroform such that detection in the Earth's magnetic field was possible. The goal of this chapter, which was to expand the range of substrates amenable to EF NMR detection with SABRE hyperpolarisation, with focusing on amines is fulfil. The three chosen amines **1**, **2** and **3** were successfully detected at the Earth's magnetic field with the help of the co-ligand DMSO. In terms of future experiments, although amines were successfully detected in the Earth's field regime, the sensitivity of these recorded spectra is still very low. The amine polarisation is almost at the limit of detection of the Earth's field spectrometer. To further improve the polarisation levels, catalyst optimisation would be possible. It has been shown that using

deuterated catalyst dramatically increased the hyperpolarisation level[215]. Tweaking the electronic and steric effects on the catalyst might also favour a more stable amine complex and thus efficient polarisation transfer[174]. The size of the DMSO co-ligand could be increased by using diethyl sulfoxide, diphenyl sulfoxide and/or other type of sulfoxide and the performance efficiency as a function of sulfoxide identity be compared[218]. A variable temperature SABRE and exchange measurements could provide a more accurate ligand exchange rate that leads to an optimum SABRE efficiency for each substrate.

The works presented in this chapter shows in the absence of a heteroatom, all protons have the same resonance frequency which is the Larmor frequency. In fact, at such low magnetic field, the difference in resonance frequency between protons is vanishingly small, leading to all protons contributing to the same peak. In the last example, the ^{19}F nuclei present in the molecule offers the observation of *J*-coupled spectra in the strong coupling regime. A diagnostic response is obtained due to the heteronuclear coupling that breaks the equivalence between proton nuclei. This allowed for differentiation between the amine hyperpolarisation and the water signal. It is also a validation that the observed signal is due to the hyperpolarised amine.

In the next chapter, the hyperpolarisation conditions of a range of compounds that possess a ^{31}P heteroatom are screened. This later is chosen because like ^{19}F, it is a spin ½ nucleus that is 100 % abundant. The ^{31}P gyromagnetic ratio (17.23 $MHz.T^{-1}$) is smaller than ^{19}F (40.078 $MHz.T^{-1}$), leading to a less sensitive response. Besides that, ^{31}P NMR provides a sensitive detection at high field NMR. In addition, phosphorus-containing molecule are also good ligand for transition metal complexes, allowing their coupling to be observed in ^{1}H NMR spectra. Therefore, these classes of compound are good alternative to fluorinated molecule for low magnetic field studies. In the Earth's field regime where chemical shift information are inexistent, the presence of a heteroatom is essential for a heteronuclear coupling and ultimately offer a diagnostic tools between different molecules or complexes. This effect will be studied in the next chapters. Beforehand the hyperpolarisation condition of these molecules will be tested at high magnetic field prior to the Earth's field detection.

Chapter 4: Optimization of hyperpolarisation conditions of phosphines, phosphites and phosphates for identifying suitable systems for low field detection

4.1 Aims: heteronuclear coupling for ZULF detection

In standard high field NMR, the detection of ^{31}P nuclei is now very common[219]. This interest is driven in part by its numerous physical advantages, when compared to other heteronuclei, but also its central role in many important materials in biology and chemistry[220, 221]. Its physical advantages stem from the fact that it is a spin ½ nucleus with a T_1 relaxation value in the range of several seconds and its 100% natural abundance. In addition, ^{31}P has a relatively high gyromagnetic ratio of 17.23 MHz.T^{-1}, which means it can be observed using high-field NMR and ultimately on the low field regime even at relatively low concentrations. The relative receptivity, which is the combination of the sensitivity and the isotopic natural abundance of a given nucleus compared to the proton is used to assess a nuclear response. For example, the relative receptivity of ^{1}H relative to that of ^{31}P is 6.6×10^{-2} is much greater than that of ^{1}H relative to ^{13}C or ^{15}N, which are 1.8×10^{-4} and 3.9×10^{-6} respectively.

The goal of this chapter is to improve the detection of the phosphorus compounds (**10** – **18**) (Figure 4.1) using ZULF NMR spectrometers (Earth's field NMR and atomic magnetometer). However, with ZULF NMR detection, strong heteronuclear coupling is a requirement due to the vanishingly small chemical shift differences that operate in the ZULF regime. In fact, it is only the heteronuclear coupling that allows an NMR signal to be detected in operational regime of standard atomic magnetometers, where the frequency range is 50 - 200 Hz[101]. In contrast, EF NMR has a broader spectral width where the difference between ^{1}H and ^{31}P detection is just ~1100 Hz. In EF NMR, the heteronuclear coupling is not required to observe ^{1}H signals but they are needed to provide a chemical signature in the absence of chemical shift resolution.

In general, molecules bearing a P-H bond exhibit strong one bond ^{1}H-^{31}P couplings of hundreds of Hz, making them suitable for ZULF NMR detection[9]. In addition, transition metal complexes with phosphine ligands often present characteristic phosphorus hydride coupling constants. For example, *trans* ^{1}H-^{31}P couplings are often around 150 Hz whereas *cis* ^{1}H-^{31}P couplings are usually approach 20 Hz[130, 131, 222]. The goal is to use these ^{1}H-^{31}P couplings to break the magnetic equivalence of ^{1}H nuclei in the very low field regime in order to allow observation of *p*-H_2 hyperpolarisation. The first step to realising this goal is to develop suitable hyperpolarisation conditions for the target molecules.

As indicated, ^{31}P NMR spectroscopy is a key tool to investigate the structures of metal complexes where it provides easily observable and sharp signals at high magnetic field for their phosphorus ligands in addition to structurally defining ^{1}H-^{31}P couplings. In fact, this spectroscopic tool is routinely used to provide evidence for reaction intermediates that exist for a short as several tens of seconds as well as for those that reflect stable products[223]. Phosphine ligands are soft and often strong sigma donors. In inorganic chemistry, phosphorus compounds are used as both spectator and function controlling ligands, where they stabilise both transitions states and product geometries. This broad versatility is reflected in homogenous catalysis where alkyl and aryl substituent phosphines are widely explored as their electronic, steric, and stereochemical properties vary according to their substituents.

A simple literature search finds examples in hydrogenation, hydroformylation, hydrolysis, hydratation, cross-coupling and carbon-heteroatom bonds formation[224, 225]. These examples build from the activation of small molecules such as H_2, N_2, H_2O, O_2 and CO_2[220, 226].

The first PHIP reaction was performed using the phosphine-containing $RhCl(PPh_3)_3$ for the conversion of acrylonitrile to propionitrile[21]. Furthermore, the first SABRE catalyst contained phosphine[135], although carbene ultimately proved far superior[56, 171]. Subsequently, many catalysts of this type have been synthesised and their activity towards PHIP and SABRE studied by changing the steric and/or electronic properties of the phosphine spectator ligands.

Although phosphorus compounds usually act as spectator ligands, they can also receive hyperpolarisation within the metal coordination sphere. Several early works on PHIP demonstrated the transfer of magnetisation from *p*-H_2 to heteronuclei like ^{31}P using INEPT protocols[227, 228]. In addition, in 2009, slow-exchanging iridium complexes used for SABRE were shown by M. Fekete et al.[173] to transfer hyperpolarisation to their carbene and phosphine ligands.

Building on this, Koptyug et al.[229] demonstrated ^{31}P enhancement of the free phosphine for the more rapidly exchanging $IrCl(H)_2(PPh_3)_3$ complex at high temperature (60 – 80 ^{o}C). This SABRE process utilises the strong ^{1}H-^{31}P ^{2}J coupling between the *p*-H_2 derived hydride ligands and PPh_3 where high temperature was requirement to trigger ligand exchange. More recently, substantial hyperpolarisation of ^{31}P nuclei was shown through SABRE in a range of regioisomeric phosphonate esters containing a hetero-aromatic motif[181]. In this study, the heteroaromatic group was used for binding and polarisation was transferred to remote ^{31}P nuclei through the scalar coupling network.

In this chapter, the research will focus on hyperpolarisation and detection of molecules that possess strong heteronuclear ^{31}P-^{1}H couplings. For this purpose, it is first necessary to select suitable compounds. Nine readily available phosphorus containing molecules were chosen for this study (Figure 4.1). The first row of Figure 4.1 presents phosphorus compound with one-bond ^{31}P-^{1}H couplings in the range of 200 to 600 Hz. In this first row, moving from phosphine **10** to the phosphine **11**, P=O bonds are introduced which is expected to change their reactivity. In addition, the steric bulk is increased in the order **11**, **12** and **13**, thereby changing the ligand affinity. The second row of molecules do not possess one-bond couplings; however, they could provide the necessary hydride-phosphine couplings when they ligate to the metal catalyst. It is the case of phosphines **14** and **14** that possess different steric bulk. Hydrogenative PHIP is attempted with **16**, which possesses an alkene bond. Finally, the phosphine sulfide **17** and **18** are also tested to link with the co-ligand dimethyl sulfoxide DMSO used in chapter 3.

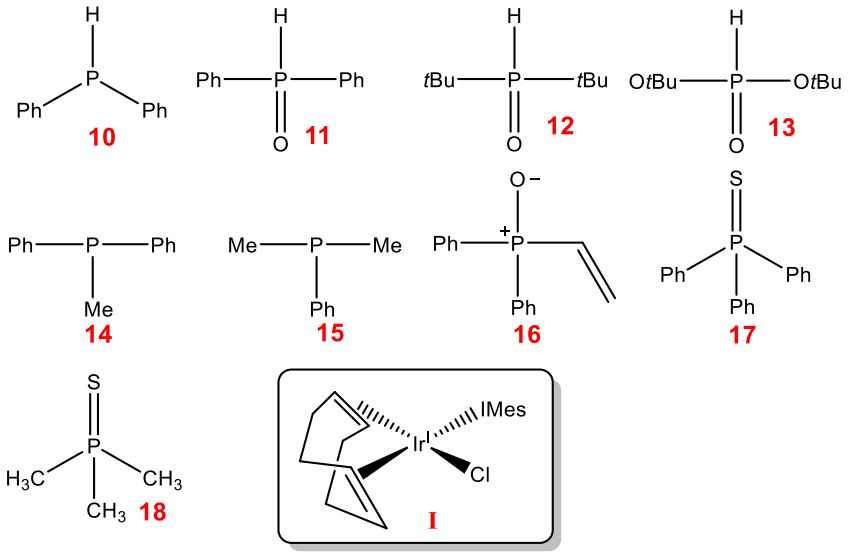

Figure 4.1: Chemical structure of **10** diphenyl phosphine, **11** diphenyl phosphine oxide, **12** diterbutyl phosphine oxide, **13** diterbutyl phosphite, **14** diphenyl methyl phosphine, **15** dimethyl phenyl phosphine, **16** diphenyl vinyl phosphine oxide, **17** Triphenylphosphine sulphide, **18** Trimethylphosphine sulphide. The chemical structure of the pre-catalyst IrCl(IMes)(COD) (where IMes = 1,3-bis (2,4,6-trimethylphenyl) imidazol-2-ylidene, COD = cyclooctadiene) is also added and called later **I**.

4.1.1 NMR detection methods

In order to achieve ZULF NMR detection of these compounds (**10** – **18**) (Figure 4.1), optimisation of hyperpolarisation conditions using high field NMR (500 MHz) is necessary. Indeed, high magnetic field provides the spectral resolution and chemical dispersion required to characterize all complexes formed in solution. Subsequently, optimisation of the hyperpolarisation conditions of complexes that provides high PHIP or SABRE activity (e.g, what ligands excess and temperature are optimum), is carried out with a minimum consumption of materials. Then, the reactions could be scaled up for detection with the Earth's field spectrometer. IrCl(IMes)(COD) **I** (Figure 4.1) will be used to catalyse the hyperpolarisation reaction of the phosphine ligands because previous studies have shown that **I** yields better hyperpolarisation response compared to other metal catalysts[174]. In the experiments described in this chapter, hyperpolarisation reactions are carried out by SABRE and/or PHIP techniques and rapid 2D NMR characterisation using *p*-H_2 are also performed.

In the forthcoming sections and chapters, the shorthand SABRE, PHIP and thermal experiments are used to denote the following protocols.

A standard SABRE experiment is carried out by pressurising the sample with 3 bar of *p*-H_2, then shaken for 10 s in a 60 G hand-held magnet array. The sample is then quickly manually transferred into the magnet for detection with a $\pi/2$ pulse. The sample is refilled with fresh *p*-H_2 for every SABRE experiment due to quick relaxation of and consumption of *p*-H_2.

A PHIP experiment is carried out by pressurising the sample with 3 bar of *p*-H_2, then it is shaken for 3 s in the Earth's magnetic field. The sample is then quickly (~2-5 s) manually transferred into the magnet

for detection with a $\pi/4$ pulse. This is in agreement with the origin a PHIP hyperpolarised signal is a two-spin longitudinal spin order term, $2(I_{1z}I_{2z})$, which produces maximum observable signal following a π/4 pulse and no signal following a π/2 pulse. Because the consumption of *p*-H_2 is very slow, multiple sequential PHIP experiments can be performed for one *p*-H_2 fill and sample shake.

A thermal experiment is performed without any fresh *p*-H_2 added in the sample. The acquisition is usually done with multiple scans and using standard 1D ^{1}H NMR parameters with appropriate recovery delays.

Optimization of the hyperpolarisation level of the complexes is explored by tuning many parameters, such as temperature, solvent, concentration, and addition of co-ligands. This procedure allowed us to develop an understanding of the chemistry involved in these reactions and has revealed some unexpected reactivity. For the purpose of efficiency, detailed spectroscopic results are presented only for compounds that have shown PHIP hyperpolarisation. Compounds that did not show any PHIP or SABRE features are just briefly described.

4.2 Hyperpolarisation of diphenyl phosphine 10

The motivation for studying phosphine **10** is it possesses a large P-H coupling that can be possibly detected in the ultra-low magnetic field regime. I beforehand needed to test its reactivity in presence of dihydrogen then hyperpolarisation conditions at high magnetic field. Furthermore, it is the only compound in the liquid state at room temperature, which could be detected thermally with the EF NMR device (see chapter 7, section 7.2).

4.2.1 Reaction of 5 eq. of 10 with IrCl(IMes)(COD), **I** and H_2

The reaction of 5 mM of **I** with H_2 and 2.72 µL **10** (5 eq.) in dichloromethane-d_2 at 295 K yielded the dihydride complex **19** Ir(H)$_2$Cl(COE)(IMes)(PPh$_2$H), alongside three isomers of Ir(H)$_2$Cl(IMes)(PPh$_2$H)$_2$, **20**, **21** and **22** according to Scheme 4.1.
In **20**, the hydride ligands provide signals in the ^{1}H NMR spectrum at -9.31 and -23.03 ppm, and are *trans* to **10** and Cl^- respectively as the corresponding J(^{1}H-^{31}P) couplings are 151 Hz and 23 Hz. In contrast, the hydride ligands in **21** are chemically equivalent as both lie *trans* to **10**. The result of this is a second order located at -10.23 ppm where |J(^{1}H-^{31}P)trans + J(^{1}H-^{31}P)cis| is 128.1 Hz. The hydride ligand signals of **22** are observed at -11.16 and -11.76 ppm, and are due to ligands *trans* to IMes and **10** respectively. **19** proved to have a short lifetime and was not characterised, although related literature supports its formation[230]. The characterisation of **20** was achieved by 2D NMR spectroscopy and the resulting data are detailed in section 9.7.1. Over time all four of these complexes convert into the *tris*-phosphine cation *cis-cis* [Ir(H)(2(IMes)(PPh$_2$H)$_3$]Cl **23** whose NMR data are listed in section 9.7.2. These changes are portrayed in Figure 4.2.

Further evidence for these assignments is provided by the corresponding ^{31}P NMR data, which before H_2 addition, shows signals for free **10** at -40.2 ppm, with a ^{2}J(^{1}H$_{ortho}$-^{31}P) of 6 Hz, and a ^{1}J(^{1}H-^{31}P) of 219 Hz along with a weak signal at -14.5 ppm for bound **10** with a much larger ^{1}J(^{1}H-^{31}P) of 360 Hz for 16-electron Ir(COD)(IMes)(PHPh$_2$). After hydrogenation, this situation changes and two doublets at -36.46

and -38.20 ppm, both split by a J(^{1}H-^{31}P) coupling of 127 Hz, are seen for **23**. Resonances for **20** are identified at 29.2 and 5.33 ppm for groups *trans* and *cis* to the hydrides alongside those of **21** and **23** at -28.35 and -37.33 ppm, respectively; these deductions were determined using HMQC experiments.

The analogous reaction was then studied with *p*-H_2 for a sample containing an initial 5-fold excess of **10** relative to iridium. The resulting NMR spectrum (Figure 4.2.a), recorded immediately after sample preparation and adding fresh *p*-H_2, yields strongly polarised hydride resonances at -9.18 and -14.12 ppm for **19**. Additional, but weaker PHIP enhanced signals are visible for **20** and **22**. Over time, unpolarised signals for **23** and **21** increase, while PHIP enhanced hydride resonances for **19** and **22** disappear. Hyperpolarised hydride resonances for **20** persist over a period of approximately 1.5 hrs. After 24 hours, **20** is no longer observed and **23** reflects 98% of the observed hydride species. Complex **21** makes up the remainder at ~2%. **23** must therefore reflect the thermodynamic product.

When a 1D EXSY experiment is performed to examine the hydride signal of **23**, no exchange with dihydrogen is observed. This is consistent with the lack observable hyperpolarisation for this complex and indicates that the phosphine ligands in this complex are not labile. While no exchange is observed, an NOE interaction with CH_3 (2.2 ppm) and phenyl (6.26 ppm) resonances of ligand **I** and a phenyl (7.29 ppm) of ligand **10** are seen confirming their spatial proximity. Similarly, the hydride signals for **21** do not show exchange with dihydrogen but do connect via NOE with a 2.2 ppm methyl resonance in **I**.

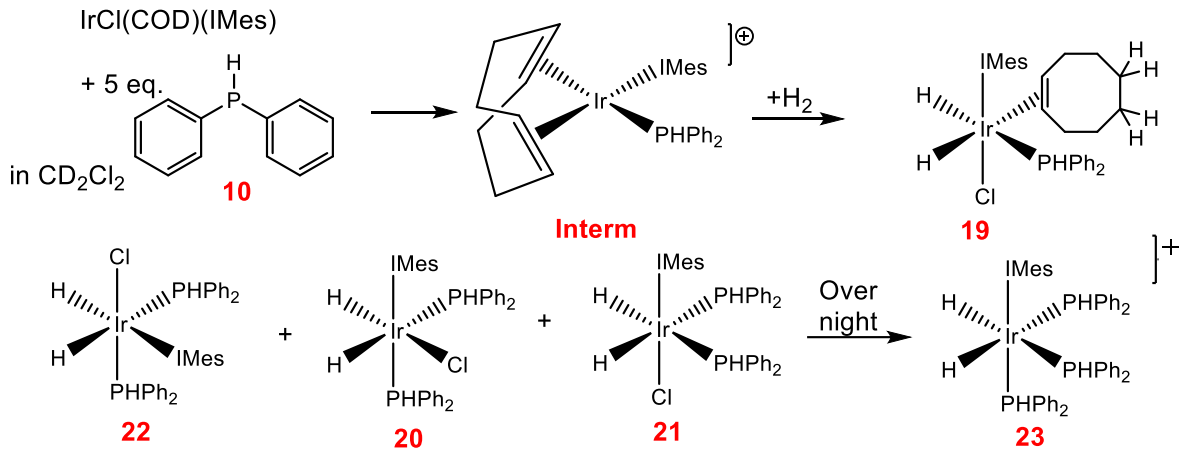

Scheme 4.1: Reaction of **I** with 5 eq. of **10** in dichloromethane-d_2 shows the formation of five dihydrides species **19**, **20**, **21**, **22** and **23** over time. The thermodynamically stable product **23** is favoured by an excess of **10**.

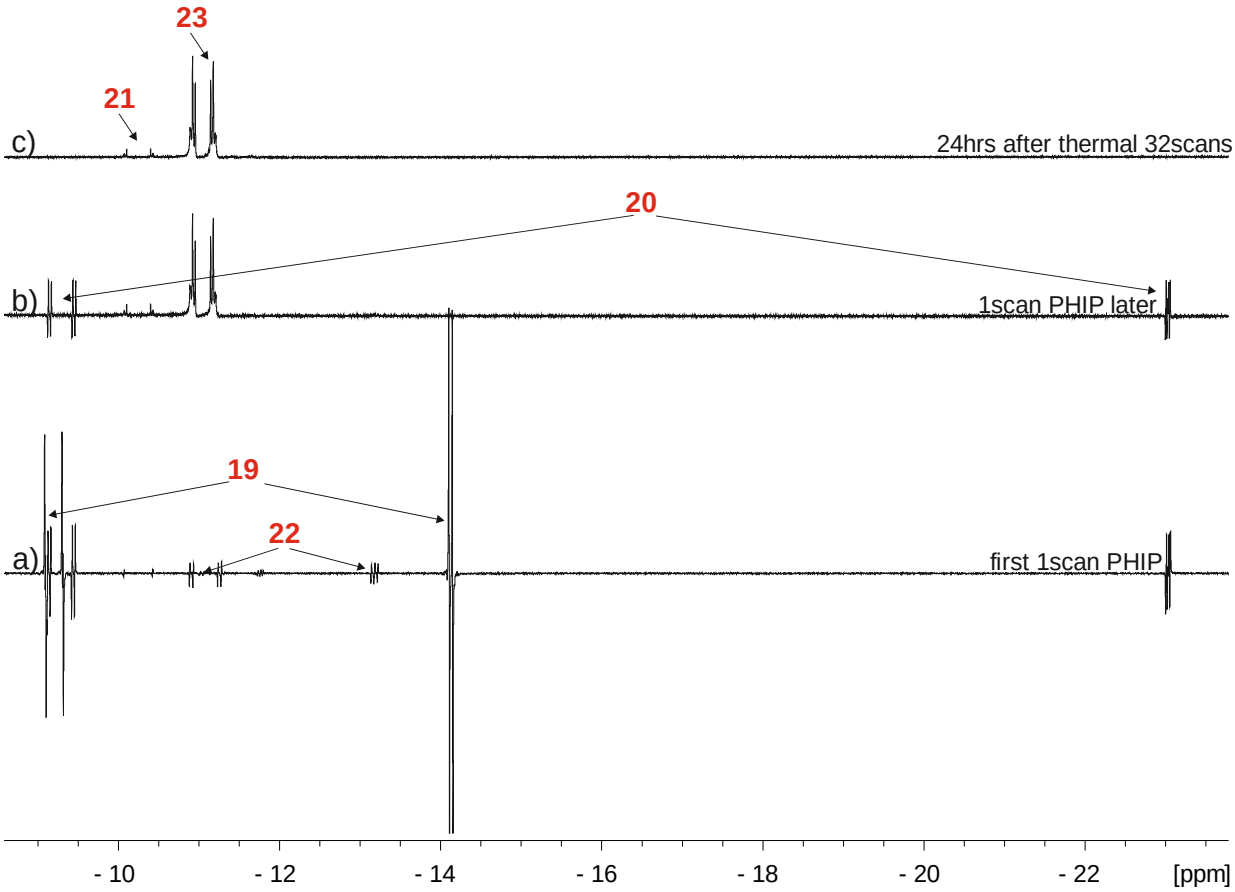

Figure 4.2: a) Reaction of 5 mM of **I** pre-catalyst, 25 mM (5 eq.) of **10** in 0.6 mL of dichloromethade-d_2 and 3 bar of *p*-H_2 leading to the formation of complexes **19**, **20**, **21**, **22** and **23**. c) The first hyperpolarised spectrum recorded shows enhanced hydrides for complex **19**, **22** and **20**. b) Subsequent (~3 min since *p*-H_2 addition) PHIP scan continue to show polarisation of complex **20**. a) 24hrs later, the thermal spectrum recorded show the thermodynamic products **21** and **23**.

The aim was to exclusively favour the formation of **20**, which is the only hyperpolarisable complex among the array of products that is stable to be observed after each *p*-H_2 addition and the reaction could be repeated for days. It contains only two ligands of **10** The kinetic formation of these species in function of the concentration of **10** was then explored in order to develop a better control of the product formation.

4.2.2 Kinetics formation and consumption of 20 21 and 23 as a function of concentration of 10

The rate of consumption and formation of complexes **20**, **21** and **23** (Figure 4.3.a and b) can be followed and shown to be dependent on the ligand concentration. The reaction of IrCl(COD)(IMes) proceeds with $PHPh_2$ to form Ir(COD)(IMes)($PHPh_2$) as the sole product prior to H_2 addition. Rapid H_2 addition then leads to **19** $Ir(H)_2Cl(COE)(IMes)(PPh_2H)$ which is only detectible through PHIP enhanced hydride ligand signals. At this point, the subsequent NMR spectra show signals for **20**, **21** and **23**.

When 2 eq. of **10** was used the initial spectrum showed ~88% of **20** and 8% of **21** and **23** are present alongside ~4% of an unidentified species. After 22 hrs, almost 100% of **21** is converted into **20** whilst

23 is steady at 8%; the unidentified species now make up ~2%. The time constants respectively for the equilibration between **20** and **21** with 2-equivalents of **10** relative to iridium are 57369 ± 60 s, 47849 ± 60 s. **23** was then very minor.

In contrast, 5 eq. of **10** allows for the faster and clean conversion of **20** to **23** with **21** again remaining inert. Thus, Figure 4.3.b, starts with 65% of **20**, 20% of **23** and 8% of **21**. The time constants for **20** converting to **23** is 1056.6 ± 5 s and 1114.3 ± 4 s.

For conclusion, these data confirm the necessity of controlling the amount of PPh_2H used if hyperpolarisable **20** is to be the major product. It was found that ~1.8 equivalents of **10** relative to iridium optimised **20** formation and its the PHIP signals.

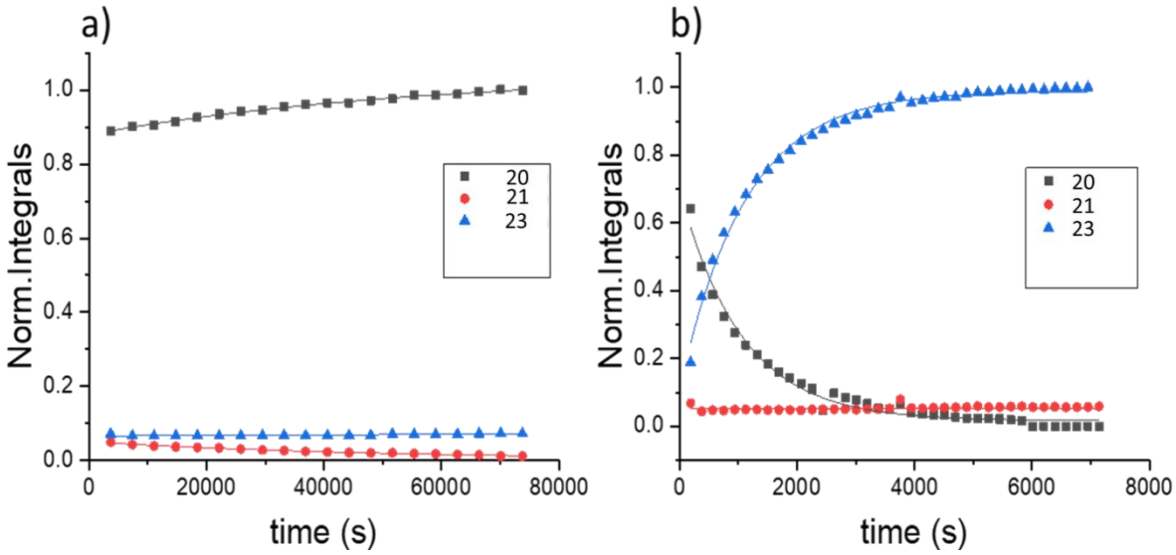

Figure 4.3: a) 5 mM of **I** with 1.1 µL 2 eq. of **10** is mixed in dichlorometane-d_2. The time constant of conversion of the complexes **20**, **21** and **23** is followed by NMR at 298 K for 22hrs. b) 5 mM of **I** with 5 eq. of **10** is mixed in dichlorometane-d_2. The rate of conversion of the complexes **20**, **21** and **23** is followed by NMR at 298 K for 2hrs.

4.2.3 Reaction of 2 eq. of 10 with IrCl(IMes)(COD), **I** and H_2

It have been identified that **20** yields PHIP signals with larger enhancement measurable for each *p*-H_2 that last for days. The aim is now to control the reaction and promote its formation by reducing the concentration of **10** in order to limit the formation of **23**, which requires coordination of three molecules of **10**. As stated above, when two equivalents (1.1 µL) of **10** are added, the results change. The enhanced PHIP signals for **19** at -9.18 and -14.12 ppm dominate in the first scan. However, an immediate change was observed in the initially weak signals for **20**, which become the only PHIP enhanced signals that remain visible (Figure 4.4.b). Over time, the PHIP enhanced signals for **20** remain dominant although a number of very minor PHIP enhanced dihydrides can be seen. These do not appear in a thermally polarised NMR spectrum recorded just 20 min after H_2 addition, which shows signals for **20** and **21** alone with relative intensities of 1: 0.05 respectively (Figure 4.4.c). For a longer reaction time, slow formation of **23** is observed (not shown here). Now, the signals for **20** dominate,

and NMR integration reveals it reflects 80% of the hydride species after 48 hrs. **21** and **23** represents the remaining 20%.

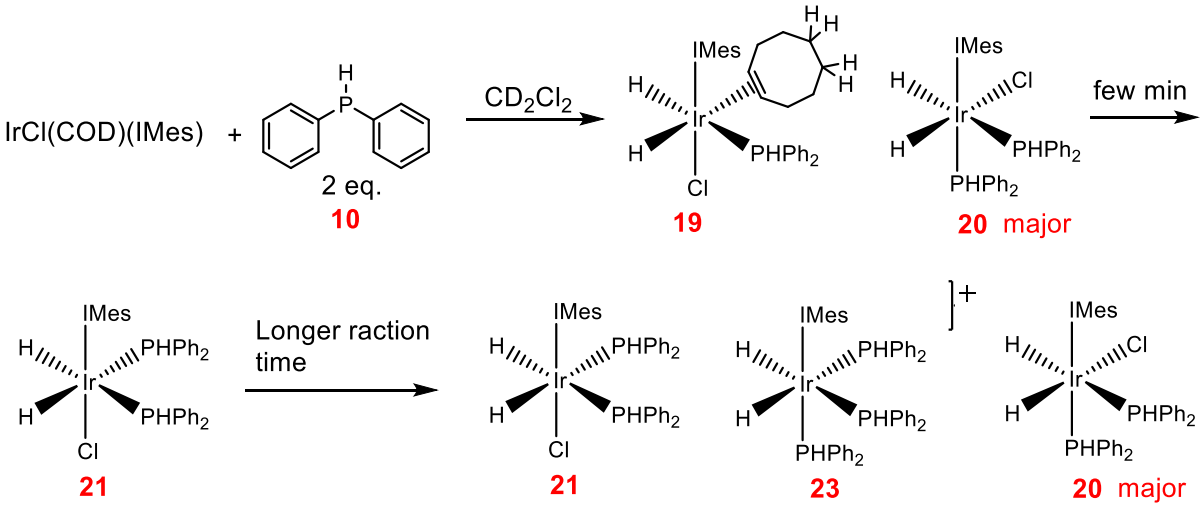

Scheme 4.2: Reaction of **I** with (2 eq.) of **10** in dichloromethane-d_2 shows the formation of three dihydride species **21**, **23** and **20**, over time with now **20** dominating.

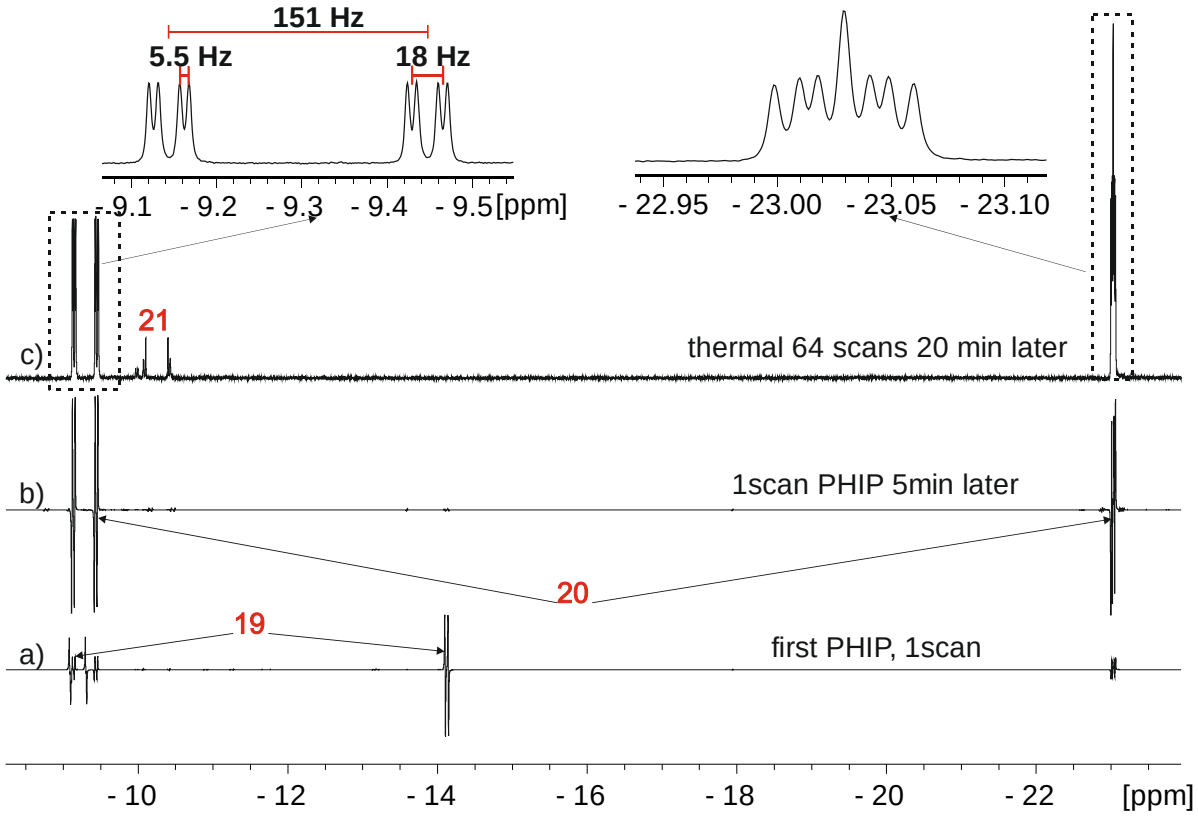

Figure 4.4: Reaction of 5 mM of **I** pre-catalyst, 1.1 µL (2 eq.) of **10** in 0.6 mL of dichloromethane-d_2 and 3 bar of *p*-H_2 observed at 500 MHz. a) 1scan PHIP NMR spectrum showing the hyperpolarised hydride signals of complexes **19** and **20**. b) The subsequent PHIP experiment now shows strong hyperpolarised hydride signal for **20** only. c) Thermally polarised spectrum recorded 20 min later with 64 scans shows **20** and **21**. Zoomed regions show the coupling patterns for **20**, where *trans* J(^{1}H-^{31}P) =

151 Hz, *cis* $J(^1H-^{31}P)$ = 18 Hz, $J(^1H-^1H)$ = 5.5 Hz. Two 18 Hz and 5.5 Hz couplings are also measured in the second pair of hydride at 23.03 ppm.

The persistence of **20** in this experiment allowed for 1D EXSY experiments to be performed, which confirmed hydride exchange for complex **20** with dihydrogen at 4.6 ppm as expected based on the observation of PHIP signals for this complex. Comparing to **23**, where no exchange and no PHIP were observed, it can be concluded that the hydride exchange in **20** must be allowed through chloride dissociation.

A SABRE experiment, with PTF of 6.5 mT before detection at higher magnetic field with a π/2 pulse, does not give any visible polarisation for the phosphine **10**. In order for SABRE to be observed, **10** must reversibly bind to the complex. The absence of SABRE hyperpolarisation indicates that **10** does not dissociate from the complex **20** on a suitable timescale at room temperature.

In order to promote dissociation of **10** from **20**, the probe temperature was increased to 313 K, which is the boiling point of the solvent, dichloromethane-d_2. No exchange of ligand **10** was observed. This further supports the hypothesis that the dissociation of the chloride anion binding *trans* to hydrides is essential for dihydrides loss allowing PHIP enhanced hydride signals to be observed.

4.2.4 Promoting 10 exchange by warming the sample

In this section, the reaction of **10** and **I** is performed in a higher boiling point solvent, toluene-d_8, in order to use higher temperatures to promote the exchange of **10**. 5 mM of **I** was mixed with 1.1 µL mM (2 eq.) of **10** in 0.6 mL of toluene-d_8. H_2 addition and subsequent NMR interrogation reveals the formation of same products as described in section 4.2.1. After 1 hr 15 min, a ^1H NMR experiment showed signals for **20** and **21**.

Upon *p*-H_2 PHIP interrogation of this sample, strong antiphase hydride signals were seen at -12.93 and -17.06 ppm in the first NMR spectrum. These are due to neutral $Ir(H)_2(IMes)(COD)Cl$. Hence, the replacement of Cl^- by PPh_2H is suppressed in this non-polar solvent. The observation of this hydride species persists for over 24 hrs as Ir(IMes)(COD)Cl reacts very slowly. Whilst **20** and **21** form, in these experiments no polarisation of their hydrides signals is evident. This is consistent with the hypothesised need for Cl^- loss in $Ir(H)_2(IMes)(PPh_2H)_2Cl$ to create the necessary 16 electron intermediate.

We can conclude that the use of dichloromethane is necessary for H_2 exchange in **20** due to increased polarity when compared to toluene-d_8.

4.2.5 Improving hyperpolarisation of complex 20 by using co-ligands

4.2.5.1 DMSO co-ligand:

We speculated that replacing one of the PPh_2H ligands in **20** by another 2-electron donor might facilitate both PHIP and exchange of **10**. The soft 2-electron donor DMSO was used first to test this hypothesis. This involved taking a sample containing 5 mM of **I** catalyst and 5 mM (1 eq.) of DMSO in presence of H_2. 1hrs 30min after addition, ^{1}H NMR interrogation reveals the partial conversion of **I** (~30%) into IrCl(IMes)$(H)_2(DMSO)_2$; a pair of hydride resonances are seen at -15.85 and -21.22 ppm. 20 min after 5 mM (1 eq.) of **10** was added to this solution many hydride containing species were formed according to ^{1}H NMR spectroscopy. These include **20**, **21**, IrCl(IMes)$(H)_2(DMSO)_2$ and two isomers of IrCl(**10**)(IMes)$(H)_2$(DMSO) that differ according to whether **10** is *trans* or *cis* to the hydride (hydride signals at -10.63 and -21.64 ppm and -14.90 and -22.08 ppm respectively). The latter pair of hydride ligands couple to a ^{31}P centre that resonates at -28.98 ppm, whilst the former couple to a signal at -14.90 ppm. 2 hrs 45 min later, the ratio of **20** : **21** : IrCl(IMes)$(H)_2(DMSO)_2$: *trans*-IrCl(**10**)(IMes)$(H)_2$(DMSO) : *cis*-IrCl(**10**)(IMes)$(H)_2$(DMSO) proved to be 1.78 : 0.54 : 0.42 : 0.58 : 0.84 respectively.

Unfortunately, *p*-H_2 interrogation under both PHIP and SABRE type experiments resulted in no polarisation being observed. Given the large number of complexes formed, these DMSO studies were not taken further.

4.2.5.2 Pyridine co-ligand:

Pyridine is then more basic than DMSO and it was tested as a co-ligand in the reaction. A different approach was used with pyridine. This process started by first mixing 5 mM of **I** and 10 mM (2 eq.) of **10** with H_2 in 0.6 mL of dichloromethane-d_2. 1hr 20min after H_2 addition, **20** and **21** were present in the ratio 2 : 0.11. Subsequently, 0.25 µL (1 eq.) of pyridine was then added to this sample and a ^{1}H NMR spectrum recorded. Whilst signals for **20** and **21** still dominate, new complexes were observed including **25**, as a weak triplet of doublets at -22.40 ppm where *cis*-J(^{1}H-^{31}P) is 15 Hz, and a weak doublet of doublets at -8.95 ppm with a *trans*-J(^{1}H-^{31}P) of 140 Hz and **26** with hydride signal at -10.25 ppm. A ^{1}H-^{31}P HMQC NMR spectrum located two ^{31}P signals for **25** at -7.64 ppm and 22.66 ppm and one for **26** at -28.54 ppm.

p-H_2 was then used to monitor this reaction. Now strong hyperpolarised signals are seen for **20** and the new species **24** as a doublet of doublets at -23.47 ppm with *cis*-J(^{1}H-^{31}P) of 18.5 Hz and -24.16 ppm with *cis*-J(^{1}H-^{31}P) of 17.6 Hz. These signals are not visible in the thermally polarised NMR spectrum. A ^{31}P signal for **24** was located at 3.87 ppm with the corresponding PHIP-HMQC.

It was already stated that **20** undergoes H_2 loss after the loss of chloride. This would create $[Ir(H)_2(IMes)(PPh_2H)_2]^+$ which can add pyridine to form **25** rather than **24**. However, the signals for **25** are not polarised. The formation of **24** would be consistent with PPh_2H loss from **20** and trapping by pyridine as the free phosphine is not polarised and there is no exchange in the selective NOE spectrum between these two species. Therefore, another effect must account for the ready detection of **24**. Examination of an NOE spectrum reveals that **24** itself undergoes very rapid H_2 loss, in fact this process

is much faster than that for **20**. Thus, it would appear that the small amount of **24** present initially is sufficient to allow its detection.

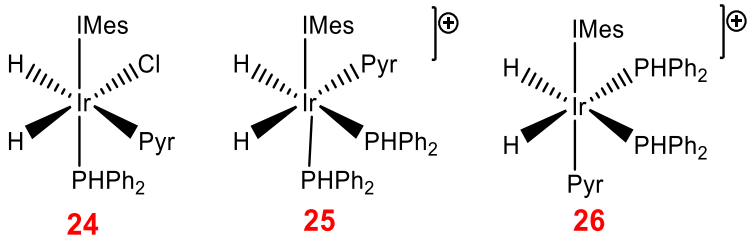

Scheme 4.3: Chemical structure of complexes **24**, **25** and **26**.

In conclusion, phosphine **10** itself could be not be hyperpolarised but its adducts, specially **20** provide strong hydride signal enhancements. In this complex, the hydrides symmetry is broken by large *trans* ^{31}P coupling. This observation is a premise for EF NMR detection of the hyperpolarised hydrides. Unfortunately when this reaction was tested using the EF NMR device, the hydride signal enhancement were not sufficient to be detected. However, 24 and 20 provided similar degree of hyperpolarisation, it was assumed that neither 24 would provide large enough signal to be detected at the EF NMR, so was not attempted. In the next sections, phosphine **11**, **12** and **13** with a P=O differing in their steric bulk are considered.

4.3 Reactivity of phosphorus containing P=O bond in phosphine 11, 12 and 13

In this section, three different sized phosphorus containing molecules **11** diphenyl phosphine oxide, **12** diterbutyl phosphine oxide, **13** diterbutyl phosphite are screened. In addition to the large P-H couplings, these molecule possesses polar P=O bonds that is expected to change their reactivity toward the metal catalyst.

4.3.1 Reactivity of diphenyl phosphine oxide 11

4.3.1.1 Testing o-methylation reaction between B and methanol using ^{31}P NMR spectroscopy

Phosphine **11**, in the form $OPPh_2H$ could interact with a metal centre via an oxygen lone pair or via oxidative addition of the P-H bond[231]. However its tautomer, $P(OH)(Ph)_2$ possess a phosphorus lone pair that could interact with the metal centre in the same way as **10**. Furthermore, as the P-OH proton is acidic the anion $POPh_2^-$ is also available[231], this ligand, could even replace chloride.

Prior to exploring the reactivity of **11** with the iridium catalyst, a sample of it was dissolved into methanol-d_4 to measure its P-H *J*-coupling. It was observed that **11** exchanges its P-H proton with deuterium and consequently the ^{31}P{^{1}H} NMR spectrum appears as a triplet at 20.60 ppm with

J(^{2}D-^{31}P) 76.1 Hz. In contrast, in the non-protic solvent dichloromethane-d_2, the ^{31}P{^{1}H} NMR spectrum of **11** shows doublet where J(^{1}H-^{31}P) is 482.5 Hz at 20.09 ppm. This first observation led us hypothesise that SABRE-Relay[216, 232] could be used to polarise the ^{31}P signal in **11**. As already stated, SABRE-Relay requires protons exchange between a polarisation carrier binding to the metal, an amine and a polarisation target that is here **11**. This is explored in section 4.3.1.2.

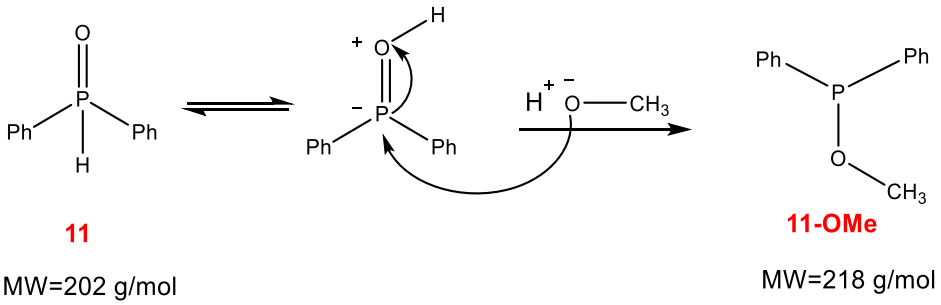

11 MW=202 g/mol

11-OMe MW=218 g/mol

Scheme 4.4: Chemical structure of the two tautomeric form of **11** and the O-methylation product.

In the effort of increasing a wider solvent range that could be used for the hyperpolarisation reaction of **11**, understanding the possible side-reactions of **11** was important.

In order to explore further possible reactions between **11** and methanol, a control reaction was therefore undertaken where **11** (1 mg) was exposed to methanol (0.8 µL) in dichlromethane-d_2. The resulting ^{1}H and ^{31}P NMR spectra immediately after the addition showed no evidence for a reaction between **11** and methanol. However, a second hypothesized signal at 30.98 ppm appears after 2 hrs, which is due to the methylation product **11**-OMe of Scheme 4.4. This was confirmed by the detection of a peak with m/z 219 in the corresponding mass spectrum of the volatiles when the reaction was completed with methanol-h_4. The corresponding ^{31}P NMR data are illustrated in Figure 4.5. Methanol is therefore not a suitable solvent for the hyperpolarisation reaction of **11**.

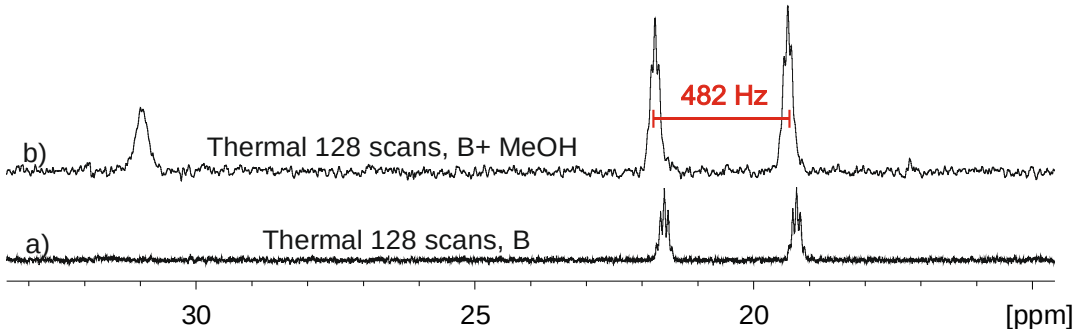

Figure 4.5: ^{31}P NMR spectra of a sample of 1 mg of **11** (a) and 0.8 µL of CH_3OH in dichloromethane-d_2 and a sample of only **11** in dichloromethane-d_2 (b). The slight shift of the offset between a and b is probably due to the presence of methanol.

4.3.1.2 Testing SABRE-Relay sensitisation of diphenyl phosphine oxide 11

In order to probe whether SABRE-Relay[191, 192] could hyperpolarise **11** via proton exchange with benzylamine a suitable sample was prepared. This involved first dissolving 5 mM of **I** pre-catalyst, and 20 mM (1.36 µL) (4 eq.) of benzylamine in dichloromethane-d_2, and then adding 3 bar of H_2 to form

$IrCl(BnNH_2)_3(H)_2(IMes)$. Then, 0.70 mg (1 eq.) of **11** was added to this solution under a nitrogen atmosphere. A ^1H NMR was recorded immediately after this. It revealed two doublets in the hydride region at -21.56 ppm with *cis*-J(^1H-^{31}P) of 18.11 Hz and at -22.62 ppm with *cis* J(^1H-^{31}P) of 19.5 Hz for the new complexes $Ir(H)_2(IMes)(NH_2Bn)_2(P(Ph)_2OH)$ **27** and $Ir^+(H)_2(IMes)(NH_2Bn)_2(P(Ph)_2O^-)$ **28** respectively which are present in similar amounts. (In Zwitterion **28**, the overall charge is zero)

Upon interrogation with *p*-H_2, strong enhanced antiphase signals appear at -23.24 and -24.96 ppm for a third complex with *cis*-J(^1H-^{31}P) couplings of 20.54 Hz and 18.65 Hz respectively. This complex is assigned as **29** [$IrCl(H)_2(IMes)(NH_2Bn)(P(Ph)_2O^-)$] and not visible in the thermally polarised NMR spectrum (Figure 4.6). A COSY-PHIP experiment shows a correlation between these two signals, confirming that they belong to the same complex. However, no correlation was observed between the resonances assigned to **27** and **28**, suggesting they belong to different complexes. Furthermore, no hydride ligand hyperpolarisation was seen for these two species. The hyperpolarised hydride ligand signals of **29** are also broad, suggesting fast ligand exchange at 298 K. The structures for **27**, **28** and **29** are shown in Scheme 4.5.

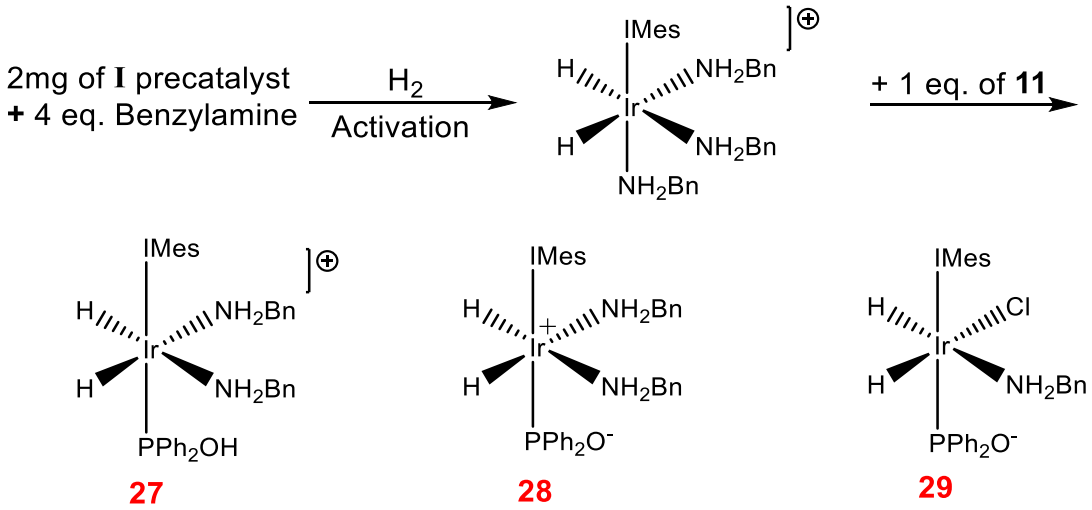

Scheme 4.5: The chemical structures of **27**, **28** (Zwitterion) and **29**.

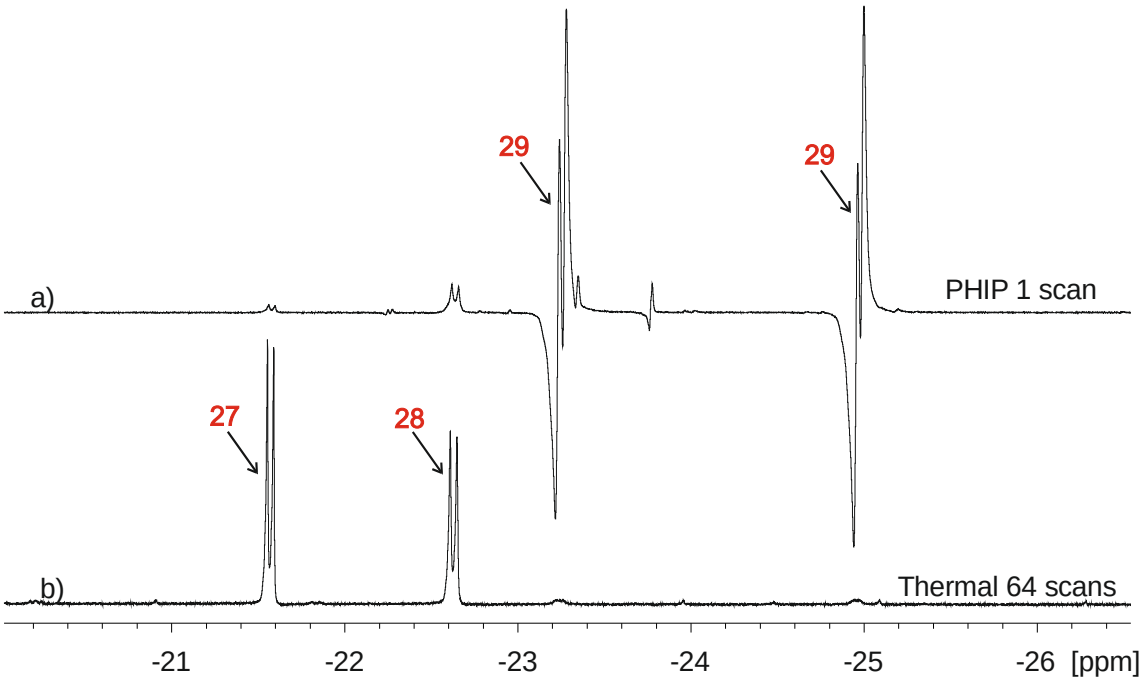

Figure 4.6: ^{1}H NMR spectra recorded for a sample consisting of 5 mM of **I** pre-catalyst, 20 mM (4 eq.) benzylamine in 0.6 mL of dichloromethane-d_2, 5 mM (1 eq.) of **11** and 3 bar of *p*-H_2. a) The PHIP NMR experiment show a strong hydride signal enhancement for **29**, which is barely visible in the thermally polarised NMR spectrum after 64 scans (b) where **27** and **28** are clearly visible.

^{1}H-^{31}P HMQC measurements (Figure 4.7) were used to locate ^{31}P signals at 26.75 ppm and 75.9 ppm for **27** and **28** respectively. In addition, for complex **29** a ^{31}P signal is located at 83.1 ppm. The large difference between these ^{31}P resonances suggests a different type of phosphorus environment but both couple similarly to the hydrides implying a direct Ir-P interaction. No P-H coupling is evident in the corresponding fully coupled spectra. It is therefore likely that **11** is binding as Ir-P(OH)(Ph)$_2$ or Ir-P(O$^-$)(Ph)$_2$. This view is consistent with the descriptions provided in the review published in 2016 by P. Sutra and A. Igau[165]. They described how the tautomerization of such a phosphine oxide to trivalent phosphinous acids in the presence of a metal catalyst and a base, is leading possibly to both Ir-P(OH)(Ph)$_2$ and Ir-P(O$^-$)(Ph)$_2$ forms existing (Scheme 4.6). They also reported the ^{31}P NMR signal position for a $Ph_2P(O^-)$ bound Ru(III) complex at 67 ppm downfield from that of Ph_2POH signal. These results are therefore in agreement with the data presented in this section.

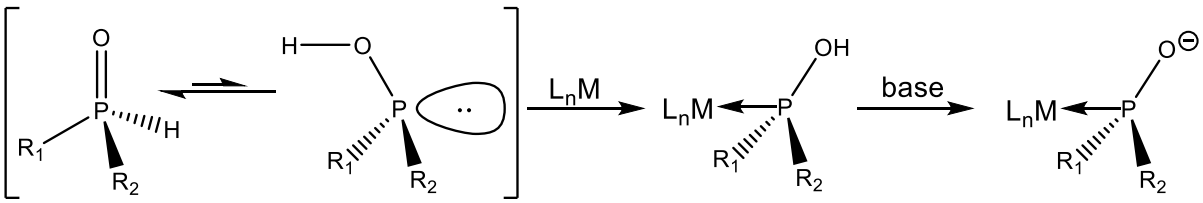

Scheme 4.6: depiction of tautomerization of secondary phosphine to phosphinous acid. This later coordinates to a transition metal catalyst M and can be deprotonated by a base to yield an anionic phosphine complex.

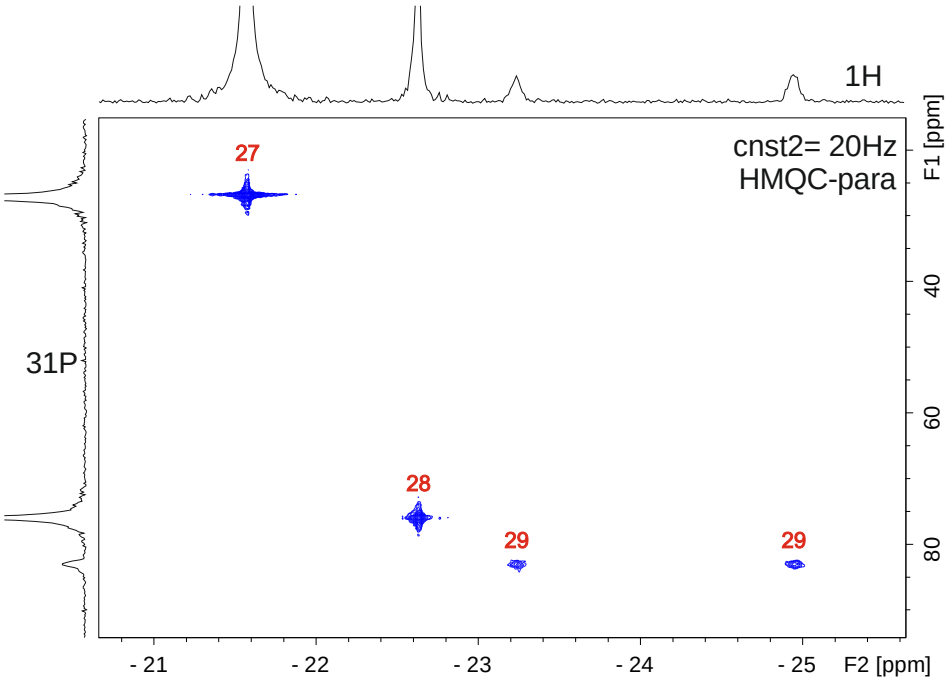

Figure 4.7: ^{1}H-^{31}P HMQC-PHIP spectrum of a sample containing 5 mM of **I** pre-catalyst, 20 mM (4 eq.) Benzylamine in 0.6 mL of dichloromethane-d_2 was first activated with 3 bar of p-H_2. After complete hydrogenation of COD and total formation of $IrCl(BnNH_2)_3(H)_2(IMes)$, 5 mM (1 eq.) of **11** was added to the sample. The ^{31}P resonance of the three complexes **27**, **28** and **29** is observed using a ^{1}H-^{31}P HMQC-PHIP experiment.

No SABRE-Relay, hyperpolarisation of the free phosphine was observed in these experiments and hence the premise that $OPPh_2H$ can be hyperpolarised remains unproven. It is speculated that this molecule does not exchange its labile proton with benzylamine's labile proton in the timescale of the NMR experiment that would allow to observe SABRE-Relay.

The ratio of products **27** to **28** proved to be dependent on the solvent. When THF was used they formed in a similar initial ratio. However, adding H_2O which is soluble in THF changed the ratio to 1 : 6.7 and hence favours the solvated anionic form **28**. The Ir-$P(OH)(Ph)_2$ and Ir-$P(O^-)(Ph)_2$ forms in the bound phosphine are therefore in equilibrium in **27** and **28**.

4.3.1.3 Reaction of **I**, B and benzylamine in methanol

It was already shown that a methylation reaction occurs when **11** is in presence of methanol, in addition to the proton exchange between their labile protons. In dichloromethane, the premise of a SABRE-Relay reaction remained unproven and the complexes **27**, **28** and **29** were identified. In this section, the aims were to test if these three species form in methanol and to investigate the role of the metal catalyst in the reaction between **11** and benzylamine. It is speculated that a possible nucleophilic reaction between **11** and benzylamine catalysed by the iridium. If this is true, it might prevent the hyperpolarisation of **11**.

5 mM of pre-catalyst **I**, 1.0 µL (3 eq.) of benzylamine and 2.8 mg (4 eq.) of **11** were all mixed at the same time in 0.6 mL of methanol-d_4 and H_2 added. ^1H NMR analysis, recorded just 5 min after H_2 addition, yields a spectrum exhibiting a hydride signal at -9.76 ppm with *trans*-J(^1H-^{31}P) and *cis*-J(^1H-^{31}P) couplings of 133 and 19 Hz respectively. A second hydride signal is seen at -21.76 ppm with triplet *cis*-J(^1H-^{31}P) values of 16 Hz that share common *cis*-J(^1H-^1H) couplings of 5 Hz due to Ir(IMes)($PO^-(Ph_2)$)$_3$ **30**. After 2hrs 30min, a white precipitate was seen at the bottom of the NMR tube and product signals for **30** could be discerned.

In the $^{31}P\{^1H\}$ NMR spectrum before H_2 addition (Figure 4.8), a signal is seen at 71.64 ppm for Ir(COD)(IMes)($P(O^-)(Ph_2)$) alongside signals for free **11** ($O{=}PH(Ph_2)$ at 21.6 ppm (J(^1H-^{31}P) = 482 Hz) and $O{=}PD(Ph_2)$ at 23.62 ppm (J(^2D-^{31}P) = 76 Hz). After hydrogenation, signals for **30** become visible at 84.4 ppm as a triplet that exhibit a *cis* J(^{31}P-^{31}P) coupling of 25.4 Hz, and at 67.7 ppm as a doublet that exhibit with a reciprocal *cis* J(^{31}P-^{31}P) of 25.4 Hz. These chemical shifts suggest **11** binds as $P(O^-)(Ph)_2$ in **30**. When this reaction is performed with *p*-H_2, no hyperpolarised hydride signals for **30** neither hyperpolarisation of free **11** were observed. As seen with phosphine **10**, the phosphine ligands **11** in this complex are not labile. The speculation that the iridium could catalyse a nucleophilic reaction between **11** and benzylamine remained also unproven.

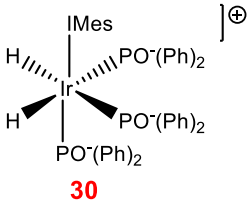

Scheme 4.7: Chemical structure for **30**

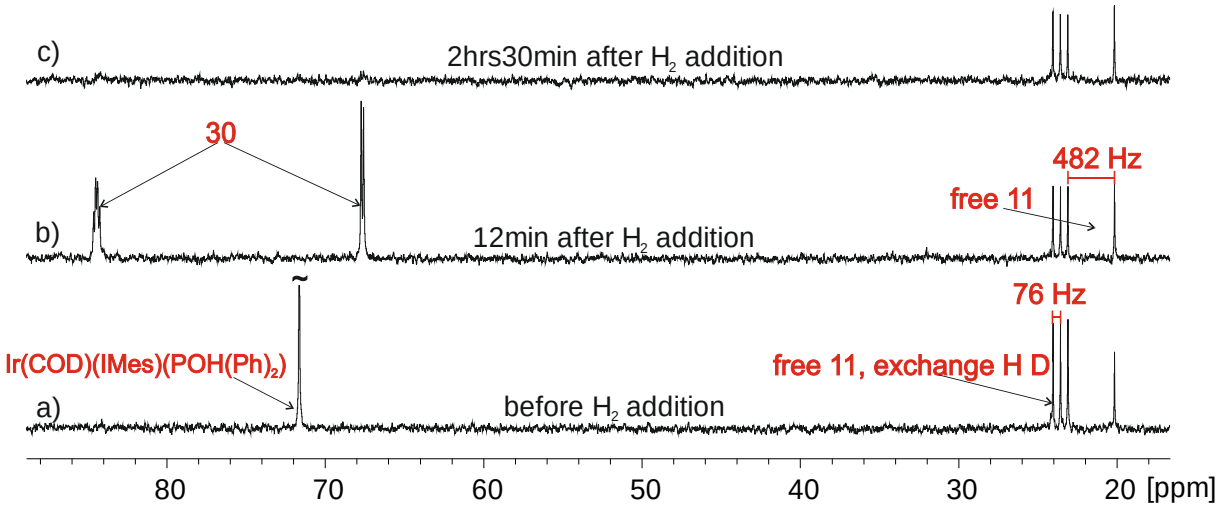

Figure 4.8: $^{31}P\{^1H\}$ NMR spectra of a sample of 5 mM of **I** pre-catalyst, 1.0 µL (3 eq.) of benzylamine and 2.8 mg (4 eq.) of **11** in 0.6 mL methanol-d_4. a) Before activation with H_2. b) 12 min after H_2 addition and 2hrs 30min after H_2 addition.

4.3.1.4 Testing the reaction between 11 and benzylamine without metal catalyst

As the hyperpolarisation reaction of **11** failed, considering all possibilities of reactions that might happen in solution was necessary. It was shown that in presence of the metal catalyst, no reaction occurred between **11** and benzylamine for a short time period. I now aimed to test the reaction between benzylamine and **11** in absence of the metal catalyst for a longer time period.

A sample of 16.5 mM (2 mg) of **11** and (2 eq.) 2 µL of benzylamine was mixed in 0.6 mL of dichloromethane-d_2. Immediately after this, a series of ^{31}P NMR spectra were recorded. They all revealed a signal for **11** at 20.5 ppm. This sample was then left at 298 K for a week. A ^{31}P NMR spectrum recorded at this point showed an additional signal at 19.26 ppm (Figure 4.9.a and b) due to the reaction product formed between **11** and benzylamine as depicted in Scheme 4.8. The product to starting material ratio proved to be 1 : 0.38 and did not change further with increase in reaction time. The formation of this reaction product is consistent with the work of Qian Chen et al. but is too slow to reflect a problem in the earlier studies[233].

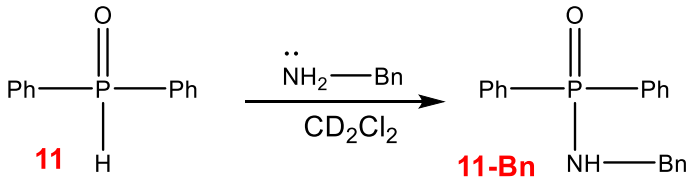

Scheme 4.8: Depiction of the formation of the phosphine acid in presence of water[233].

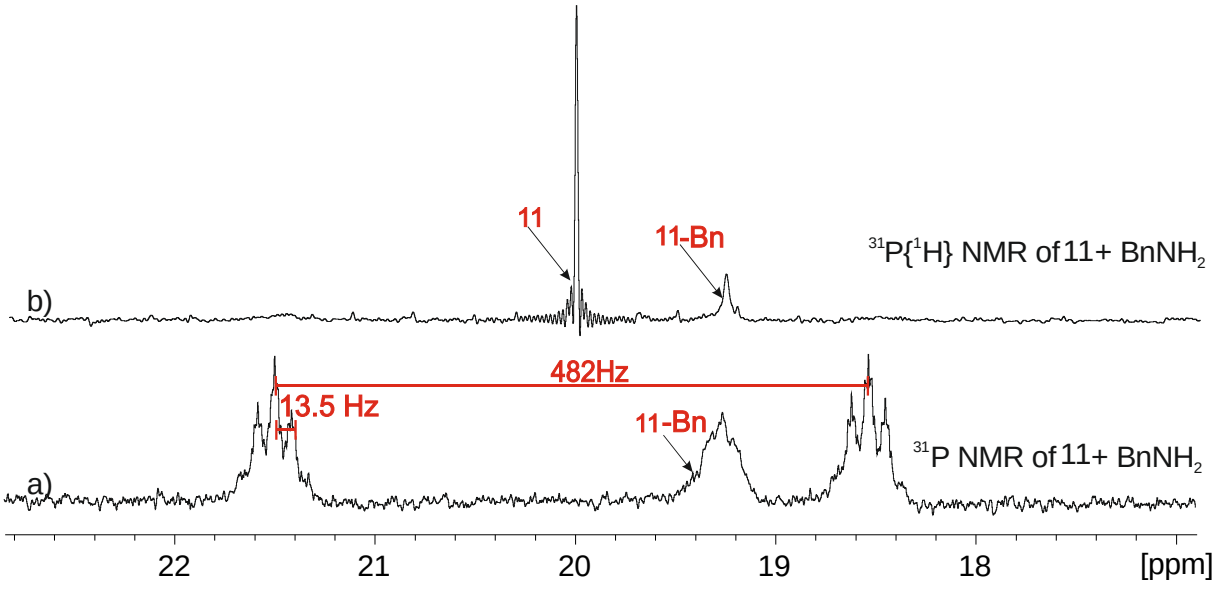

Figure 4.9: Sample of 2 mg of **11** and 2 µL of benzylamine was mixed in 0.6 mL of dichloromethane-d_2. ^{31}P NMR spectra (a, non-decoupled ^{1}H) and (b, decoupled to ^{1}H) recorded a week after show free b and an additional signal at 19.26 ppm.

For a general conclusion, **11** is very reactive. It was proven to react spontaneously with methanol and benzylamine. It may also react with any nucleophile present in solution in presence of a base. In presence of a deuterium donor, here methanol-d_4, an isotope exchange in the P-H bond occurs. The

attempt of SABRE-Relay reaction with **11** and benzylamine also failed. Instead, the two products **27** and **28** formed and were in equilibrium in solution due to Ir-P(OH)$(Ph)_2$ and Ir-P$(O^-)(Ph)_2$ forms of **11** being present. However, **29** is only observed in the hyperpolarised ^{1}H NMR spectrum due its small formation. Its detection with the Earth's field NMR instrument where no temperature control exist is therefore not possible.

4.3.2 Hyperpolarisation of diterbutyl phosphine 12

Compound **12** is analogous to **11** and possesses two *t*-Bu substituents instead of the two phenyl groups. The *t*-Bu are bulkier than the phenyl substituents and might offer a different coordination affinity to the metal. Indeed, the steric effect of the *t*-Bu groups are also used in organic chemistry to tailor reactions[234]. For example, in organic Diels-Alder reaction, the *t*-Bu groups are known for kinetic stabilisation and accelerating the rate of the reaction by a factor of 200[235]. In this section, the steric effect of the *t*-Bu groups is tested in the hyperpolarisation reaction of **12**.

In the case of **12**, an equilibrium between the PH(O)R_2 and P(OH)(R_2) is established directly in solution[231]. The former yields a ^{31}P signal at 65 ppm with a P-H splitting for 425 Hz. The latter appears at 66.6 ppm and exhibits no P-H splitting. Their ratio at equilibrium proved to be 0.87 : 1 in favour of the PH form. Hence, it is believed **12** should readily bind to iridium. Unfortunately, when such a reaction with **I** was attempted, no stable phosphine complexes resulted. It is concluded that the reactivity of the phosphine oxide of this ligand prevents its coordination and other factors such as steric bulk.

4.3.3 Reaction of diterbutyl phosphite 13 with IrCl(IMes)(COD), (**I**) and H_2

Compound **13** is a phosphine oxide with two O*t*Bu ether substituents that provide greater steric bulk than phenyl. A series of ^{1}H NMR spectra were recorded on two 5 mM samples of **I** containing 1.25 µL (2 eq.) and 3.16 µL (5 eq.) of **13** respectively in dichloromethane-d_2. After H_2 addition 17 dihydride containing species were detected with similar ratios (Figure 4.12.a) in both samples. In their ^{31}P NMR spectra, no evidence for the bound ligand **13** was seen. However, a strong signal at -3.75 ppm with a ^{1}J(^{31}P-^{1}H) coupling of 678 Hz for free **13** was evident.

PHIP experiments were performed on these samples, which lead to two hydride ligand signals showing enhancement being seen at -23.67 ppm, that exhibit a *cis*-J(^{31}P-^{1}H) splitting of 22.1 Hz, and at -25.44 ppm that exhibit a *cis*-J(^{31}P-^{1}H) splitting of 18.3 Hz. These were attributed to $IrCl(H)_2$(IMes)(POH(O*t*Bu)$_2$)(O=PH(*t*Bu)$_2$) **31**(Figure 4.12.b). Unfortunately, no ^{31}P signals could be located for this product. As these hydride signals were weak they would not be sufficient to be observed in the Earth's field NMR spectrometer. Nonetheless these data are included as they suggest this phosphine can stabilise the iridium centre through at Ir-OP interaction.

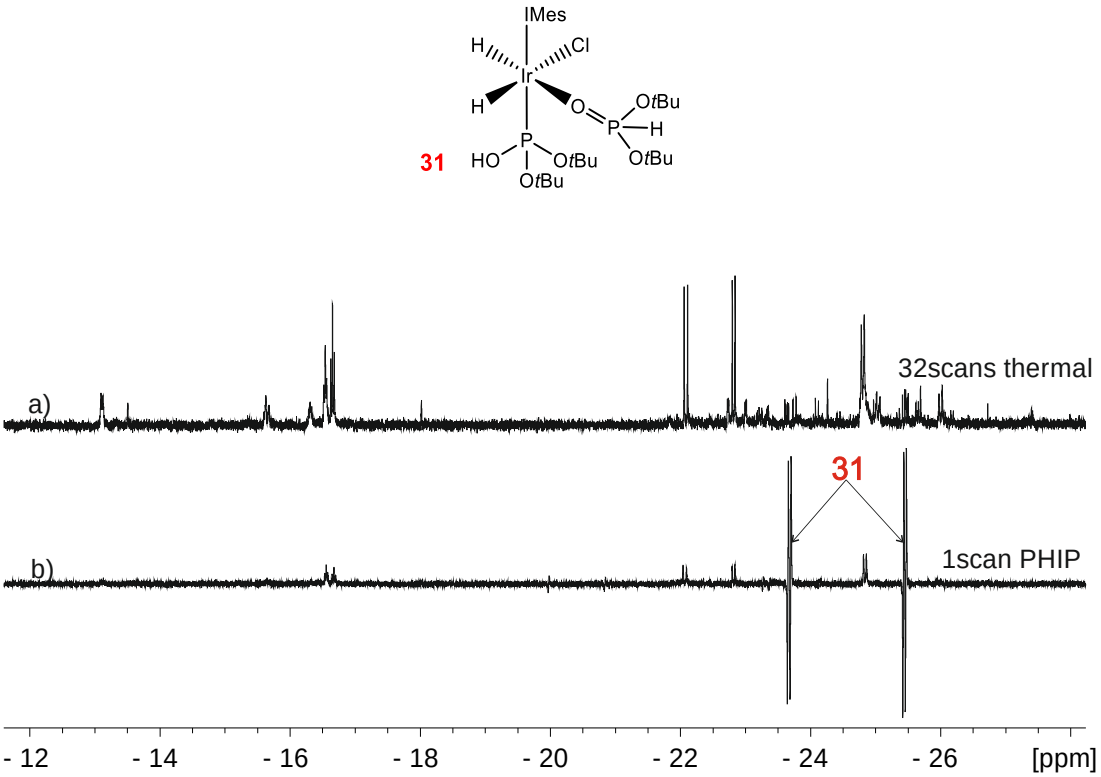

Figure 4.12: Sample of 5 mM of **I** and 10 mM (2 eq.) of **13** in 0.6 mL of dichloromethane-d_2 used to record a) ^{1}H NMR yielded a 17 dihydride containing species in the hydride region and b) ^{1}H NMR PHIP experiment that yielded a weak enhanced antiphase hydride signal for **31** which is quantified with the apparent poor SNR.

The oxygen atom present in the phosphine oxides **11**, **12** and **13** led to the observation of an unexpected reaction when their hyperpolarisation by the iridium catalyst **I** was studied. In all case, this resulted in the failure of either the ligands or their adducts to hyperpolarise. The following sections describe the results of studies on the simpler phosphines **14** and **15** that no longer contain oxygen.

4.4 Hyperpolarisation of 14 and 15 with benzylamine as co-ligand

4.4.1 diphenyl methyl phosphine 14

We have seen that the phosphine ligands bind too tightly to the metal catalyst to be hyperpolarised by SABRE. However, their adducts provided sometimes hyperpolarised hydride signals with symmetry broken. In the aim to find stable complexes with a large *trans* or *cis* hydride - phosphorus coupling that could provide high levels of hyperpolarisation with *p*-H_2, it was necessary to screen a large number of phosphorus compounds. **14** has been extensively used as ligand for metal complexes over the past decades[236]. Although **14** does not have a one-bond ^{31}P-^{1}H coupling, it can provide for chemical or magnetic differences and thereby phosphorus may hyperpolarise.

5 mM of **I** and 1.0 µL (3 eq.) of benzylamine were first mixed in dichloromethane-d_2 and activated with H_2. The formation of Ir(IMes)$(H)_2(BnNH_2)_3$Cl, is indicated with a single hydride resonance at -23.96

ppm. 5 mM (1 eq.) of **14** was then added and a ^{1}H NMR spectrum immediately recorded (Figure 4.13.a). Five products **32**, **33**, **34**, **35** and **36**, in the initial ratio 0.15 : 0.64 : 1.22 : 1 : 2.68 were identified.

These correspond to two isomers of $Ir(H)_2(BnNH_2)(IMes)(PMePh_2)_2$, **34** and **35**. In the former, there are two inequivalent hydride resonances. One appears at -10.12 ppm which lies *trans* to **15** and thereby exhibits a large $^{2}J(^{1}H\text{-}^{31}P)$ coupling of 136.5 Hz and the other at -23.29 ppm which is *cis* to two phosphines and *trans* to $BnNH_2$ (the *cis* $^{2}J(^{1}H\text{-}^{31}P)$ coupling is 16.5 Hz). The corresponding resonance in **35** appears at -11.30 ppm and is second order due to fact that the two hydride ligands are equivalent and *trans* to **14**; this can be readily understood by the appearance of the corresponding resonance, see Figure 4.13. In addition to these products, signals for $Ir(H)_2(BnNH_2)_2(IMes)(PMePh_2)$ **33** and $IrCl(H)_2(IMes)(PMePh_2)_2$ **36** are also present in these NMR spectra. The structure of **33** contains two equivalent hydride ligands, both *trans* to $BnNH_2$, while that of **36** exhibits one *trans* to chloride and one *trans* the $PMePh_2$. Consequently, they yield hydride ligand signals at -23.06 ppm, -8.93 ppm and -24.51 ppm respectively with appropriate $J(^{1}H\text{-}^{31}P)$ splittings. The remaining product, **32**, is $IrCl(H)_2(BnNH_2)(IMes)(PMePh_2)$. Its hydride ligand signals appear at -23.15 and -25.68 ppm due to their position *trans* to the hard donors $BnNH_2$ and Cl^- respectively.

After 24hrs at 273 K, ^{1}H NMR analysis shows evolution of the equilibrium between these species as the ratio became 3.18 : 1.94 : 4 : 0 : 2.1. Therefore, **32**, **33** and **34** are thermodynamically more stable, while **35** and **36** are kinetic products.

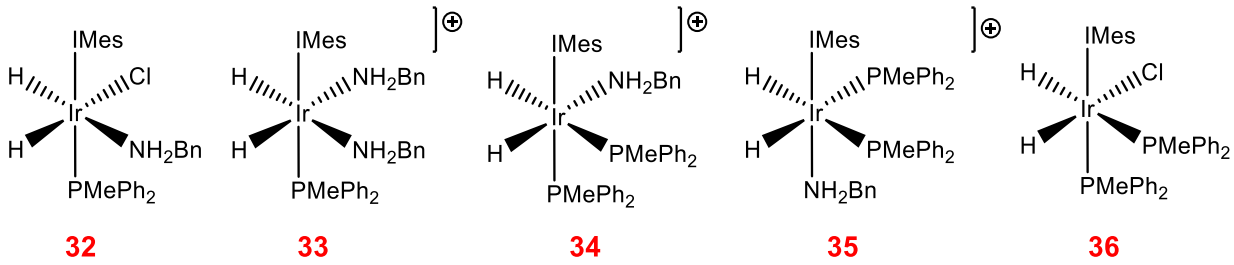

Scheme 4.9: Chemical structure of the five dihydride containing species **32**, **33**, **34**, **35** and **36**.

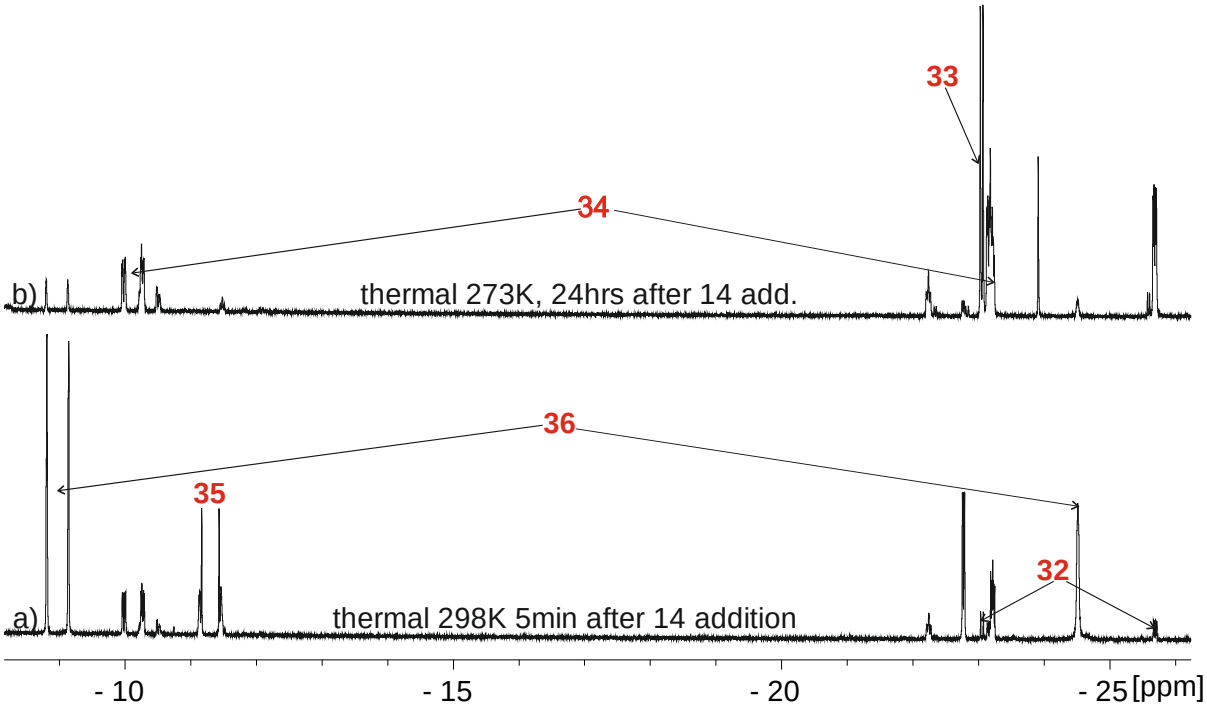

Figure 4.13: A sample of 5 mM of **I** and 1.0 µL (3 eq.) of benzylamine was mixed in dichloromethane-d_2 under H_2. After formation of $Ir(IMes)(H)_2(BnNH_2)_3Cl$, 0.70 mg (1 eq.) of **14** was added. a) 1H NMR spectrum just 5min after **14** addition showing the presence of 5 species **32**, **33**, **34**, **35** and **36**. b) 24hrs after **14** addition showing evolution of the equilibrium.

p-H_2 was then used to investigate these species. NMR Spectra connecting ^{1}H and ^{31}P at 298 K were recorded to locate the phosphorus resonances for the five dihydrides containing products. These show that **32** yields $^{31}P\{^{1}H\}$ NMR signals at -5.44 ppm, **33** at -6.96 ppm, **34** at -26.38 and -16.26 ppm, **35** at -22.48 ppm and finally **36** at -12.91 and -12.32 ppm

Prior to PHIP experiments, the probe temperature was cooled to 273 K in order to sharpen the hydride signals of **36**, which were rather broad in appearance at 298 K. This *tris*-phosphine complex is actually highly electron rich, and therefore it is not surprising it undergoes rapid H_2 loss, which accounts for the broadening. The first PHIP reactions performed showed a signal enhancement of 1.5-fold for free benzylamine at 1.57 ppm (NH_2), 3.82 ppm (CH_2) and 7.30 ppm (Ph), in addition to a strong antiphase hydride signal for **32** (Figure 4.14). The signal enhancement of benzylamine is low comparable to the signal enhancement previously obtained for benzylamine alone in chapter 3. Weaker, hydride ligand signal enhancements are seen in this NMR spectrum for **34** and **36**. When the experiment was repeated at 298 K, the hydride signals enhancement proved even weaker, thus suggesting optimal ligand exchange at 273 K.

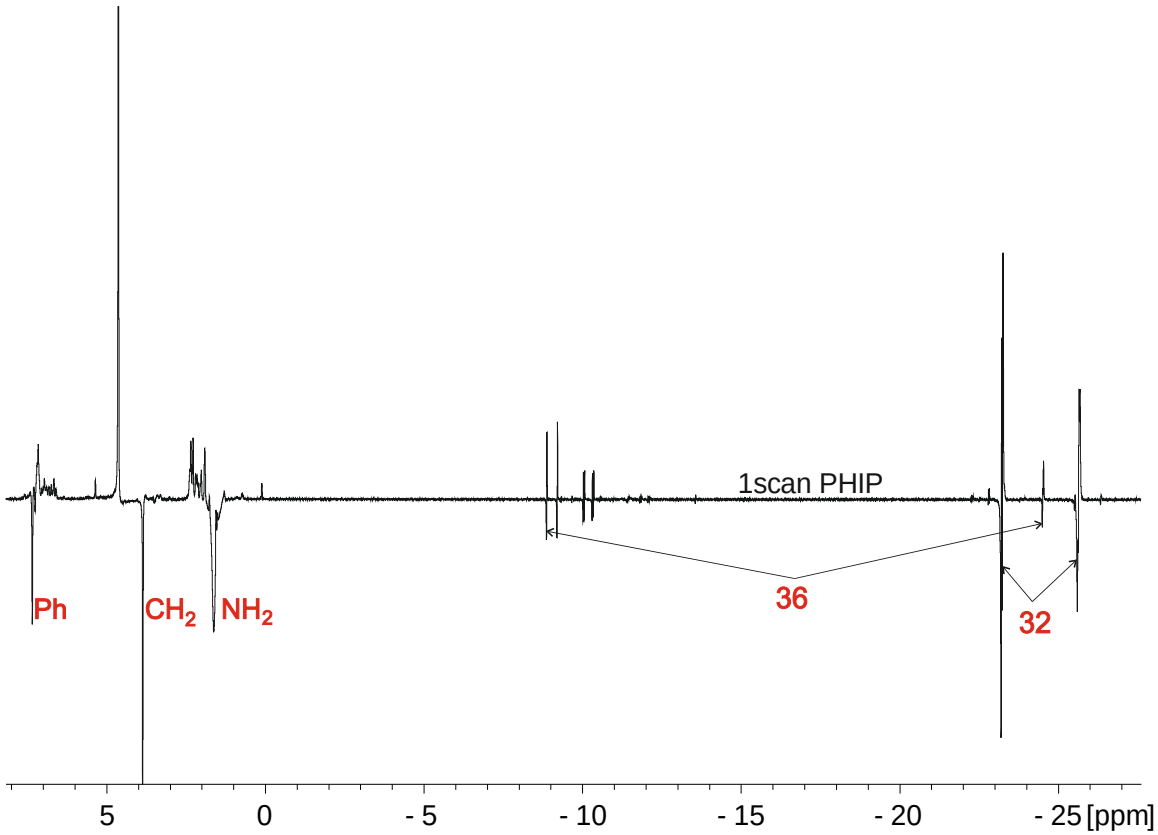

Figure 4.14: 5 mM of **I** and 1.0 µL (3 eq.) of benzylamine in dichloromethane-d_2 in presence of H_2. After activation, 0.70 mg (1 eq.) of **14** was added and ^{1}H NMR PHIP (1 scan) showing signal enhancement for free benzylamine and antiphase enhanced signal for hydrides of various complexes.

$^{31}P\{^1H\}$ SABRE was also carried out with this sample, which was unexpectedly successful. Figure 4.15.b shows an enhanced ^{31}P signal for **32** at -5.44 ppm. Surprisingly, the hydride ligand symmetry in **32** is broken by the *trans* Cl^- and NH_2Bn ligands, which leads to a flow of polarisation into the axial ligand via differential hydride couplings in PHIP effect. Weaker signals are also observed at -6.86, -12.87 and -23.0 ppm corresponding respectively to the ^{31}P resonances of **33**, **34** and **35**.

In conclusion, hyperpolarisation transfer to ^{31}P in **32**, **33**, **34** and **35** was an unexpected result. Although the ligand **14** is not involved in the exchange process on the NMR timescale, the axial flow of the magnetisation allows ^{31}P hyperpolarisation on the complex. Furthermore, all the phenyl resonances overlapped.

Due to the large number of complexes formed, their complete characterisation was challenging. Consequently, the related ligand **15** was used to inform on these assignments.

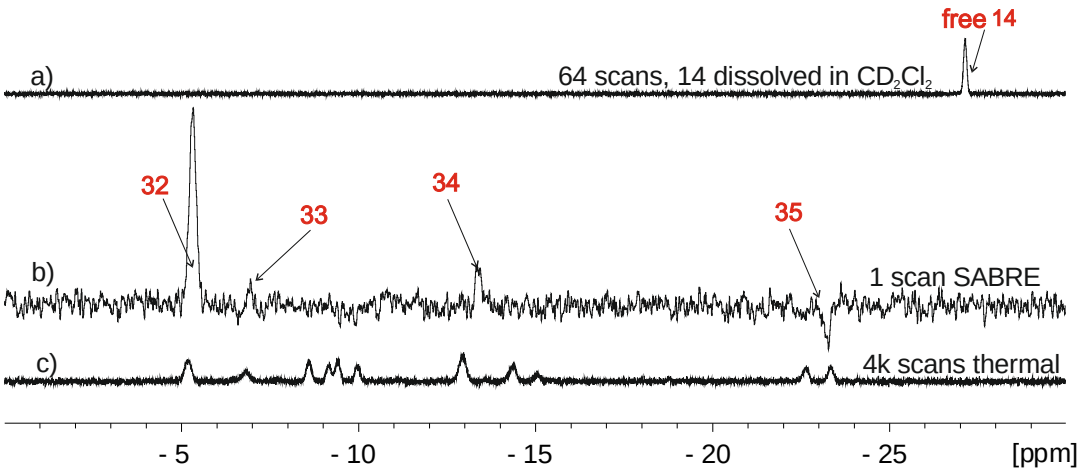

Figure 4.15: a) $^{31}P\{^{1}H\}$ NMR spectrum of a sample containing **14** dissolved in dichloromethane-d_2 acquired with 64 scans. b) 5 mM of **I** and 1.0 µL (3 eq.) of benzylamine in dichloromethane-d_2 in presence of H_2. After activation, 0.70 mg (1 eq.) of **14** was added and a one scan $^{31}P\{^{1}H\}$ SABRE NMR spectrum recorded 24hrs later c) $^{31}P\{^{1}H\}$ NMR spectrum of the same sample as b) averaged 4k time.

4.4.2 Dimethyl phenyl phosphine 15

$Ir(IMes)(H)_2(BnNH_2)_3Cl$ was again obtained in dichloromethane-d_2 before 2 eq. of **15** was added. A ^{1}H NMR spectrum recorded immediately after this showed a complex signal at -11.73 ppm somewhat characteristic of an $[A_2X_2]$ spin system[106]. Subsequently these were attributed to signals for $Ir(H)_2(IMes)(NH_2Bn)(P(Me)_2Ph)_2$ **38** and $Ir(H)_2(IMes)(P(Me)_2Ph)_3$ **39** (Figure 4.16). The former has two phosphine ligands *trans* to hydride and a benzylamine ligand *cis* to them whilst the later has three phosphine ligands coordinated to the metal. A third species, $IrCl(H)_2(IMes)(P(Me)_2Ph)_2$ **37**, which yields hydrides signals at -10.31 and -23.45 ppm, with the former exhibiting a diagnostically large *trans* $J(^{1}H\text{-}^{31}P)$ of 140 Hz alongside a *cis* $J(^{1}H\text{-}^{31}P)$ of 22.7 Hz and the $J(^{1}H\text{-}^{1}H)$ of 6.5 Hz due to the interaction with the *cis* hydride. This forms as a very minor product.

48 hrs later, only the signals for **38** and **39** remain in the hydride region of the ^{1}H NMR spectrum, hence they are thermodynamically stable. Complete characterisation data of these two complexes are given in chapter 9, section 9.7.3. $^{31}P\{^{1}H\}$ HMQC NMR spectroscopy located a resonance in **38** at 37.66 ppm whereas for **39** signals were located -44.85 and -47.7 ppm. Short PHIP-HMQC experiments with *p*-H_2 were used to assign the ^{31}P signals which, yielded broad peaks where no coupling could be measured.

This sample was then examined with *p*-H_2, at 273 K. A weakly enhanced hydride resonance was observed for **37** despite its very low concentration but no ^{31}P signal gains were seen.

In conclusion, **15** reacts with **I** to form different products to those seen with **14**. This difference may be assigned to the size of **15** with a cone angle of Θ = 122°, much smaller than **14** with a cone angle of Θ = 136°. The cone angle Θ is a Tolman parameter, which measures the bulkiness of the phosphine ligand and defines its ability to compete for coordination to a metal centre. The products derived from **14** and **15** show much reduced PHIP activity and were not examined further.

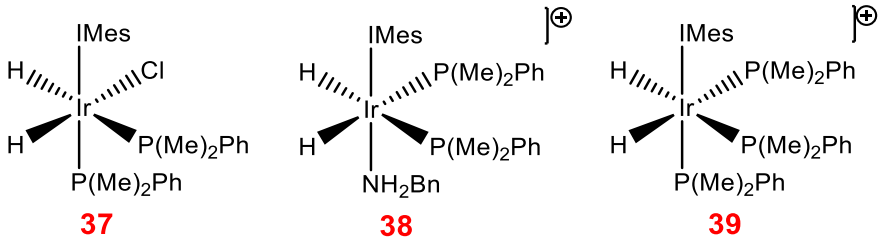

Scheme 4.10: chemical structure of complexes **37**, **38** and **39**

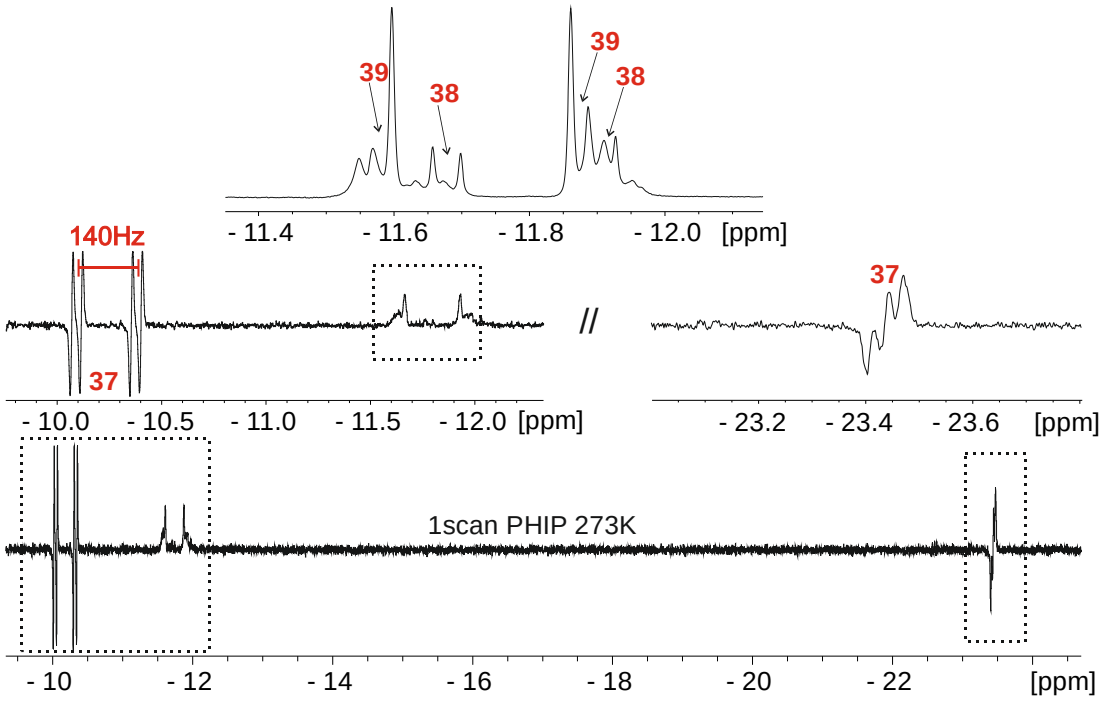

Figure 4.16: 5 mM of **I** and 15 mM (3 eq.) of benzylamine in dichloromethane-d_2 were mixed under H_2. After complete conversion to Ir(IMes)$(H)_2(BnNH_2)_3Cl$, 0.89 µL (2 eq.) **15** was added. ^{1}H NMR shows three signals in the hydride region for **37**, **38** and **39**. PHIP experiment at 273 K exhibits weak antiphase signal enhancement for **37**.

4.5 Hyperpolarisation of diphenyl vinyl phosphine oxide using various Rh catalysts

We have seen how the phosphine oxide failed to lead to any stable complexes. This is a consequence of its poor ligation properties. In order to enhance ^{31}P and see results at low field, *p*-H_2 must add to form a product with two inequivalent protons. This can be achieved through an organic reaction with phosphine **16** that contains vinyl and phosphine oxide functionalities.

The purpose was then to hydrogenate the alkene with *p*-H_2 and then to observe the PHIP enhanced signal of hydrogenated CH_2-CH_3 bond.

We first used **I** as the metal hydrogenation catalyst. No hydrogen product was observed when 5 mM (2 mg) of **I** was mixed with 3.6 mg 3 eq. of **16**. I then decided to test the hydrogenation reaction in presence of the three co-ligands benzylamine, pyridine and DMSO separately. The procedure was to create the 18-electron $Ir(H)_2(IMes)(L)_3$ (where L is benzylamine, pyridine and DMSO) with each co-ligand by mixing 5 mM of **I** and (3 eq.) of the co-ligand. Then after activation, 2.8 mg (3 eq.) of **16** was added and subsequently the mixture was reacted with *p*-H_2. The general observation was that the alkene slowly converted to alkane. However, this conversion is too slow that no PHIP enhanced signals for the CH_2 and CH_3 groups were observed. **I** is not suitable therefore for the PHIP reaction of **16**.

Next, the rhodium complex $[Rh(COD)(PPh_3)_2]BF_4$ (**II**) was used but it again proved unsuccessful in dichloromethane. This reaction was then repeated with the co-ligand acetonitrile. For this work, 1 mg of (**II**), 0.32 µL (2 eq.) of acetonitrile and 7.14 mg (10 eq.) of **16** were mixed together in dichloromethane and H_2 added. The two known complexes[237], **40** $[Rh(H)_2(CH_3CN)(PPh_3)_3]^+$ and **41** $[Rh(H)_2(CH_3CN)_2(PPh_3)_2]^+$ form in an initial 2 : 1 ratio (Figure 4.17.a). **40** yields a hydride ligand that resonates at -10.06 ppm and is split by a *trans* $^2J(^{31}P\text{-}^1H)$ coupling of 147.5 Hz, a *cis* $^2J(^{31}P\text{-}^1H)$ coupling of 23 Hz and a *cis* $^2J(^1H\text{-}^1H)$ coupling of 9 Hz. The second hydride signal at -16.69 ppm is *cis* coupled to ^{31}P through $^2J(^{31}P\text{-}^1H)$ splitting of 26 Hz and 13.9 Hz. **41** hydride's is a doublet of triplet located at -16.99 ppm and split by a *cis* $^2J(^{31}P\text{-}^1H)$ coupling of 16.8 Hz and a *cis* $^2J(^{31}P\text{-}^1H)$ coupling of 13.04 Hz. These species equilibrate over time, such that after 24hrs **40** is completely converted to **41**. The former is therefore a kinetic product whilst the latter is thermodynamically stable (Figure 4.17.a).

In the ^{31}P NMR spectra before H_2 addition, free **16** is located at 22.6 ppm alongside with signal for **II** at 26.45 with a $J(^{31}P\text{-}^{31}P)$ of 145.6 Hz. After hydrogenation, signals for **40** are seen at 25.68 and 39.69 ppm whereas **41** signal is at 45.15 ppm secured by a HMQC-PHIP.

The corresponding PHIP experiments showed weakly enhanced hydrides signal for **40** and weak signals of the hydrogenation product **16'**, at 1.26 and 2.67 ppm (Figure 4.17.b, left top spectrum). The strongly enhanced signal at 1.52 ppm is due to COA. Signals for the vinyl resonances of **16** at 6.73 and 6.31 ppm remain and so the hydrogenation process is slow (Figure 4.17.b, right bottom spectrum).

Although, antiphase PHIP signals for the new CH_2 and CH_3 groups are observed, they remain very weak compared to their thermal signals. No further investigations were carried out with **16**. For future improvement, the use of a different Rh catalyst might improve this situation.

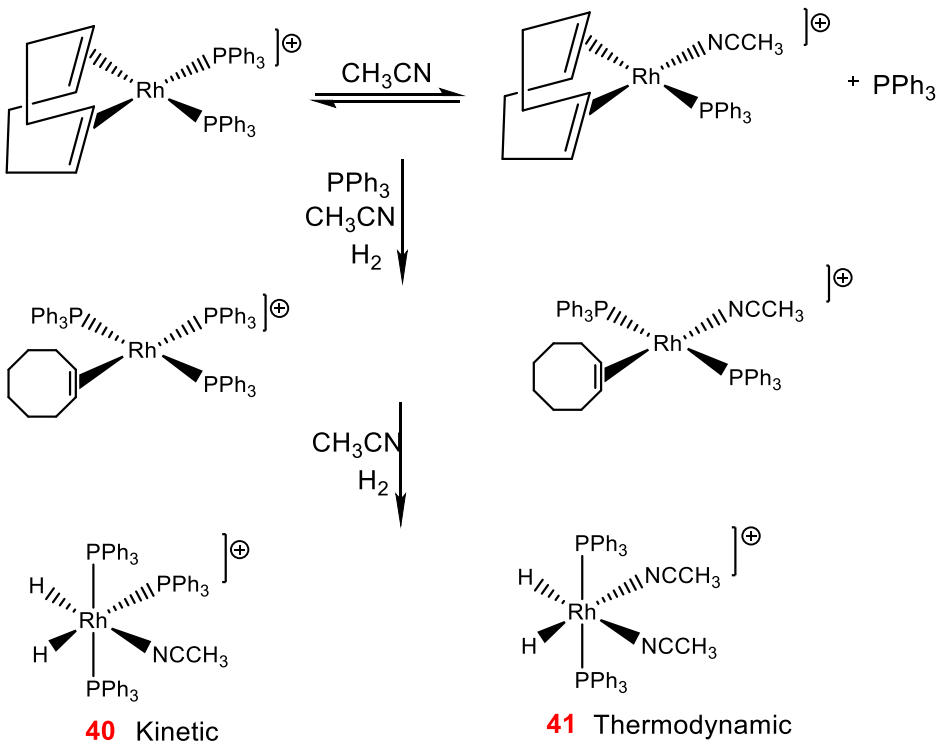

40 Kinetic **41** Thermodynamic

Scheme 4.11: a) 1 mg of (**II**) and 7.14 mg (10 eq.) of **16** 0.6 mL of in dichloromethane-d_2. The starting complex is 16 electrons, after hydrogenation of the COD and ligation of the hydride, the complex is still 16 electrons, which is unstable. b) 1 mg of (**II**), 0.32 µL (2 eq.) of acetonitrile and 7.14 mg (10 eq.) of **16** 0.6 mL of in dichloromethane-d_2 yield two species **40** and **41**.

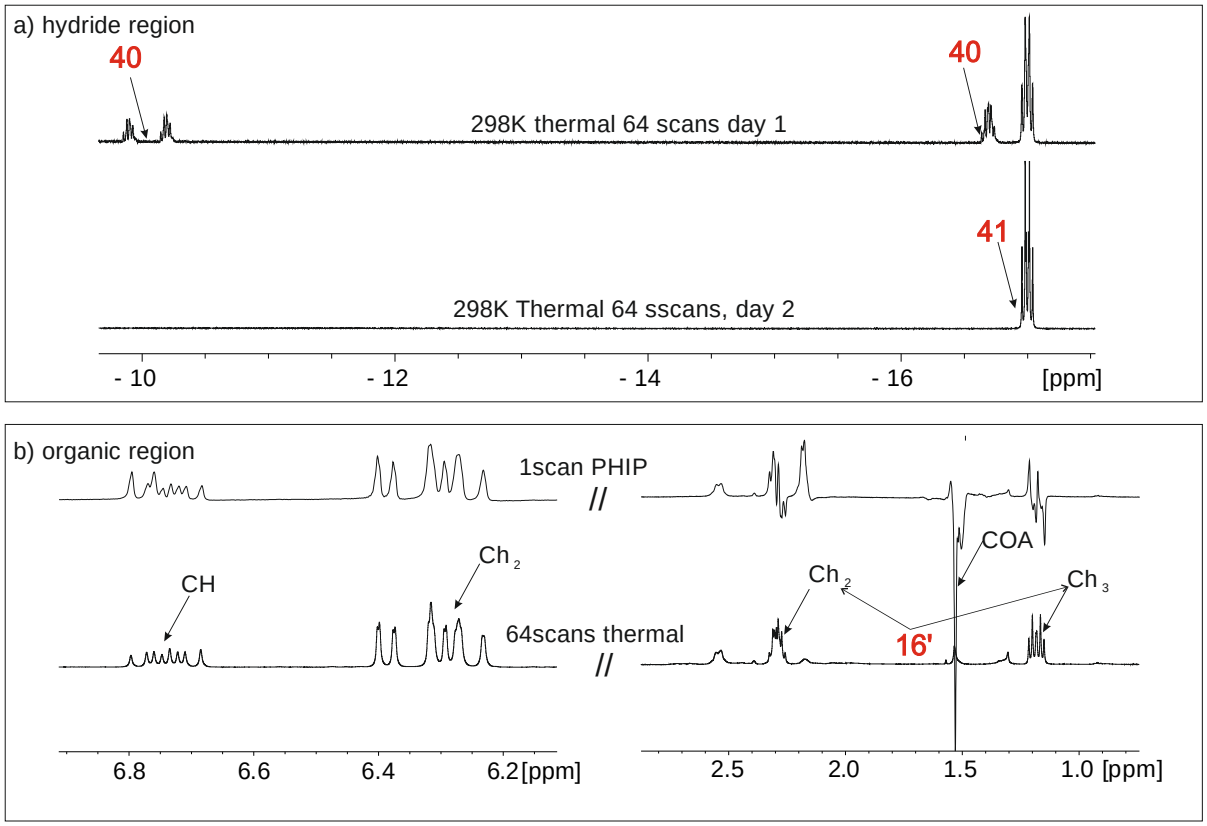

Figure 4.17: a) 1mg of (**II**), 0.32 µL (2 eq.) of acetonitrile and 7.14 mg (10 eq.) of G was mixed then *p*-H_2 added. Hydride region of ^{1}H NMR (top spectrum) at 298 K showing two complexes **40** and **41**. (bottom spectrum) After 24hrs at 298 K, **40** completely converts to **41**. b) organic region of 1 scan PHIP ^{1}H NMR (top spectrum) experiment recorded in day 1, shows weakly antiphase signals of the hydrogenation product, CH_2 and CH_3 of **16'**. The strong enhanced signal at 1.52 ppm is the COA. 64 scans ^{1}H NMR (bottom spectrum) highlights the vinyl resonances of **16** at 6.73 and 6.31 ppm for CH and CH_2.

4.6 Hyperpolarisation of triphenylphosphine sulfide (17) and trimethylphosphine sulfide (18) through SABRE

In this section, two different sized phosphines sulfide **17** and **18**[238] are tested for hyperpolarisation. These molecules are expected to interact with the iridium centre through the sulfur atom, which is a weak nucleophile.

4.6.1 Triphenylphosphine sulfide (17)

When 5 mM (2 mg) of **I** was reacted with 2.76 mg (3 eq.) of **17** under H_2, no hydride signal was observed in the ^{1}H NMR spectrum. Furthermore, the ^{31}P{^{1}H} NMR spectrum before and after hydrogen addition shows just a free signal for **17** at 43.08 ppm, suggesting no ligation occurs.

The co-ligands pyridine and DMSO were therefore tested. A 5 mM sample of **I** was prepared containing 3 eq. of pyridine and 2 eq. of **17** in dichloromethane-d_2. A further 5 mM sample of **I** with 2 eq. of DMSO and 3 eq. of **17** was prepared. H_2 was added to both these solutions which proved to form $IrCl(H)_2(IMes)(co\text{-}L)_2$ where the co-ligand is pyridine or DMSO. No ligation of **17** occurred in either case. Therefore, **17** has a very low affinity for the metal suggesting its steric bulk prevents coordination.

4.6.2 Trimethylphosphine sulfide (18)

The smaller phosphine sulfide **18** was also examined. This time, a 5 mM solution of **I** was reacted with 4 eq. of **18** under H_2. Now the hydride region of the resulting ^1H NMR spectrum indicated the formation of numerous hydrides containing species. However, the ^{31}P NMR spectrum showed just one signal, at 38.03 for iridium bound **18** alongside the free material in a ratio 0.19 : 1. A broad H_2 signal at 4.6 ppm was also seen so the sample was examined by NMR 256 K. The hydride region of this ^1H NMR spectrum (Figure 4.18.a) showed signals for two main products, **42** at -21.58 and -26.46 ppm, and **43** at -23.84 and -27.14 ppm, neither of which showed evidence of H-P coupling.

The correspond HMQC-PHIP measurements, however, did identify ^{31}P resonances for **42** at 40.03 and 41.20 ppm, suggesting it corresponds to $IrCl(H)_2(IMes)(\mathbf{18})_2$ with *trans* and *cis* arrangement of **18** which must bind through sulfur. No ^{31}P signal was located for **43** in this measurement, thus making it difficult to identify its chemical structure. **43** may be a water complex due to the far negative location of the hydrides on the ppm scale.

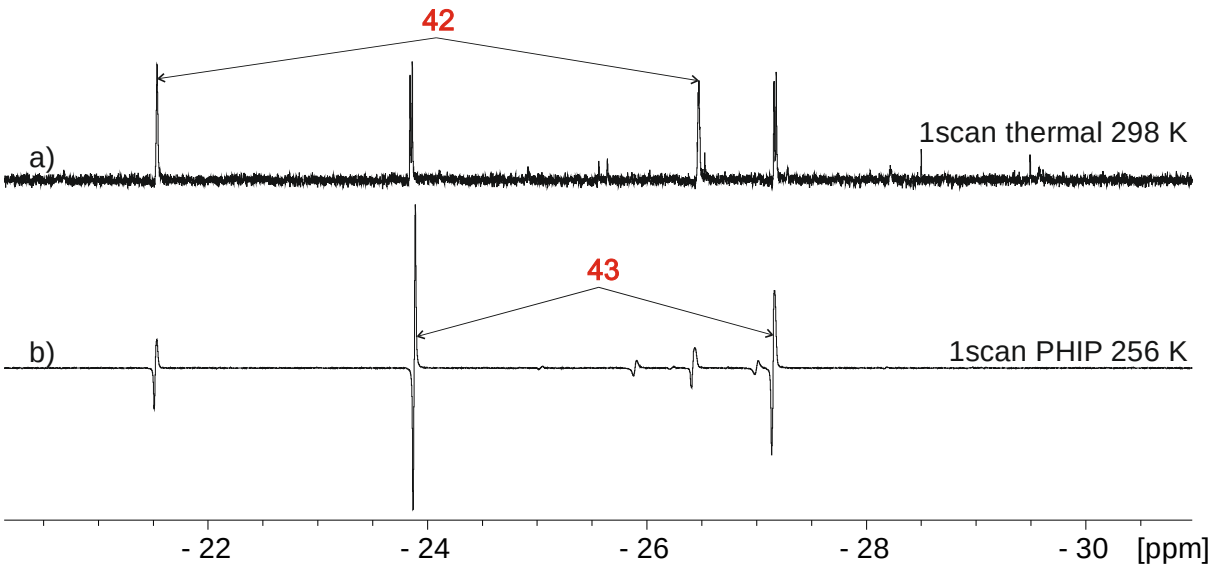

Figure 4.18: Hydrides region of NMR spectra recorded at 256 K from a sample of 5 mM solution of **I** with 4 eq. of **I** under H_2 showing signals of **42** at -21.58 and -26.46 ppm, and **43** at -23.84 and -27.14 ppm. a) 1 scan thermally polarised spectrum and b) 1 scan PHIP hyperpolarised spectrum.

When PHIP is performed, no hyperpolarised signals are observed at 298 K. At 256 K PHIP signal enhancement is seen for both of the hydride resonances in **42** and **43**. **43** proving to be more reactive to H_2 exchange than **42**. When the DMSO co-ligand was introduced no new species were detected.

Whilst these results are interesting, **18** is not suitable for use in my low field analysis due to the lack of signal at room temperature.

Studies with the phosphine sulphides revealed very weak binding making them unsuited to this work.

4.7 Conclusions

It was already seen that in order for SABRE to work, both substrate and hydride ligands must undergo exchange on a suitable time scale for polarisation transfer to take place. This time frame is 0.6 sec (1/2 $J_{H\text{-}X}$) if a coupling of 1.2 Hz is involved. It is known that phosphines like PPh_3 bind too efficiently, in other words, irreversibly in the NMR time scale at 298 K [229]. Hence, the phosphorus containing ligands (**10** – **18**) in Figure 4.1 were explored. Several of these molecules exhibit strong one bond ^{1}H-^{31}P couplings of hundreds of Hz, which places them in the range that is useful for detection with an atomic magnetometer (50 ~ 300 Hz). Furthermore, after being reacted with **I** in presence of H_2, the species formed display large *trans* hydride-^{31}P couplings of ~150 Hz and *cis* hydride -^{31}P coupling of ~20 Hz which lie in the range detectable in the ultra-low field. I have examined these systems, changing many parameters, such as temperature, solvent, concentration, and co-ligand to achieve maximum hydride signal intensity. Unfortunately, these systems fail to form suitable SABRE complexes that hyperpolarise the phosphine ligands.

One feature observed with these compounds is that the phosphine ligands do not reversibly bind to the metal centre in the NMR timescale at 298 K. The non-reversibility of the phosphine binding means SABRE cannot hyperpolarise the free ligand. However, in some of them exchange of the hydrides is observed through the prior dissociation of a chloride Cl^- atom or a co-ligand. These hyperpolarised hydride signals have the symmetry broken due to the ^{31}P couplings.

Of all the compounds tested, only phosphine **10** displayed strongly enhanced PHIP hydride ligand signals at room temperature in complex **20**. Unfortunately, its EF NMR detection was unsuccessful. Neat **10** was also the only compound in the liquid state, for which thermal Earth's field NMR spectra were recorded (see chapter 7, section 7.2). All the other materials were solids.

Phosphine **11** was tested with benzylamine as co-ligand in the aim of testing SABRE-Relay with the P-H bond. It yielded three complexes $Ir(H)_2(IMes)(NH_2Bn)_2(P(Ph)_2OH)$ **27**, $Ir(H)_2(IMes)(NH_2Bn)_2(P(Ph)_2O^-)$ **28** and $IrCl(H)_2(IMes)(NH_2Bn)(P(Ph)_2O^-)$ **29** where the latter was most interesting in terms of hyperpolarisation. It provided a strong enhanced hydride signals at 273 K. However, this reaction cannot be reproduced using the Earth's field NMR spectrometer due to the lack of temperature control. Interestingly, in the three species **27**, **28** and **29**, large differences in chemical shift resulting from the different ^{31}P environment $P(Ph)_2O^-$ and $P(Ph)_2OH$ is seen. In addition, the phosphine oxide **11** react spontaneously with methanol and benzylamine. It might also be reactive toward any nucleophile present in solution.

Phosphine oxides **12** and **13** have a P=O and O-P=O functionalities respectively, which makes them react with the Ir-complex in a way that was not suitable for hyperpolarisation. For **12**, the equilibrium between the $PH(O)R_2$ and $P(OH)(R_2)$ form identified by ^{31}P NMR occurs naturally. Evidence of a very weak interaction with the metal centre was seen when reacted with **I**, hence **12** is too bulky. In the case of **13** many species are formed with the only identified species being

$IrCl(H)_2(IMes)(POH(O\textit{t}Bu)_2)(O=PH(\textit{t}Bu)_2)$ **31** for which weakly enhanced hydride signals were seen. This result also illustrates the stabilisation of the iridium centre through an Ir-OP interaction.

For phosphine **14**, five distinct species **32**, **33**, **34**, **35** and **36** were obtained upon reaction with **I** and benzylamine. Hyperpolarisation on both hydride and benzylamine ligands was successfully achieved for **32** and **36** hydride signals only at 273 K, hence making their detection at the low field impossible with the current instrumentation. A strong ^{31}P SABRE response was also achieved at room temperature for **32**. Phosphine **15** was chosen for characterisation purposes, assuming it will have the same reactivity as phosphine **14**, which turned out to be not true. Indeed three complexes **37**, **38** and **39** different from the one seen with **14** are formed. The two latter did not show any PHIP activity while the former **37** which displays a large *trans* ^{31}P-^{1}H coupling of 140 Hz does polarise weakly at 273 K.

For **16**, although weak antiphase PHIP signals for the CH_2 and CH_3 in the hydrogenation product **16'** are observed, they remain very weak compared to their thermal signals. Screening other Rh complexes as catalysts for the hydrogenation reaction might yield better PHIP activity. At the same time, two products **40** $[Rh(H)_2(CH_3CN)(PPh_3)_3]^+$ and **41** $[Rh(H)_2(CH_3CN)_2(PPh_3)_2]^+$ are seen with the former being the kinetic product whilst the latter is the thermodynamic product.

With the two last sulfide phosphines, **17** and **18**, evidence of a very weak binding interaction with the metal catalyst is observed, independent of the bulkiness of the phosphine sulfide. They are therefore not suited for hyperpolarisation.

As a result of these experiments, it has been learned that it is possible to use the hydride-phosphorus couplings under SABRE to sensitize a bound phosphine. For this effect to be useful for ZULF detection, very substantial PHIP hydride signal gains are needed at 298 K. In the next chapter, a further series of complexes formed with DSMO and traditional trialkyl and aryl phosphines are explored. The goal is to create magnetically and chemically inequivalent hydride and phosphorus environments that are amenable to hyperpolarisation via PHIP. An understanding of the thermal reactions that take place between the metal precursor complexes and the chosen phosphine ligands and dihydrogen is needed prior to optimising the PHIP data. The next chapter will focus on those thermal reactions.

Chapter 5: Thermal reactivity of Iridium phosphine complexes

5.1 Introduction

One of the aims of this research is to create a compound that gives rise to inequivalent hydride signals in its ^{1}H NMR spectrum that are split by a ^{31}P coupling and can be hyperpolarised using *p*-H_2. It was hypothesised that this will make it possible to detect a hydride signal at low field in the absence of chemical shift resolution. In the previous chapter, the hyperpolarisation of a range of phosphine ligands (**10**-**18**, see chapter 4, section 4.1.3) bearing a large ^{1}H-^{31}P coupling was attempted using IrCl(IMes)(COD) (**I**) and Rh(COD)$(PPh_3)_2]BF_4$ (**II**). Unfortunately, none of these provided a large enough signal gain to be detected in the Earth's magnetic field. In this current chapter, another approach is tested whereby 18 electron Ir(III) dihydride complexes that have magnetically inequivalent hydrides due to ^{31}P couplings are hyperpolarised.

To explore this concept particular focus on the starting complex $IrCl(DMSO)_3$ (**III**) was paid. The synthetic procedure for **III** and an analogous rhodium complex was first published in 2003 by Milstein et al.[239], in a study aiming to develop cheaper transition metal catalysts that are less toxic and have reduced air sensitivity than many analogous phosphine systems. Indeed, sulfoxides have similar electron donating properties to phosphines. In 2013, Dr Sajid Khan presented in his PhD thesis[240], the reaction of $IrCl(DMSO)_3$ (**III**) with excess triphenyl phosphine (**45**) and H_2 and described how both *bis* and *tris*-substitution occurs to form $IrCl(H)_2(PPh_3)_2(DMSO)$ and $IrCl(H)_2(PPh_3)_3$. Importantly, when *p*-H_2 is added, both of these complexes exhibit PHIP enhanced hydride signals. He showed that the *bis*-phosphine complex was more reactive to *p*-H_2 addition than the *tris*-phosphine complex due to a stabilisation of the Ir(III) by the three donors ligands. In addition to the enhanced hydride ligands, the methyl protons of the free DMSO were also enhanced, indicating that the free DMSO exchanges with the bound DMSO in a SABRE type experiment.

The reactivity of $IrCl(DMSO)_y(P)_x$ (where P_x are shown in Figure 5.1) [y = 2, 1, 0 when x = 0, 1, 2] towards H_2 addition was therefore explored prior to tackling the hyperpolarised reactions. Prior to hydrogenation, reaction of $IrCl(DMSO)_3$ (**III**) with eight different phosphines was monitored. This complex undergoes *mono*, *bis* and *tris* substitution of DMSO by phosphine to form the corresponding 16 electron complexes $IrCl(DMSO)_2(P_x)$, $IrCl(DMSO)_1(P_x)_2$ and $IrCl(P_x)_3$ according to the excess of phosphine added. Some of these complexes have the ability to undergo C-H bond activation of the phosphine ligand and subsequently orthometallation reactions take place. This yields 18 electron complexes, which are in equilibrium with the 16 electron precursors. The comparable reactivity of these complexes was then monitored towards H_2, where they form various 18-electron dihydride species. The similarities and differences in behaviour are highlighted in the following sections. The selected phosphine ligands (Figure 5.1) are all different in size and electron donation ability, which is expected to change their reactivity upon reaction with **III** and H_2. The formation of a series of thermodynamic and kinetic products is explored using NMR measurements. The results are detailed below.

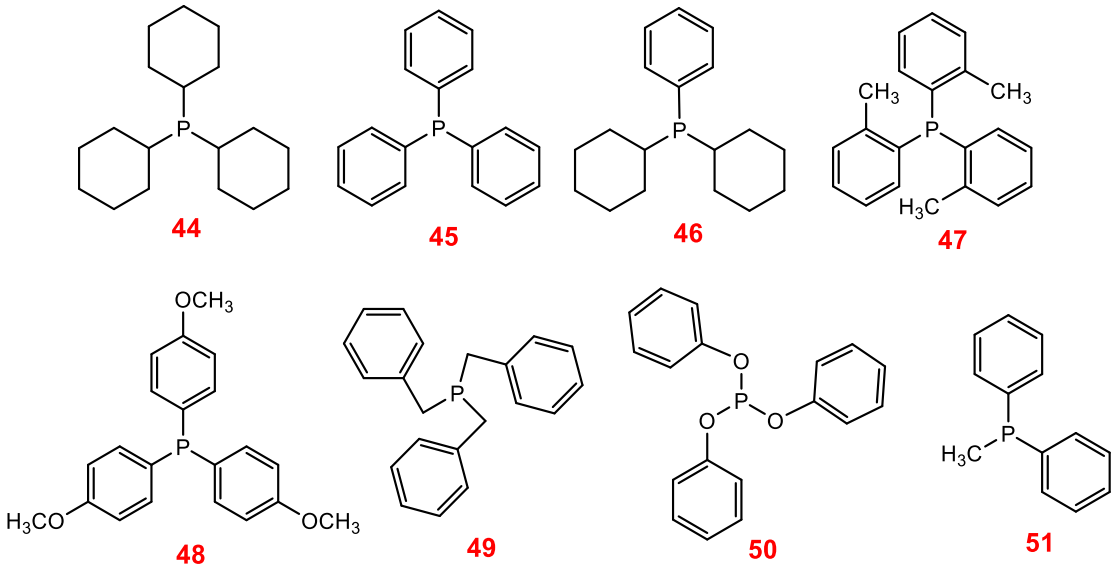

Figure 5.1: Phosphines reacted with **III**. **44** etricyclohexylphosphine; **45** triphenylphosphine; **46** dicyclohexyl phenyl prosphine; **47** Tri(*p*-tolyl)phosphine; **48** Tris(4-methoxyphenyl) phosphine; **49** Trisbenzyl phosphine; **50** Trisphenyl phosphite and; **51** methyl diphenyl phosphine[241, 242].

5.2 Reactions of $IrCl(DMSO)_3$ with H_2 in dichloromethane and methanol

A control reaction was undertaken where a sample of $IrCl(DMSO)_3$ (**III**) (4 mg) was dissolved in dichloromethane. The resulting NMR spectrum is shown in Figure 5.2.b, and instead of the three DMSO ligand signals anticipated, a signal for free DMSO was visible at 2.59 ppm in addition to a number of bound DMSO resonances visible between 3.3 and 3.9 ppm. The corresponding $^{13}C^{1}H$ 2D NMR spectrum was also complicated, containing several DMSO-methyl signals. Milstein et *al*. discusses this phenomena in their published synthesis of **III**[239], where they stated that this complex equilibrates with a *bis*-iridium dimer and free DMSO as shown in Figure 5.2.a. In methanol, they described how the chloride bridges can be replaced by hydroxide or methoxide. Hence, the reactions of this system to H_2 are likely to be complex.

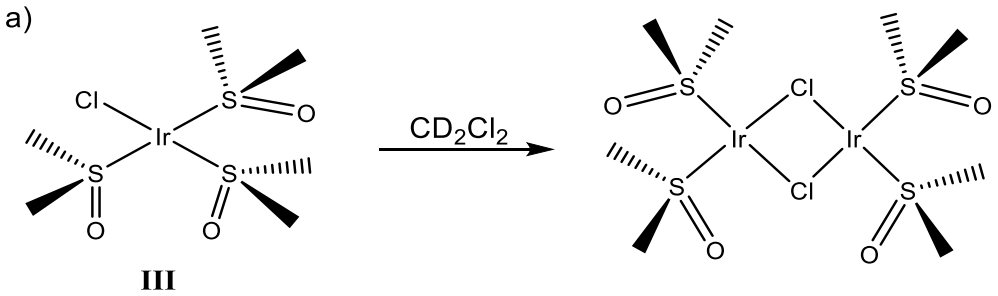

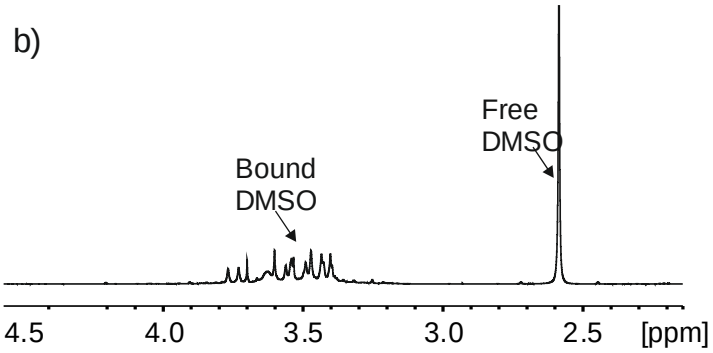

Figure 5.2: b) ^{1}H NMR spectrum at 298 K of a solution of IrCl(DMSO)$_3$ (**III**) (4 mg) in dichloromethane forming a bis-Ir dimer with two chloride bridges. This data are in agreement with Milstein et al[239].

3 bar of *p*-H_2 was then added to this mixture, the ^{1}H NMR spectrum in Figure 5.3 is recorded. This ^{1}H NMR spectrum shows signals in the hydride region for just two complexes: a peak at -16.01 ppm for *fac*-IrCl(H)$_2$(DMSO)$_3$, and peaks at -16.27 and -19.51 ppm for *mer*-IrCl(H)$_2$(DMSO)$_3$ (with a ^{1}H-^{1}H coupling of 5.8 Hz). The thermal spectrum also shows only the presence of these two species (not shown here). Immediately after H_2 addition, the apparent ratio of these ***fac-52*** and ***mer-52'*** isomers was 75 : 25 but after 24 hrs it inverts to become 30 : 80 showing the impact of kinetic selectivity and thermodynamic stability. The ***fac-52*** isomer is the kinetic product, while the ***mer-52'*** isomer is the thermodynamic product. If these species form via H_2 addition to **III**, hydrogen clearly must add preferentially over the DMSO-Ir-DMSO axis in a process with lower activation energy than addition over the DMSO-Ir-Cl axis, leading to the ***mer-52'*** isomer. Hence, the examination of the NMR data collected under the phosphine **45** and hydrogen are needed to test if these products impact on the reaction outcome. The reactivity of **III** is then tested in other organic solvents, such as methanol and toluene, in order to avoid creating bridged compounds upon dissolution.

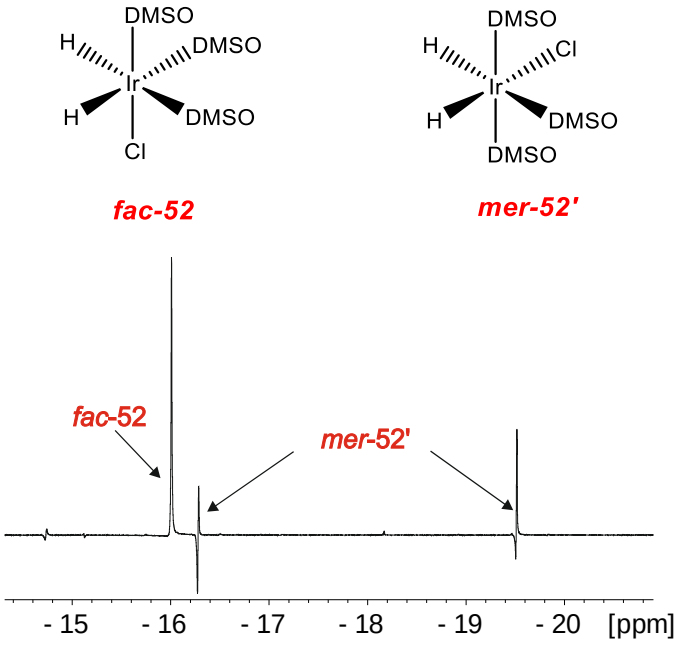

Figure 5.3: ^{1}H NMR spectrum at 298 K of a solution of IrCl(DMSO)$_3$ (**III**) (4 mg) in dichloromethane-d_4 in presence of *p*-H_2 where the two isomers IrCl(H)$_2$(DMSO)$_3$ are identified. The *cis* dihydride isomer, namely *fac*-IrCl(H)$_2$(DMSO)$_3$ at -16.01 ppm and two doublet peaks for the *trans* hydrides of *mer*-IrCl(H)$_2$(DMSO)$_3$. The spectrum recorded without *p*-H_2 also shows only the presence of these two species (not shown here).

5.2.1 Reaction of $IrCl(DMSO)_3$ with PPh_3 (45) in toluene

A 10.4 mM solution of of $IrCl(DMSO)_3$ (**III**) (3 mg) in toluene, synthetized using the procedure described in the literature[239], was mixed with 0.15 mL of a 74 mM solution of PPh_3 (**45**) at 298 K, also in toluene. The final solution contains 8.32 mM of $IrCl(DMSO)_3$ (**III**) and with 19.5 mM (1.78 eq.) of **45**. A ^1H NMR spectrum was recorded immediately at 298 K and the signals for **III** had effectively vanished. To be noted that for characterisation purpose, higher concentration of (**III**) and phosphine **45** were used.

It was expected to see signals for the phosphine containing 16 electron Ir(I) complexes: $IrCl(DMSO)_2(P_{45})$ (two isomers, *cis* (^{31}P singlet) and *trans* (^{31}P singlet)); $IrCl(DMSO)(P_{45})_2$ (two isomers, *cis* (two ^{31}P doublets) and *trans* (^{31}P singlet)) and $IrCl(P_{45})_3$ (^{31}P doublet and triplet). However, this NMR spectrum (Figure 5.4.a) proved to contain four hydride resonances that indicated aromatic C-H bond activation has taken place; these arise from two *mono*- and two *bis*-phosphine complexes, labelled **53**, **54**, **55** and **56**. Using standard 2D NMR characterisation methods, these 18 electron Ir(III) complexes were characterised. No signals for *fac*-$IrCl(H)_2(DMSO)$ or *mer*-$IrCl(H)_2(DMSO)_3$ were seen in these NMR spectra in accordance with the hydride group coming from the aryl ring of the phosphine.

Since no H_2 was added to this sample when the proton NMR spectra recorded, the presence of hydride ligand signals suggest the formation of several orthometallation products where the hydride ligand signal results from the C-H bond activation step. **54** and **55** are *mono*-phosphine containing isomers of the orthometallation product $[IrCl(H)[(C_6HPPh_2)](DMSO)_2]$. They differ according to whether their hydride ligand is *trans* to DMSO or chloride. As each hydride couples to a single ^{31}P centre, their hydride resonances appear as doublets at -13.80 ppm and -17.08 ppm, respectively. The second two products, **53** and **56** are *bis*-phosphine containing isomers of $[IrCl(H)[(C_6HPPh_2)](DMSO)(PPh_3)]$, where the hydride ligand signals now appear at -13.26 ppm and -18.02 ppm, respectively, due to their location *trans* to DMSO and chloride. The hydride resonances of **53** and **56** appear as doublets of doublets.

Initially, the ratio of **53** : **54** : **55** : **56** in solution was 1 : 0.22 : 0.17 : 0.63, suggesting that the *bis* phosphine products are the kinetic products (reaction time ca. 10 minutes). Over longer time periods, this ratio changes as these species equilibrate and a fifth product appears through the detection of a doublet of doublet resonance in the hydride region at -17.57 ppm (**57**). The ratio of these five species is 1 : 0.35 : 0.33 : 0.55 : 0.24 respectively after 120 hrs. **57** is also a *bis*-phosphine, like **53** and **56**, but now the two ^{31}P nuclei are *trans* to one another. Complete NMR data for these four products is given in chapter 9, section 9.6.10. Only partial data for product **57** is given due to resonances overlaps.

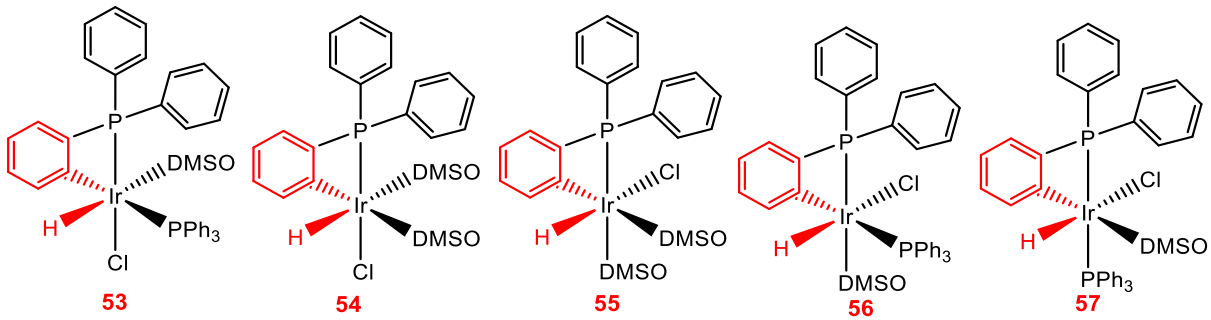

Scheme 5.1: Chemical structure of C-H bond activation products **53**, **54**, **55**, **56** and **57** formed from reaction of **III** with the phosphines **45** in toluene.

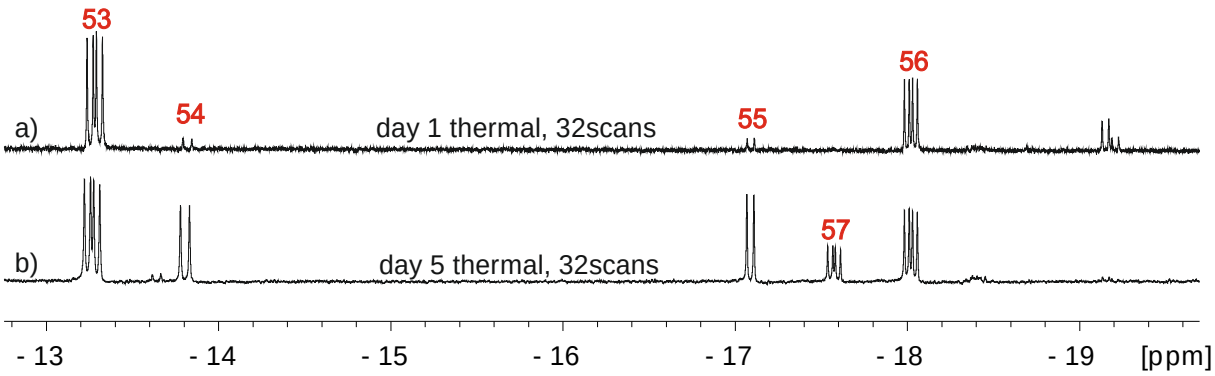

Figure 5.4: Schematic showing products formed when 10.4 mM $IrCl(DMSO)_3$ (**III**) and 74 mM PPh_3 (**45**) equilibrate at 298 K in toluene (upper). a) ^1H NMR spectrum recorded 3.5 hrs after the start of reaction (298 K), revealing hydride ligand signals for **53**, **54**, **55** and **56**. b) Corresponding spectrum recorded 124 hrs later; the slow formation of **57** is indicated.

In the $^{31}P\{^1H\}$ NMR, there are also signals for 16 electron Ir(I) complexes $IrCl(DMSO)_2(P_{45})$ at 23.16 and 20.15 ppm, which form on phosphine addition. These signals grow in intensity whist retaining identical relative ratios as the amount of added phosphine increases until eventually they reduce as *bis* substitution is favoured. At this point, coupled signals at 18.42 (doublet, J = 23.7 Hz) and 17.01 ppm (doublet, J = 23.7 Hz), and at 23.53 (doublet, J = 22.6 Hz) and 16.34 ppm (triplet, J = 23.1 Hz) appear due to $IrCl(DMSO)(P_{45})_2$ and $IrCl(P_{45})_3$ (Figure 5.5). The $^{31}P\{^1H\}$ NMR spectra of Figure 5.7 are representative of those collected during this reaction and illustrate this point.

These four complexes reflect 16 electron precursors to the C-H bond activation products that have been discussed. Consequently, they disappear slowly as the corresponding C-H bond activation products form; after 6 days of reaction at 298 K their signals have essentially vanished from the associated NMR spectra, with those for their Ir(III) orthometallation products now dominating. However, the degree of formation of these 16 electron species is comparable to those of the C-H bond activation products, hence suggesting equilibrium between them.

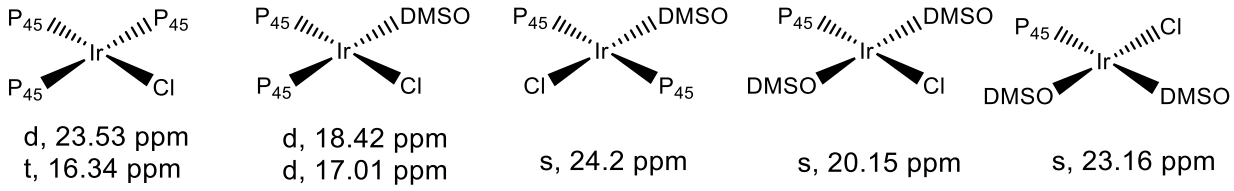

Figure 5.5: Proposed structures of the 16 electrons Ir(I) complexes formed after substitution of DMSO by PPh_3 and their respective $^{31}P\{^1H\}$ resonances. These species are in equilibrium with the 18 electron Ir(III) C-H bond activation complexes.

HSQC 2D correlation spectra connecting ^1H and $^{31}P\{^1H\}$ at 273 K were recorded to locate the phosphorus resonances for the hydride containing products (Figure 5.6.a and b). These show that **53** yields $^{31}P\{^1H\}$ NMR signals at -3.18 and -77.95 ppm with J = 88.6 Hz, **54** at -70.79 ppm, **55** at -73.58 ppm, **57** at 2.22 ppm and -65.60 ppm and finally **56** at -2.75 and -92.37 ppm. A common feature of these products is the observation of phosphorus resonances far into the negative ppm range, in agreement with the formation of a strained four membered ring by orthometallation[243].

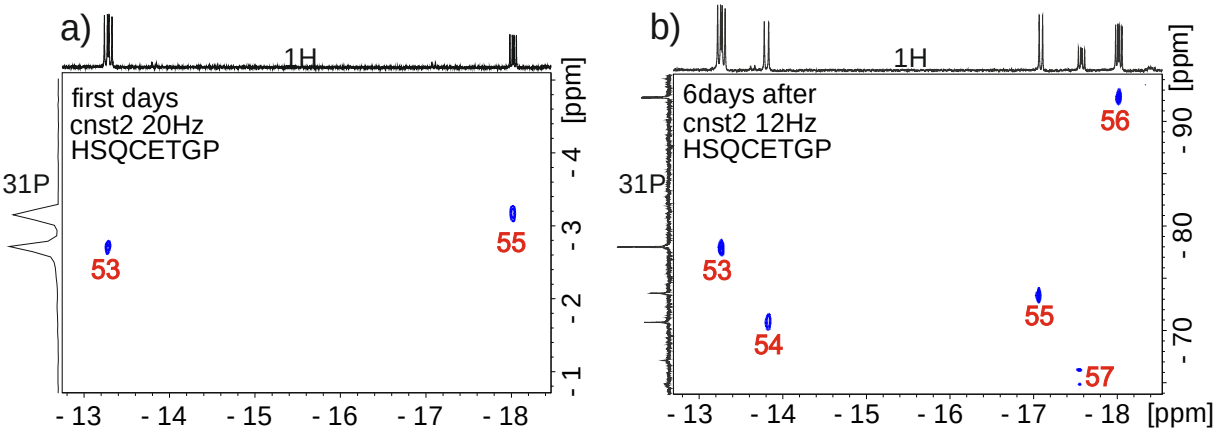

Figure 5.6: 2D ^{1}H-$^{31}P\{^{1}H\}$ NMR correlation spectra recorded on a solution of $IrCl(DMSO)_3$ (**III**) 10.4 mM (3 mg) and 0.15 mL of a 74 mM solution of PPh_3 (**45**) in toluene. a) At 273 K after 24 hrs of reaction with a focus on the ligand not involved in C-H activation. b) At 273 K six days later, showing the peaks for the phosphines involved in the C-H activation.

It is interesting to note the different signal intensities for the hydride ligands in the ^{1}H NMR and the phosphine ligand in the ^{31}P NMR signal intensities. The former only indicates the corresponding C-H activation products, whilst the latter allows us to see the whole speciation. When, a dilute solution (10.4 mM) of **III** and 1.78 equivalents (0.15 mL) of **45** was mixed together, signals in the ^{1}H NMR spectrum (Figure 5.7) are strong for **53** and **56** but the $^{31}P\{^{1}H\}$ NMR spectra (Figure 5.8) suggest instead that the two isomers of $IrCl(DMSO)_2(P_{45})$ dominate. As the amount of **45** is slowly increased, the intensity of the hydride signals for **53** and **56** grows along with those of $IrCl(DMSO)_2(P_{45})$. However, hydride signals for **54** and **55** also become evident (Figure 5.7). The ratio of **53** : **56** as evident through the hydride ligand signals remains constant at 1 : 0.6 throughout these measurements. The ratio of **54** : **55** is 1 : 0.95 and also constant, as is the ratio of the two isomers of $IrCl(DMSO)_2(P_{45})$ where two DMSO ligands *cis* : *trans* (1 : 0.6). These ratios are constant in the three stage of **45** addition where the NMR temperature was at 298 K and the reaction time 3 hrs 30 min. From the second aliquot addition, signals for two $IrCl(DMSO)(P_{45})_2$ can also be seen (Figure 5.8.c). Eventually, the formation of $IrCl(P_{45})_3$ is indicated but its C-H activation product is not evident. These data confirm that **53** and **56** form more readily than **54** and **55**.

After 6 days, the Ir(I) species have effectively been consumed. Furthermore, **57**, a further hydride containing product is produced. This is a third isomer of **53**/**56** and its hydride ligand signal, at -17.57 ppm, is a doublet of doublets where $J(^{31}P\text{-}^{1}H)$ = 12 and 18 Hz, correlates to $^{31}P\{^{1}H\}$ signals at 2.22 ppm and -65.60 ppm that both exhibit large $^{31}P\text{-}^{31}P$ *trans* couplings of 365 Hz. **57** forms slowly compared to the other species. Hence, there is a larger activation barrier to its formation when compared to **53**/**56**.

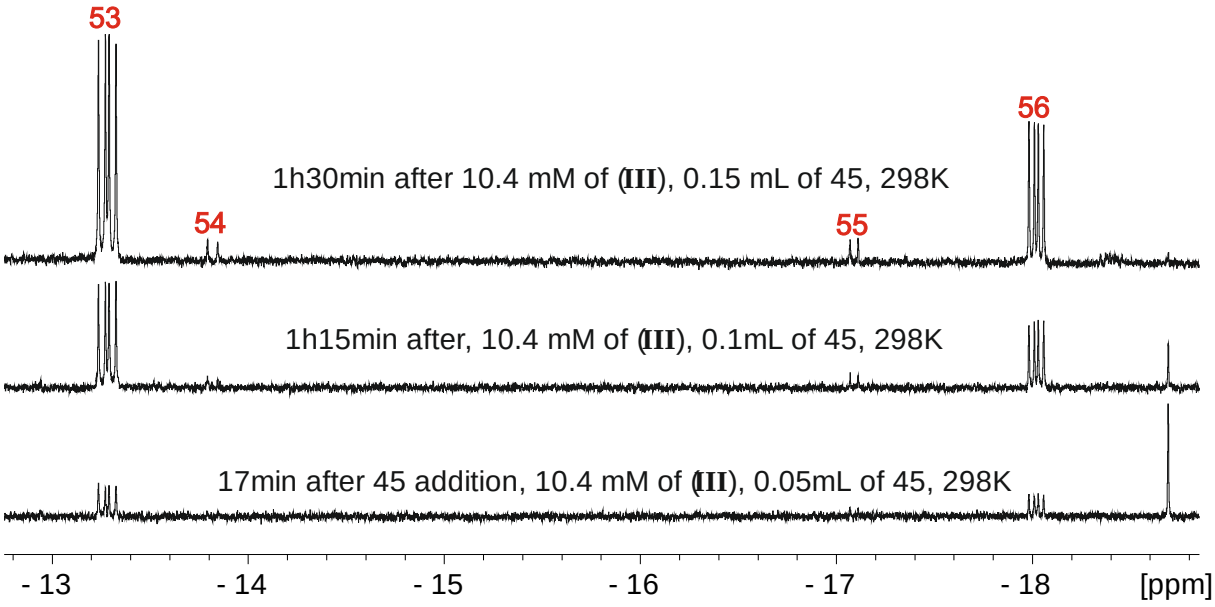

Figure 5.7: Solution of $IrCl(DMSO)_3$ (**III**) 10.4 mM (3 mg) and 0.15 mL of a 74 mM solution of PPh_3 (**45**) at 298 K in toluene. Three successive additions of 0.05 mL of a 74 mM solution of **45** where each time a ^1H NMR spectrum is immediately recorded corresponding to a, b and c. The singlet at -18.65 ppm is tentatively assigned as a C-H bond activation from (**III**), which very unstable and disappears as shown here.

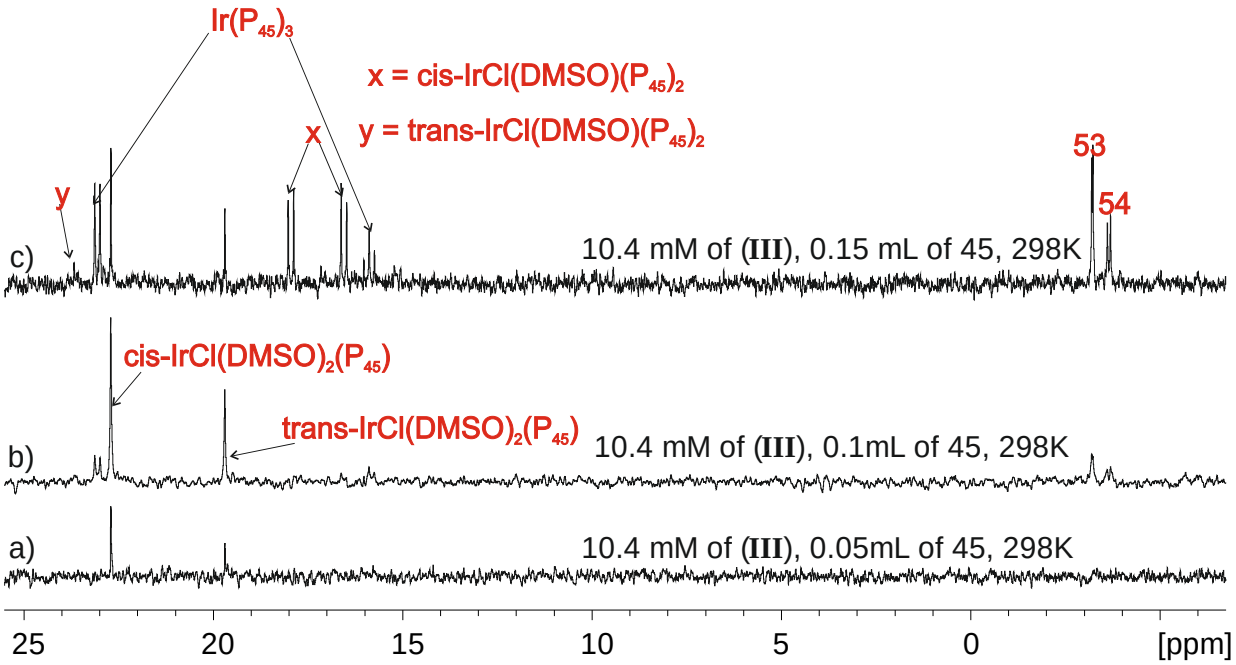

Figure 5.8: Solution of $IrCl(DMSO)_3$ (**III**) 10.4 mM (3 mg) and 0.15 mL of a 74 mM solution of PPh_3 (**45**) at 298 K in toluene. Three successive additions of 0.05 mL of a 74 mM solution of **45** where each time a $^{31}P\{^1H\}$ NMR spectrum is immediately recorded corresponding to a, b and c. These spectra are zoomed on the positive region to highlight the 16 electron species.

The aim was now to test the effect of H_2 addition with these 16 electron and 18 electron products formed after reaction between **III** with **45**. The ultimate goal of these experiments was to study hyperpolarisation reactions of the iridium phosphine complexes with *p*-H_2. These NMR results have

shown that reaction of **III** with **45** yields a series of C-H bond activation products that will act as starting materials for these reactions. The reaction of these starting materials with H_2 and their *p*-H_2 activity will be explored in the forthcoming sections.

5.2.2 Reaction of $IrCl(DMSO)_3$, PPh_3 (45) and H_2 in toluene

As described earlier, the addition of 1.78 eq. **45** to $IrCl(DMSO)_3$ (**III**) proceeds to form a series of 16 electron complexes alongside **53, 56, 54** and **55**. Inner and outer sphere hydrogenation mechanisms are extensively described in the literature [244-247]. H_2 was added to a series of such solutions and a number of dihydride products were formed. The structure of these products and routes to their formation are shown in Figure 5.10. They can be readily differentiated according to the chemical shift and couplings of their hydride ligands. The ratio of these products proved to depend on the reaction time and temperature.

The reaction of **III** with **45** and H_2 in methanol-d_4 was followed and found to proceed cleanly to a mixture of two 18 electrons phosphine complexes (**58** and **62** whose formation are shown in Figure 5.10) without any other visible products. However, the degree of reaction is less than in toluene, and consequently the hydride signals exhibit low SNR. When the analogous reaction was examined in toluene, good PHIP (higher SNR) was observed (see Chapter 7) and this solvent was selected for subsequent study. Therefore any experiments in methanol are not pursued.

Tolman parameters[248] are important indicators of phosphine reactivity. The cone angle Θ measures the bulkiness of the phosphine ligand and defines its ability to compete for coordination to a metal centre. In contrast, ν_{co} provides an indication of the phosphines ability to donate electron density to the metal centre. The cone angle of **45** is 145° and ν_{co} is 2069 cm^{-1} [248]. These two parameters influence the reactivity of **45** toward the metal sterically and electronically.

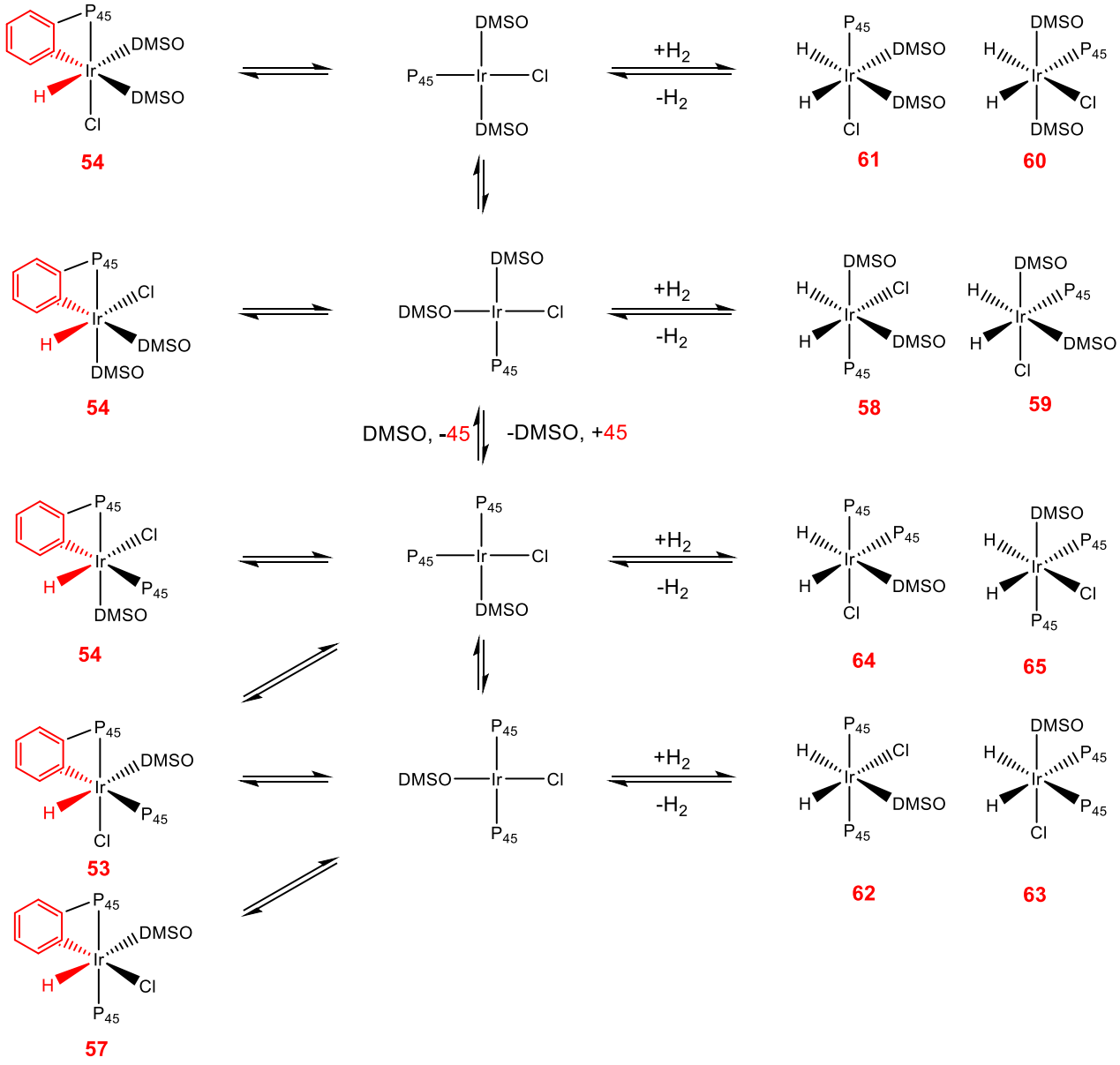

Figure 5.10: Reaction of $IrCl(DMSO)_3$ (**III**), **45** and H_2 leads to a large number of hydride ligand containing products ($Ir(H)_2Cl(DMSO)_3$ not shown). The Ir(III) products are in equilibrium with their Ir(I) precursors. The region-chemistry of these reactions leads to a number of possible product isomers. Only those detected by NMR are shown.

It was hypothesised that the ratio and nature of products formed are closely dependent to the relative amount of **45**. It is important to selectively favour the formation of the *bis*-phosphine **62** as it is shown that it is more reactive to *p*-H_2 in hyperpolarisation reactions and therefore may result in higher signal gains (see chapter 6, section 6.2). To investigate this effect, a sample containing (2.5 mg) 8.6 mM of $IrCl(DMSO)_3$ (**III**) and (0.59 eq.) of **45** in 0.6 mL of toluene-d_8 was prepared. H_2 (3 bar) was added to the sample and after 30 min, hydride ligand signals for $Ir(H)_2Cl(DMSO)_3$, **53**, **54**, **55** and **56** are readily observed in the corresponding ^{1}H NMR spectrum, in addition to those for the new dihydride products **58**, **59** and **62** of Figure 5.10. These changes are portrayed in Figure 5.10. The dihydride products appear in the ratio 1 : 1.85 : 0.62 at this stage. A further isomer of the *mono* phosphine substituted dihydride, **60**, also appeared at longer reaction times. When a further (0.59 eq.) of **45** is added, and 2 hrs 35 min of reaction takes place, the ratio of **59** : **58** : **60** : **62** in solution proved to be 0.28 : 0.36 : 0.48 : 1. 30 min later, the ratios were measured as 0.22 : 0.38 : 0.53 : 1, implying that these products

slowly equilibrate in solution. As expected, the formation of the *bis*-phosphine containing dihydride **62** was found to be more prevalent as the amount of phosphine increased. A corresponding reduction in the amount of $Ir(H)_2Cl(DMSO)_3$ was also observed. The C-H activation products slowly convert to the corresponding dihydrides during these reactions.

In order to observe the effect of the relative amount of **45** on the products equilibria, the ratio was further increased. Figure 5.11 portrays the evolution of these hydride ligand signals as a function of reaction time, for a sample containing **III** and 1 eq. of **45**. After one hour the ratio of **59** : **58** : **60** : **62** was 1 : 0.79 : 0.17 : 0.92 and all the initial C-H bond activation product has been consumed. After one day the dihydride product ratios reach 0 : 0.68 : 0.59 : 1 (**59** : **58** : **60** : **62**) after which they become constant. For conclusion, the rate of appearance of **59** > **62** > **58 > 60**. However, thermodynamically, there order of stability is **62** > **58** > **60** > **59**. At low temperature, where the ligand exchange pathways are inhibited **58**, **62** and **60** were fully characterised. (see chapter 9, section 9.6.11)

Table 5.1: Selected ^{1}H and ^{31}P NMR data for **58**, **59**, **62** and **60**.

	58	**59**	**60**	**62**
^{1}H (1) (ppm)	-15.50	-10.94	-11.59	-14.30
^{1}H (2) (ppm)	-19.64	-15.25	-19.36	-20.12
^{31}P (ppm)	4.96		-1.30	9.20
^{2}J (^{31}P-1) cis (Hz)	19.2	14.2	10.4	19.5
^{2}J (^{31}P-2) cis (Hz	17.8			14.7
^{2}J (^{31}P-2) trans (Hz)		165.8	148.0	
^{2}J (1- 2)	5.9	5.3	4.7	5.8

It was shown that the reaction of **III** with 0.69 eq. of **45** and the reaction of an equimolar concentration of **III** and **45** provides the same products with a similar ratio and order of stability. In both cases, **62**, which was of interest, is prevalent. Next, the effect of the addition of an excess of **45** on the product distribution is tested.

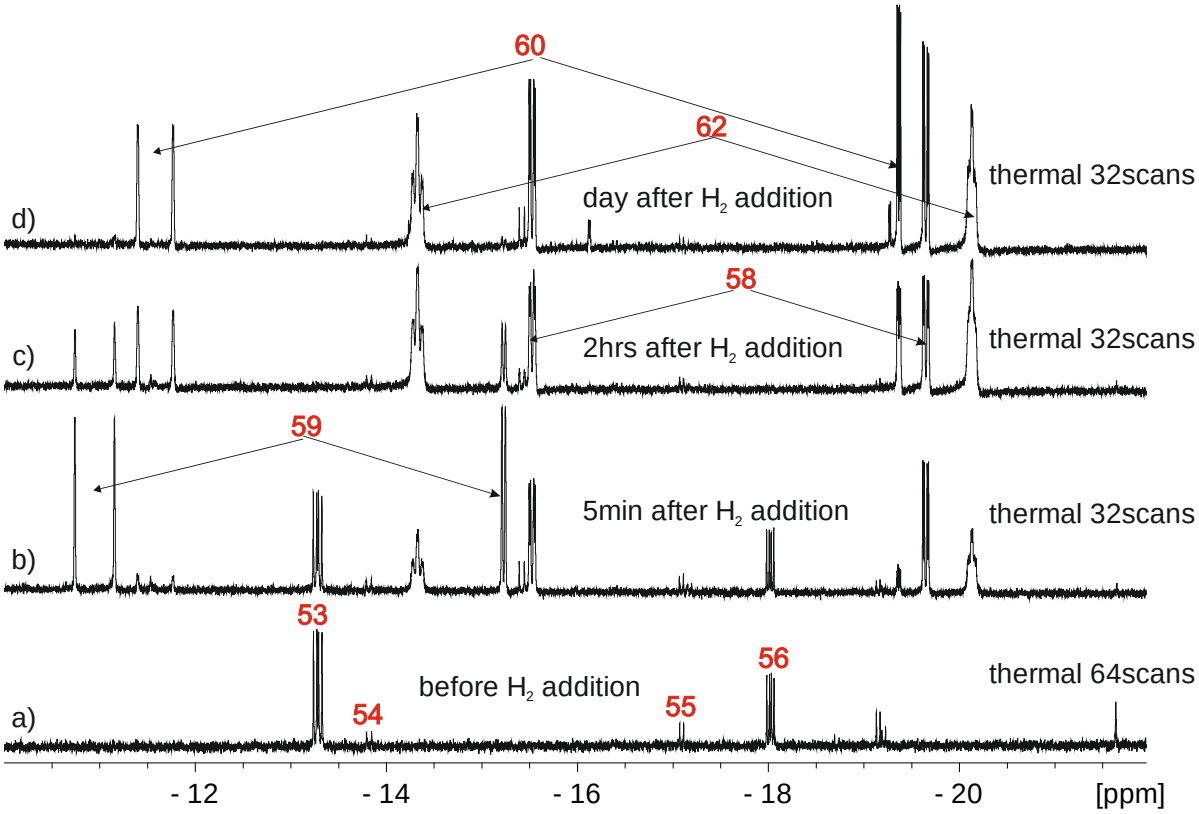

Figure 5.11: Sample of 8.6 mM of $IrCl(DMSO)_3$ (**III**) and 1 eq. of **45** in 0.6 mL of toluene-d_8 was used to record four ^1H NMR spectra at 298 K with 32 scans. a) before H_2 addition, b) 30 min after H_2 addition, c) 2 hrs after H_2 addition and d) 24 hrs after H_2 addition. These four spectra demonstrate the presence of the multiple identified species at these different stages.

5.2.3 Reaction of $IrCl(DMSO)_3$ with an excess of 45 and H_2 in toluene

When the same reaction as in 5.2.2 was performed with an excess of **45**, a single product appears to form rapidly. This process involved mixing $IrCl(DMSO)_3$ (**III**) and 3 eq. of **45** in toluene-d_8. After addition of H_2, the ^1H NMR spectrum showed two sets of hydride resonances at -10.65 and -20.47 ppm due to **66**. The hydride ligand resonances appearance demonstrates the coordination of three phosphine ligands (Figure 5.12) in this product. The hydride resonating at -10.65 ppm is split by a *trans* ^2J (^{31}P-^1H) coupling of 131.1 Hz, a *cis* ^2J (^{31}P-^1H) coupling of 20.6 Hz and a *cis* ^2J (^1H-^1H) coupling of 5.1 Hz. The second hydride signal at -20.47 ppm is *cis* coupled to ^{31}P through ^2J (^{31}P-^1H) splitting of 14.7 Hz and 28.0 Hz. This product is known and proved to be stable, hence does not degrade[229, 240, 249]. Key NMR data for **66** that agrees with that in the literature[229]. The reaction of this sample with *p*-H_2 is described in Chapter 6, section 6.2.3.

In conclusion, by using an excess of **45**, the unwanted phosphine *tris*-substitution occurs. The goal was to limit the reaction to the *bis*-phosphine substitution. Therefore, the equimolar concentration between **III** and **45** was maintained. The same ratio between the metal catalyst the other phosphines will also be used.

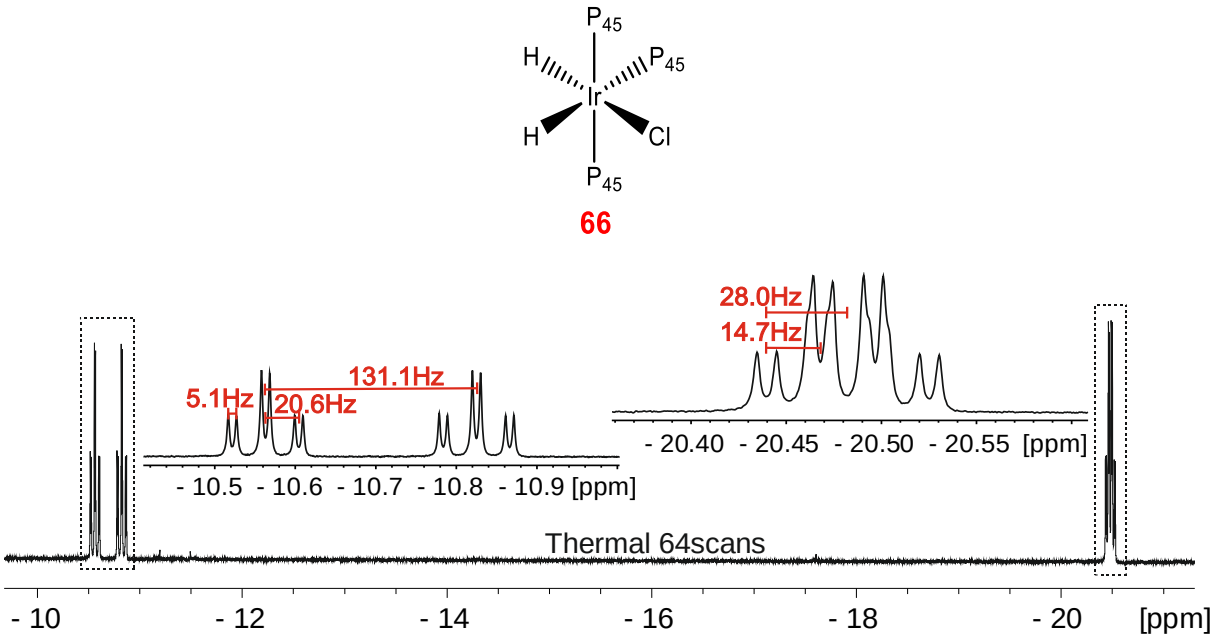

Figure 5.12: Zoom on the hydride signal of **66** in the ^{1}H NMR spectrum at 298 K of a solution of IrCl(DMSO)$_3$ (**III**) and (3 eq.) of **45** in 0.6 mL of toluene-d_8. The coupling pattern demonstrate a *tris*-phosphine substitution.

5.3 Reactivity of **III** with a range of phosphines yielding C-H bond activation

Reaction of Ir^{I}Cl(DMSO)$_3$ (**III**) in the absence of H_2 with the aromatic phosphines that contain *ortho* protons, P_{47}-P_{50}, of Scheme 5.2 yields NMR spectra (Figure 5.13) with multiple hydride resonances in accordance with the formation of several C-H bond activation products, as described for **45**. However, the exact product(s) formed depend on the phosphine. Figure 5.13 presents the corresponding hydride regions of four ^{1}H NMR spectra associated with phosphines **47**, **48**, **49** and **50** in toluene. Figure 5.14 shows the corresponding ^{31}P{^{1}H} NMR spectra, which highlight the full speciation of the C-H bond activation products and 16 electron precursors when (**III**) is reacted with **47**, **48**, **49** and **50** in toluene.

Only one example stands out. When **50** is utilized, a single product forms with a hydride ligand *trans* to phosphine; the hydride signal at -9.25 ppm shows a coupling of 276.4 Hz to ^{31}P. The majority of these hydride signals are split by 14-20 Hz ^{31}P couplings, suggesting the products exhibit similar hydride-*cis* phosphine ligand arrangements to those found with **45**.

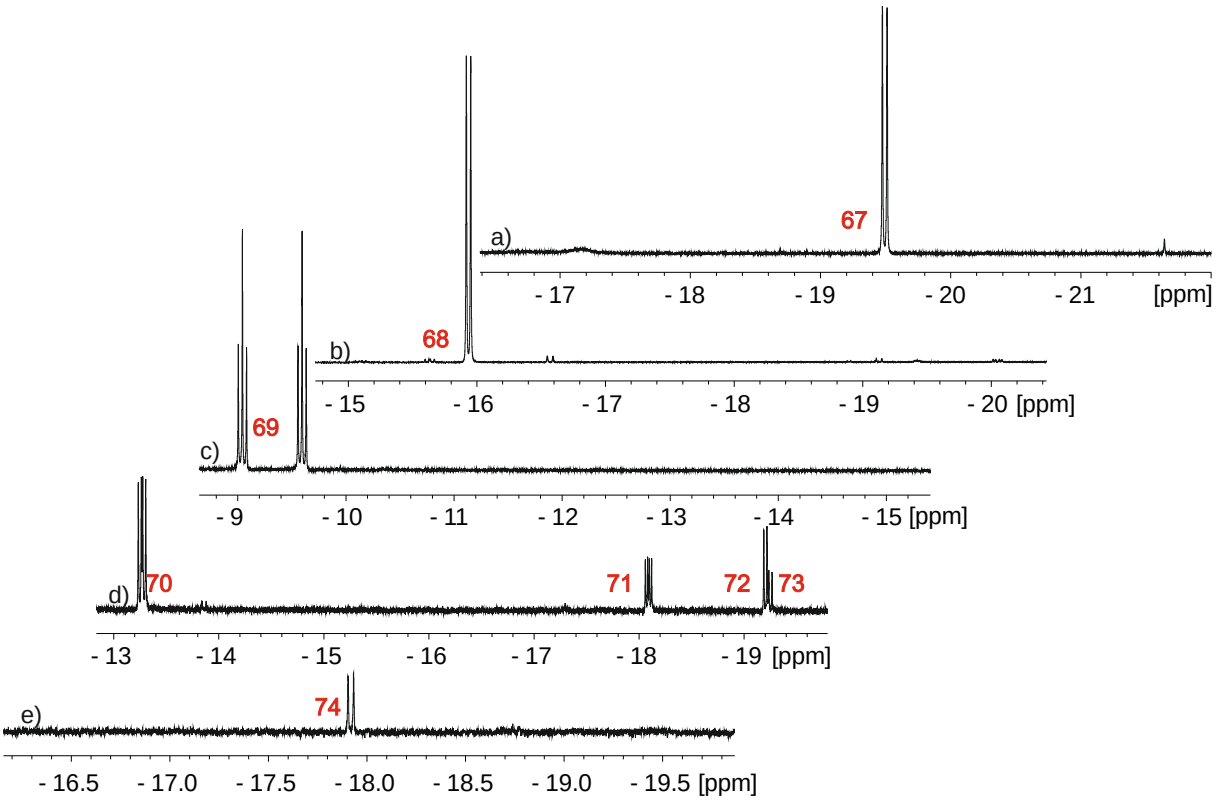

Figure 5.13: Reaction of $Ir^{I}Cl(DMSO)_3$ (**III**) with each of these phosphines in toluene trigger a C-H bond activation that give the hydride signals in the ^{1}H NMR spectra. In spectra a, b, c, and d the phosphines **47**, **49**, **50** and **48** was used respectively.

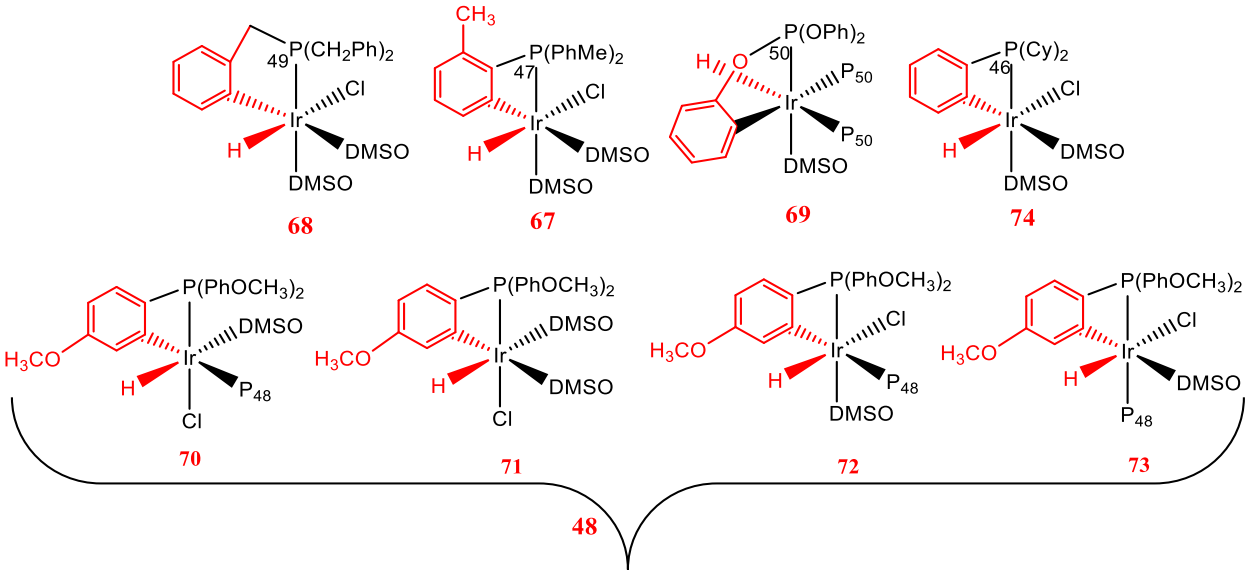

Scheme 5.2: C-H bond activation product(s) formed from reaction of **III** with the phosphines **47**, **48**, **49**, and **50** in toluene.

Sterically bulky phosphines **49** and **47** appear to exhibit more selective reactivity. Each yields a single C-H bond activation product **68** and **67**, identified through a hydride resonances at -19.43 ppm and -15.93 ppm respectively. These correspond to *mono*-substituted species where the hydride ligand is *trans* to chloride and the signals are both split into doublets through a 20 Hz *cis* coupling to ^{31}P.

In the $^{31}P\{^{1}H\}$ NMR spectra (Figure 5.14) associated with **47** specifically, a signal at -29.8 ppm also appears due to the free phosphine, alongside peaks at -7.7 ppm for the hydrogenation product, at 11.9 ppm for 16 electron $IrCl(DMSO)_2(P_{47})$. Hence the C-H bond activation product **67** located 22.8 ppm is in equilibrium with $IrCl(DMSO)_2(P_{47})$. The same situation holds true for **49**, where now the free phosphine ^{31}P NMR signal appears at -15.02 ppm, at 1.17 and 8.63 ppm for the isomers of $IrCl(DMSO)(P_{49})_2$ and $IrCl(DMSO)_2(P_{49})$ and at 30.49 ppm for the C-H bond activation product **68**. The prevalence of the C-H activation product is higher with **49** when compared to **47**.

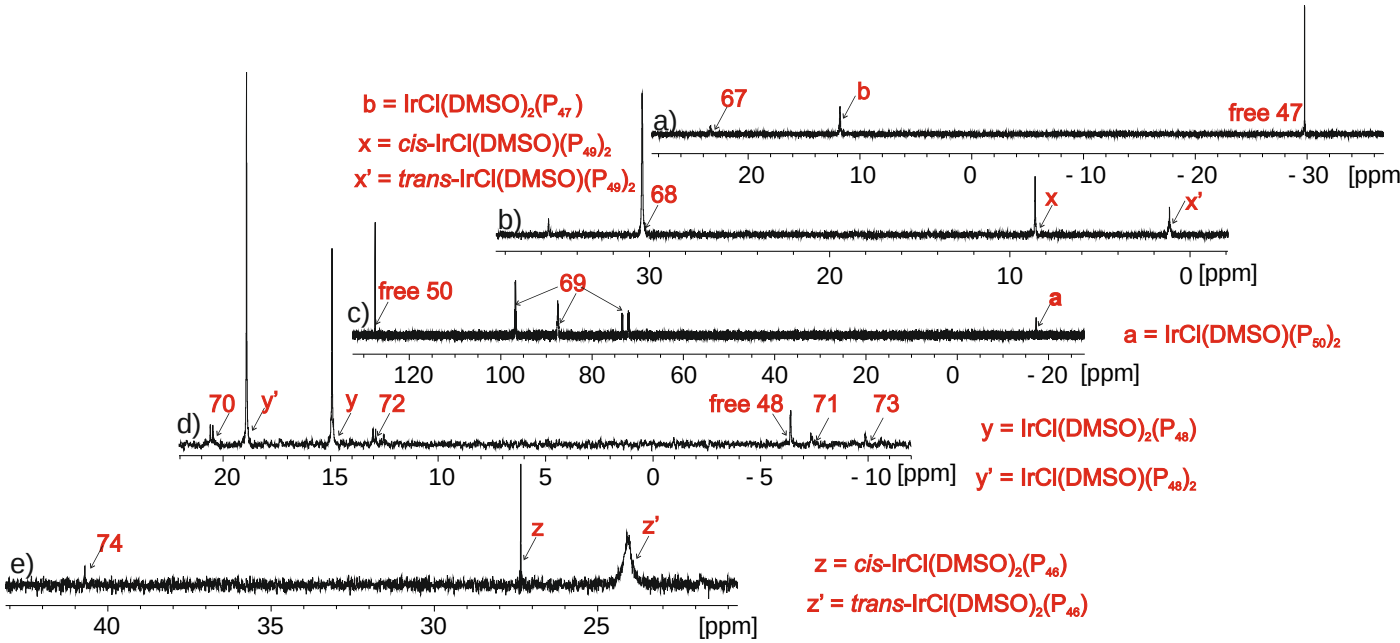

Figure 5.14: Reaction of $Ir^{I}Cl(DMSO)_3$ (**III**) with each of these phosphines in toluene trigger C-H bond activation and 16 electron complexes that give the numerous ^{31}P signals in the $^{31}P\{^{1}H\}$ NMR spectra. In a, b, c, and d the phosphines **47**, **49**, **50** and **48** was used respectively.

Under the same conditions, electron poor, but less sterically bulky **50**, yields 70% of the corresponding *tris* substituted C-H bond activation product alongside several minor species. Using a larger excess of **50** increased the prevalence of the *tris* substituted C-H bond activation product **69** to 91 %. It yields a hydride resonance at -9.25 ppm that couples to a *trans* phosphine ligand via a J_{HP} splitting of 275 Hz. The remaining 9% of the second sample was the *cis bis*-phosphine C-H bond activation product, which yields a hydride signal at -15.10 ppm. In the corresponding $^{31}P\{^{1}H\}$ NMR spectrum (Figure 5.14.c), three ^{31}P signals are observed for the major product at 96.74, 87.44 and 72.65 ppm. In addition, a signal at 127.47 ppm and -17.4 ppm are seen for the free **50** ligand and $IrCl(DMSO)(P_{50})_2$. No *mono* substitution products are seen.

When **48** is used, high complexity returns, and four C-H bond activation products form, that parallel those seen with **45**. The ratio of these products, identified as **70** : **71** : **72** : **73**, is 1 : 0.15 : 0.5 : 0.54. The hydride signals at -13.27 and -18.09 ppm for **70** and **72** appear as doublets of doublets, characteristic of hydride ligands *cis-cis* to two inequivalent phosphines. The additional hydride resonances at -19.20 and -19.25 ppm are due to *mono*-phosphine isomers **71** and **73**. $^{31}P\{^{1}H\}$ NMR spectroscopy at 298 K (Figure 5.14.d), reveals two dominant singlets at 18.90 and 14.93 ppm associated with 16 electron complexes of the form $IrCl(DMSO)_2(P_{48})$ and $IrCl(DMSO)(P_{48})_2$. Hence

whilst the ^{1}H NMR spectra enable the ready detection of four C-H bond activation products they are really quite minor species.

With phosphine PCy_3 (**44**), no hydride-containing product is formed when two equivalents of **44** are added. Hence no orthometallation of the cyclohexyl ring occurs. This suggests that the stability of any such orthometallation products is low. However, additional ^{31}P NMR signals provide evidence for the formation 16 electron $IrCl(DMSO)_2(P_{44})$ and $IrCl(DMSO)(P_{44})_2$ at 21.27 and 17.49 ppm respectively, with additional signals at 45.02 and 9.78 ppm for the phosphine oxide and free phosphine **44**.

Finally, when $PPhCy_2$ (**46**) is examined, evidence for a mono substituted C-H bond activation product **74** is found in the ^{1}H NMR spectrum when one ligand equivalence is added. The corresponding $^{31}P\{^{1}H\}$ NMR spectrum (Figure 5.14.e) shows two strong signals at 24.19 and 27.40 ppm for two isomers of 16 electron $IrCl(DMSO)_2(P_{46})$, in addition to a weak signal for the C-H bond activation product at 40.72 ppm. In this case no signals for the free phosphine remain.

In conclusion, the aromatic ring containing phosphines are likely to undergo C-H bond activation. No further characterization of these C-H activation products was undertaken. The aim was simply to study the reactions of these *in-situ* prepared complexes with H_2. The results of these studies are described in the forthcoming sections and require access to 16-electron precursors.

Table 5.2: Selected ^{1}H and ^{31}P resonances of the C-H activation products of phosphines **67**, **68**, **69** and **70**-**73**

	67	**68**	**69**	**70-73**
$^{1}H_1$ (ppm)	-19.48	-15.96	-9.25	-13.27
$^{1}H_2$ (ppm)	NA	NA	NA	-18.09
$^{1}H_3$ (ppm)	NA	NA	NA	-19.20
$^{1}H_4$ (ppm)	NA	NA	NA	-19.25
$^{31}P_1$ (ppm)	11.78	29.88	72.70	20.52
$^{31}P_2$ (ppm)	NA	NA	87.44	-7.37
$^{31}P_3$ (ppm)	NA	NA	96.75	12.96
$^{31}P_4$ (ppm)	NA	NA	NA	-9.86
J($^{1}H_1$-^{31}P) (Hz)	18.1	17.2	275.2	14.4
J($^{1}H_2$-^{31}P) (Hz)	NA	NA	19.1	11.1
J($^{1}H_3$-^{31}P) (Hz)	NA	NA		15.4
J($^{1}H_4$-^{31}P) (Hz)	NA	NA		15.2
J(^{31}P-^{31}P) (Hz)	NA	NA	$J(P_1\text{-}P_3)$ = 17.1 $J(P_1\text{-}P_2)$ = 28.0 $J(P_2\text{-}P_3)$ = 21.0	J_{72} = 23.7 J_{70} = 24.2

5.4. Phosphines with similarities of reactivity with 45 in presence of H_2

The analogous reactions of **48**, **46** and **49** with $IrCl(DMSO)_3$ (**III**) and H_2 are now considered. The reaction products formed in these reactions were found to be similar to those formed from **5**. Scheme 5.3 and Table 5.3, summarise these findings.

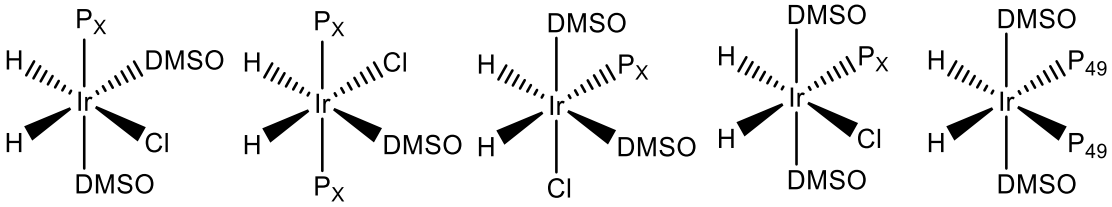

X = 46, 48 and 49

Scheme 5.3: Dihydrides products formed when **III** reacts with H_2 and a phosphine ligand P_X where X = **48**, **46** or **49**

Table 5.3: Ratio of the various dihydride products seen 5 minutes after the start of the reaction of **III** with H_2 and a phosphine ligand **48**, **46** or **49**, and at the end of the study.

Phosphines	Ratio of Products				
	71, 75, 79	**72, 76, 80**	**77, 81,**	**74, 78, 82**	**83**
48 start	0.37	0.07	0.54	0.02	NA
48 end	0.46	0.17	0.05	0.32	NA
46 start	0.69	0	0.23	0.08	NA
46 end	0.65	0.27	0	0.08	NA
49 start	0.05	0.29	0	NA	0.66
49 end	0.77	0.12	0.03	NA	0.08

Discussions and comments on these data are given in the forthcoming sections.

5.4.1 Reactions with (4-methoxyphenyl) phosphine 48

Figure 5.15 shows the time course of the reaction of $IrCl(DMSO)_3$ (**III**) with 1 eq. of **48** tris(4-methoxyphenyl) and then 20 minutes later 3 bar of H_2 in toluene-d_8. It leads to the formation of **75**, **76**, **77** and **78**, which are analogous to the products already described for **45**. Based on the earlier observations, the addition of H_2 can take place to **III** or the 16 electron phosphine substitution products which are in equilibrium with the C-H bond activation products. Immediately after the addition of **48**, small hydride signals are evident for the four C-H activation products **70**-**73** discussed earlier. This sample was removed from the spectrometer and H_2 added. It was shaken and immediately interrogated by NMR. Significant reactivity was evident in this NMR spectrum despite the fact the hydride ligand signals for the four C-H bond activation products appeared with similar intensity to those detected without H_2. The hydride region became very complex and integration suggests that a series of new hydride products form to be 8 times higher than the sum of **70**-**73**. Hence, it can be deduced that at least 88 % of this sample was made up of 16-electron species capable of adding H_2. As none of these signals are due to $Ir(H)_2(DMSO)_3Cl$, it can be concluded that the displacement of DMSO by phosphine is very rapid. It is possible, therefore, that H_2 can add to $Ir(DMSO)_3P_1$, $Ir(DMSO)P_2$, IrP_3 species depending on the speed of phosphine substitution. At the 5 minute stage, the ratio of $Ir(DMSO)_2P_1$-H_2 : $Ir(DMSO)P_2$-H_2 : IrP_3-H_2 is 2.43 : 0.21 : 0. Hence, it is shown that the *mono* phosphine substitution products dominate, presumably due to the prevalence of $IrCl(DMSO)_2(P_{48})$. Table 5.3 details the ratio of the structural isomers of these products.

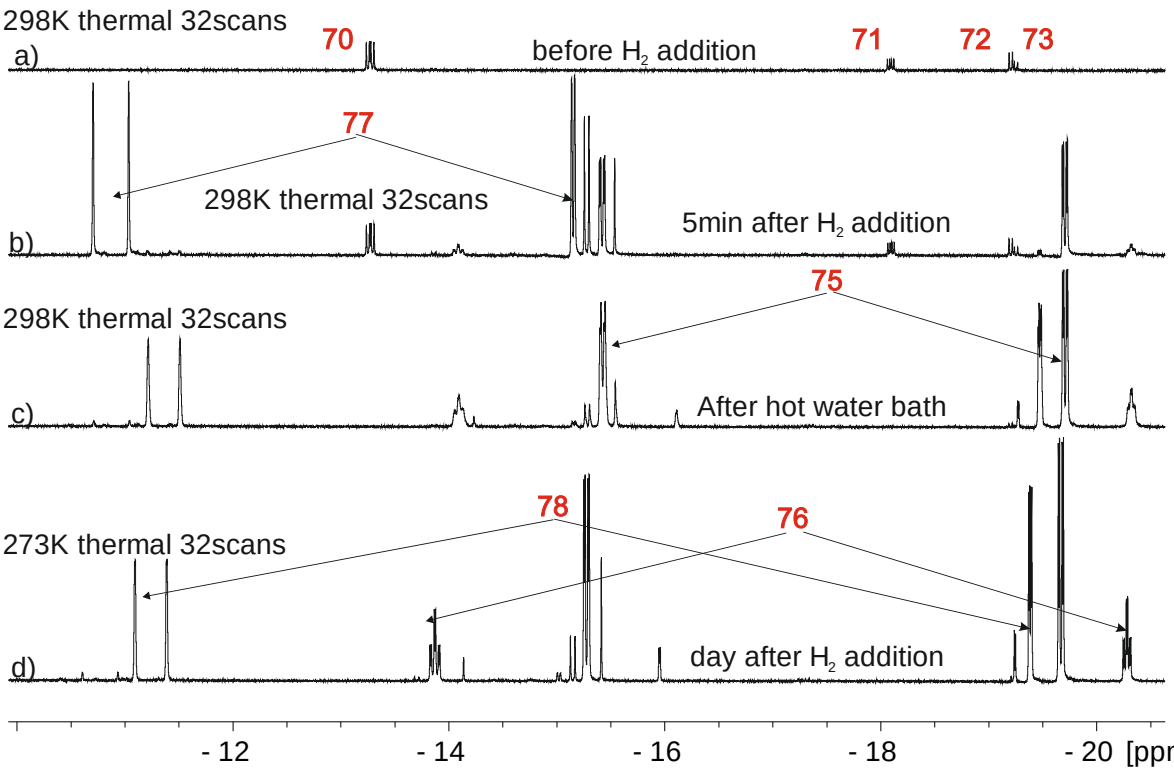

Figure 5.15: Sample of 17.2 mM of $IrCl(DMSO)_3$ (**III**) and 1 eq. of **48** in 0.6 mL of toluene-d_8 was used to record four ^1H NMR spectra at 298 K with 32 scans. a) before H_2 addition at 298 K, b) 5min after H_2 addition at 298 K, c) after putting the sample in a hot water bath for 10 min allows the total conversion of the C-H bond activation products and d) 24hrs after H_2 addition at 273 K. These four spectra testifies the presence of many identified species at these different stages.

The sample was warmed to 50 °C and left for 10 minutes and a second ^1H NMR spectrum recorded. This showed that the total hydride signal intensity remained roughly the same as in the spectrum at 5 minutes after allowing for the fact that the C-H bond activation products have been consumed. Hence, for conclusion all of the 16 electron complexes were consumed in 5 minutes. However, the hydride signal intensities for the dihydride products changed during this period. It was notable first that **77** converted into **75** and **78,** which were present in the ratio 1 : 0.70 and that more **76** formed. Hence, some free phosphine remained at the 5 minute stage and consequently it can be concluded that under these conditions H_2 addition is faster to $IrCl(DMSO)_2(P_{48})$ than phosphine substitution. After 24hrs, no further evolution of these species was evident as they were still present in the same ratio. It would seem likely therefore that **77** forms as a kinetic product of H_2 addition, whilst **75** and **78** are thermodynamically more stable.

In support of these deductions, a series of $^{31}P\{^1H\}$ NMR spectra (Figure 5.16) were also recorded at 298 K. These initially showed signals for free **48** at -6.39 ppm, C-H bond activation products at 20.53 ppm, -7.36 ppm, -9.86 ppm and 12.96 ppm, and singlets at 18.90 and 14.93 ppm due to the 16 electrons complexes $IrCl(DMSO)_2(P_{48})$ and $IrCl(DMSO)(P_{48})_2$. The ^{31}P NMR signal in **75** appears at 0.46 ppm, in **76** at 3.86 ppm, in **77** at -1.59 ppm and in **78** at -5.02 ppm.

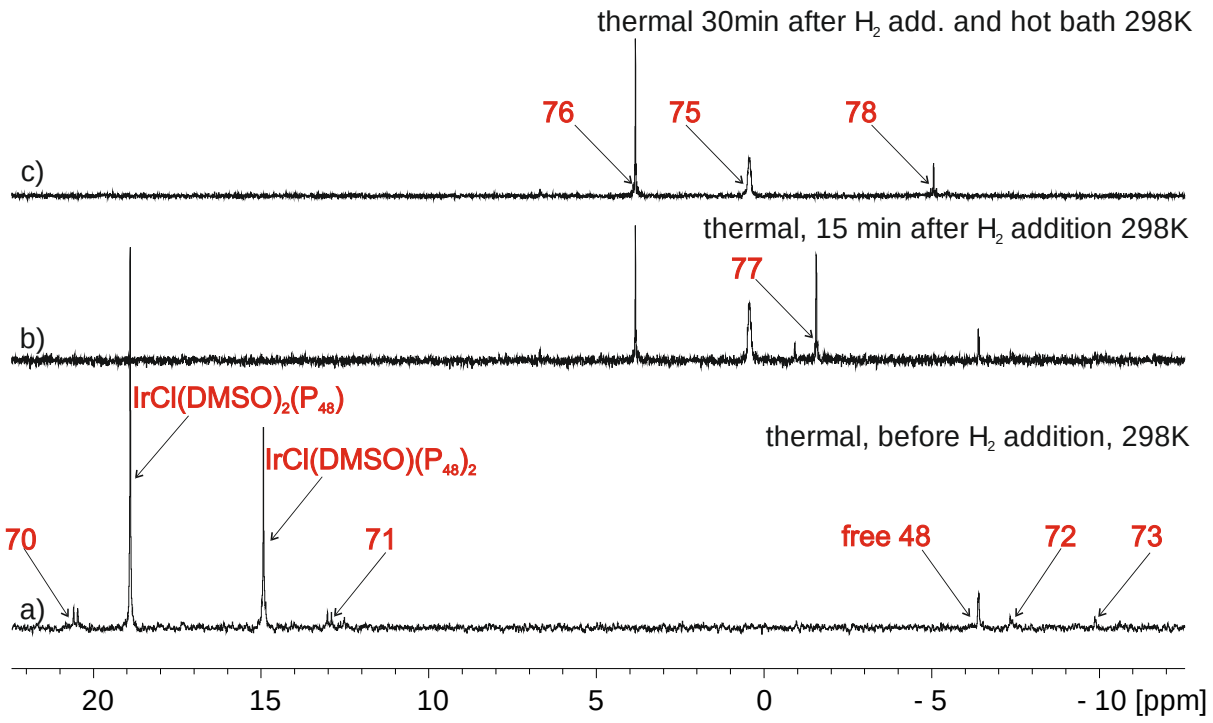

Figure 5.16: Sample of 5 mg of $IrCl(DMSO)_3$ (**III**) with 3.60 mg 1 eq. of **48** Tris(4-methoxyphenyl) used to record three $^{31}P\{^1H\}$ NMR spectra and the speciation of different product at different stage of the reaction. a) Before H_2 addition at 298 K. b) 15 min after H_2 addition and c) After 30 min after H_2 addition and the sample warmed in a hot water bath (~50 °C).

5.4.2 Reactions with di-cyclohexyl phenyl phosphine 46:

Mixing 17.2 mM of $IrCl(DMSO)_3$ (**III**) (5 mg) and 1 eq. of **46** (2.8 mg) in toluene-d_8 led after H_2 activation to the same four isomers observed with **45** and **48**.

When di-cyclohexyl phenyl phosphine (**46**) was examined, very limited C-H bond activation took place and the control NMR spectrum revealed very limited reaction prior to the addition of H_2. The corresponding ^1H NMR spectrum (Figure 5.17) after H_2 addition contained a number of hydride ligand signals. These are attributed to $Ir(DMSO)_2P_1\text{-}H_2$ products as no signals were seen at 298 K for $Ir(DMSO)P_2\text{-}H_2$ or $IrP_3\text{-}H_2$ products. Three isomers of $Ir(DMSO)_2P_1\text{-}H_2$ were evident in the ratio 1 : 0.34 : 0.11 (**79** : **81**: **82**). One hour later, in the NMR spectrum of Figure 5.17.b, **81** had disappeared, whilst **80** ($Ir(DMSO)P_2\text{-}H_2$) was detected alongside **79** and **82**. The ratio of these three products was now 0.41 : 1 : 0.12 (**80** : **79** : **82**) respectively. As with **48**, the substitution of DMSO by phosphine in $IrCl(DMSO)_2(P_{46})$ is slow. **82** is also a kinetic product and **80** and **82** are thermodynamically more stable. As the hydride resonance of **80** is only visible when the NMR probe is cooled to 273 K, rapid ligand dissociation is suggested at 298 K.

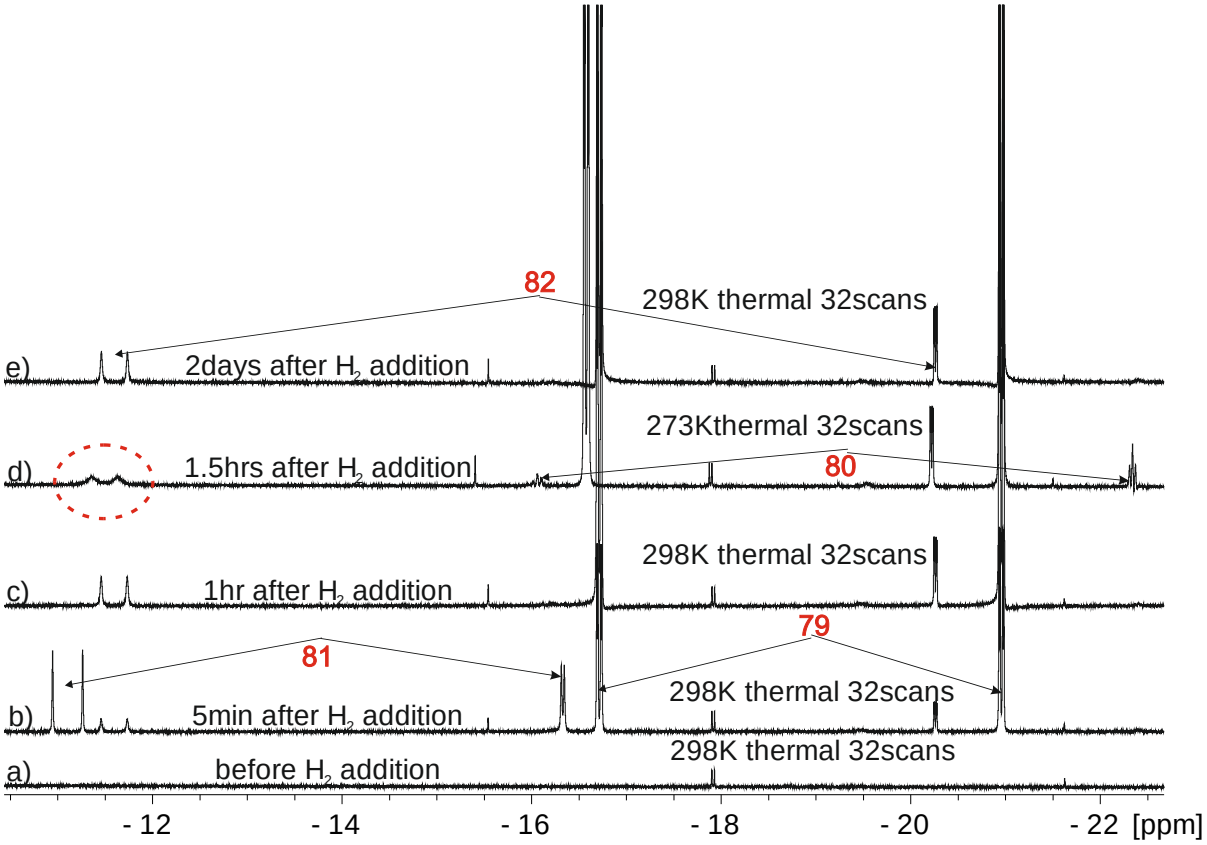

Figure 5.17: Sample of 17.2 mM of $IrCl(DMSO)_3$ (**III**) and (1 eq.) of **46** in 0.6 mL of toluene-d_8 was used to record five ^1H NMR spectra at 298K with 32 scans. a) before H_2 addition at 298 K, c) 5min after H_2 addition at 298 K, c) 1hr after H_2 addition at 298 K d) 1.5hrs after H_2 addition at 273 K and e) 48hrs after H_2 addition. These five spectra testifies the presence of many identified species at these different stages.

After hydrogenation at 298 K, the two signals in the $^{31}P\{^1H\}$ NMR spectra at 24.19 and 27.40 ppm for the two isomers of 16 electron $IrCl(DMSO)_2(P_L)$ were rapidly consumed. These were replaced with those for $IrCl(H)_2(DMSO)_2(P_{46})$, **79** and **81** at 9.95 and 3.49 ppm respectively alongside those for **80** ($IrCl(H)_2(DMSO)(P_{46})_2$) at 10.73 ppm. The C-H bond activation product, yielding a signal at 40.72 ppm, disappeared very slowly over 48 hrs.

5.4.3 Reactions with Tris-benzyl phosphine 49:

In the case of Tris-benzyl phosphine (**49**), the products formed are similar to those seen with **45**, although an additional isomer of $Ir(H)_2Cl(DMSO)(P_{49})_2$, also forms and $Ir(H)_2(DMSO)_3Cl$ is detected. This tells us that **49** is less reactive than the other phosphines as substitution at $Ir(DMSO)_3Cl$ by **49** is slow and incomplete in the timescale of the measurements.

The $^{31}P\{^1H\}$ NMR spectra in Figure 5.18 recorded during this investigation provided evidence to support these deductions. Signals could be seen at 1.17 and 8.63 ppm for $IrCl(DMSO)(P_{49})_2$ and $IrCl(DMSO)_2(P_{49})$ which react rapidly with H_2 to give **84** with a ^{31}P signal at 7.92 ppm, and **83** with a

signal at 3.81 ppm. The signals of the C-H bond activation product **68** at 30.49 ppm and the free **49** at -15.66 ppm remained.

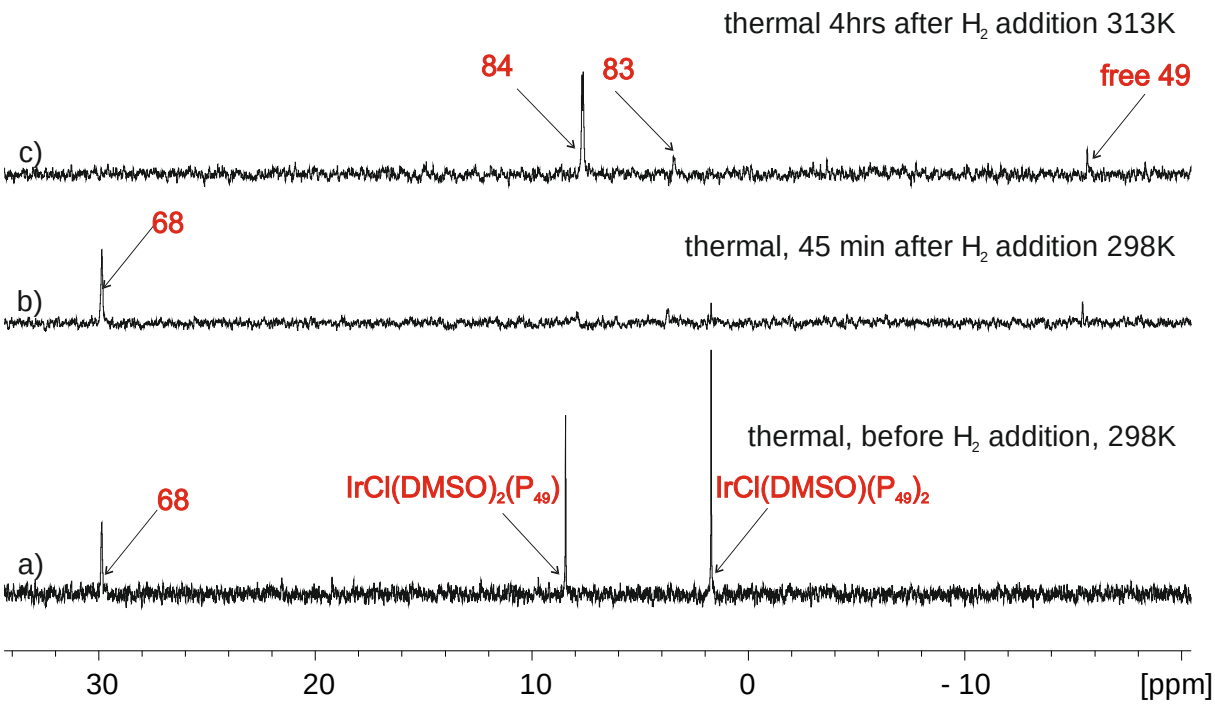

Figure 5.18: Sample of 2 mg of $IrCl(DMSO)_3$ (**III**) with 0.60 mg (1 eq.) of Tris-benzyl phosphine (**49**) used to record three $^{31}P\{^1H\}$ NMR spectra and the speciation of different product at different stage of the reaction. a) Before H_2 addition at 298 K. b) 15 min after H_2 addition at 298 K and c) After 14hrs after H_2 addition at 313 K

In the initial NMR spectrum before H_2 addition, one C-H bond activation product **68** is readily visible (Figure 5.18.a). This time, the first NMR spectra were recoded 18 minutes after H_2 addition. The resulting ^1H NMR spectrum (not shown here) contained several hydride ligand signals for $Ir(H)_2(DMSO)_3Cl$: C-H bond activation products **68** : $Ir(DMSO)_2P_1\text{-}H_2$: $Ir(DMSO)P_2\text{-}H_2$ in the ratio 0.76 : 2.40 : 0.30 : 1.31. The $Ir(DMSO)_2P_1\text{-}H_2$ complex is evident as two isomers **83** and **85**, where the former dominates with hydride ligand signals at 16.08 and 20.49 ppm; and 11.62 and 19.82 ppm. There are also two isomers of $Ir(DMSO)P_2\text{-}H_2$, **84** and **87** which yield hydride ligand signals respectively at -15.40 and -21.54 ppm; and 10.68 ppm.

Hydride ligand signal for the C-H bond activation product was of the same intensity at that of the sum of the other products and had not changed from the starting spectrum before H_2 addition. Additionally a signal for free phosphine was still visible.

In view of this apparent slow reactivity, the sample was warmed first to 308 K for 30 minutes and then to 313 K for 2.5 hrs. At this point, all of the C-H bond activation product signals vanished and **83** dominates the iridium products. There are several signals for $Ir(H)_2(DMSO)_3Cl$ type species, alongside with **85**, **83**, **87** and **84**; the latter minor product proving to be highly PHIP active (see section 6). The ratio of these species was 0.22 : 1 : 0.1 : 0.1 respectively.

In conclusion, it was shown that the phosphines **45** - **49** present similar reactivity and the identical four products are formed when reacted with **III** in toluene. However, the phosphine **49** yielded a fifth

product, namely **87**, which is not observed with the other phosphine ligands. The next section describes the reactions of $Ir(DMSO)_3Cl$ with the phosphines **47**, **50** and **51** which were found to exhibit different reactivity to those of **45** – **49**.

5.5 Reactivity of tri(o-tolyl)phosphine 47 with $IrCl(DMSO)_3$ and H_2 in toluene

In the case of the reaction of ortho-tolyl phosphine **47** with **III** and then H_2, the *mono*-phosphine complex **88** is formed in addition to the single mono substituted C-H bond activation product **67** that yields a hydride signal at -19.49 ppm. The two hydride ligands of the new species $IrCl(H)_2(DMSO)_2(P_{47})$ **88** resonate at -16.24 and -20.59 ppm. Interestingly, after 30 min of reaction, the C-H bond activation product **67**, **88**, and $IrCl(H)_2(DMSO)_3$ are present in the ratio 2.1 : 1 : 1.1. As these spectra contain signals for the dihydride addition product of **III**, it can be concluded that **47** fails to rapidly substitute DMSO in **III**; a ^{31}P signal for free **47** is still visible.

This sample was then cooled to 263 K for the purpose of **88** characterisation over the next 24 hrs. Figure 5.19.c was recorded at the end of this period. It shows that signals for C-H bond activation product **67** are still present, alongside those for **88** and $IrCl(H)_2(DMSO)_3$, in the ratio 0.49 : 0.9 : 1.1. However, the overall amount of the dihydride products was decreasing. The sample was then warmed in a 50 ^oC water bath for 10 min before being held at 313 K in the NMR probe for 12 min. The hydride signal in the ^1H NMR spectrum for the C-H bond activation product **67** has essentially vanished, with the ratio of **88** : $IrCl(H)_2(DMSO)_3$ becoming 0.37 : 1. Furthermore, slow decomposition of this sample continues to occur over time. The result of this is that **88** could not be characterised from these data.

In order to characterise **88**, the excess of DMSO needed to be removed. A toluene solution of 30 mg of **III** was reacted *in-situ* with 1 eq. of **47** for two hours allowing the formation of phosphine *mono*-substitution. Then the solution was dried under vacuum and the excess of DMSO washed off with hexane. The resulting crude $IrCl(DMSO)_2(P_{47})$ was exposed to H_2 and **88** cleanly forms. Now, after two days at 263 K, no degradation of **88** was observed.

According to Tolman steric and electronic parameters[248], **47** is the bulkiest ($\Theta = 194^o$) of the phosphine series, hence it is not surprising that it undergoes only *mono*-substitution. **47** has three methyl electron donating groups yielding a slight electronegativity with respect to the other phosphines (ν_{co} = 2066 cm^{-1}). It has been observed that the phosphines that have similar reactivity with **45** (ν_{co} = 2068.9 cm^{-1}) are the electron withdrawing phosphines **48** (ν_{co} = 2068 cm^{-1}).

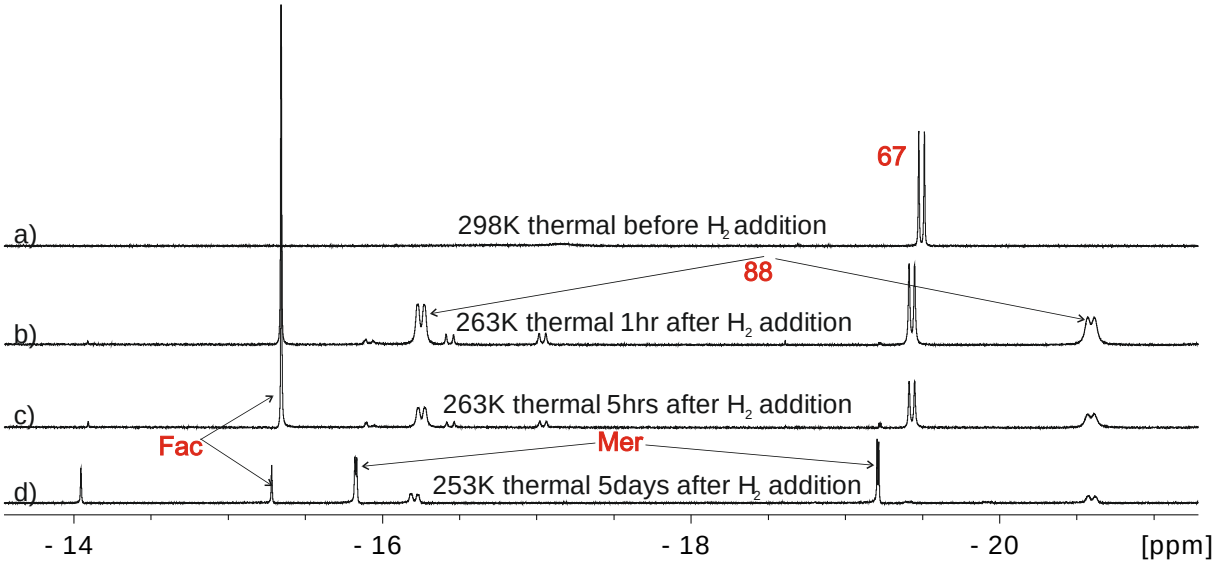

Figure 5.19: Sample of 17.2 mM of $IrCl(DMSO)_3$ (**III**) and (1 eq.) of **47** in 0.6 mL of toluene-d_8 was used to record four ^1H NMR spectra with 32 scans. a) before H_2 addition at 298 K, b) 30mins after H_2 addition at 263 K, c) 24hrs after H_2 addition at 263 K d) 120hrs after H_2 addition at 253 K. These four spectra testifies the degradation of **88** over time.

5.6 Reactivity of Triphenyl phosphite 50 with $IrCl(DMSO)_3$ and H_2 in toluene

When equimolar amounts of **III** and triphenyl phosphite **50** react under H_2, unwanted isomers of $IrCl(H)_2(DMSO)_3$ dominate. It was therefore, chosen to study this reaction with an excess of **50**.

First, the reaction of (2.5 mg) 8.6 mM of $IrCl(DMSO)_3$ (**III**) and (3 eq.) 2.9 mg of Triphenyl phosphite (**50**) in 0.6 mL of toluene-d_8 alone was followed at 298 K. This led to the formation of the *tris*-phosphine substituted C-H bond activation product **69** with hydride resonance at -9.31 ppm; Figure 5.20.a. 5 min after H_2 addition to this sample, the ^1H NMR spectrum showed no significant changes, suggesting low reactivity. The NMR probe was then warmed to 333 K and the sample left inside for 3 hrs. The formation of **89** and **90** in addition to **69** was now observed in the ratio 3.4 : 2 : 4.4. The two new products are the $Ir(DMSO)P_2$-H_2 and IrP_3-H_2 products in Figure 5.20. Selected resonance for these three products are given in Table 5.4. 24 hrs later, the evolution of the equilibrium is 2.5 : 3.1 : 3, showing a decrease of the C-H activation product and more formation of $Ir(DMSO)_2P_1$-H_2 : $Ir(DMSO)P_2$-H_2 : IrP_3-H_2 species.

A different reactivity is observed when there is an excess of phosphine **50**. Warming the NMR probe up to 333 K did not accelerate **69** conversion, which was present throughout the measurements.

In the $^{31}P\{^1H\}$.0 NMR, after H_2 addition, new resonances in addition to the three previously assigned ^{31}P resonances of the *tris*-phosphine C-H activation product, are observed at 84.12 and 87.24 ppm for **89** and **90** respectively that are secured by the HSQC experiment. The *J*-couplings for these two products data are given in Table 5.4.

Table 5.4: Selected ^{1}H and ^{31}P NMR resonances for **69**, **89** and **90**.

	69	**89**	**90**
^{1}H (1) (ppm)	-9.31	-10.55	-9.25
^{1}H (2) (ppm)	-9.31	-19.67	-9.25
^{31}P (1) (ppm)	96.74	98.4	87.24
^{31}P (2) (ppm)	84.48	84.12	
^{31}P (3) (ppm)	72.25		
$^{2}J(^{31}P\text{-}1)$ (Hz)	275.7	224.5	261.1
^{2}J ($^{31}P\text{-}2$) (Hz)	19.1	15.9	21.5
^{2}J (1-2)		4.8	
J (^{31}P-^{31}P) (Hz)	$J(P_1\text{-}P_2)$ = 21.0 $J(P_1\text{-}P_3)$ = 31.0 $J(P_3\text{-}P_2)$ = 18.0	$J(P_1\text{-}P_2)$ = 19.5	$J(P_1\text{-}P_2)$ =22.0 $J(P_1\text{-}P_3)$ = 29.0 $J(P_3\text{-}P_2)$ = 27.0

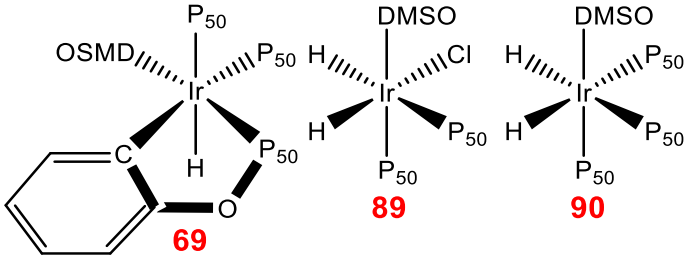

Scheme 5.4: chemical structure of **69**, **89** and **90**

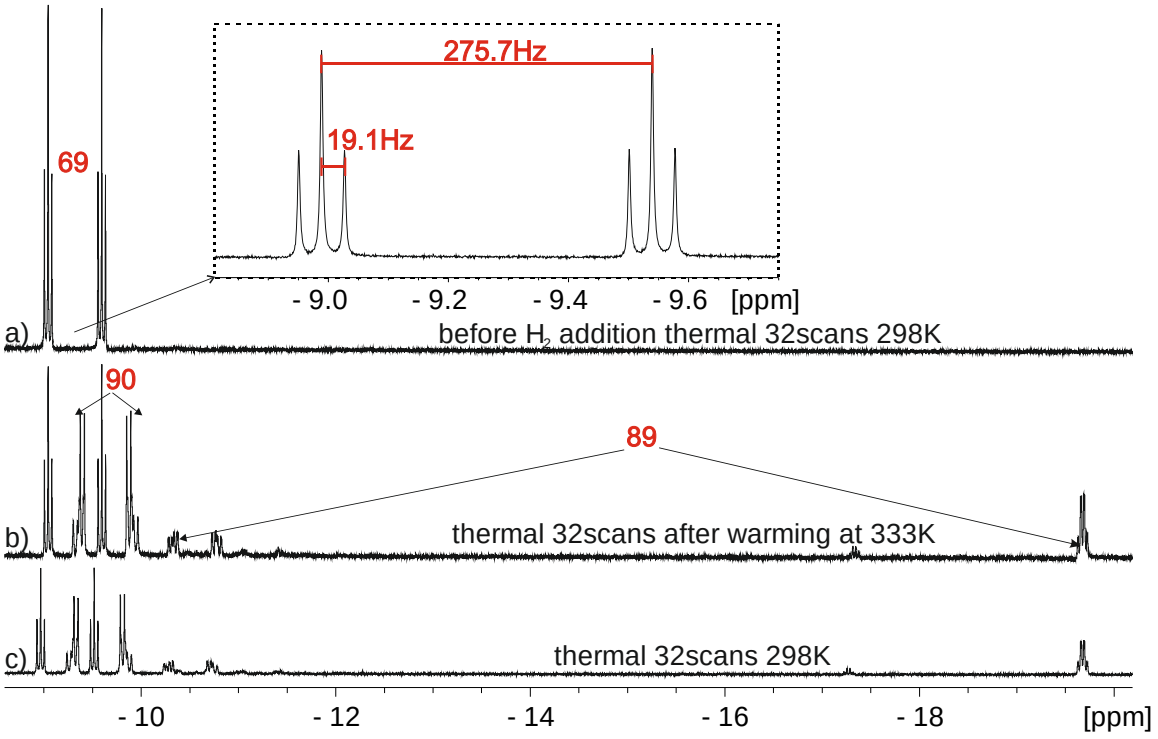

Figure 5.20: Sample of (2.5 mg) 8.6 mM of $IrCl(DMSO)_3$ (**III**) and (3 eq.) 2.9 mg of **50** in 0.6 mL of toluene-d_8 was used to record three ^{1}H NMR spectra with 32 scans. a) before H_2 addition at 298 K, b) after putting the sample in a hot water bath for 10min and warming the probe to 333 K does not

convert the C-H activation product c) 5hrs after H_2 addition at 298K. These three spectra testifies the presence of many identified species at these different stages.

5.7 Reactivity of methyl diphenyl phosphine 51 with $IrCl(DMSO)_3$ and H_2 in toluene

When 2.5 mg (8.6 mM) of $IrCl(DMSO)_3$ (**III**) is mixed with 1.4 µL (2 eq.) of methyl diphenyl phosphine (**51**) in toluene, a reaction takes place. The $^{31}P\{^1H\}$ NMR spectrum initially contains a singlet at -27.2 ppm for the free phosphine. However, a doublet at 9.8 ppm with 23.9 Hz separation and triplet at -1.36 ppm with 23.8 Hz separation then appear for 16 electron $IrCl(P_{51})_3$. Surprisingly, no C-H bond activation products form. Under H_2, further ^1H NMR interrogation reveals a single hydride resonance at -10.33 ppm (Figure 5.21). This signal exhibits a second order appearance indicative of a *tris*-phosphine complex. $Ir(H)_2Cl(P_{51})_3$ **91** has two equatorial phosphines yielding a resonance at -10.65 ppm (a doublet of 14.8 Hz) and a single axial phosphine signal at -18.9 ppm (a triplet of5.1 Hz). The ready formation of this product with **51**, is consistent with the small cone angle (136) of the phosphine.

Table 5.5: Selected ^1H and ^{31}P NMR resonances for **91**.

	91
^1H (1) = (2) (ppm)	-10.33 Second order multiplet
^{31}P (1) = (2) (ppm)	-10.65
^{31}P (3) (ppm)	-18.9
$^2J(^{31}P\text{-}^{31}P)$ (Hz)	5.1

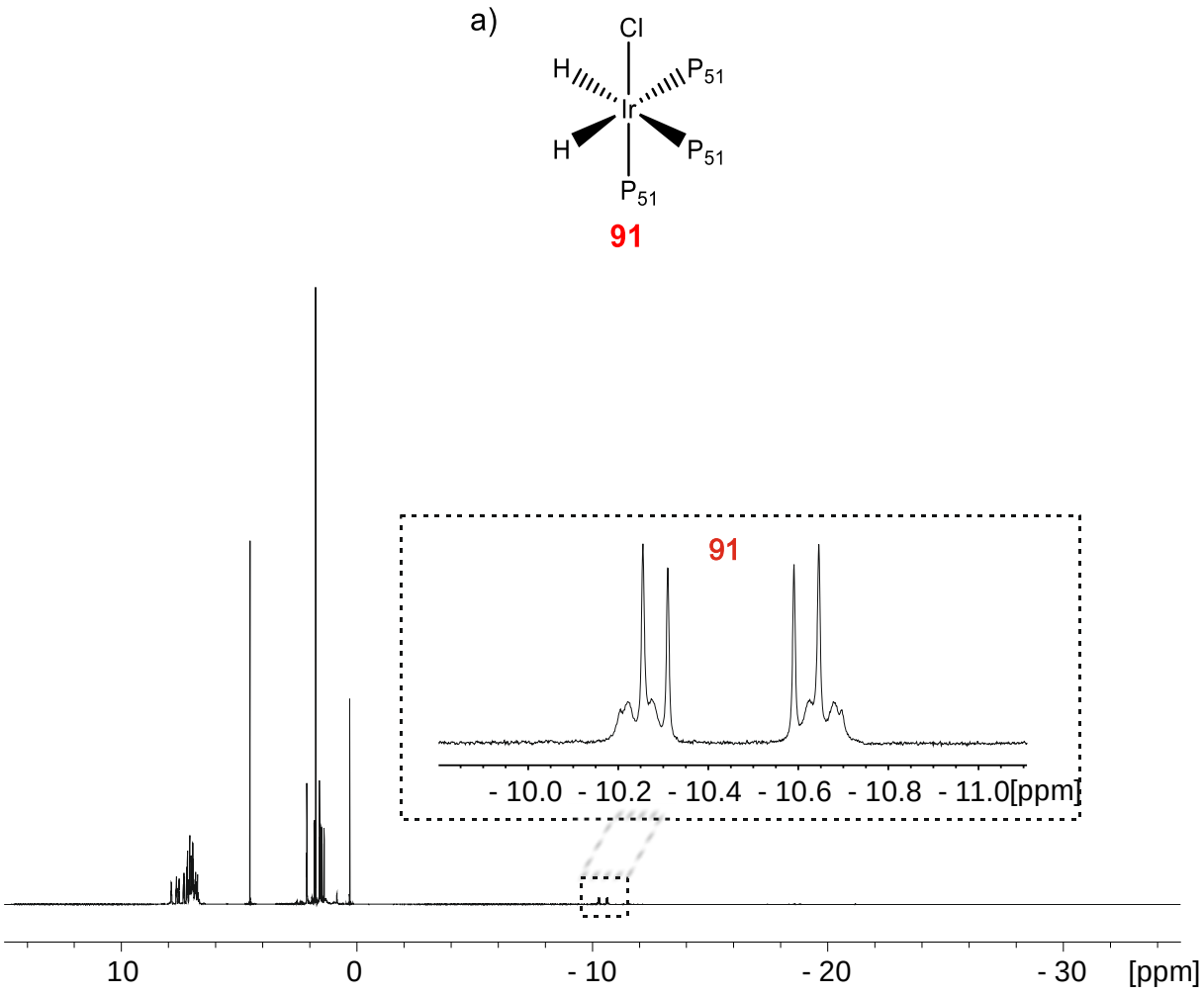

Figure 5.21: Sample of 2.5 mg (8.6 mM) of $IrCl(DMSO)_3$ (**III**) is reacted with 1.4 µL (2 eq.) of **51** in toluene-d_8. a) chemical structure of complex **91**. b) ^1H NMR spectrum shows in the hydride region single product **91**

Now, the next step is to study the reactivity of the non-aromatic *tris*-cyclohexyl phosphine with **III**.

5.8 Reaction of $IrCl(DMSO)_3$, *tris*-cyclohexyl phosphine 44 and H_2 in toluene

3 mg (11.9 mM) of $IrCl(DMSO)_3$ (**III**) and (2 eq.) 2.5 mg of *tris*-cyclohexyl phosphine **44** were dissolved in 0.6 mL of toluene-d_8 and a series of NMR spectra recorded. The corresponding $^{31}P\{^1H\}$ NMR signals provided evidence for the formation of 16 electron $IrCl(DMSO)_2(P_{44})$ and $IrCl(DMSO)(P_{44})_2$ through the detection of signals at 21.27 and 17.49 ppm respectively (Figure 5.22.a). Additional signals were seen at 45.02 and 9.78 ppm for the phosphine oxide and free phosphine **44**. After activation with dihydrogen (H_2) the ^1H NMR spectrum proved to exhibit two hydride ligand resonances at -16.90 and -21.06 ppm for the complex subsequently identified as **92** (Figure 5.23.a). This forms by the addition

of H_2 to $IrCl(DMSO)_2(P_{44})$. These two hydride ligands couple to a ^{31}P resonance that was located at 21.72 ppm (Figure 5.22) through *cis-cis* $^2J(^{31}P\text{-}^1H)$ couplings of 19.74 Hz and 17.56 Hz respectively.

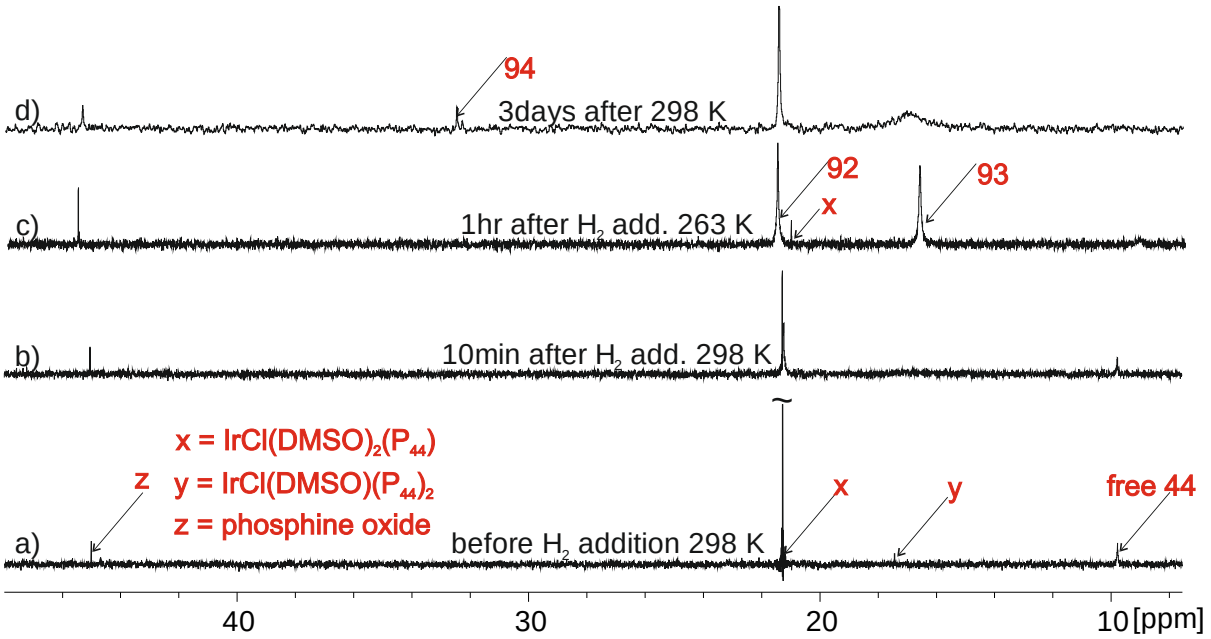

Figure 5.22: Series of $^{31}P\{^1H\}$ NMR spectra showing the hydride region of a sample containing 3 mg (11.9 mM) of $IrCl(DMSO)_3$ (**III**) and 2 eq. (2.5 mg) of **44** in 0.6 mL of toluene-d_8 under H_2. a) Thermal $^{31}P\{^1H\}$ NMR spectrum recorded at 298 K before H_2 addition, showing the phosphine oxide, free **44** and the 16 electron complexes $IrCl(DMSO)_2(P_{44})$ and $IrCl(DMSO)(P_{44})_2$. b) Analogous NMR spectrum to (a) just 10 min after H_2 addition. c) Analogous NMR spectrum, 1hr after hydrogenation at 263 K showing **92**, **93** and the presence of the starting material. d) Analogous NMR spectrum at 253 K after three days at 298 K all three ^{31}P signals of **92**, **93** and **94**.

In addition, two very broad ^1H NMR signals are also observed at around -16.09 and -22.66 ppm for a second complex, **93**. Surprisingly, the free H_2 signal at 4.55 ppm is now very broad, suggesting very rapid exchange between these species. In order to sharpen these peaks, the NMR probe was cooled first to 273 K and then 253 K (Figure 5.23. b and c). At 253 K the hydride ligands now appear as triplets of doublets with *cis* $^2J(^{31}P\text{-}^1H)$ couplings of 20.6 Hz and 14.1 Hz respectively, and a mutual *cis* $^2J(^1H\text{-}^1H)$ coupling of 6.1 Hz. **93** is therefore the H_2 addition product of 16 electron $IrCl(DMSO)(P_{44})_2$; its ^{31}P resonance appears at 16.73 ppm.

After 3 hrs at 253 K, the ratio of **92** : **93** was 0.087 : 1. The sample was then warmed to 298 K for 28 hrs prior to cooling to 253 K (Figure 5.23.d) and recording a new NMR spectrum. **92** had vanished from the NMR spectrum and a third species **94** was evident with **93** in the ratio 1 : 6. The new species **94** is tentatively assigned to the mutually *trans*-dihydride product $Ir(H)_2Cl(DMSO)(P_{44})_2$. It yields a hydride resonance at -10.52 ppm with a ^{31}P coupling of 12.0 Hz. Related trihydride complexes with a meridional ligand arrangement yield analogous hydride ligand signals in this region[250].

An EXSY experiment was recorded by exciting the hydride signal for **94**. Spatial proximity to four proton resonances of the cyclohexyl ring at 2.19, 1.82, 1.70 and 1.58 ppm was observed. HMQC NMR located the ^{31}P signal for this complex at 31.5 ppm. It is therefore notable that this complex only forms in the presence of DMSO.

In order to only favour the formation of **92**, 2.5 mg of (**III**) was mixed with 0.8 eq. of **44** in 0.6 mL toluene solution. The reaction proved after H_2 addition to yield selectively **92**. It is very important for hyperpolarisation reaction to prevent formation even a small fraction of **94** due to the very rapid *p*-H_2 consumption by this complex. (see chapter 6, section 6.5)

In agreement with the large cone angle of **44** (170°) no *tris*-phosphine complexes were detected.

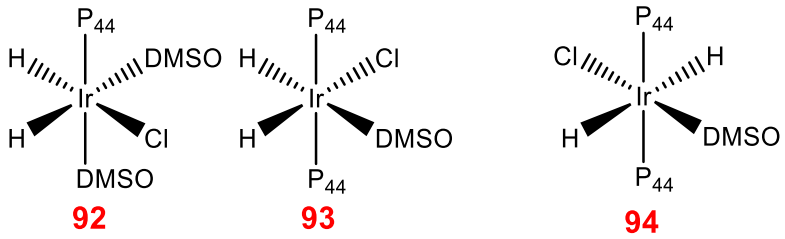

Scheme 5.5: chemical structure of **92**, **93** and **94**

Table 5.6: Selected ^{1}H and ^{31}P NMR resonances for **92**, **93** and **94** complexes

	92	**93**	**94**
^{1}H (1) (ppm)	-16.90	-16.09	-10.52
^{1}H (2) (ppm)	-21.01	-22.66	NA
^{31}P (ppm)	21.70	16.72	31.53
^{2}J (^{31}P-1) (Hz)	19.6	20.6	24.1
^{2}J (^{31}P-2) (Hz)	17.6	14.1	NA
^{2}J (1-2)	5.9	6.1	NA

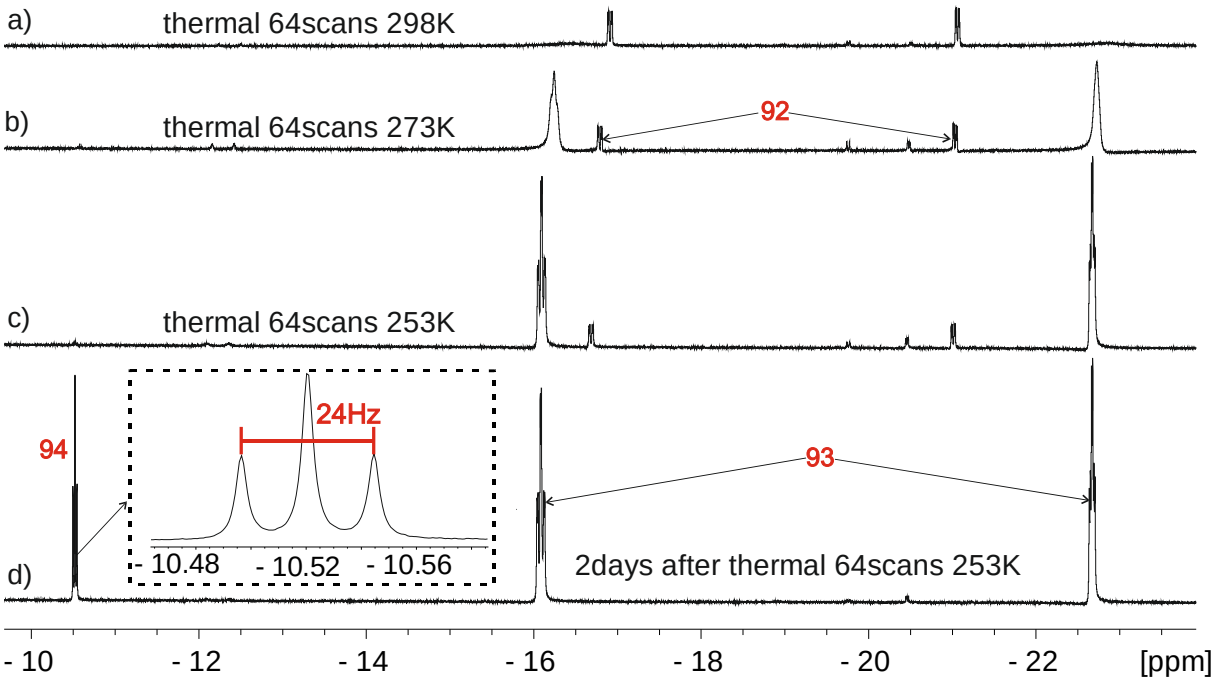

Figure 5.23: Series of ^{1}H NMR spectra showing the hydride region of a sample containing 3 mg (11.9 mM) of $IrCl(DMSO)_3$ (**III**) and 2 eq. (2.5 mg) of **44** in 0.6 mL of toluene-d_8 under H_2. a) Thermal ^{1}H NMR spectrum recorded at 298 K showing only **92** and broad features for **93**. b) Analogous NMR spectrum

to (a) but at 273 K. c) Analogous NMR spectrum at 253 K. d) Analogous 253 K NMR spectrum after two days at 298 K before cooling reveals the consumption of **92** and formation of **94** alongside **93**.

5.8.1 Securing the identity of 94

In an effort to improve the characterisation of **94** a sample of IrCl(COD)PCy_3 (**IV**) was prepared. 2.5mg of **IV** was then exposed to 1.5 eq. of **44** in toluene-d_8. The result $^{31}P\{^1H\}$ NMR spectrum yielded a strong signal for **IV** at 14.75 ppm alongside a signal for free **44** at 9.8 ppm. No reaction products were evident. The addition of H_2 to this solution at 298 K caused an immediate reaction, which was viewed at 253 K by NMR spectroscopy (Figure 5.24.a). The hydride region shows the presence of many species that contain both H_2 and phosphine. No signals for **94** were detected. This complex reactivity is not unexpected and this reaction has been examined previously by Vrieze *et al*.[251, 252]. They reported the partial dehydrogenation of PCy_3 to create the $PCy_2(\eta^2\text{-}C_6H_9)$ ligand.

1 µL of DMSO was then added to this sample and an NMR spectrum was recorded immediately at 253K (Figure 4.24.b). Signals indicative of the formation of **92**, **93** and **94** were immediately evident. These species were present in the ratio 0.07 : 1 : 0.35 respectively. It is therefore notable that all these three complexes contain DMSO.

When this reaction was examined in dichloromethane similar behaviour was found.

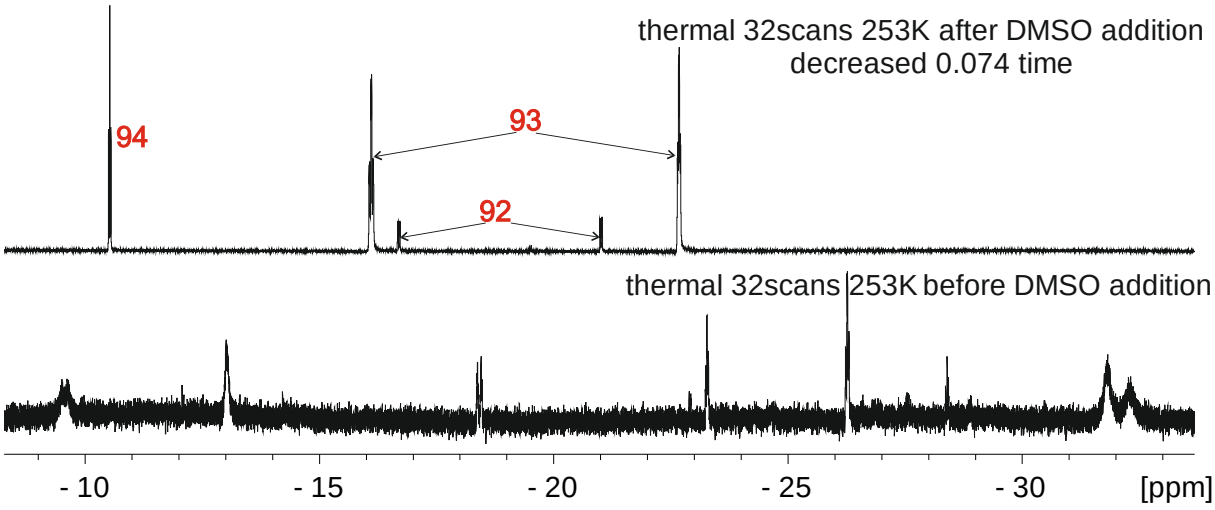

Figure 5.24: NMR spectra confirming DMSO is a requirement for the detection of **94.** 2.5mg of IrCl(COD)PCy_3 (**IV**) and 1.5 eq. of PCy_3 (**44**) were combined in toluene-d_8 presence of H_2. a) The ^1H NMR at 253 K prior to DMSO addition confirms many hydride complexes form. b) Addition of 1 µL of DMSO leads to their conversion to an equilibrium mixture **92**, **93** and **94**.

5.9 Conclusions

The reaction of eight aromatic and non-aromatic phosphines with $IrCl(DMSO)_3$ (**III**) and H_2 has been studied in this chapter. The selected phosphines differ in size and electronegativity. Two major observations were made. Firstly, these ligands have the ability to displace DMSO from **III** and that leads to an array of 16 electron *mono* and *bis* phosphine substitution products. Secondly, C-H bond activation of the bound phosphine is common, which means these 16-electron complexes are in equilibrium with their orthometallation products. The reversibility of the C-H bond activation step was demonstrated through the reaction of these species with H_2, which proceeds in all cases. It was found that warming the sample accelerated this process.

Reaction of the equilibrium concentrations of the 16 electron phosphine-containing complexes led rapidly to the formation of these dihydride products. Depending on the phosphine employed, substitution of DMSO by the phosphine could be slow or fast. When slow, H_2 proved to add to **III** and form two isomers of $IrCl(H)_2(DMSO)_3$. These later products are also seen when there is a large excess of **III** compared to phosphine.

Phosphines **45**, **46**, **48** and **49** exhibit similar reactivity to H_2. Their Tolman parameters suggest they all have similar electron donating character (ν_{co} = 2068 cm^{-1}) and slight different cone angles.

58, **62**, **59** and **60** are analogues of **79**, **80**, **81** and **82**, analogues to **83**, **84**, **85** and **86** and analogues to **75**, **76**, **77** and **78**. Just after H_2 addition, all first three listed complexes are present alongside with C-H activations products in the hydride region of the ^1H NMR spectrum. The second spectrum recorded in the following minutes reveals slow conversion of complex **81** to the isomer **82**, **85** to the isomer **86**, **77** to the isomer **78** and **59** to the isomer **60**, which are the most stable. **79**, **80** and **82**; **83**, **84** and **86**; **75**, **77** and **78** and finally **58**, **62** and **60** are the thermodynamics product that are stable for days.

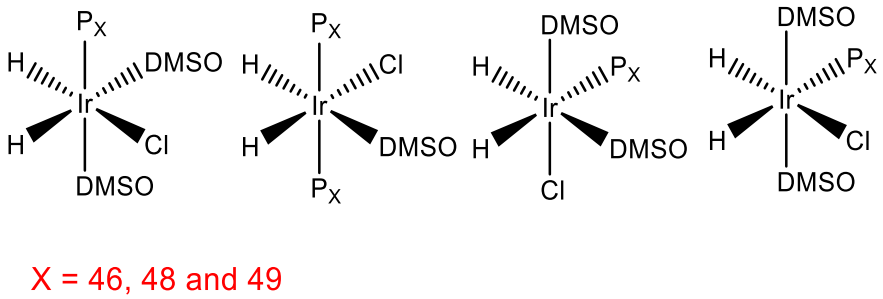

Scheme 5.3: Dihydrides products formed when **III** reacts with H_2 and a phosphine ligand P_X where X = **48**, **46** or **49**

The non-aromatic phosphine **44** does not form a C-H bond activation product following reaction with **III**. Upon reaction with H_2 though the outcome depends on the excess of **44**. If the reaction between **44** and **III** is equimolar, *mono*-phosphine **92** dominates whereas with an excess of **44** the formation of highly reactive **93** occurs. This species undergoes very rapid H_2 loss, which is slowed at low temperature. Slow equilibration to form the *trans*-hydride product **94** is suggested at longer reaction times.

47 is the bulkiest (Θ = 194°) phosphine of the series. It is therefore expected that due to steric constraints **47** undergoes *mono*-substitution of DMSO, yielding **88**. **47** has three methyl electron donating groups yielding a slightly different electronegativity with others phosphine (ν_{co} = 2066 cm^{-1}).

In contrast, **51** displaces all three DMSO yielding the single product **87**, due to its small size. In the series of phosphines presented, **51** has one of the smallest cone angle (136°). It is therefore expected to bind more ligands on the metal. In term of electron donating properties (ν_{co} = 2067.0 cm^{-1}) it is very similar to phosphine **47**.

50 shows an unusual behaviour. Its reaction with **III** is very slow when equimolar of the two reactants are used. However, when an excess of **50** is used, the *tris*-phosphine C-H bond activation product **69** alongside with the *bis*-phosphine **89** and **90** are formed. **50** has the smallest cone angle (130°) and the largest electronegativity (ν_{co} is 2085.3 cm^{-1}) in range of phosphine studied so far. According to the cone angle it is expected to trigger more DMSO substitution and the large electronegativity more charge transfer to the metal, thus stabilising the Ir(III) in the high oxidation state.

Clearly, therefore, these eight phosphines react differently with **III** and H_2. These differences and similarities are linked to the electronic properties of the phosphine. Now that the products present in these systems have been identified, their reactivity towards *p*-H_2 can be authoritatively explored, which will be the focus of the next chapter.

Chapter 6: Hyperpolarised reactions of Iridium phosphine complexes

6.1 Introduction

In this chapter, *p*-H_2 enhanced NMR is used to monitor the complexes formed during the reactions of the eight phosphines (P_x) in chapter 5, Figure 5.1 with $IrCl(DMSO)_3$ (**III**). This sixth chapter is therefore a continuation of the fifth chapter where these reactions were described through studies with normal H_2 gas and the corresponding thermodynamic and kinetic products identified. The motivation of studying these hyperpolarisation reactions at high field was driven by the possibility of subsequently detecting these hyperpolarised species using ultra low field NMR devices. Consequently, the product signals are optimised for reaction temperature, solvent and ligand excess. Furthermore, the mechanism of dihydrogen dissociation is determined as it should correlate with signal enhancement. The hyperpolarisation level and lifetime of these products are important factors that are rationalised and used to define the experiments that will subsequently be carried out in the Earth's magnetic field.

For low field ^1H study there is a need for a large heteronuclear coupling to break the magnetic equivalence of the hydrides. The nature of the hydride-phosphorus couplings are therefore important. For example, a *cis* hydride-phosphorus coupling is around 20 Hz, whilst a *trans* hydride-phosphorus coupling is approximately 150 Hz, both of which could provide access to PHIP enhanced Earth's field NMR spectra. Combining high hyperpolarisation levels with large heteronuclear couplings will therefore allow ultra-low field NMR detection. Indeed, in the low field regime, where strong coupling prevails the heteronuclei couplings are the only available information due to the vanishingly small chemical shifts differences. It is therefore necessary to study and optimise the hyperpolarisation conditions at high field before attempting observation in the Earth's field.

In addition, the aim is to reveal with *p*-H_2 any additional species that were invisible thermally due to their low concentration. This is well illustrated in the literature where similar techniques have been used to detect reaction intermediate. For example, in 1999 by Joost Lohman et al.[253] showed that a series of complexes of the form $RhX(CO)(PR_3)_2$ [X = Cl, Br or I; R = Me or Ph] react with H_2 to form a series of binuclear complexes of the type $(PR_3)_2H_2Rh(\mu\text{-}X)_2Rh(CO)(PR_3)$. They described how PHIP allows the mapping of this previously unseen reaction and therefore enables the complexity of a hydrogen reaction system to be fully appreciated. Similarly, Richard Eisenberg and co-workers[254] have used *p*-H_2 to detect low concentration products of reaction of $[RhCl(PPh_3)_2]_2$ with *p*-H_2, which showed that the binuclear di-hydride $[Rh(H)_2(PPh_3)_2(\mu\text{-}Cl)_2Rh(PPh_3)_2]$ and the tetrahydride complex $[Rh(H)_2(PPh_3)_2(\mu\text{-}Cl)]_2$ are readily formed. Magnetisation transfer methods were used to demonstrate the importance of these complexes during alkene hydrogenation. Martin Partridge et al.[255] have also used *p*-H_2 hyperpolarisation to detect a minor *cis-cis-cis* isomer of $Ru(CO)_2(H)_2L_2$ (L = PMe_3, PMe_2Ph, and $AsMe_2Ph$). Such methods offer therefore an exciting opportunity for low-field NMR to see normally invisible species.

6.2. Hyperpolarisation of tris-phenyl phosphine 45 using $IrCl(DMSO)_3$ in toluene

In this first examination with **45** a single equivalent of phosphine is used relative to iridium. This involved the study of the reaction of (2.5 mg) 8.6 mM of $IrCl(DMSO)_3$ (**III**) and (1 eq.) 1 mg of tris-phenyl phosphine (**45**) in 0.6 mL of toluene-d_8, which was monitored following addition of 3 bar of *p*-H_2. Recalling chapter 4, section 4.1, a PHIP (PASADENA) type experiment is recorded by shaking the NMR tube at the Earth's magnetic field for 3 sec and subsequently transferring it in the magnet where a $\pi/4$ pulse is applied. Five sequential PHIP ^{1}H NMR experiment were pre-set on the spectrometer. The sample was shaken, then introduced into the spectrometer and measurement commenced. The resulting, first, hyperpolarised ^{1}H NMR spectrum revealed huge hyperpolarised responses (SNR = 5775) for the *mono*-phosphine **59** and the *bis*-phosphine **62** at -10.94 and -20.25 ppm and -14.30 and -20.12 ppm. A weaker response for the hydride ligands of the *mono*-phosphine **58** was seen at -15.50 and -19.64 ppm (Figure 6.1.a). These three species therefore form on a suitable time scale that allows for observable polarisation but the *p*-H_2 is destroyed quickly and the signal gain remains visible for just 10 sec. In Chapter 5, **59** and **58** were proposed to form from **55**, whilst **53**, **56** and **57** were in equilibrium and proposed to form **62**.

Upon refilling the sample with fresh *p*-H_2 and repeating the experiment, only signals for **58** and **62** were detected through their hyperpolarised response (Figure 6.1.b). The signals for **62** are slightly larger in signal intensity in this measurement when compared to those of **58**. However, upon repeating this process they repolarised with the same relative intensity. This suggests that **59** rearranges to **58** thermally, and that both **58** and **62** add H_2 reversibly. Therefore, it will not be possible to observe the short lifetime product **59** at the Earth's magnetic field where many signals averaging are needed.

In the organic region of these ^{1}H NMR spectra, negative hyperpolarised signals are seen for free DMSO at 1.74 ppm and the bound DMSO at 2.37, 2.95 and 2.98 ppm. The polarisation transfer to DMSO is explained by the SABRE mechanism. Therefore, this free DMSO signal would be maximal if π/2 pulse was used.

In conclusion, the reaction of **III** and **45** leads to the formation of the *mono*-phosphine **58** and the *bis*-phosphine **62**. They are both detectable through strongly polarised hydride ligand signals that can be observed by flushing fresh *p*-H_2 into the sample and recording its PHIP NMR signal. This process can be repeated multiple times over a period of days. It is interesting to note that **59** is only observed in the first of these PHIP measurements due to its rapid conversion into the other materials. In addition, though to the polarised hydride ligand signals, a number of resonances in the organic reaction of these NMR spectra exhibit SABRE. These are due to the polarisation transfer from the hydride ligands to the DMSO ligand and indicate a continuous exchange of ligands.

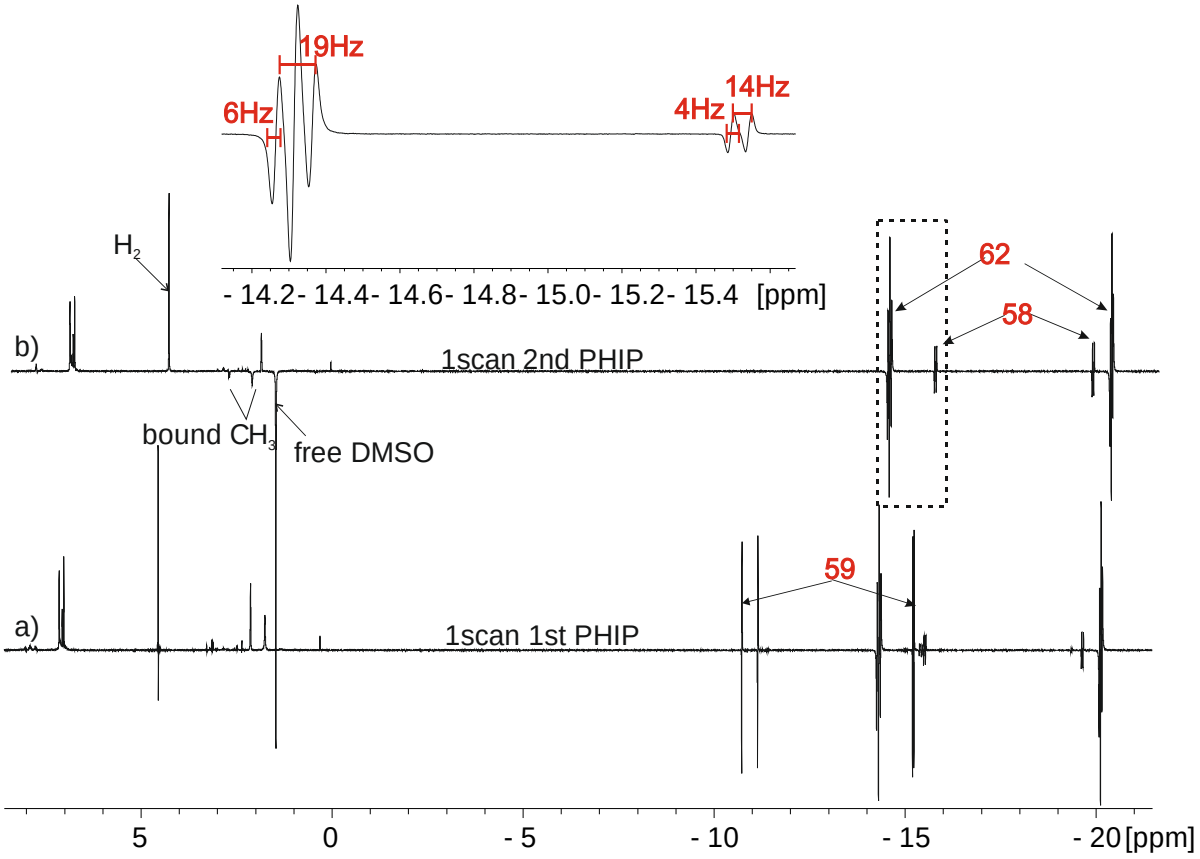

Figure 6.1: Sample of 8.6 mM of $IrCl(DMSO)_3$ (**III**) and (1 eq.) of **45** in 0.6 mL of toluene-d_8 was used to record two ^1H PHIP NMR spectra at 298 K with 1 scan. a) First PHIP reaction with 3 bar of *p*-H_2 showing hyperpolarised antiphase signal for **59**, **58** and **62**. b) 2nd PHIP reaction after the sample was refilled with fresh *p*-H_2 that show now hyperpolarised signals for only **58** and **62**, and free and bound DMSO. A zoom of the hydride region highlights the ^1H-^1H and ^1H-^{31}P coupling for **58** and **62**.

6.2.1 Magnetisation transfer from hydrides to ^{31}P

A test to look for SABRE hyperpolarisation transfer to ^{31}P was also performed. The NMR tube was filled with 3 bar of *p*-H_2, and shaken for 5 s in the Earth's magnetic field (~50 μT). A $^{31}P\{^1H\}$ NMR SABRE acquisition was then completed and ^{31}P signals for both **58** and **62** were seen at 5.01 ppm and 9.18 ppm, respectively (Figure 6.2.a). The $^{31}P\{^1H\}$ signal enhancement for the resonance in **58** is weaker than that for **62**, which is in agreement with the level of ^1H hyperpolarisation.

Two types of data set were collected with ^1H-decoupled measurements to probe this behaviour. The decoupler centre was first located at the middle of the hydride resonances ~ -15 ppm and then -4 ppm, which places it midway between the hydride and aryl phosphine signals. These two experiments resulted in similar type of spectra and the first method in Figure 6.3 was arbitrary chosen to be presented.

It is notable that when the sample is shaken in the μ-metal shield a stronger SABRE enhancement is observed for both ^{31}P signals (Figure 6.2.b). This suggests that direct rather than relayed transfer of polarisation from the hydride ligands to ^{31}P is optimal[118]. The antiphase shape of the hyperpolarised ^{31}P signal suggests that heteronuclear $2I_yS_z$ type magnetisation is created in the experiments carried

out at the Earth's magnetic field[106]. However, the in-phase shape of the **62** signal recorded with the mu-shield is consistent with an in-phase type magnetisation term, e.g. I_y [106].

It is worth noting however that in 2015, Igor V. Koptyug et al.[229] demonstrated that magnetisation can also be transferred to the phosphine ligand. In this study, it was shown in similar complex $IrCl(H)_2(PPh_3)_3$ that efficient hyperpolarisation transfer occurs from *p*-H_2 to both ^{31}P and ^{1}H nuclei at 60°C and 80°C at a micro-Tesla field of 1 µT and 0.1 µT. They also showed that a hydride dissociation rate between 3.5 and 5.3 s^{-1} provided best polarisation transfer to ^{31}P nuclei. They showed that the lifetime of both H_2 and PPh_3 in the bound state is on the order of hundreds of millisecond. In the next sections, the hydride dissociation rate will be measured and H_2 addition mechanism investigated in order to establish a better understanding of these complexes.

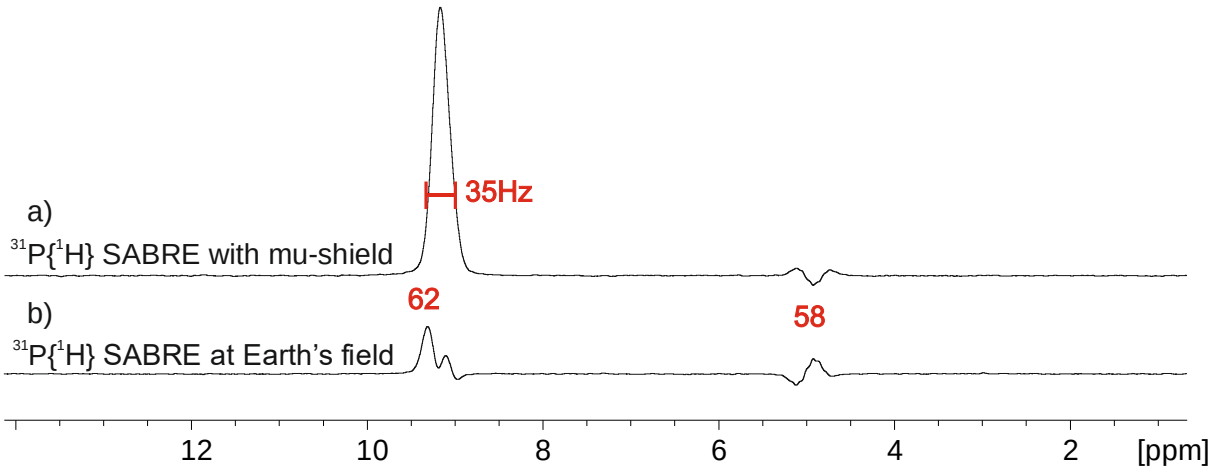

Figure 6.2: $^{31}P\{^{1}H\}$ SABRE NMR experiments on a sample of 8.6 mM of $IrCl(DMSO)_3$ (**III**) and 1 eq. of **45** in 0.6 mL of toluene-d_8 at 298 K. a) After shaking in a mu-shield for 5 s and b) at shaking in the Earth's field for 5 s.

6.2.2 Kinetics and *p*-H_2 addition mechanism

The rate of H_2 loss was assessed for the two complexes **62** and **58** by EXSY[256, 257, 258]. The hydride dissociation rates for **62** and **58** proved to be 3.72 ± 0.01 s^{-1} and 0.10 ± 0.01 s^{-1} respectively. In the corresponding thermal NMR spectrum, the ratio of **62** to **58** proved to be 1 : 0.75. The relative rates of H_2 loss therefore link to the flux of H_2 through the system and potential signal gain according to the product of their concentrations and exchange rate. In this case, this suggests that the hydride ligand signals should appear in the hyperpolarised spectrum in an 1 : 0.16 ratio neglecting relaxation, which is consistent to the ratio measured.

The level of ^{31}P polarisation should be linked to the hydride polarisation level, the H-H coupling and the reciprocal of the propagating coupling. A dissociation rate of between 3.5 and 5 s^{-1} has been suggested by Igor V. Koptyug et al. to be optimal[229, 257]. Thus, a dissociation rate of 0.10 ± 0.01 s^{-1} is likely to be too slow for optimal transfer. Based on these results, the prediction that **62** can likely be detected using the EF NMR device can be made whereas **58** is unlikely to be observed.

The procedure for unveiling the mechanism of H_2 exchange in such complexes is to sequentially increase the concentration of one of the ligands (Cl^-, DMSO or H_2) and then measure the rate of H_2

loss. If the rate decreases with the increase of the varied ligand concentration, then H_2 exchange is preceded by dissociation of this ligand. This method was tested for DMSO. Four dissociation rates were measured where 5, 10, 15 and 50 equivalents of DMSO were present. The corresponding H_2 dissociation rates were 1.06 ± 0.06 s^{-1}, 0.710 ± 0.002 s^{-1}, 0.570 ± 0.004 s^{-1} and 0.25 ± 0.16 s^{-1} for each of these additions, which clearly show a decrease in $k_{diss}(H_2)$ across the series (Table 6.1). Hence, the mechanism for H_2 loss is dissociative and preceded by DMSO dissociation. Figure 6.3 shows the proposed mechanism. All of the species formed in this mechanism are neutral, which is consistent with the use of toluene as solvent.

Table 6.1: sample of (2.5 mg) 8.6 mM of $IrCl(DMSO)_3$ (**III**) and (1 eq.) 1 mg of **45** in 0.6 mL of toluene-d_8 dissociation rate of H_2 in function of the amount of DMSO added to the sample. The EXSY measurements were performed on complex **62**.

DMSO concentration Added equivalence	**0**	**5**	**10**	**15**	**50**
68 (H_2) (s^{-1}) (at **298 K**)	3.72 ± 0.01	1.06 ± 0.06	0.710 ±0.002	0.570 ±0.004	0.25 ± 0.16

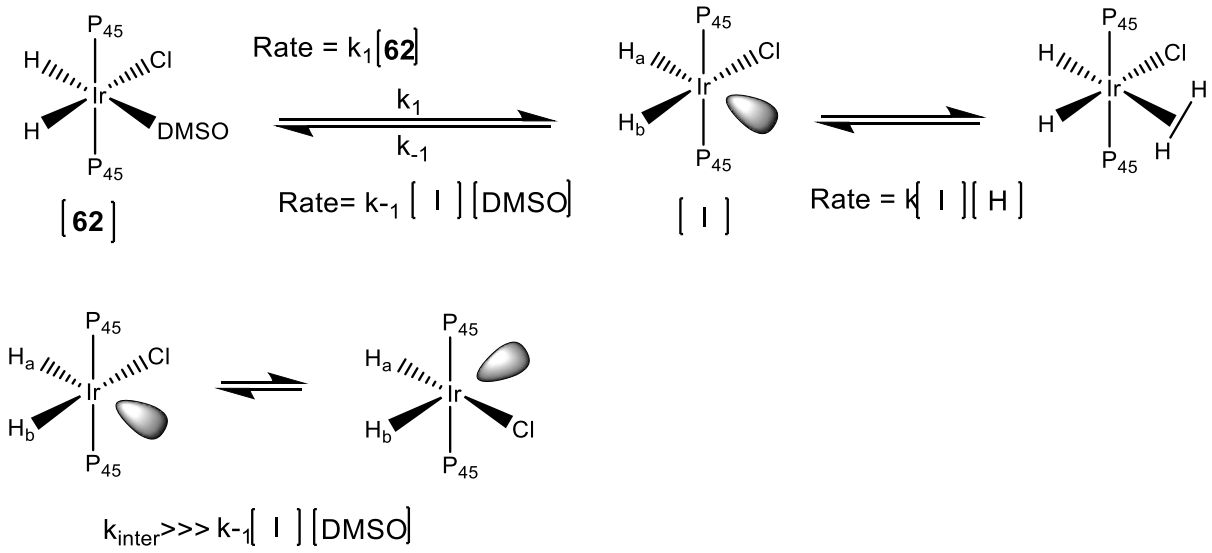

Figure 6.3: The dihydride dissociation mechanism in $IrCl(H)_2(PPh_3)_2(DMSO)$ complex is sketched where the DMSO dissociation leading the intermediary I with a vacant site allows subsequent H_2 association.

In conclusion, the three complexes **59**, **58**, and **62** provide high hyperpolarised hydride signals that may be visible at low field. As already stated, **58** and **62** are thermodynamic products whereas **59** is kinetic product that disappears very rapidly. It is therefore expected to detect with the Earth's NMR devices the only stable products with optimal hydride dissociation rate. The main characteristic of these three complexes is they all have a DMSO ligand *trans* to hydride.

6.2.3 Hyperpolarisation with an excess of 45

In this second experiment, 3 equivalents of **45** were used relative to iridium. This is due to the fact that in chapter 5, section 5.3.3, when $IrCl(DMSO)_3$ (**III**) and (3 eq.) of **45** was dissolved in 0.6 mL of

toluene-d_8 and reacted with H_2, the thermal ^{1}H NMR spectrum showed two set of hydride resonances at -10.65 and -20.47 ppm for $IrCl(H)_2(P_{45})_3$ **66**. When such a reaction is now performed with *p*-H_2, the ^{1}H NMR PHIP spectrum shows additional weak antiphase hydride signals for **62** (Figure 6.4). This species was not detected under these conditions in the absence of hyperpolarisation (section 5.3.3) due to its very low concentration. *p*-H_2 has therefore allowed the detection of a low concentration species. **66** has previously been proven to react with *p*-H_2 and magnetisation was transferred to ^{31}P nuclei[229].

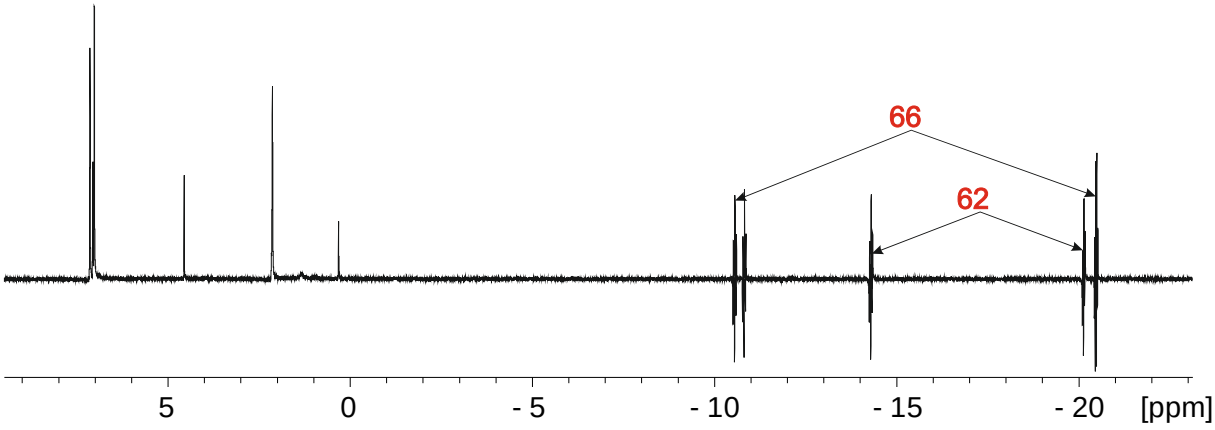

Figure 6.4: Single scan ^{1}H NMR spectrum of a sample of $IrCl(DMSO)_3$ (**III**) with 3 eq. of **45** in toluene-d_8 under *p*-H_2 showing hyperpolarised hydride ligand signals for **62** and **66**.

A hyperpolarised $^{31}P\{^1H\} - ^1H\{^{31}P\}$ HMQC experiment was used to confirm this assignment (Figure 6.5). ^{31}P signals for **66** are seen at -3.00 and 15.93 ppm along with a signal for **62** at 9.18 ppm.

To conclude, employing an excess of **45** yields the formation of a new *tris*-substituted phosphine complex **66** in addition to **62**, that both weakly hyperpolarise with *p*-H_2. However, the hydride signal enhancements are now too weak with the apparent poor SNR of the hyperpolarised spectrum, to be detected at the Earth's magnetic field at 298 K.

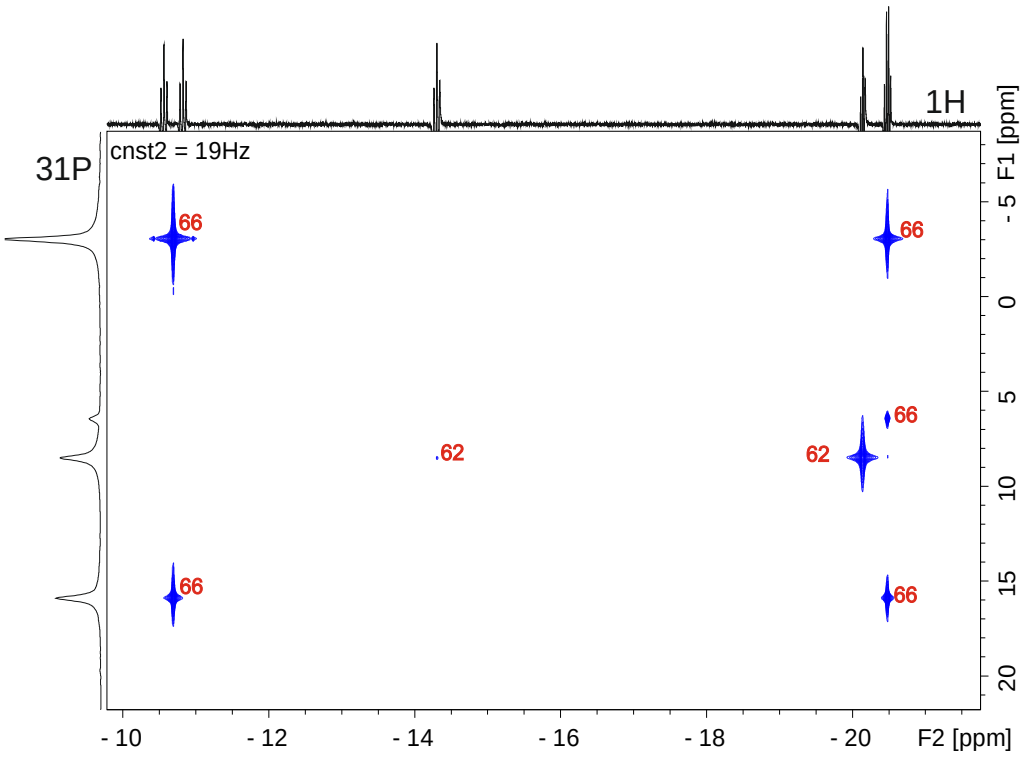

Figure 6.5: HMQC-PHIP $^{31}P\{^{1}H\}$ – ^{1}H NMR correlation spectrum recorded at 298 K with two scans for a sample of $IrCl(DMSO)_3$ (**III**) and (3 eq.) of **45** in 0.6 mL of toluene-d_8 showing **66** with the two axial ^{31}P resonance is located at -3.00 ppm whereas the equatorial ^{31}P is at 15.93 ppm. The presence of the ^{31}P resonance of **62** is also observed.

6.3 Modification of 45: introducing a linker between phosphorus and the aromatics

The phosphines **49** and **50** were also examined. Phosphine **49**, ($P(CH_2Ph)_3$) has an CH_2 spacer between the Ph group and phosphorus centre, while phosphine **50** ($P(OCH_2Ph)_3$) has an oxygen spacer. Consequently, these differences should influence the dynamics of ligand exchange in any metal complexes they form. As ligand exchange rates control the size of the PHIP response a different behaviour is expected. A system with optimal exchange at ambient temperatures as the experiment cell EF NMR has a limited temperature window is needed.

6.3.1 Tris-benzyl Phosphine 49: methyl linker

For **49**, an 8.6 mM (2.5 mg) sample of $IrCl(DMSO)_3$ (**III**) containing 1 eq. of phosphine was dissolved in toluene-d_8 and 3 bar of p-H_2 added. Ten single scan ^{1}H-PHIP NMR measurements were then made, one after the other, at 298 K. These revealed enhanced antiphase hydride signals for **84** $Ir(H)_2Cl(DMSO)(P_{49})_2$ (Figure 6.6.a). Interestingly, the level of signal enhancement proved to increase with reaction time instead of decrease. This would suggest **84** forms slowly, and then undergoes H_2 exchange.

Upon warming, to 308 K (Figure 6.6.b and c respectively) a significant increase in the hydride signal intensity levels for **84** was observed, but these were now augmented by those of a second species, **83** $Ir(H)_2Cl(DMSO)_2(P_{49})$ (section 5.5.3). Upon warming further to 313 K, whilst both of these species remained visible, the level of hydride signal enhancement did not increase further. Hence, no further experiments beyond 313 K were undertaken. Furthermore, the resulting PHIP polarisation proved observable for ~20 minutes. This indicates slow *p*-H_2 consumption and confirms the reversibility of H_2 addition.

EXSY experiments were then recorded to assess this exchange from **84** which, proved to have a rate of $5.8 \pm 1\ s^{-1}$ at 313 K, which lies in the optimal regime. Spatial proximity between the aromatic protons of the phosphine and the CH_3 protons of the DMSO to the hydride was also observed. Phosphine **83** is therefore not ideal for Earth's field NMR detection due to the higher than ambient temperature needed for optimal ligand exchange. However, atomic magnetometer detection (nano-Tesla regime) might be possible because the sample chamber is warm.

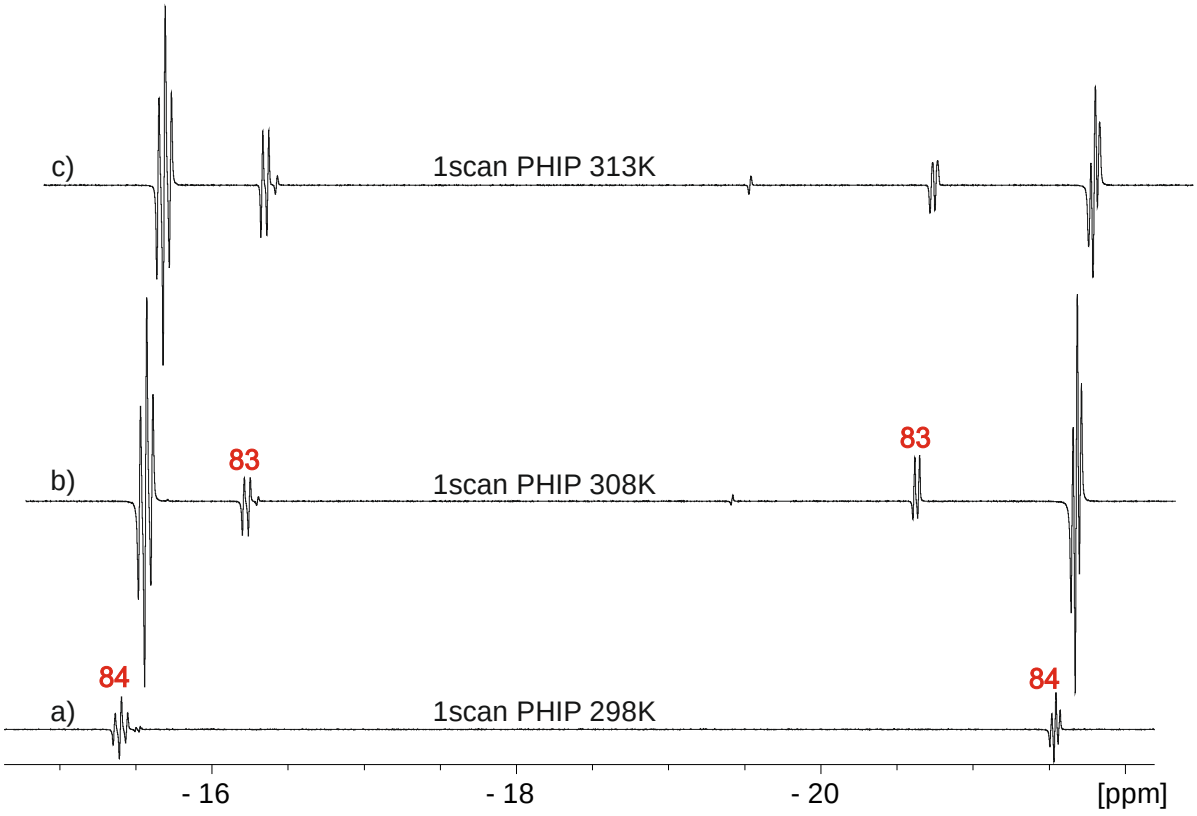

Figure 6.6: The hydride region of several PHIP enhanced single scan NMR spectra at different temperatures resulting from the reaction of 8.6 mM of $IrCl(DMSO)_3$ (**III**) and 1 eq. of **49** in 0.6 mL of toluene-d_8 with 3 bar of *p*-H_2. a) 298 K; signal for **84** only. b) 308 K; signals for **83** and **84** seen. c) 313 K; signals for **83** and **84** appear with reduced intensity relative to (b).

6.3.2 Triphenyl phosphite 50: oxygen linker

Triphenyl phosphite (**50**) was tested in a similar way as phosphine **49**. At 298 K, the resulting PHIP data revealed dominant hydride ligand signal gains for *mer*-$IrCl(H)_2(DMSO)_3$ at -16.33 and -19.31 ppm (Figure 6.7.a). However, when the PHIP reaction was performed at 333 K, huge hydride ligand signal enhancements were seen for two new complexes that were not visible thermally (chapter 5 section

5.7). These are identified as **95**, $IrCl(H)_2(DMSO)(P_{50})_2$, which yields a doublet of triplets located at -16.60 ppm with two *cis*-J(HP) splitting of 21.95 Hz and a signal at -20.10 ppm where *cis*-J(HP) is 21.12 Hz. In contrast, **96** $IrCl(H)_2(DMSO)_2(P_{50})$, yields a doublet of doublets at -16.60 ppm which overlaps with the **95** triplet, and a further signal at -19.64 ppm with a *cis*-J(HP) splitting of 22.84 Hz. These species are direct analogues to **62** and **58**. Weaker hydride signals are evident for **89**, identified in section 5.7. These PHIP enhanced magnetisations are observable for several hours, even at 333 K, so the H_2 exchange rates must be slow otherwise the *p*-H_2 effect would vanish quickly.

Hence while **50** is not suited for Earth's field NMR detection at room temperature, **95** and **96** could possibly be detected in the *nano* Tesla regime using an atomic magnetometer at elevated temperatures.

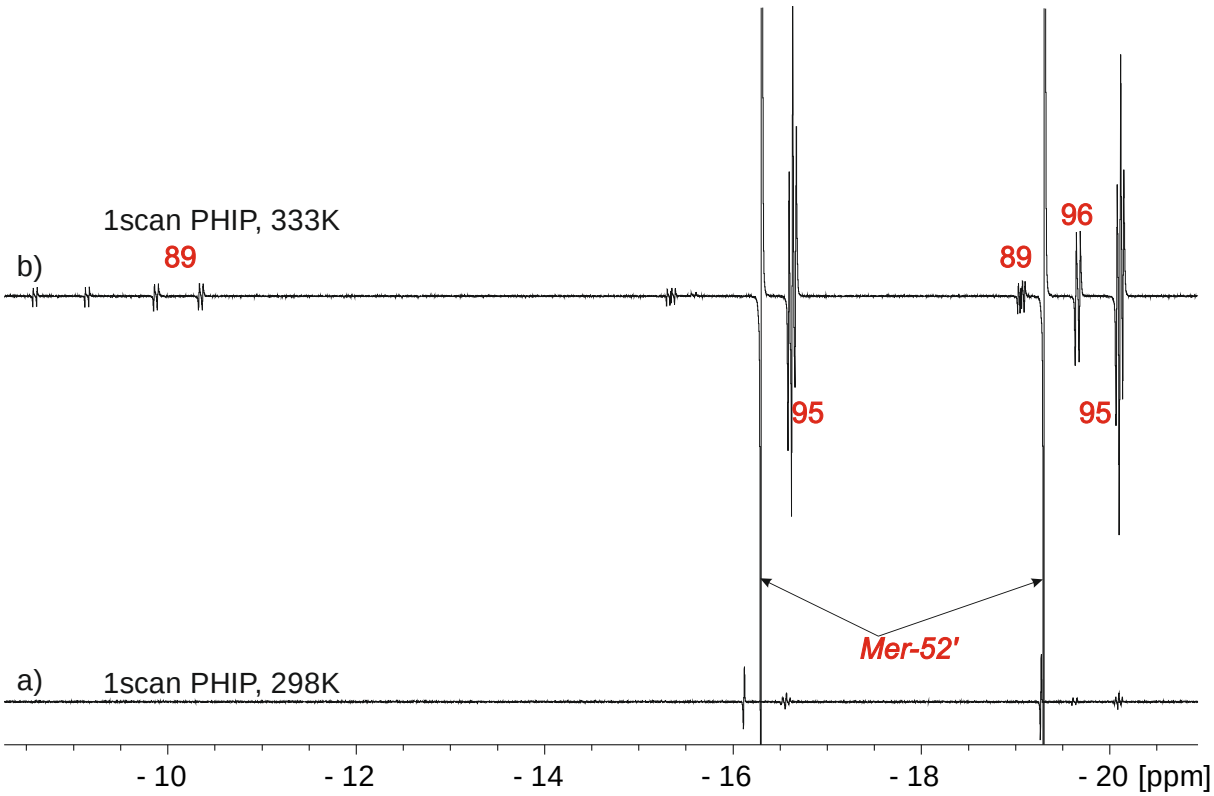

Figure 6.7: Enhanced PHIP ^1H NMR spectra from a sample of 8.6 mM of $IrCl(DMSO)_3$ (**III**) and 1 eq. **50** toluene-d_8 under *p*-H_2. a) Hydride region of a spectrum at 298 K showing weak enhancement of *mer*-$IrCl(H)_2(DMSO)_3$ and **95** hydrides. b) Hydride region of a spectrum at 333 K showing strong enhancement of *mer*-$IrCl(H)_2(DMSO)_3$, **95** and **96** hydrides. Additional weak signal enhancement of **89** is also observed in this spectrum.

These measurements with **49** and **50** have demonstrated that variations in the phosphine impact on the PHIP enhancement levels, the temperature of the optimal response and speciation. In the next section, several additional phosphines are considered.

6.4 Modification of 45: effect of substituents on the aromatic groups

6.4.1 Tris(4-methoxyphenyl) phosphine 48

Tris(4-methoxyphenyl) phosphine (**48**) was examined in a similar way using a sample consisting of ~7 mM $IrCl(DMSO)_3$ (**III**) and 1 eq. of **48** in toluene-d_8. A PHIP measurement was first made at 298 K (Figure 6.8). The resulting ^1H NMR spectrum proved to exhibit strong antiphase hydride resonances for **75** and **76** that are analogues of **58** and **62**. In addition, their hydride dissociation rates proved to be measurable as 0.120 ± 0.002 s^{-1} and 4.27 ± 0.03 s^{-1} respectively at 298 K.

In the thermally polarised NMR spectrum the ratio of **75** to **76** proved to be 1 : 0.38 whereas the corresponding PHIP enhanced signal ratio was 0.09 : 1. **76** therefore leads to a proportionally greater signal gain in agreement with the more rapid ligand exchange rate. The precise SNR of the hydride signals in the hyperpolarised spectrum (1 scan, rg = 1) is estimated in comparison to the thermal spectrum (128 scans, rg = 71.8). This later shows a SNR of 23 while the former have a SNR of 518, hence confirming massive hydride PHIP response.

These levels of hydride signals gain allowed the detection of ^{31}P transfer under SABRE (see section 6.6).

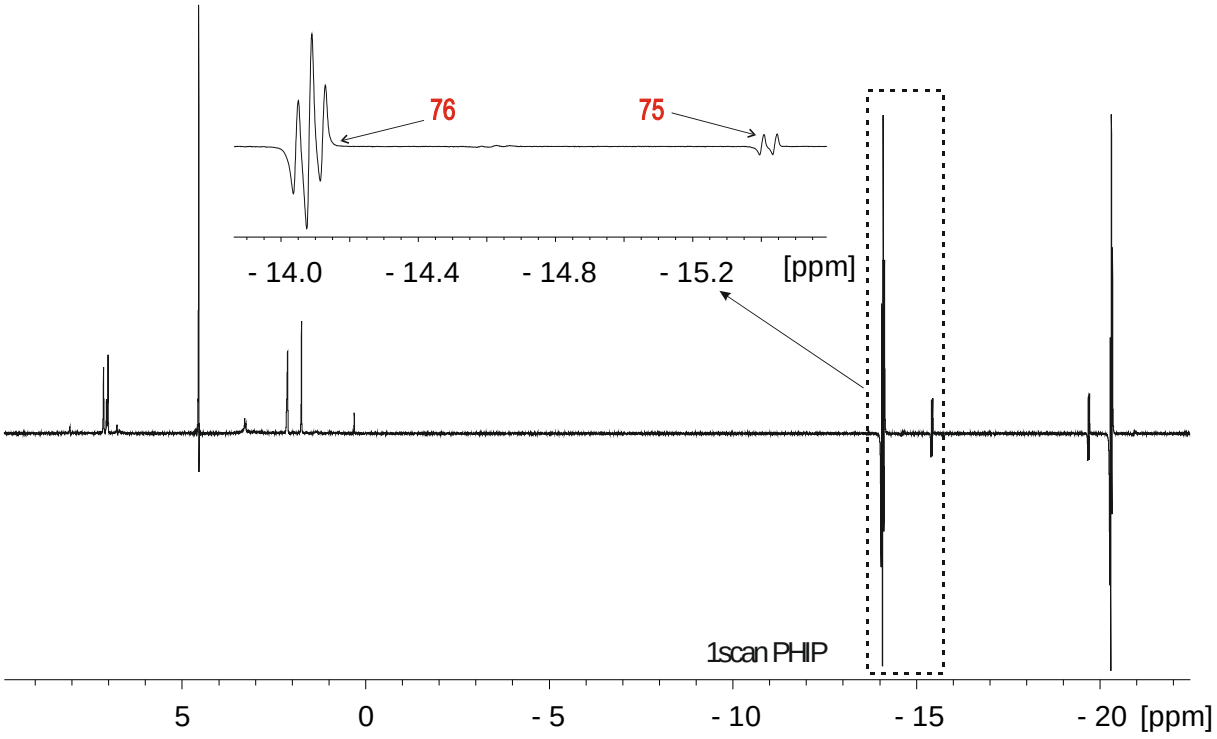

Figure 6.8: Enhanced PHIP ^1H NMR spectrum of a sample of 6.94 mM of $IrCl(DMSO)_3$ (**III**) and 1 eq. of **N** in toluene-d_8 reacted with p-H_2 for a ^1H PHIP experiment. High antiphase hydride enhancement is observed for both **75** and **76**.

6.4.2 Tris (p-tolyl) phosphine 47: effect of electron donating groups

The corresponding data for tris (*p*-tolyl) phosphine (**47**) at 298 K showed weakly polarised but exchange broadened hydride ligand signals for **88** (Figure 6.9). Consequently, the NMR probe was cooled to 273 K and the PHIP reaction re-examined. Similar levels of hydride ligand signal enhancement resulted to those seen at 298 K. The resonances themselves though appeared with different line widths and relative intensities. This is consistent with the EXSY data, which revealed the hydride ligand sites interchange positions at a rate of 23.6 ± 0.9 s^{-1} despite the fact H_2 loss has a rate of just 1.9 ± 0.3 s^{-1}. This electron rich phosphine is therefore not suitable for hyperpolarisation.

No magnetisation transfer to ^{31}P was observed, in accordance with the weak hydride signal enhancement.

47 is also the bulkiest phosphine on series, consequently the aryl groups are expected to clash with the equatorial hydride ligands, hence increasing their loss rate. However, a decrease to the hydride kinetics is observed, that might be influenced here by other parameters. It is also speculated that it surely sterically hinders hydride exchange as per the reduced kinetics noted. In conclusion, **88** is the complex that yields the weakest hydride signal enhancement and it provides the slowest dissociation rate of hydrides. These two factors are closely related for hyperpolarisation.

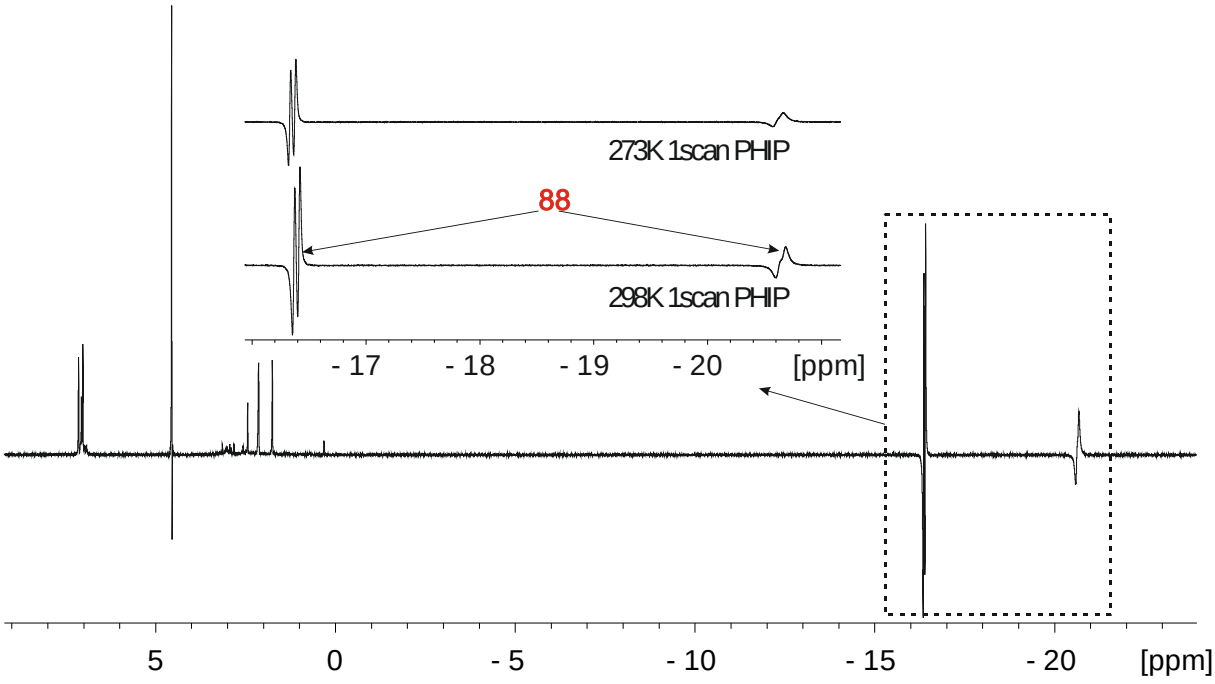

Figure 6.9: Enhanced PHIP ^1H NMR spectrum from a sample of 8.7 mM of $IrCl(DMSO)_3$ (**III**) and 1 eq. 1.1 mg of **47** in toluene-d_8 with 3 bar of *p*-H_2. A zoom on the hydride region shows a weak hydride signal enhancement of **88** at both 298 K and 273 K.

6.5 Hyperpolarisation of *tris*-cyclohexyl phosphine 44 using $IrCl(DMSO)_3$ (**III**) in toluene

In order to examine tris-cyclohexyl phosphine (**44**), a sample containing 0.5 eq. for an 8.6 mM loading of $IrCl(DMSO)_3$ (**III**) was prepared in toluene-d_8. The low phosphine excess was expected to result in the formation of $IrCl(H)_2(DMSO)_2(PCy_3)$, **92**, upon reaction with H_2. The resulting PHIP enhanced ^1H NMR spectrum at 298 K confirmed this as strong antiphase hydride ligand signals are seen for **92** (Figure 6.10). It should be noted that signals for the *fac* and *mer* isomers of $IrCl(H)_2(DMSO)_3$ were also seen. Comparison with a 1 scan thermally polarised spectrum allowed a PHIP enhancement value of 880 fold to be determined for **92**. **44** is therefore a good candidate for Earth's field NMR detection due to his high hydride signals enhancement, which is achieved at ambient temperature. Upon repeating this process with 2 eq. of **44** relative to **III** though no PHIP signal enhancements result despite the fact that signals for **92** remain visible in the thermally polarised ^1H NMR spectrum alongside those for **93** $IrCl(H)_2(DMSO)(PCy_3)_2$. For conclusion, **93** drives very rapid *p*-H_2 consumption preventing observable hyperpolarisation of **92**. Hence, a more selective route to **92** is desired.

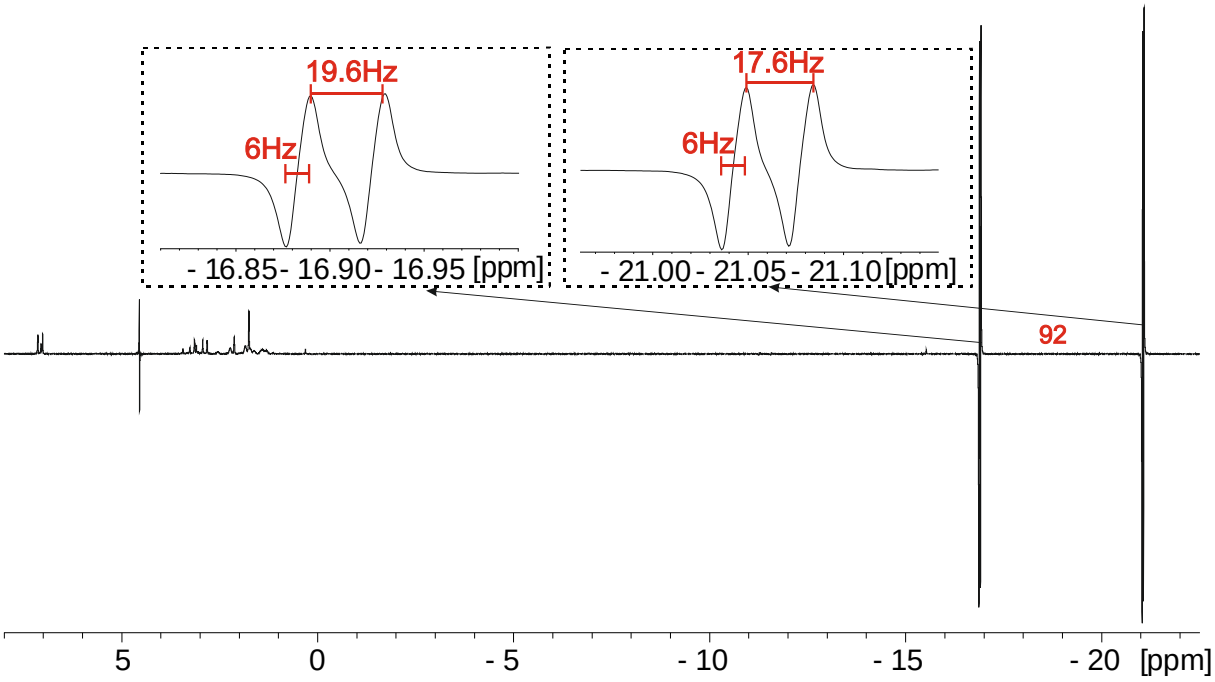

Figure 6.10: PHIP enhanced ^1H NMR spectrum obtained during the reaction of 8.6 mM of $IrCl(DMSO)_3$ (**III**) with 0.5 eq. of **J** in toluene-d_8 under 3 bar of *p*-H_2. Strong hydride ligand signals enhancements result for **92** at 298 K. The expanded regions highlight the clearly visible heteronuclear ^1H-^{31}P and the homonuclear ^1H-^1H couplings.

6.5.2 Using another precursor IrCl(COD)(PCy_3) (**IV**) in toluene and dichloromethane

A different way to create **92** proved to be to start with an iridium precursor that contained one PCy_3 (**44**) ligand. The necessary IrCl(COD)(PCy_3) (**IV**) was prepared according to the procedure described in (chapter 9, section 9.4.4). 0.54 mM (2 mg) of **IV** was then mixed with 5 eq. of DMSO in 0.6 mL of dichloromethane. The resulting PHIP study yielded a very large hydride signal enhancement of 2000 fold (~8 % polarisation) for **92**. However, the subsequent measurements revealed that the level of hyperpolarisation decayed to zero very rapidly in just 2 s. Each PHIP NMR scan last 2 s (Figure 6.12.a). The solvent was therefore changed to toluene, and twelve sequential PHIP experiments recorded. Similarly strongly hyperpolarised hydride signals were now visible in all of the 12 NMR measurements (Figure 6.12.b). Toluene therefore reflects a much better solvent for PHIP study with this ligand and for use in EF NMR detection. In addition, the first hyperpolarised PHIP spectra recorded with these two samples shows similar level of signal intensity (Figure 6.11 a and b). The initial rise observed in the first scan (Figure 6.11.b) is explained by the difference in temperature in the lab and inside the NMR probe, where the measurement take place. In fact, the lab has a temperature of 291-293 K whereas the spectrometer was set to 298 K. The sample therefore settles in this probe temperature which is optimal for hyperpolarisation.

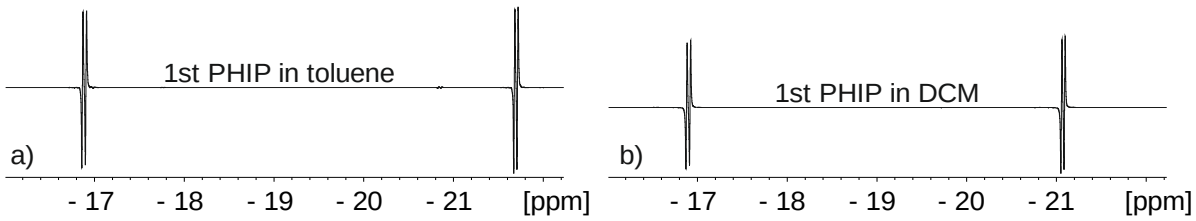

Figure 6.11: First PHIP enhanced hydride signals spectra of a series of sequential experiments recorded from a sample of a) 0.54 mM of IrCl(COD)(PCy_3) (**IV**) with 5 eq. of DMSO in 0.6 mL of toluene-d_8 and b) Similar sample was made in dichloromethane-d_2 showing both first spectrum have comparable signal intensity.

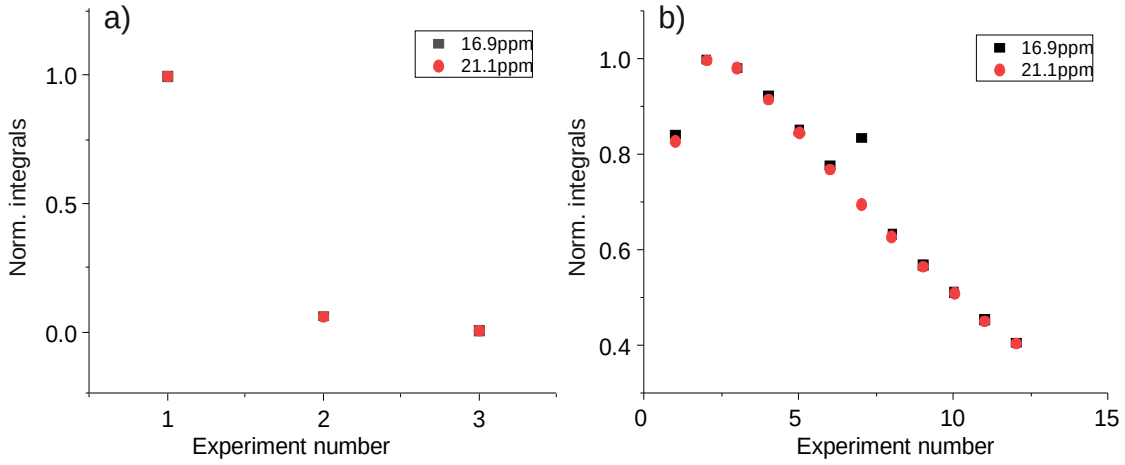

Figure 6.12: a) Normalised integrals of three sequential PHIP hydride signals recorded from a sample of 0.54 mM of IrCl(COD)(PCy_3) (**IV**) with 5 eq. of DMSO in 0.6 mL of dichloromethane showing the hyperpolarised hydride signals decaying to zero after the second scan. b) An equivalent sample in toluene produced enhanced hydride signal integrals that persisted after the twelves scan.

6.5.3 Kinetics and *p*-H_2 addition mechanism using the precursor IrCl(COD)(PCy_3) (**IV**)

Understanding the mechanism of H_2 addition is essential for improving the hyperpolarisation reaction. The same approach described previously for **45** with **III** in section 6.2.3 was therefore applied. This involved taking a dichloromethane solution of 0.54 mM **IV** and successively adding 5 eq., 10 eq. and finally 15 eq. of DMSO. At each stage, EXSY was used to probe the rate of dihydrogen loss at 298 K. The results are reported in table 6.2. A decrease in H_2 loss rate is observed as the concentration of DMSO increases. This suggests that the mechanism of H_2 loss is dissociative and happens after the dissociation of DMSO. Figure 6.13 shows the proposed mechanism for this. DMSO loss is slow compared to trapping of the resulting intermediate with H_2. The rate determining step is therefore independent of the concentration H_2. It should be noted that all of the species formed in this mechanism are neutral and this is favoured in low polarity dichloromethane. It has also to be noted that this mechanistic measurement carried in dichloromethane was at the beginning of the phosphines studies; before it was determined that toluene was better for PHIP.

Table 6.2: H_2 dissociation rate at 298 K as function of DMSO concentration

DMSO concentration Added equivalence	**5**	**10**	**15**
k(H_2) (s^{-1}) (298 K)	3.23 ± 0.01	1.033 ± 0.002	0.662 ± 0.002

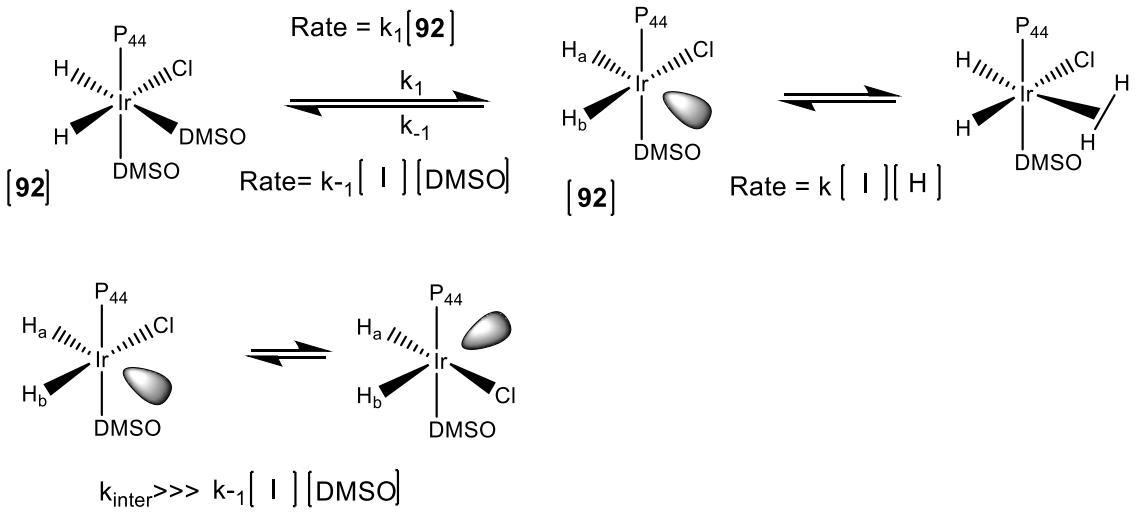

Figure 6.13: Proposed mechanism of H_2 dissociation in **92** $IrCl(H)_2(DMSO)_2(P_{44})$. The H_2 addition is preceded by dissociative loss of DMSO a vacant site on the intermediate **I**. In the intermediate, there is an interconversion between the chloride and the vacant site.

6.6 Hyperpolarisation of 46 using $IrCl(DMSO)_3$ (**III**)

In this final study, 1 eq. of di-cyclohexyl phenyl phosphine (**46**) was examined with 17.2 mM of $IrCl(DMSO)_3$ (**III**) in toluene-d_8. 3 bar of *p*-H_2 was added and a PHIP enhanced ^1H NMR spectrum was recorded immediately at 298 K (Figure 6.14). This yielded strong antiphase hydride ligand signals for **79** *cis*-$IrCl(H)_2(DMSO)_2(PPhCy_2)$, **80** *cis,cis*-$IrCl(H)_2(DMSO)(PPhCy_2)_2$ and **81** *trans*-$IrCl(H)_2(DMSO)(PPhCy_2)$ that are analogous to **58**, **62** and **59** respectively. As stated in chapter 5, **46** presents the same reactivity as **45** upon reaction with **III** and H_2. In the second PHIP experiment, only hydride ligand enhancements for **79** and **80** are observed. In the thermally polarised spectrum,the signals for **81** are replaced by those for **82** over time. Neither of these signals appear polarised at this point.

Hydride dissociation rates for **79** and **80** are 0.400 ± 0.001 s^{-1} and 5.22 ± 0.04 s^{-1}, respectively. Due to the very high thermal ratio of formation of **79** over **80** (1 : 0.02), it is therefore expected that **79** yields higher PHIP signal, even if its hydrides dissociation rate is not optimal. Only a small fraction of **80** is present solution, which gives the observed PHIP signal at an optimal hydride dissociation rate.

Interestingly, when the results of reacting **III** with 1 eq. of **45** and **46** are compared, the relative size of the PHIP enhanced hydride ligand signals for the *mono* and *bis* phosphine substituted products inverts. For PCy_2Ph the *mono*-phosphine complex is favoured while for PPh_3 is it is the *bis*-phosphine. This fits with the steric bulk of **46** favouring *mono* substitution.

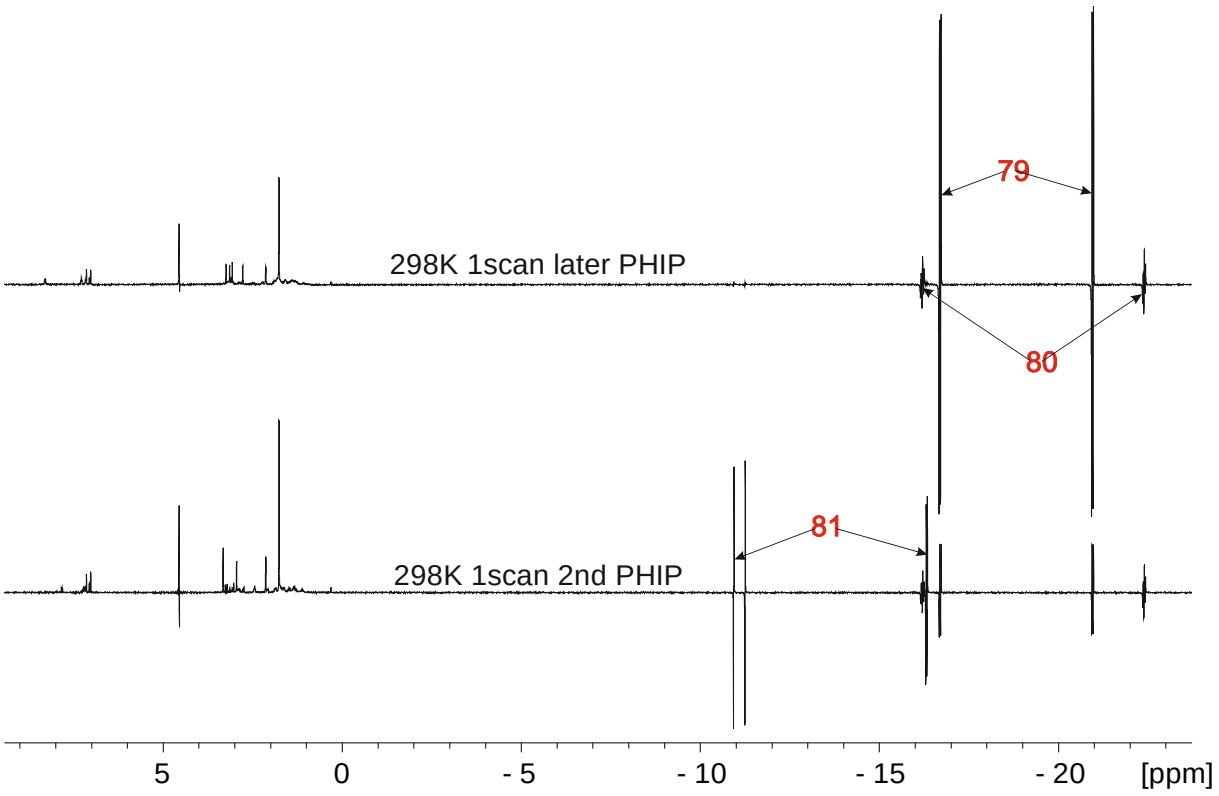

Figure 6.14: a) Hyperpolarised ^1H NMR spectrum recorded from a sample of 17.2 mM of $IrCl(DMSO)_3$ (**III**) and 1 eq. of **46** in 0.6 mL of toluene-d_8 under 3 bar of *p*-H_2 showing strong hydride signals enhancement for **79**, **80** and **81** in the first PHIP ^1H NMR spectrum. b) The later resulting PHIP ^1H NMR spectrum shows strong hydride signals enhancement of only for **79**, **80**.

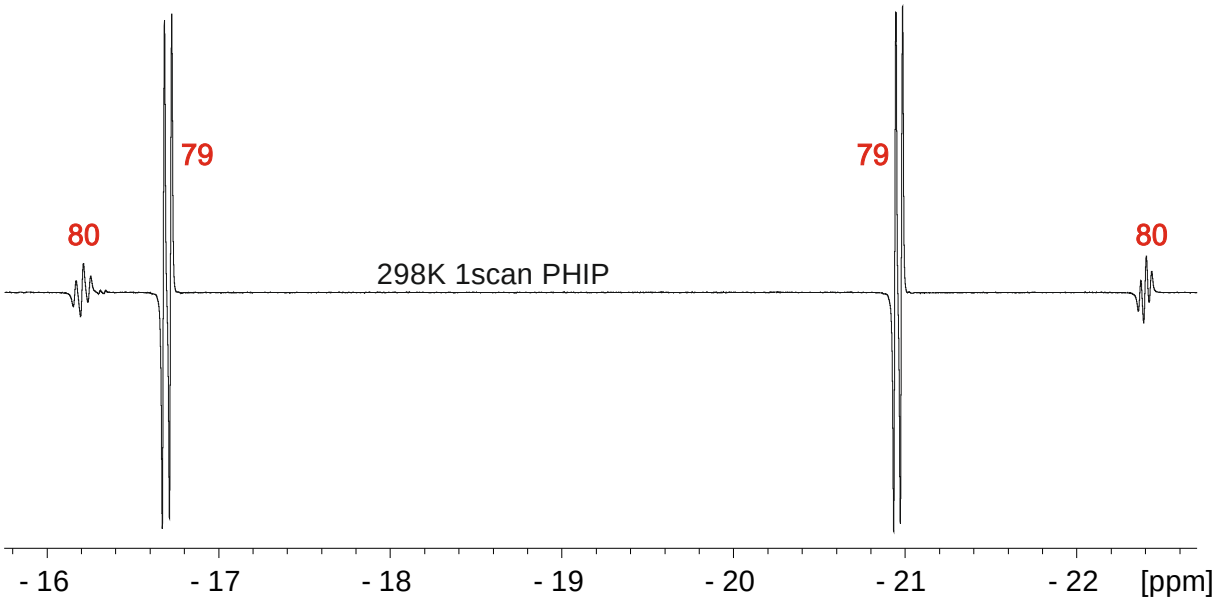

Figure 6.15: Zoom of the hydride region for a hyperpolarised ^{1}H NMR spectrum recorded from a sample of 17.2 mM of $IrCl(DMSO)_3$ (**III**) and 1 eq. of **46** in 0.6 mL of toluene-d_8 under 3 bar of *p*-H_2. It highlights the stronger hydride signal enhancement for **79** compared to **80**. The opposite behaviour was observed when the phosphine **45** is employed.

6.7 Rational analysis of all hyperpolarisation reactions

Table 6.3: Summary of some properties of the stable complexes that provides enhanced antiphase hydride signals after PHIP experiments

Complexes	**92**	**58**	**62**	**88**	**75**	**76**	**79**	**80**	**83**	**84**	**95**	**96**
H_2 loss rate (s^{-1})	3.2	0.1	3.7	1.9	0.12	4.3	0.40	5.2	NA	5.8	NA	NA
SNR hyperpolarised signal, number of scan 1, receiver gain 1	2475	5775	5775	530	5518	5518	4367	4367	1608	1608	4134	4134
Optimal temperature	298	298	298	298	298	298	298	298	313	313	333	333
Phosphine cone angle	170	145	145	194	145	145	161	161	165	165	130	130
Phosphine CO stretching (cm^{-1})	2056.4	2068.9	2068.9	2066	2068	2068	NA	NA	2066.4	2066.4	2085.3	2085.3
Transfer to ^{31}P	Y	Y	Y	N	Y	Y	Y	Y	Y	Y	N	N

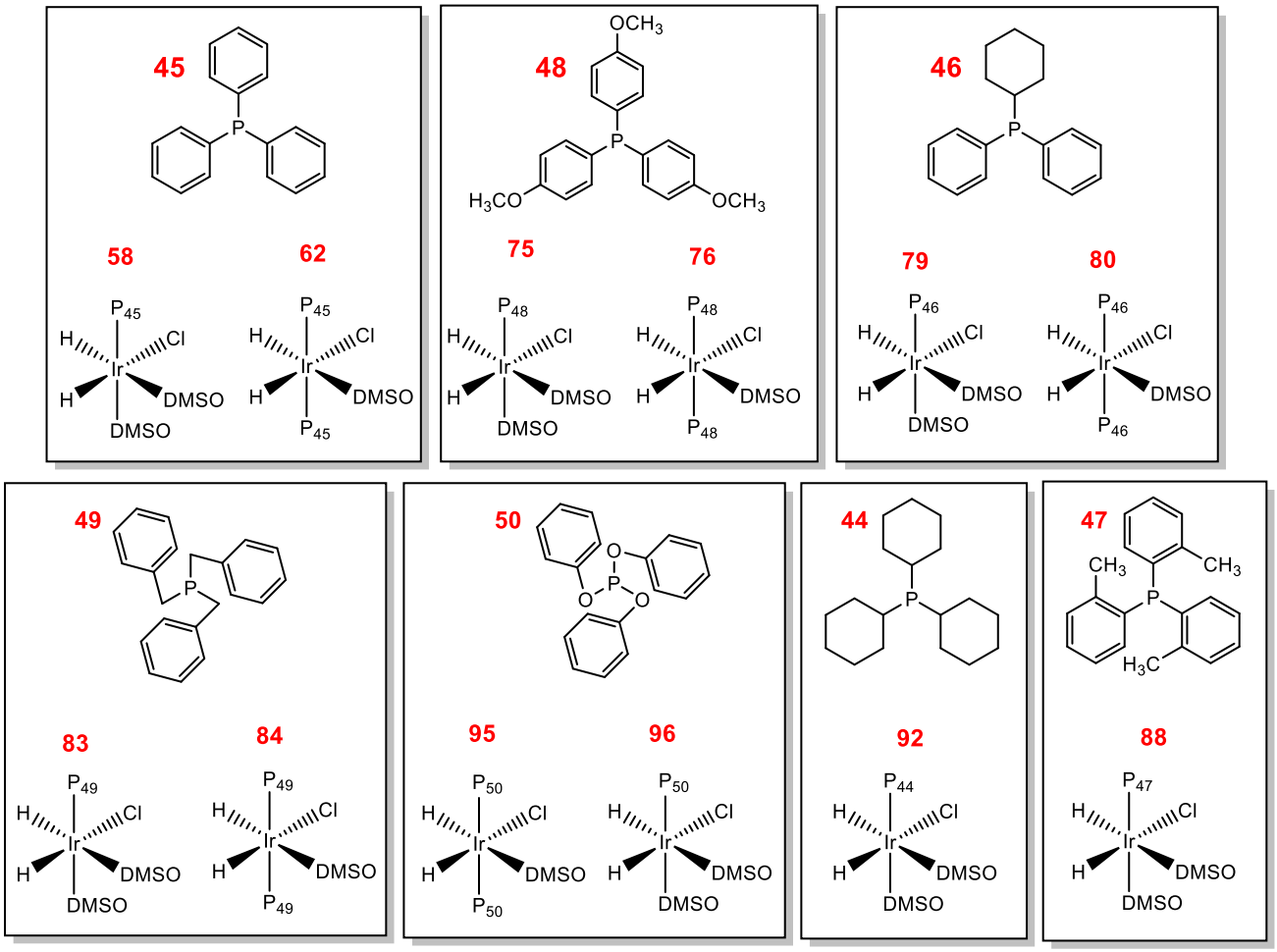

Figure 6.16: Schematic description of the stable complexes that provides enhanced antiphase hydride signals after PHIP experiments

A comparative analysis of the complexes (Figure 6.16) physical and chemical properties is given in this section in order to rationalise their hyperpolarisation behaviour.

Seven of these phosphines ligands proved to undergo *mono*, *bis* and in some cases *tris*-phosphine substitution upon reaction with (**III**) with similar amounts of phosphine. Consequently, they reacted with H_2 to form many dihydrides species according to their thermally polarised NMR spectra (see chapter 5). These products undergo H_2 loss on different timescales and therefore continuously react with *p*-H_2 to produce hyperpolarised hydrides signal for a number of species of the form $IrCl(H)_2(DMSO)(P_X)_2$ and $IrCl(H_2)(DMSO)_2(P_X)$ (where x = **45**-**50**) as presented in Figure 6.16.

The aromatic phosphines yield highly enhanced hyperpolarised signal for their *bis*-phosphine complexes, whereas non-aromatic (**44**) and partially aromatic (**46**) phosphines provide maximum hydride signal enhancement for their *mono*-phosphine complexes. The complexes that proved to yield the most enhanced hydride ligand signals have the same order of rate of dihydrogen loss (between 3 ~ 5 s^{-1}). Furthermore, successful polarisation transfer to ^{31}P is observed for all of the phosphine ligands except **47** and **50**. The SNR of the hyperpolarised spectra of these phosphine complexes are all very high (couple of thousands) in agreement with their signal intensities except for phosphine **47**, which yielded the poorest enhancement.

The eighth phosphine **51** proved to form *trans-trans* $IrCl(H)_2(DMSO)(P_{51})_2$ **91**, and was unpolarised.

The Tolman parameters are rationalised in these studies for the understanding the hyperpolarisation reactions.

For **45**, the cone angle Θ is 145° and ν_{co} is 2069 cm^{-1}. The ratio between the thermally polarised hydride signals for the *bis*-phosphine products **62** and *mono*-phosphine products **58** is 0.68 : 1 while this ratio becomes 7.7 : 1 in the hyperpolarised spectrum. Thus, **62**, which is less favoured thermally, provides the best hydride signals enhancement. H_2 dissociation rate measured for **62** and **58** are respectively 3.72 ± 0.01 s^{-1} and 0.10 ± 0.01 s^{-1}, which is in agreement with their PHIP response. **62** provided much better hydride signal enhancement and suggests that **62** has the most optimal dihydrogen loss rate. In addition, more electron density is given to the metal with the *bis*-phosphine, hence suggesting the more the metal is electron rich, the better the hyperpolarisation response is.

According to Tolman electronic and steric parameters, **48** has the same cone angle as **45**, and a smaller ν_{co} of 2066 cm^{-1} than **45** [248]. Hence, the less electronegative **48** ligand gives less electron density to the Ir(III). Nonetheless, good hydride signal enhancement was achieved with the *bis*-phosphine **76**. The ratio of hyperpolarised hydride signals between *bis*-phosphine **76** and *mono*-phosphine **75** was 1: 0.1 whereas this ratio fall to 1 : 2.63 in the thermally polarised spectrum. Therefore, the less thermally favoured formed **76** prove to be more PHIP efficient. In addition, similar dihydrides exchange rate to those of **62** and **58** was measured for **76** and **75**, which are now respectively 4.27 ± 0.03 s^{-1} and 0.120 ± 0.002 s^{-1}. These value prove again that the optimal dihydrides loss rate for PHIP being between 3 ~ 5 s^{-1} [229].

47 is the bulkiest (Θ = 194°) phosphine of the series. This is supported by the exclusive formation of the dihydride product *mono*-phosphine **88** and the *mono*-phosphine C-H bond activation product **67**. The poor PHIP efficiency is a consequence of the slow hydrides dissociation rate for **88** (1.9 ± 0.3 s^{-1}) and the rapid hydride site interchange (23.6 ± 0.9 s^{-1}). Furthermore, the PHIP spectrum has the poorest SNR in the series. **47** and **49** have the same electronic parameter value (ν_{co} = 2066 cm^{-1}), hence it can be thought that only the steric parameter is influencing here its observed reactivity. It is also not surprising that no polarisation transfer to ^{31}P atom is observed with **88**.

The cone angle Θ of **46** is 161° while no data could be found for its electronic parameter. The ratio of formation in the thermally polarised spectrum of the *mono*-phosphine **79** and the *bis*-phosphine **80** is 1 : 0.02 whilst in the hyperpolarised spectrum it is 1 : 0.15. The big cone angle therefore favour *mono*-substituted phosphine complex, which provides larger signal enhancement. In term of the kinetics of the hydrides, **80** and **79** exhibit a dissociation rate of respectively 5.22 ± 0.04 s^{-1} and 0.400 ± 0.001 s^{-1}. It is therefore not surprising that **79** yields larger hyperpolarised hydride signals in agreement with its high thermodynamic stability. Even though less hyperpolarised signal is observed for **80** relative to **79**, it is still the case that the efficiency is better for **80** than **79**, which is consistent with the exchange rates.

The cone angle Θ of **49** is 165° and the electronic parameter ν_{co} is 2066.6 cm^{-1}. The ratio of formation in the thermally polarised spectrum for the *mono*-phosphine **83** and the *bis*-phosphine **84** is 1 : 0.21 whilst in the hyperpolarised spectrum at 308 K, it is 1 : 30.3. Therefore, the thermodynamically favoured mono-phosphine **83** proves to be less PHIP efficient. **84** yields massive hydride signals enhancement at 308 K, suggesting optimal ligand exchange rate at this temperature. This later was assessed at 313 K to be 5.8 ± 1 s^{-1} where the error of the measurement is much bigger in this case.

50 has a smallest cone angle Θ (130°) and has the highest electronic parameter (ν_{co} = 2085.3 cm^{-1}) in the series of phosphines described so far. It is thus the most electron rich and hence activating. In the thermally polarised spectrum, the *bis*-phosphine **95** and *mono*-phosphine **96** hydride resonances were not observed whilst in the hyperpolarised spectrum they became dominant products at 333 K and are

in the ratio of 1 : 0.28. The small cone angle favours *bis* – *tris* phosphine substitution, which is in agreement with the thermodynamically stable products **69**, **89** and **90** (see chapter 5, section 5.7). The high electronic parameter and the increase of phosphine coordination trigger more charge transfer to the metal. Unfortunately, no kinetic data was recorded. Similar behaviour was observed with **49**, which also gave best hydrides signals enhancement at high temperature. Surprisingly, despite the massive hydride enhancement of the hydride, no polarisation transfer to ^{31}P atom occurred.

Of the list of phosphines used, **44** has one of the biggest cone angle (170°) and the smallest electronic parameter (ν_{co} = 2056.4 cm^{-1}). Due to its big size, it is not surprising that **44** only *mono* and *bis* substitute DMSO in **III** and does not react further to form a *tris*-phosphine, even in a large excess. The kinetics data measured with **88** (3.23 ± 0.01 s^{-1}) shows similar rate range when phosphine **45**, **48** and **46** are used as ligands, confirming the hydride dissociation rate being optimal for 3 ~ 5 s^{-1} for PHIP.

6.8 Conclusions

In this sixth chapter, the hyperpolarisation reactions of a series of iridium – phosphines complexes were studied at high field to select the optimum conditions that would be needed for their detection at the Earth's magnetic field. In total, three out of 12 complexes, namely **92**, **62** and **75** are potential Earth's field NMR candidates for detection. Complexes such as **83** and **95** also provided huge hyperpolarised hydride signals. However, this was observed at 313 K and 333 K, respectively rather than 298 K. They can therefore both be potentially detected with an atomic magnetometer in the nano-Tesla field regime where the sample is close the hot Rb vapour cell. In the next chapter, the detection of species with **44**, **45** and **46** will be carried out in the Earth's magnetic field. Phosphine **48** could be also detected in the Earth's magnetic field but its adducts **75** and **76** has the same spins topology as **K** adducts **58** and **62**. They would give similar EF NMR spectra.

Chapter 7: Earth's field NMR detection of iridium phosphine complexes

7.1 Introduction

In this chapter, the aim is to use the phosphine complexes that provided large hydride hyperpolarisations at room temperature at high magnetic field and detect them using the Earth's field NMR device. This will involve using complexes of the type $IrCl(DMSO)_x(H)_2(P)_y$ [x = 2, 1, 0 when y = 0, 1, 2] which proved to yield continually refreshed hydride signal enhancements on the order of 1000-fold at high field as detailed in Chapter 6. While the very small absolute chemical shift differences between the hydride signals is vanishingly small in the Earth's magnetic field (on the order of a few mHz), rendering the hydrides essentially chemically equivalent, their difference in *J* coupling to ^{31}P breaks their symmetry such that they maintain magnet inequivalence. For example, *trans* or *cis* hydride ligands provide coupling constants to ^{31}P on the order of 150 Hz and 20 Hz, respectively. This should enable their detection as hyperpolarised hydride signals in this strong coupling regime. Chapter 6 contained examples of both *mono*-phosphine and *bis*-phosphine complexes that meet these criteria and so there are a number of possible complexes with different spin topographies that can be examined.

In parallel, thermal detection of phosphine **20** is also provided. As described in Chapter 4, it was found that some of the phosphines (**20**-**18**) react with IrCl(COD)(IMes) (**I**) under H_2 to form several dihydride species for which both the hydride and ^{31}P nuclei exhibit PHIP enhancements. Unfortunately, when these systems were examined in the Earth's magnetic field, no signal was detected. Chapter 5 and 6 detailed a further series of complexes formed by reacting $IrCl(DMSO)_3$ (**III**) and $IrCl(COD)(PCy_3)$ (**IV**) with the phosphine ligands (**44**-**51**) and H_2. The magnetically inequivalent hydride ligands in these products also showed strong PHIP. The following sections present *in-situ* Earth's field detection data for the systems that gave the highest level of hydride ligand hyperpolarisation at high field and were therefore suitable for detection in the Earth's field. These studies involve the reaction of **III** with the phosphines PPh_3 (**45**), PCy_3 (**44**) and PCy_2Ph (**46**) and *p*-H_2 in toluene. The formation of *cis-cis* $IrCl(H)_2(DMSO)(P_x)_2$ and *cis* $IrCl(H)_2(DMSO)_2(P_x)$ (where x = **45**, **44** and **46**) is probed. *cis* $IrCl(H)_2(DMSO)_2(P_{44})$ can also be obtained from reaction of **IV** with excess of DMSO in either toluene or dichloromethane. The impact of the two different routes to forming this complex on the level of hyperpolarisation observed using *in situ* EFNMR detection is also explored.

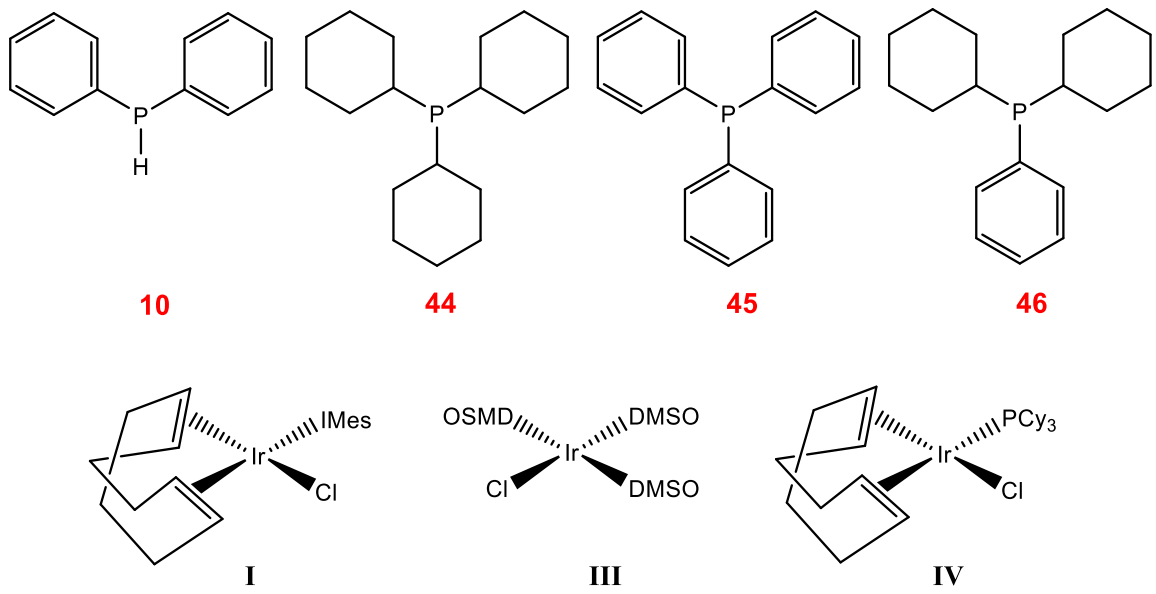

Figure 7.1: Chemical structures of the phosphines **10**, **44**, **45** and **46** used in the Earth's magnetic field studies and metal catalyst IrCl(COD)(IMes) (**I**), $IrCl(DMSO)_3$ (**III**) and $IrCl(COD)(PCy_3)$ (**IV**)

7.2 Detection of diphenyl phosphine 10 using EF NMR

As described in Chapter 4, prior to the investigation of the iridium-phosphine complexes, the hyperpolarisation of a range of phosphine was explored, phosphite and phosphate compounds with a view of detection in the ultra-low-field regime. Of particular interest, were compounds such as diphenyl phosphine (**10**), which features a large $^1J(^1H, ^{31}P)$ coupling of 220 Hz. Phosphine **10** was suitable for detection in the Earth's magnetic field without *p*-H_2 hyperpolarisation because it is a liquid at room temperature and a large volume was available.

A bottle of 200 mL of neat phosphine **10** was placed in Earth's field NMR probe and a ^1H 1D spectrum was acquired using pre-polarisation for 4 s in a field of 18.8 mT and signal averaging of 256 scans. The resultant spectrum is shown in Figure 7.2. A dominant doublet with a splitting of 6 Hz centred at 2708 Hz was identifiable after only two scans. These central peaks are due to the aromatic protons and the observed 6 Hz coupling matches that for the aromatic ^1H-ortho protons to ^{31}P at high field. The two flanking peaks at 2606 Hz and 2823 Hz appear more like satellites of the main peak but in fact are due to the single P-H proton that experiences a 1-bond coupling to the ^{31}P of 220 Hz.

In order to confirm this interpretation a density matrix simulation using the Spinach library in Matlab[109] was performed. The real system has twelve spins (^1H and ^{31}P) which is above the number that can be simulated in a reasonable period of time using a standard density matrix approach. The spin system was therefore simplified to neglect one phenyl ring and use just seven spins (six ^1H and one ^{31}P). The *J*-couplings between the ^1H-ortho and ^{31}P nuclei were set to 6 Hz and the single bond ^1H and ^{31}P coupling was set to 220 Hz. All other couplings were set to zero. Despite these significant simplifications, there is excellent agreement between the experimental spectrum (black) and simulation (blue) as shown in Figure 7.2. This includes the asymmetric position of the central doublet relative to the flanking peaks that is due to the strong coupling regime.

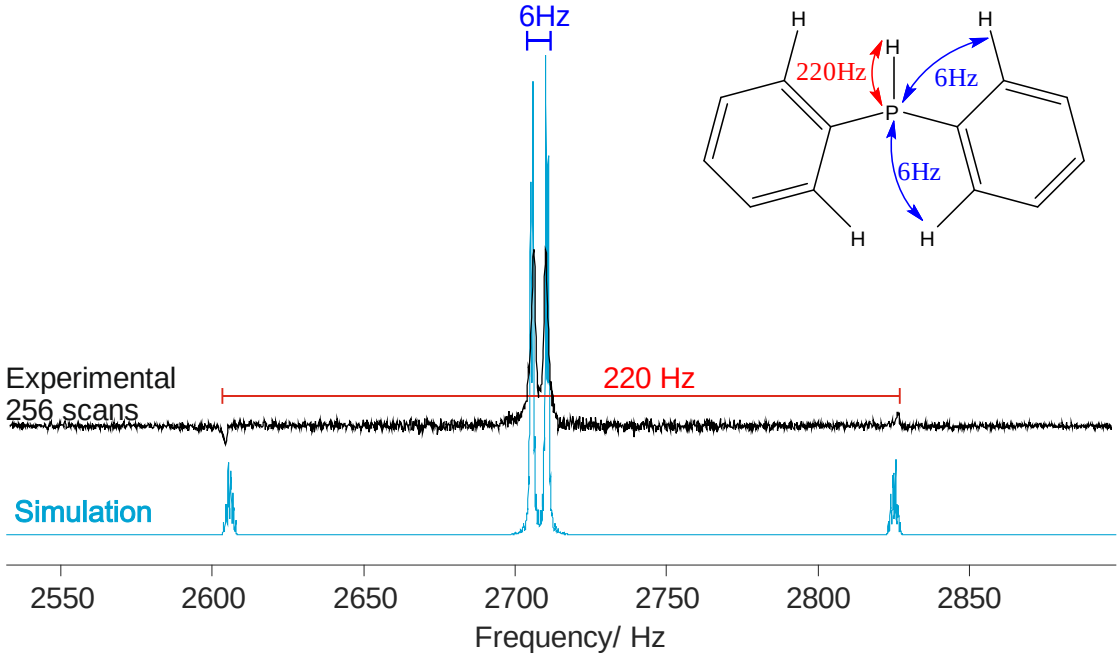

Figure 7.2: In black, ^{1}H NMR spectrum of 200 mL of phosphine **10** acquired in the Earth's magnetic field after pre-polarisation for 4 s at 18.8 mT. The signal averaging was 256 scans. In blue, density matrix simulation obtained using Spinach[109] in Matlab.

As described in Chapter 4, when phosphine **10** was mixed with complex **I** and H_2 in solution, the *bis*-phosphine *cis-trans* $IrCl(H)_2(IMes)(\mathbf{10})_2$ **20** complex was observed, alongside with other species. While PHIP hyperpolarisation of the hydrides of **20** was observed at high field, no SABRE transfer to the free phosphine in solution occurred. The level of polarisation of the hydrides was insufficient to be observed in the Earth's magnetic field. Therefore, no further EF NMR investigations were carried out on this phosphine.

7.3 Detecting hyperpolarised hydrides using EF NMR

7.3.1 EF NMR detection of hydride complexes containing PPh_3

As shown in Figure 7.3, the reaction of $IrCl(DMSO)_3$ (**III**) with **45** (PPh_3) and H_2 in toluene results in two interesting products, **62** and **58** (Scheme 7.2) along with other products (detailed in Chapter 5, section 5.3.2). These two species provide a high level of renewable hydride signal hyperpolarisation at 298 K. Their structures confirm that the hydride ligands are both chemically and magnetically inequivalent. It should be noted that at high field the hydride signal intensity levels of **62** are almost 4 times bigger than that of **58**. In addition, the organic region of these ^{1}H NMR spectra also show a signal enhancement for free DMSO that was evaluated as 19-fold. Small enhancement of the two bound CH_3 of DMSO were also visible.

Scheme 7.2: Spin systems and associated J coupling values for **62** and **58** as measured at high field (500 MHz).

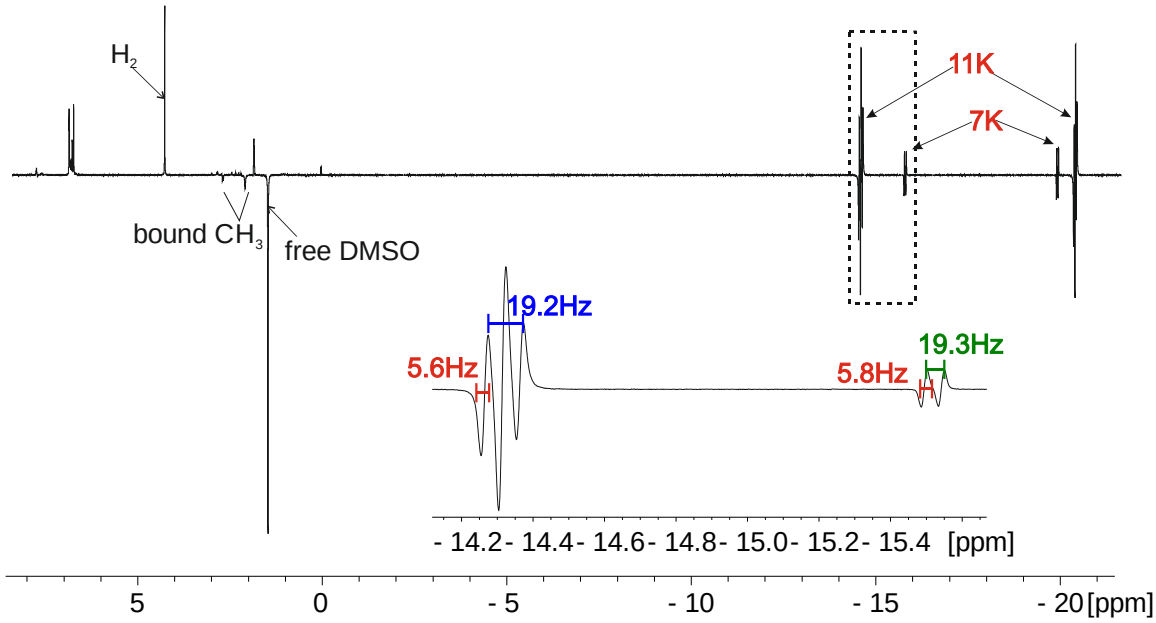

Figure 7.3: Enhanced PHIP ^{1}H NMR spectrum recorded from a sample of 8 mM of **III** with 1 eq. of **45** in toluene-d_8 under 3 bar of *p*-H_2 showing the hydride signals for **62** and **58** as well as free and bound DMSO.

7.3.1.1 *In-situ* Earth's field NMR detection of the reaction of $IrCl(DMSO)_3$ (**III**), with 45 and H_2 in toluene

An *in situ* hyperpolarisation measurement with Earth's field NMR detection was performed for a sample of 10 mM of **III** and 1.8 eq. of **45** in 4 mL of toluene. The hyperpolarised EF NMR spectra were acquired using the 45° *r.f* pulse sequence of Figure 9.5 section 9.5.4 and 256 scans, with *p*-H_2 bubbling throughout each scan. Following the initiation of *p*-H_2 bubbling, a delay of 2 s was added to allow hyperpolarisation build-up in the Earth's magnetic field and the signal was detected following the application of a π/4 *r.f* pulse and a 20 ms acquisition delay. The resultant spectrum (Figure 7.4.a) contained two antiphase peaks, separated by 35 Hz, which is the sum of the two ^{1}H-^{31}P couplings (19.2 and 14.8 Hz) in complex **62**. The smaller antiphase separation is 6 Hz, which matches with the known ^{1}H-^{1}H coupling. The assignment of these peaks to **62** is consistent with the high-field NMR results (Figure 7.3), which showed much higher levels of PHIP hyperpolarisation for **62** compared to the **58**.

These data therefore demonstrate the ability to record an Earth's field NMR spectrum with a sub10 mM concentration of **62** under *p*-H_2 and signal averaging. This is in contrast to all previous *para*hydrogen-enhanced EF NMR results, where only free ligand hyperpolarisation was observed.

In order to support the assignment of the experimental spectrum, a simple density matrix simulation was performed (Figure 7.4, b) for **62**. This simulation used just four spins: the two hydrides and two ^{31}P nuclei. All others spins, including the protons on the phosphine and DMSO ligands, are neglected to simplify the calculation. The values for the two *cis* ^{1}H-^{31}P couplings were set to 14.8 Hz and 19.6 Hz and the hydride ^{1}H-^{1}H coupling was 5.8 Hz. The best fit to the experimental spectrum was observed for a starting state of $2(I_{1z}I_{2z})$, where I_{1z} and I_{2z} represent the z-components of the spin angular momentum operators for spins 1 and 2 (the hydrides). The simulation included the application of an ideal π/4 pulse followed by signal acquisition in the Earth's magnetic field (65.8 μT) under the influence of the full heteronuclear and homonuclear *J* coupling interactions. When the ^{31}P-^{31}P (36 Hz) was set to zero in the simulation, there was no visible effect on the predicted ^{1}H NMR signal. Hence this was subsequently set to 0. As can be observed, the main feature of the simulated spectrum is an anti-phase doublet separated by the sum of the two ^{31}P-^{1}H couplings, in agreement with the experimental spectrum. The additional smaller features in the simulation are not observed experimentally, although if present these would likely be below the level of the noise. The agreement between the experiment and simulation further supports the assignment of the peaks to the *bis*-phosphine complex **62**.

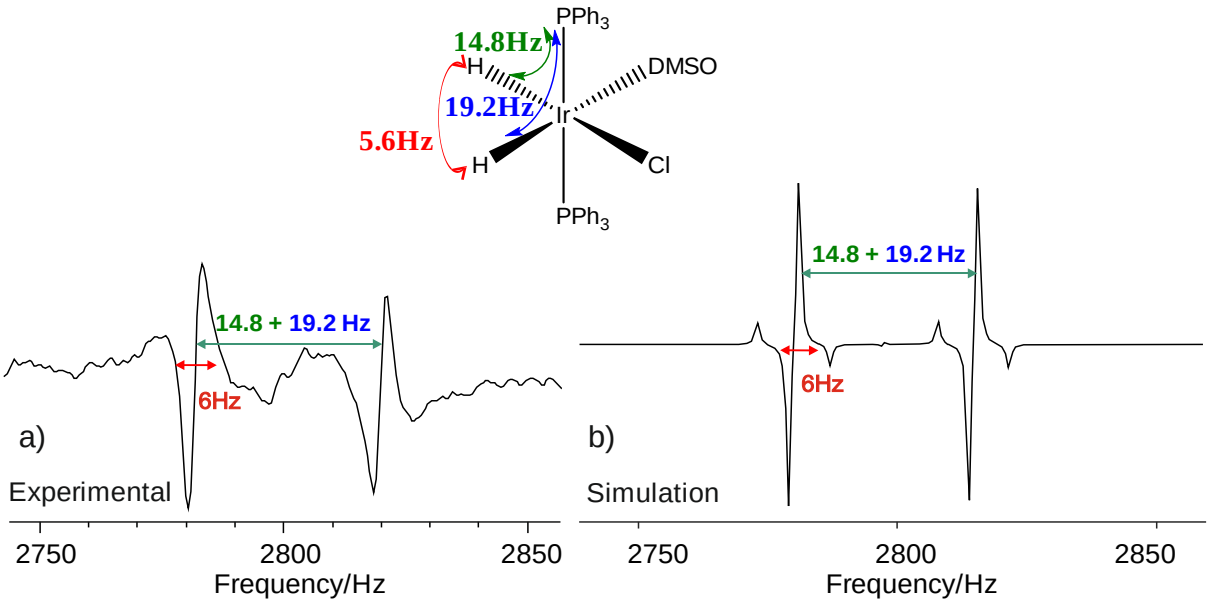

Figure 7.4: a: Earth's field NMR spectrum from a sample of 10 mM of **III** was reacted with 18 mM (1.8 eq.) of **45** in 4 mL of toluene-d_8 showing two antiphase peak separated by 35 Hz. The inner separation of the antiphase peak of each peak is 6 Hz. b) Simulated spectrum using a Matlab program showing perfect match with the experimental spectrum.

In order to confirm that only signal originating from **62** was being observed in the EF NMR spectrum, simulations of **58** was also run in Matlab. The two complexes were simulated using the same experimental procedures as described in Figure 7.4.b. Both hydrides starting states $2(I_{1z}I_{2z})$ and $(I_{1z} - I_{2z})$ were tested for the two complexes **58** and **62**. It should to noted that in both complexes, the intensity of the signal is much higher for $2(I_{1z}I_{2z})$ than $(I_{1z} - I_{2z})$ states according to the simulations (Figure 7.5).

In the case of **58** three spins, two hydrides and one phosphorus, were used, neglecting the other proton spins present in the molecule. The coupling values were set to 19.3 Hz and 17.8 Hz, respectively, for the two *cis* ^{1}H-^{31}P couplings and the ^{1}H-^{1}H coupling was set to 6 Hz. The spectrum was obtained using the hydride starting state $2(I_{1z}I_{2z})$ and an ideal π/4 pulse. It shows two antiphase peaks with a separation of 18.6 Hz (Figure 7.5.b), which is the average of the two ^{1}H-^{31}P couplings. The inner separation of each peak is 6 Hz, the same measured for the ^{1}H-^{1}H coupling. A noticeable feature is that the antiphase peaks are now 'down-up' and 'up-down' instead of 'down-up' and down-up'. This feature is observed in the simulation when the difference between the two hydrides-phosphorus couplings become small (19.3 and 17.8 Hz) so the relative phase of the two peaks change to become opposite. This simulated spectrum of **58** is a poor match to the experimental spectrum and so further supports the assignment of the experimental peaks to **62**.

When the **58** spin systems was simulated using the dihydrides starting state $(I_{1z} - I_{2z})$ and an ideal π/2 pulse was applied, the spectrum in Figure 7.5.a was observed, which contains four more peaks. Similar to the spectrum of Figure 7.5.b, the two small antiphase peaks are separated by 18.6 Hz, in addition to the inner and outer hydride-hydride coupling of 6 Hz.

A simulation of the **62** spin system using the dihydrides starting state $(I_{1z} - I_{2z})$ and an ideal π/2 pulse was also carried out and the spectrum in Figure 7.5.c obtained. The two antiphase peak have a separation equal to the sum of the hydride-phosphorus coupling (19.2 and 14.8 Hz). Similar to the spectrum in Figure 7.5.a, they are split on either side by a 6 Hz coupling, which is the value of the hydride-hydride coupling.

For completeness, the simulation of the **62** spin system with the dihydrides starting state $2(I_{1z}I_{2z})$ and an ideal π/4 pulse is included in Figure 7.5.d, and shows good agreement with the experimental spectrum in Figure 7.4.a.

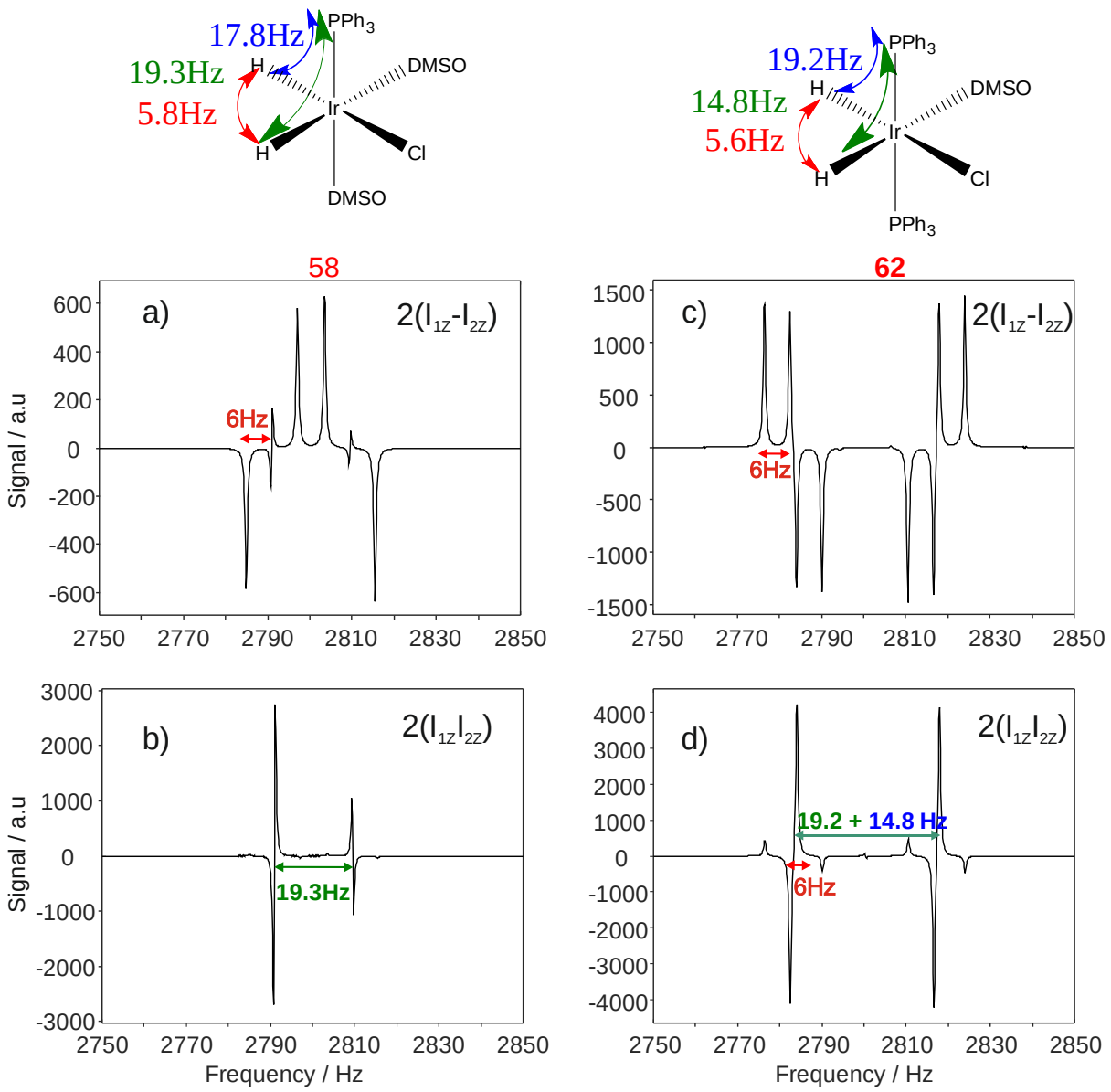

Figure 7.5: Matlab simulations of the **58** spin system (^{1}H, ^{1}H and ^{31}P) where the dihydrides starting state is (a) $(I_{1z} - I_{2z})$ and (b) $2(I_{1z}I_{2z})$. Matlab simulations of the **62** spin system (^{1}H, ^{1}H, ^{31}P and ^{31}P) where the dihydrides starting state is (c) $(I_{1z} - I_{2z})$ and (d) $2(I_{1z}I_{2z})$.

7.3.1.2 Deuterated phosphine ligands increase the hyperpolarisation level

When deuterated PPh_3-d_{15} (**45**) is used, a higher polarisation level is achieved (due to higher apparent SNR of Figure 7.6.b) meaning just 128 scans are now needed to see a more well resolved Earth's field spectrum of **62** with better SNR that with protio-PPh_3. The increase in SNR is potentially due to less polarisation transfer to the phosphine protons and/or an increase in hyperpolarisation lifetimes. Figure 7.6 shows a spectrum (b) recorded from a solution of 9.26 mM of **III** with 1.8 eq. of deuterated **45** and protio-**45** (a) in 4 mL of proto-toluene. It should be noted that the use of a protio-solvent is

possible because the low sensitivity of EF NMR means that only signals hyperpolarised via PHIP are observable.

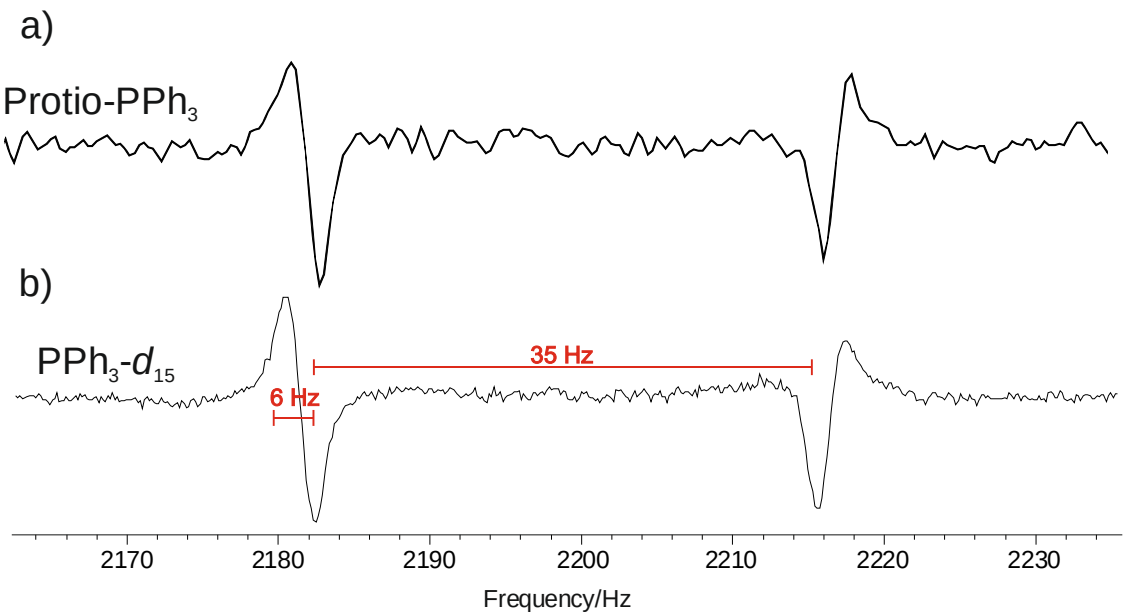

Figure 7.6: EF NMR spectrum obtained from a sample of 9.26 mM of **III** with 1.8 eq. of deuterated **45** in 4 mL of proto-toluene. b) Higher signal intensity of the spectrum was obtained with deuterated phosphine with less signal averaging (128 scans) compared to spectrum (a) recorded with protio-PPh_3.

7.3.1.3 Probing the effect of the PTF and pulse angle in 62 hyperpolarisation

The presence of labile dimethyl sulfoxide in **62** allows both hyperpolarised hydrides and sulfoxide to be detected simultaneously in the Earth's magnetic field. These two ligands are hyperpolarised in two different ways. For the hydrides, hyperpolarisation results directly from the breaking of the symmetry of the *p*-H_2-derived protons upon binding to the complex, which leads to evolution of the initial *p*-H_2 singlet state into observable magnetization during the 2 s period of *p*-H_2 bubbling in the Earth's magnetic field. The subsequent application of a π/4 pulse yields the ^{1}H EFNMR spectrum in Figure 7.7.a, where hydride hyperpolarisation is observable after only 8 signals averages. As it is the coupling to the ^{31}P that breaks the symmetry of the hydrides, a specific polarisation transfer field (PTF) is not required to observe this PHIP response.

By contrast, DMSO is hyperpolarised via SABRE (see section 2.3.3) and therefore a PFT of 6.5 mT is necessary to create the matching condition in the *J*-coupling system that allows for efficient polarisation transfer from the hydrides to the DMSO ligand. In order for significant polarisation build-up on DMSO in free solution to occur, this field is turned on for 10 s and is followed by a π/2 pulse in the Earth's field for detection. The hyperpolarised signal for DMSO appears as a single peak (Figure 7.7.b) after only 4 scans. The hydride signal is not observed in this case. This supports the proposal that the origin of the hydride hyperpolarisation for **62** is a two-spin longitudinal spin order term, $2(I_{1z}I_{2z})$, which produces maximum observable signal following a π/4 pulse and no signal following a π/2 pulse.

Both hydride and DMSO responses can, however, be detected simultaneously in the Earth's field following transfer in a PTF of 6.5 mT if a π/4 is applied because this pulse leads to observable signals for both the hydride spin state $2(I_{1z}I_{2z})$ and the longitudinal magnetisation of the DMSO (I_z). This is illustrated in Figure 7.6.c, where a polarisation transfer time of 1.5 s was used. Repeating this experiment with a longer PTF duration (10 s) leads to an increase in the intensity of the DMSO signal relative to the hydrides, as it allows for more SABRE transfer into the DMSO (Figure 7.7.d).

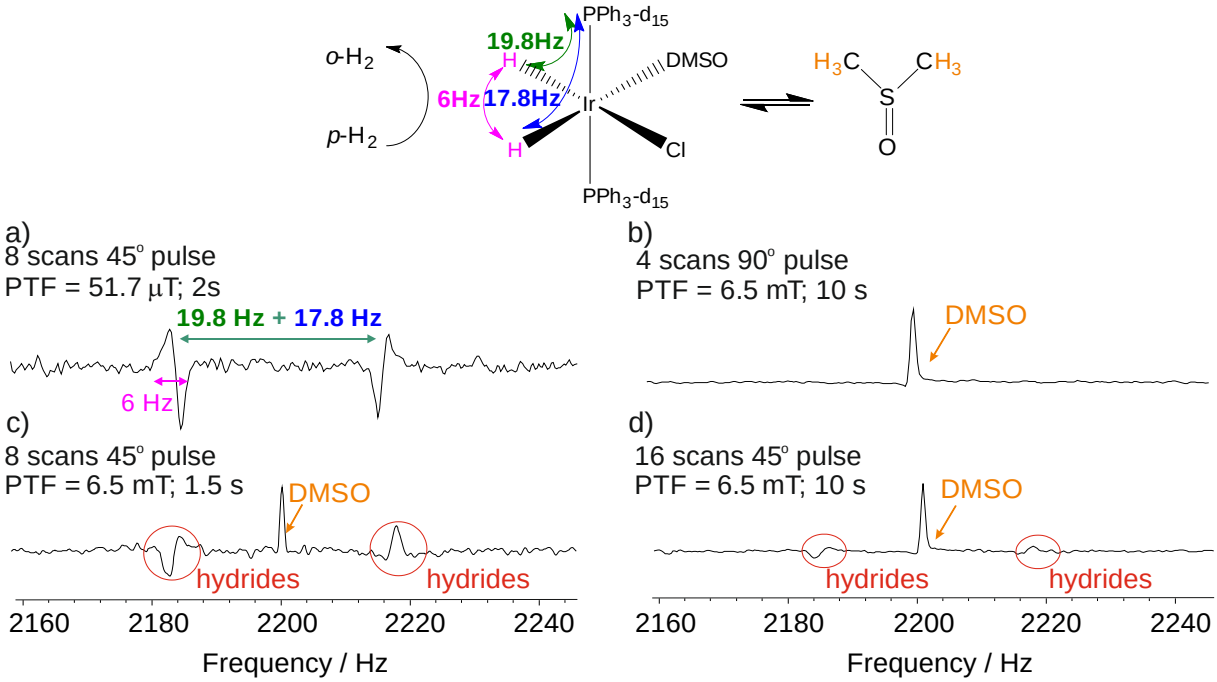

Figure 7.7: ^{1}H EF NMR spectra recorded on a sample of 9.26 mM of **III** with 1.8 eq. of deuterated **45** in 4 mL of toluene under *p*-H_2. a) 8 scans with a PTF of 51.7 µT for 2 s before a π/4 pulse. b) 4 scans with a PTF of 6.5 mT for 10 s before a π/2 pulse. c) 8 scans with a PTF of 6.5 mT applied for 1.5 s before a π/4 pulse. d) 16 scans with a PTF of 51.7 µT applied for 2 s before a π/4 pulse.

7.3.2 EF NMR detection of hydride complexes containing PCy_3 (44)

7.3.2.1 In-situ detection of $IrCl(COD)(PCy_3)$ (**IV**) with excess of DMSO in dichloromethane

In the previous section, only the *bis* phosphine complex **62** was observed. A suitable *mono*-phosphine complex showing 2000-fold hydride ligand signal enhancements (8% polarisation at 11.7 T) was obtained at high field by mixing $IrCl(COD)(PCy_3)$ (**IV**) with an excess of DMSO in dichloromethane-d_2 (Figure 7.8). The organic region of the spectrum displayed an enhancement of free DMSO signal estimated to be 34-fold (not shown here). The key complex that showed strong PHIP was $IrCl(H)_2(DMSO)(PCy_3)$ **92**, (Scheme 7.3).

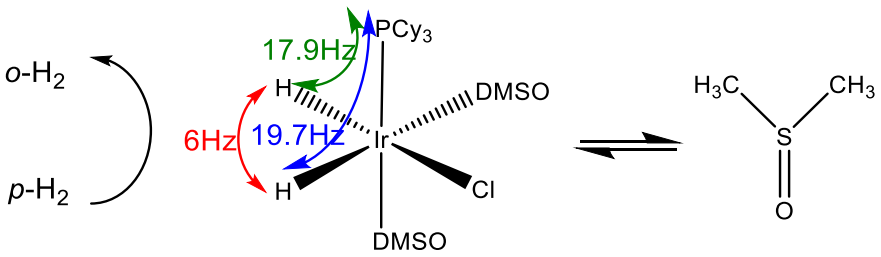

Scheme 7.2: Complex **92** undergoes both DMSO and hydride ligand exchange.

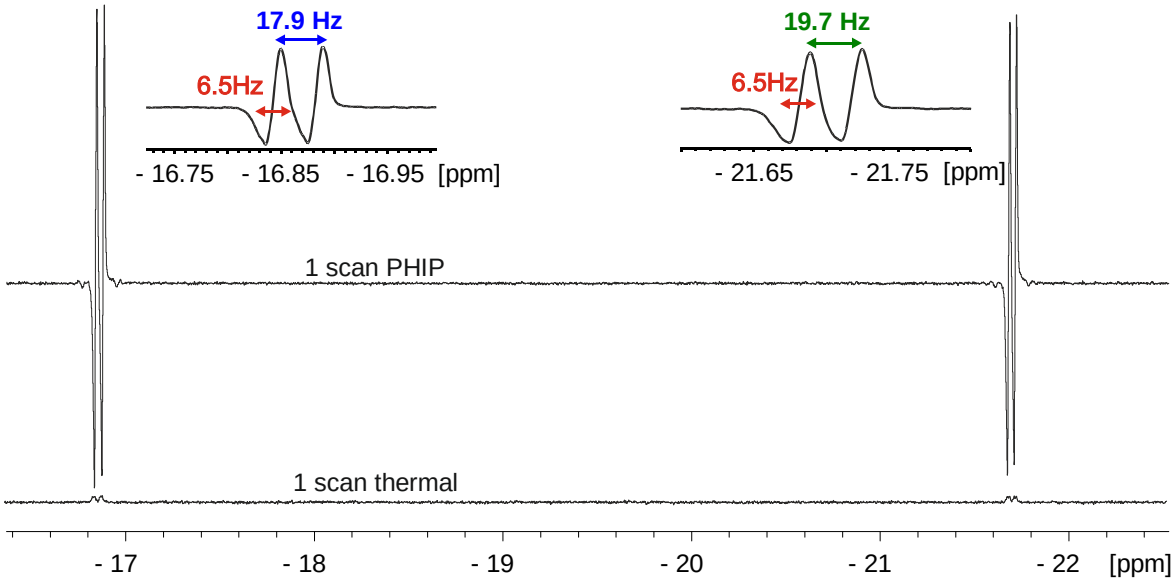

Figure 7.8: Hydride region of a PHIP enhanced ^{1}H NMR spectrum recorded from a sample 2 mg of IrCl(COD)PCy$_3$ (**IV**) with 5 eq. of DMSO in dichloromethane-d_2 under 3 bar of p-H$_2$. The key J couplings involved in the **92** spin system are highlighted.

The first sample tested for EF NMR detection contained 5.27 mM (13 mg) of **IV** with 5 eq. DMSO in 4 mL dichloromethane-d_2. Figure 7.9.a shows the spectrum recorded after p-H$_2$ was bubbled for 3 s where no PTF current was applied and so only the Earth's magnetic field (64.4 µT) was experienced by the sample's spins. Subsequently, a π/4 pulse was applied and the EF NMR spectrum was recorded. The resultant spectrum (Figure 7.9.a, 128 scans) exhibits a central component and broader components with and ~20 Hz separation. A second spectrum (Figure 7.9.b), where a PTF of 6.5 mT was applied for 10 s followed by a π/2 pulse, shows a more intense and narrowed central component, consistent with DMSO hyperpolarisation, along with a broader signal feature that could correspond to the hydrides. However, unambiguous assignment was challenging due to the broad peaks and poor SNR.

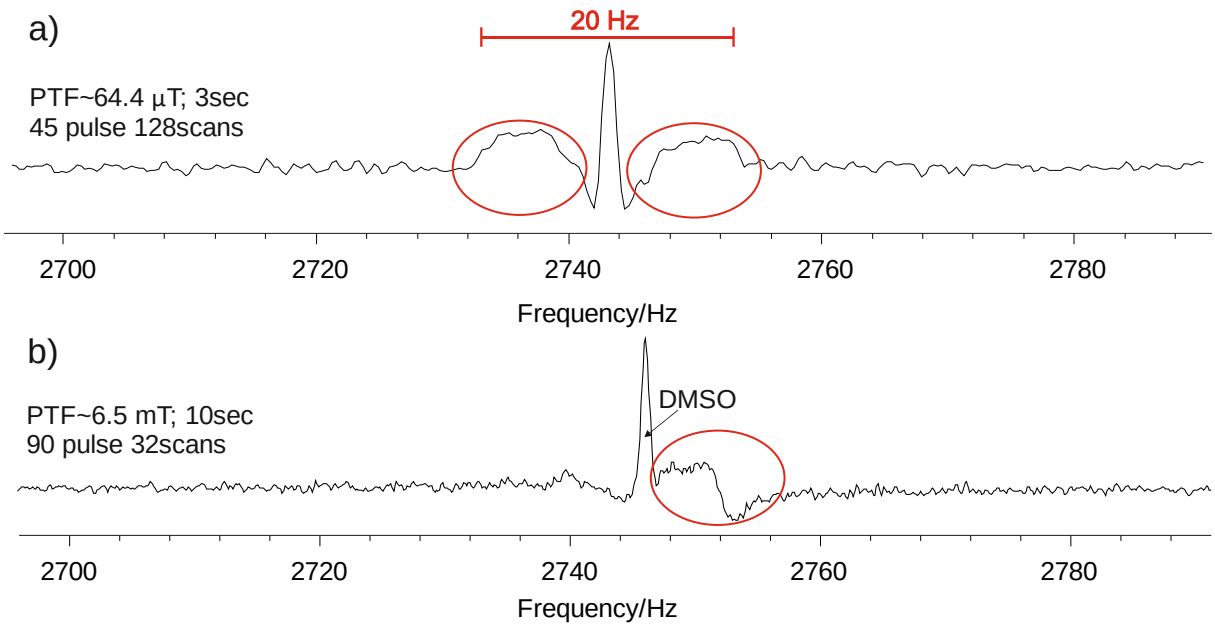

Figure 7.9: ^{1}H EF NMR spectra recorded from a sample of sample of 5.27 mM (13 mg) of **IV** with 5 eq. DMSO in 4 mL dichloromethane-d_2. a) 128 signal averaging where a PTF of 64.4 µT switched on for 3 sec before a π/4 pulse. b) 32 signal averaging where a PTF of 6.5 mT was turned on for 10 sec before a π/2 pulse applied.

To simplify the spectrum and help understand the observed features, a new sample was made with DMSO-d_6. The aim was to observe only hydride hyperpolarisation in the EF NMR spectrum. A sample of 10.5 mM (26 mg) **IV** with 5 eq. DMSO-d_6 in 4 mL dichloromethane-d_2 was made. No additional field was applied during the 3 sec *p*-H_2 bubbling, hence the spins experienced only the 64.4 µT Earth's magnetic field. Subsequently, a π/4 pulse was applied. After 128 scans and reprocessing with more data-points and zero-filling, Figure 7.10.a was obtained. This spectrum presents a significantly different anti-phase peak pattern compared to that observed for **62** in Figure 7.3. The separation between adjacent peaks is 6 Hz, which is assumed to be the hydride - hydride coupling, whereas the separation between the two external peaks is 38 Hz, which is the sum of the two hydride - phosphorus couplings (19.7 + 17.9 Hz).

To explore the features of the experimental spectrum, a density matrix simulation was performed (Figure 7.10.b) for **92**. This simulation involved three spins: the two hydride ^{1}H and one ^{31}P that are assumed to be directly involved in the evolution of the hyperpolarisation of the hydride spin order in **92**. All others spins, including the protons on the phosphine, were neglected. The values for the two *cis* ^{1}H-^{31}P couplings were set to 17.9 Hz and 19.7 Hz and the hydride ^{1}H-^{1}H coupling was 6 Hz. Unlike in the case of **62**, the best fit to the experiment was observed for the starting state $(I_{1z} - I_{2z})$, which provides optimal signal following a π/2 pulse. However, given the very low SNR of the experimental spectrum, questions remain about assignment of this spectrum in addition to the discrepancy in peak shapes, large absorptive (experimental) vs small dispersive (simulation).

These initial experiments were carried out in dicloromethane-d_2, which is not ideal for EF NMR experiments due to it low boiling point. Furthermore, it was found at high field that toluene produced a longer lasting PHIP response. Therefore, in an effort to increase SNR through longer experiments with more signal averages, the solvent to toluene was instead used, which has a much higher boiling point and so suffers less from solvent loss during repeated periods of *p*-H_2 bubbling. Similar results were obtained in terms of the form of the EF NMR spectrum but there was not significant improvement in SNR despite the increase in signal averaging.

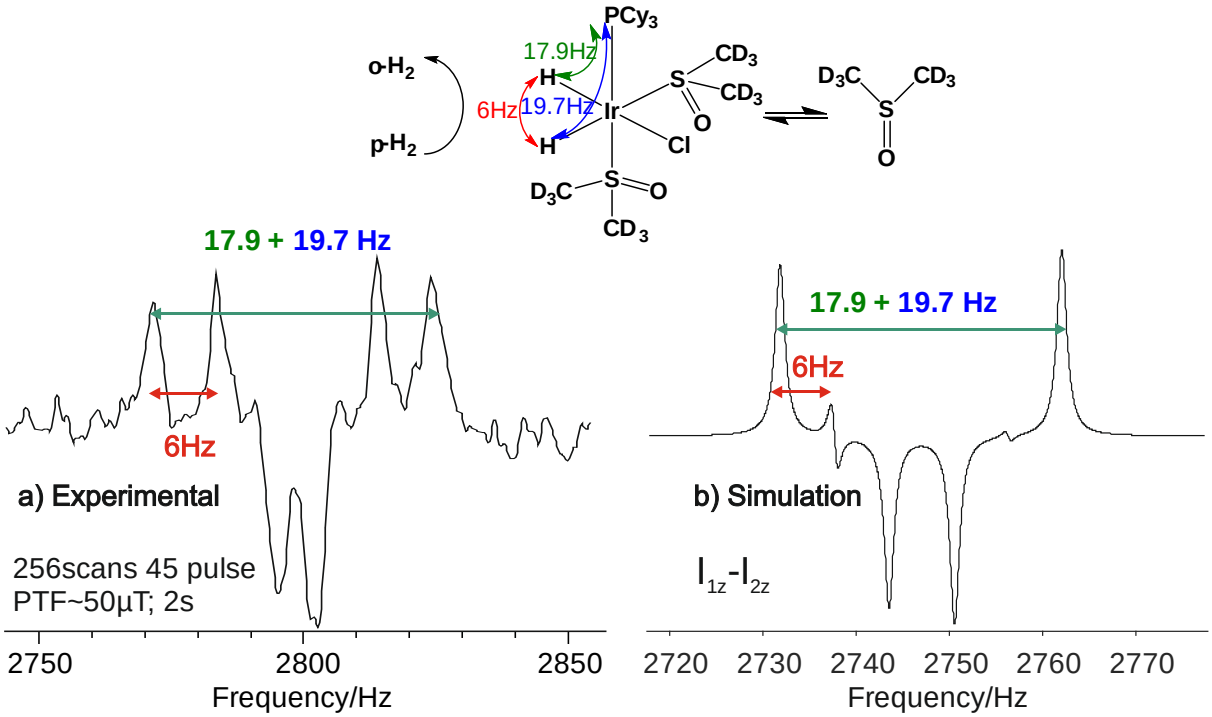

Figure 7.10: a: Experimental hyperpolarised *in-situ* EF NMR spectrum from a sample of 10.5 mM (26 mg) of **IV** with 5 eq. DMSO-d_6 in 4 mL dichloromethane-d_2. The spectrum acquired with 128 scans where a PTF of 64.4 µT was applied for 3 s before a π/4 pulse, showing signal of **92** in the Earth's magnetic field. b: Simulated spectrum involving 3 spins ^{1}H, ^{1}H, ^{31}P where the starting state is $(I_{1z} - I_{2z})$.

In order to confirm that only the hydride starting state $(I_{1z} - I_{2z})$ is contributing to the EF NMR spectrum, the state $2(I_{1z}I_{2z})$ was also simulated for the **92** spin system using a π/4 pulse. It yielded Figure 7.11, which is very different to the experimental spectrum obtained in Figure 7.10.a. It has to be noted that this spectrum is of the same form observed as the spectrum obtained for **58** in Figure 7.5.b. In fact, **92** and **58** have similar spins configurations with very small differences in *J*-couplings values and therefore this is to be expected.

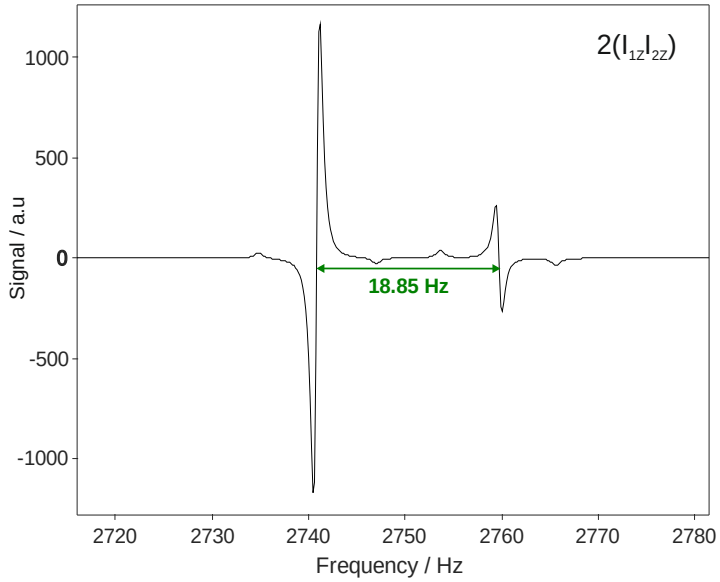

Figure 7.11: Simulation of **92** spin systems involving 3 spins ^{1}H, ^{1}H, ^{31}P where the starting state is $2(I_{1z}I_{2z})$.

7.3.2.2 Using the precursor (**III**) with PCy_3-d_{33} (44) in toluene to hyperpolarise 92

It is also possible to form hyperpolarised **92** by changing the precursor to **III** and mixing with **J** and DMSO. To maximise polarisation, it is important in this reaction to limit the phosphine to the *mono*-substitution due to rapid destruction of *p*-H_2 by the undesired *bis*-phosphine product **93** (see chapter 6, section 6.5). Therefore, for the EFNMR experiments the sample contained 13.5 mM (26 mg) of **III** with 0.7 eq. of PCy_3-d_{33} in 4 mL toluene. The deuterated **J** phosphine was used to maximise the hyperpolarisation level.

For the spectrum in Figure 7.12.a, *p*-H_2 was bubbled in a PTF of 51.7 μT for a duration of 3 s before a π/4 pulse was applied. While the lines are not as well resolved and SNR is reduced, the ^{1}H EF NMR spectrum is in agreement with the result in Figure 7.10.a, where **92** was formed from complex **IV**. Figure 7.12.a shows a spectrum on **92** that is consistent with that observed using the other precursor and hence the density matrix simulation. However, broader lines are observed, giving lower SNR and poorer quality spectrum.

The spectrum in Figure 7.12.c was recorded by changing the pulse angle to π/2, which yielded a similar spectrum as in Figure 7.9.a. The simulation of **92** suggested that the hyperpolarised state is $(I_{1z} - I_{2z})$, which provides optimal signal with a π/2 pulse. Therefore, the same spectrum as Figure 7.12.a with an increase in SNR would be expected to be observed. However, a narrow peak appears in the centre of the spectrum. I would not expect to see a signal from DMSO under these conditions (polarisation transfer field) and so it is not clear what the origin of this signal is.

However, if a SABRE experiment with PTF = 6.5 mT (Figure 7.12.b) is performed, a change in the form of the spectrum with a dominant central peak is seen, which would expected to be the DMSO under these conditions. An additional antiphase feature of 10 Hz apart from the central peak, is also observed which is likely to originate from the hydrides. However, the form of these peaks is quite

different to Fig 7.12.a. As expected, repeating the experiment with a π/2 pulse (Figure 7.12.d) does not change the form of the spectrum but only leads to a modest increase in SNR.

Further investigation is required to fully understand these spectra. However, this system proved to be very difficult to reproduce. When the amount of phosphine **44** is slightly increased (due to experimental imperfection), the formation of the very reactive *cis-cis* $IrCl(H)_2(DMSO)(P_{44})_2$ **93** occurs and no signal is observed. This confirms that hyperpolarisation of **92** is possible with these two different precursors. However, due to the need to avoid the formation of the *bis*-phosphine **93** by using less than one equivalent of phosphine when **92** is formed from **III**, formation with **IV** is the preferred route.

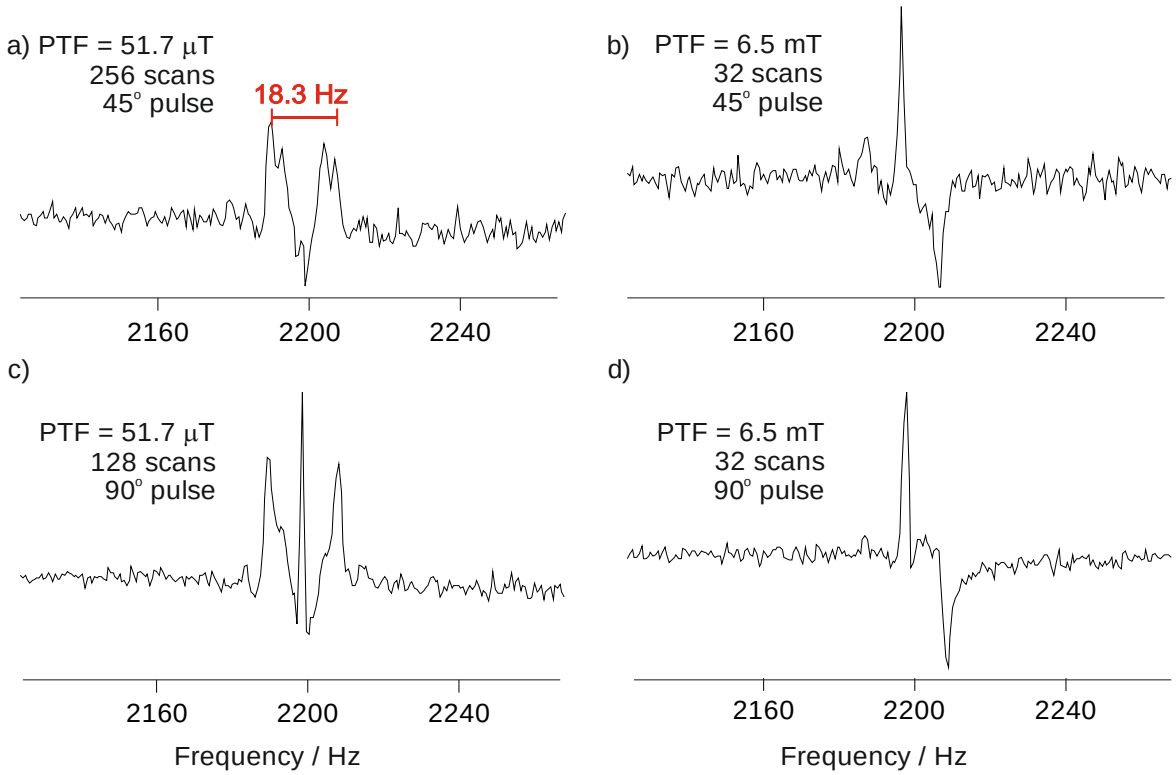

Figure 7.12: Earths field NMR spectra recorded on a sample of 13.5 mM (26 mg) of **III** with 0.7 eq. of PCy_3-D_{33} in 4 mL toluene. a) 128 scans, with a PTF of 51.7 μT for 3 sec before a π/4 pulse. c) 128 scans with a PTF of 51.7 μT applied for 3 s before a π/4 pulse. b) 32 scans with a PTF of 6.5 mT for 10 s before a π/4 pulse. d) 32 scans with a PTF of 6.5 mT applied for 10 sec before a π/4 pulse.

7.3.3 EFNMR detection of hydride complexes containing $PPCy_2Ph$ (46)

The final phosphine to be studied using EF NMR was $PPCy_2Ph$ (**46**). 10.4 mM (20 mg) of **III** was mixed with 10.28 mg (0.9 eq.) of **46** in 0.4 mL of toluene. When *p*-H_2 was bubbled through the cell in the Earth's magnetic field for 2 sec and NMR experiments were recorded using a π/4 pulse no signal was detected after 512 scans. However, when the same experiment was repeated with a π/2 pulse, a signal was recorded, which after reprocessing yielded the spectrum Figure 7.13.b. A pattern dominated by two broad peaks with a 34 Hz separation was obtained. The broad feature of the peak is explained consistent with the very short FID signal that decays in only 50 ms (Figure 7.13.a).

We have seen in chapter 6 section 6.7 that the complexes responsible for the hydride hyperpolarisation signals were the *mono*-phosphine $IrCl(H)_2(DMSO)_2(P_{46})$ **79** and the *bis*-phosphine $IrCl(H)_2(DMSO)(P_{46})_2$ **80**. However, the strongest signal was originated from **80**. With such low sensitivity detection as Earth's field NMR, it is likely that the signal recorded only originates from **80**.

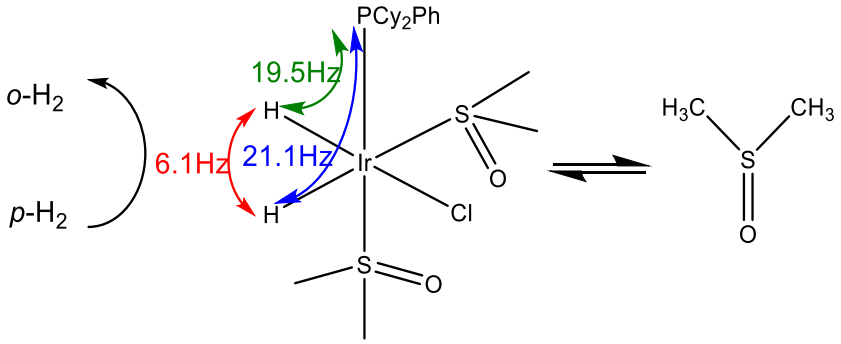

Scheme 7.3: Complex **79** continuously exchanges DMSO and hydride ligands, which are coupled with a phosphine ligand **46** to provide the hyperpolarised *J*-spectra in the Earth's magnetic field.

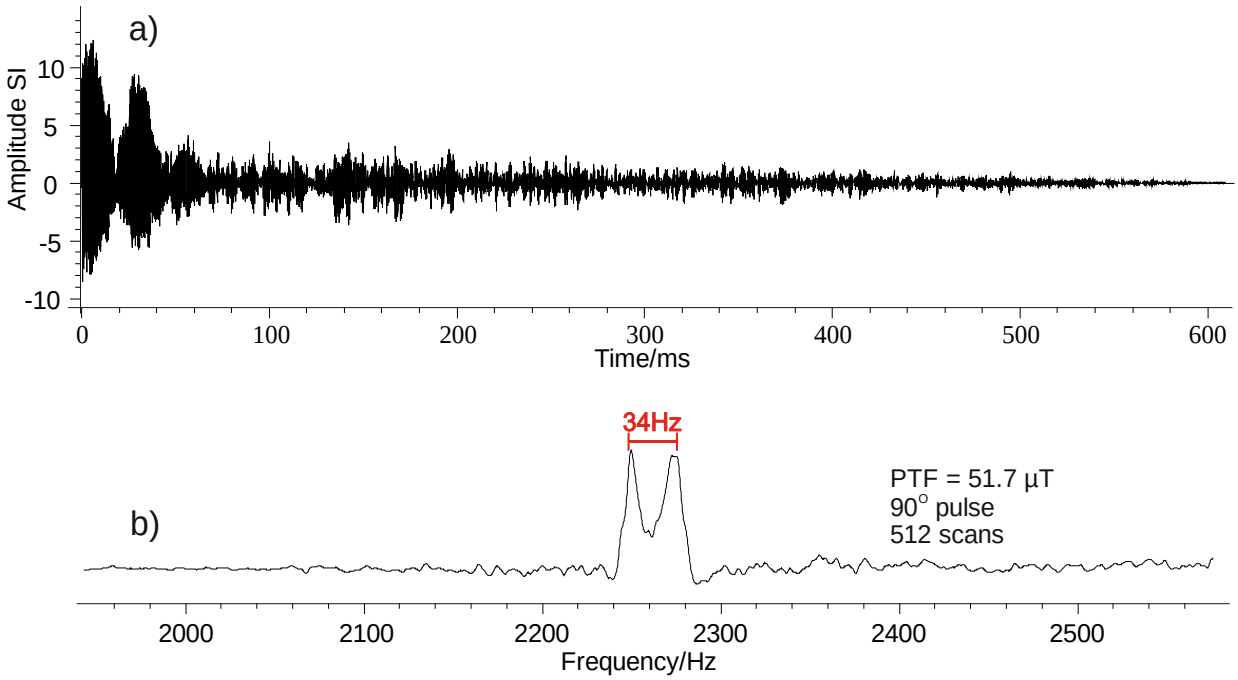

Figure 7.13: ^{1}H NMR FID (a) and spectrum (b) recorded with a π/2 pulse and 512 signal averaging from a sample of 10.4 mM (20 mg) of **III** mixed with 10.28 mg (0.9 eq.) of **46** in 0.4 mL of toluene in presence of *p*-H_2.

The observation of DMSO hyperpolarisation proved to be possible with this system. By applying a 6.5 mT PTF for a duration of 10 sec, then followed by a π/2 pulse a peak centred at 2216 Hz was obtained after 32 scans (Figure 7.14). In this case, a simultaneous detection of both hydride and DMSO signals was not possible due to the very weak hydride signal in the Earth's field.

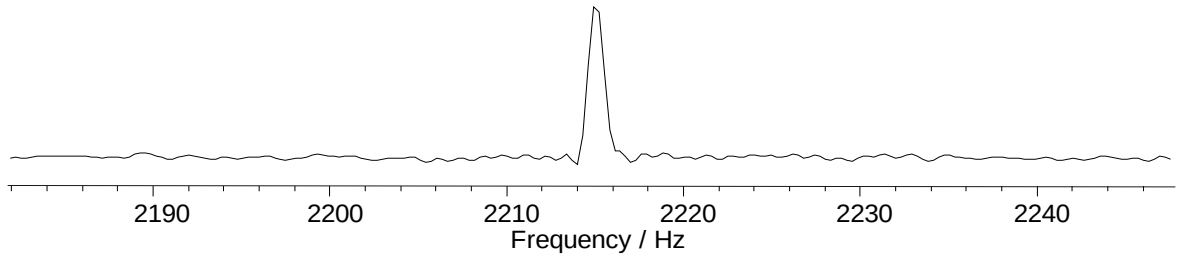

Figure 7.14: SABRE ^{1}H EF NMR spectrum of free DMSO recorded by applying a PTF of 6.5 mT for 10 sec before a π/2 pulse.

7.3.3.1 Simulations of ^{1}H EFNMR spectra for $IrCl(H)_2(PPCy_2Ph)(DMSO)_2$ (79)

In order to understand the EF NMR results, a density matrix simulation of the spins involved in complex **79** was carried out in Matlab. This simulation involved three spins, the two hydrides and one ^{31}P centre. As I did for the previous simulations, I simplified the systems by neglecting all others spins, including the protons on the phosphine and DMSO ligands. The values for the two *cis* ^{1}H-^{31}P couplings were set to 21.1 Hz and 19.5 Hz and the hydride ^{1}H-^{1}H coupling was 6.1 Hz. Two possibilities were considered where the density matrix of the hydrides are approximated by the starting states $(I_{1z} - I_{2z})$ or $2I_{1z}I_{2z}$.

In the first case, the dihydrides starting state is the term $(I_{1z} - I_{2z})$. A $\pi/2$ pulse was then applied with the transverse relaxation time T_2 set to 500 ms and 50 ms, respectively, yielding the two spectra in Figure 7.15 c and d. The spectrum in Figure 7.15d is similar to the **92** experimental spectrum, which would be expected in this case due to their similar parameters (number of spins and similar couplings). By mimicking the experimental conditions that shows a rapid decay of the FID in 50 ms, a spectrum with much broader peaks and lower signal intensity was obtained (Figure 7.15c). This spectrum shows some similarity with the experimental spectrum in Figure 7.13.b, with the two broad features and a separation of 33 Hz.

The second possibility is that the dihydrides starting state is the term $2I_{1z}I_{2z}$. A $\pi/4$ pulse was applied and the transverse relaxation time T_2 was set to 500 ms and 50 ms, respectively, which yielded the spectra in Figure 7.15 a and b. The spectrum in Figure 7.15b is in agreement with all other simulated spectra of 3 spin systems (**92** and **58**) where the starting state was $2I_{1z}I_{2z}$. When the FID decay is fast, the signal become broad and its intensity decreases. In this case, two broad features are obtained but with a separation of 20 Hz, which does not match with the experimental spectrum. It can therefore be concluded that this simulated state is not observed experimentally.

In this last experiment, the quality of the recorded data is limited by the very fast relaxation and hence broad peaks. However, a tentative assignment can be made to **79** with the starting state $(I_{1z} - I_{2z})$ as observed for complex **92**.

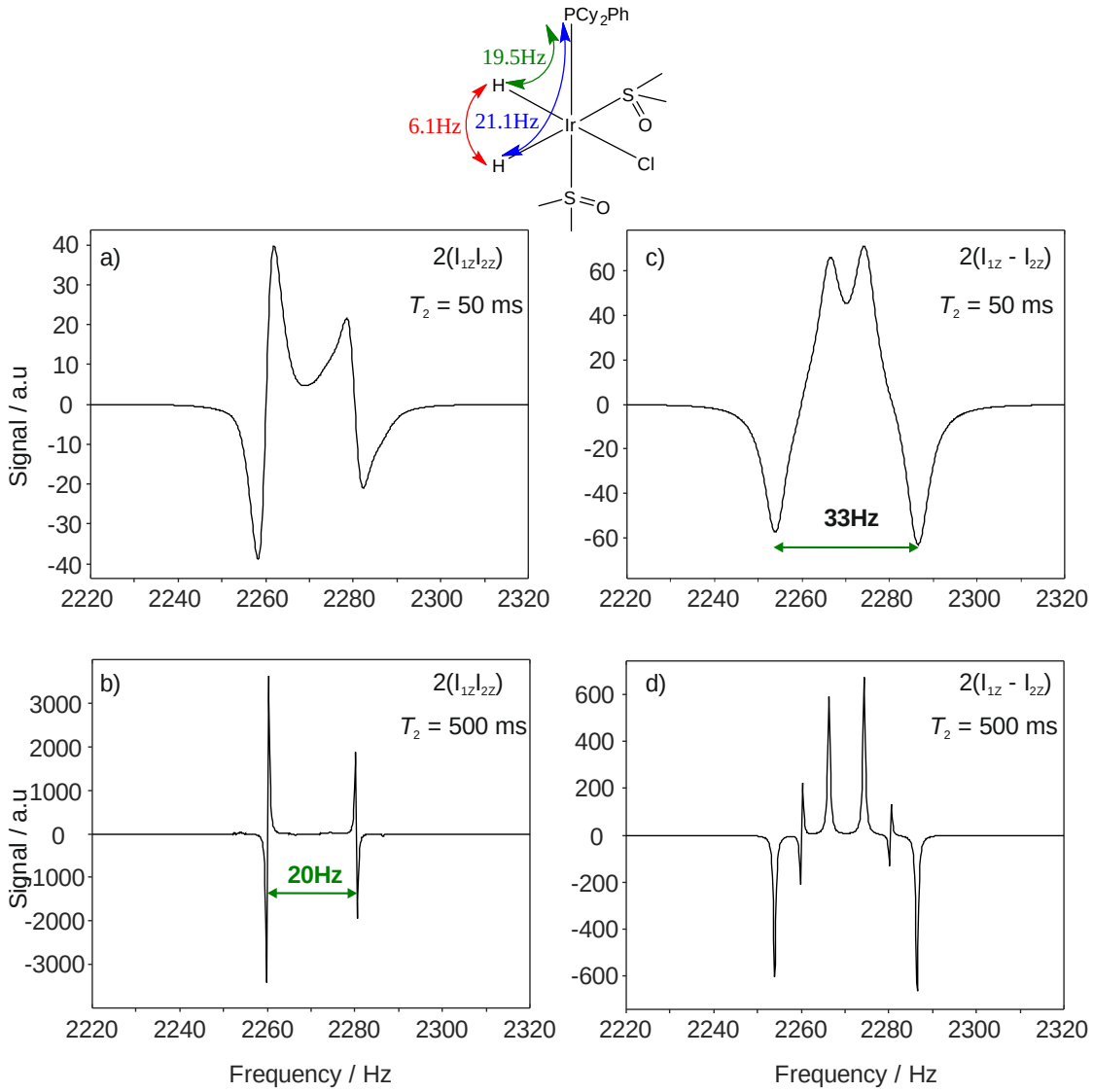

Figure 7.15: Simulated ^{1}H NMR spectra of **79** spins systems (^{1}H, ^{1}H and ^{31}P). a and b, the dihydrides starting state is the $2I_{1z}I_{2z}$ term and the transverse relaxation time T_2 was respectively set to 50 and 500 ms. c and d, the dihydrides starting state is the $(I_{1z} - I_{2z})$ term and the transverse relaxation time T_2 was respectively set to 50 and 500 ms.

7.4 Conclusion

This chapter demonstrates EF NMR detection of a new class of iridium-dihydride-phosphine complexes with *para*hydrogen hyperpolarisation. Previously, only free substrate hyperpolarised through SABRE or hyperpolarised product using hydrogenative PHIP has been reported using EF NMR detection[207]. Tessari et al.[81] have also reported a simultaneous ^{19}F and ^{1}H NMR detection on a sample of a fluorinated alkyne using hydrogenative PHIP. Therefore, the results presented in this Chapter show the detection of hyperpolarised hydride signals in the ultra-low field regime for the first time. The continuous exchange of the hydride ligands on a suitable timescale allows hyperpolarisation to be observed through signal averaging under conditions of continuous bubbling of *p*-H_2. The optimisation of the hyperpolarisation conditions of phosphine ligands at high field has led to the identification of

three suitable systems for which *p*-H_2 hyperpolarisation was sufficiently efficient to be observed directly in the ultra-low-field regime. The key to observing these sensitized hydride ligands is that they experience phosphorus coupling, which breaks their symmetry, and that the timescale of the hydride exchange is suitable for a build-up of hyperpolarised hydride via signal averaging with the *in situ* EFNMR detection system. In these experiments, 20 mM of starting material was used, which therefore led to sub-millimolar of metal complex being detected, since the high-field studies show that several other species are also present in solution.

This novel result was demonstrated for a range of phosphines reacting with **III** and *p*-H_2 to form several *mono* and *bis* substituted dihydrides phosphine complexes. The three systems tested provide a unique EF NMR signature based on the coupling network and the spin-states that are hyperpolarised in the Earth's field. The phosphines PPh_3 (**45**), PCy_3 (**44**) and PCy_2Ph (**46**) all provided sufficient hyperpolarised hydride signals at 298 K to be detectable with the Earth's field NMR spectrometer. It is found that both PHIP and SABRE of the hydride and DMSO ligands can be selectively or simultaneously detected and optimised using a PTF of 6.5 mT or 50 µT. However, the hydrides hyperpolarisation is not field dependent and can therefore be viewed at any magnetic field.

Density matrix simulations of the hydride spin systems were also carried out. This tool provided insight into the hyperpolarised states that are observed in the strong coupling regime. The results show good agreement between experimental and simulated spectra for **62** and **92**, while the very broad signals for the **79** made a comparison with simulation difficult. Interestingly, the best-fit simulations suggest a different starting state for the *bis*-phosphine complex, **62**, compared to the *mono*-phosphine complex, **92**. These experiments, therefore, provide a good starting point and model for future studies on the evolution of hydride ligand hyperpolarisation. This has significant implications for the understanding of polarisation transfer in PHIP and SABRE in the ZULF regime.

In terms of future work, variable temperature control could be integrated with the EF NMR apparatus in order to explore the effect of the hydride exchange rate on observed hyperpolarisation for a broader range of complexes. Many of the experimental spectra suffer from low SNR and required many signal averaging. Hence, designing a larger reaction cell would allow the use of larger volume and so would provide a better EF NMR signal. As mentioned in chapter 6, section 6.8, **III** reacts with PBn_3 (**49**) and $POPh_3$ (**50**) to form the *mono*-phosphine **83** and *bis*-phosphine **95** that also provided very large hyperpolarised hydride signals at 313 K and 333 K, respectively. These systems would be interesting to explore with the goal of direct observation in the nT regime with an atomic magnetometer, which operates most efficiently at these temperatures.

Chapter 8: Conclusion and future works

8.1 General conclusion

The primary aim for this PhD thesis was to identify and optimise chemical systems (compounds and complexes) that react with *p*-H_2 to provide strong and renewable hyperpolarised NMR signals at 298K suitable for detection in the ZULF regime. Particular emphasis was placed on finding systems that possess a large ^{1}H-X coupling (X = ^{19}F, ^{31}P) to unlock signal differentiation in the Earth's magnetic field. Standard high-field NMR was used to characterize and determine the molecular structure of the target species and to test, quantify and optimise their hyperpolarisation levels on reaction with *p*-H_2. The most promising systems in terms of hyperpolarisation efficiency were subsequently explored using Earth's field NMR detection.

8.1.1 Summary of the experimental work

In the first experimental chapter, the SABRE hyperpolarisation of the amines **1**, **2** and **3** at high field was described. These reactions were tested alongside with the co-ligand, dimethyl sulfoxide which allowed the access of complexes IrCl(IMes)(DMSO)$(H)_2$(**x**) where **x** = **1** or **2**. This co-ligand increased the signal enhancement seen for the free amines. This increase is due to the formation of these complexes whose ligand exchange (amines and hydrides) rates better match those needed for hyperpolarisation transfer which is too slow in the classical *tris*-substituted Ir(IMes)$(H)_2$(**x**)$_3$[135]. The DMSO co-ligand present in IrCl(IMes)(DMSO)$(H)_2$(**x**) lowers the Gibbs free energy of activation barrier to amine loss thereby achieving this effect. The enthalpy $\Delta H^{\ddagger}$, which is a measure of bond breaking and formation in the rate controlling the transition state , is higher for amine **1** than amine **2** in these species, which is expected for the better donor **1** and confirmed in the pKa for **1** (9.33) being higher than for **2** (4.70). In all of these complexes, the positive entropy $\Delta S^{\ddagger}$ for amine loss is in agreement with a dissociative mechanism. These values are typical of those seen for related pyridine derived systems[212]. For conclusion, a co-ligand strategy is beneficial to the SABRE hyperpolarisation of amines via readily available IrCl(COD)(IMes) (**I**).

The *in-situ* detection of these amines in the Earth's field in chloroform, which has a boiling point of 61^{o}C proved suitable. Previously, only SABRE hyperpolarisation and detection at EF NMR of pyridine and derivatives in methanol, which has a similar boiling point, were reported. Thereby it is firstly report the amines hyperpolarisation and detection at the EF NMR with the help of DMSO. In the absence of a heteroatom coupling, the ^{1}H EF NMR signal of these amines is a single peak as expected that is centered at the proton's Larmor frequency. However, with the third amine **3**, which possess ^{19}F atoms, heteronuclear coupling breaks symmetry and a complex pattern is observed. This allows us to confirm that polarisation of water as a contaminant leads to a signal with an opposite sign. Subsequently, pursuing studies with systems that bear heteronuclear couplings like ^{31}P-^{1}H are predicted to give the desired diagnostic tools for ZULF NMR.

In the second results chapter, the aim were to hyperpolarise a series of novel ligands (**10**-**18**) containing phosphorus proton couplings as a signal differentiation tool for ultra-low field. Preliminary studies at high magnetic field were carried out to optimise the hyperpolarisation conditions for each

ligand. For this purpose, these molecules were reacted with the metal catalysts **I** and $[Rh(COD)(PPh_3)_2]BF_4$ (**II**) in the presence of *p*-H_2 at 298 K. Unfortunately, whilst reacting to form a series of novel complexes, these products proved unsuitable for SABRE. However, in some cases, strong hyperpolarisation of phosphorus coupled hydride ligand signals were observed. This feature was explored as a route for EF NMR detection. Unfortunately, the signal gains were not sufficient to allow these species to be detected. In addition, it was observed with the phosphine oxides that the two forms O=PH and PO^-H are readily available for triggering nucleophilic reactions in solutions. For example, $OPPh_2H$ react slowly with benzylamine to form $O=PPh_2$-NH-Bn. This molecule is also O-methylated in presence of methanol. These reactions have been previously reported in the literature[233]. The phosphine sulfide have poor affinity to metal centre, independent to the size has also been demonstrated.

Based on these observations, the hypothesis was that the EF NMR detection of PHIP polarised hydride resonances with different ^{31}P couplings would be possible with better signal gains. Moving forward in the next results chapter, this was tested whilst retaining a link to the DSMO co-ligand effect whilst using *in-situ* synthesis. These complexes contained traditional trialkyl and aryl phosphines and link to those found in the first series of SABRE active catalysts[179]. The goal was to clearly detect magnetically and chemically inequivalent hydride and phosphorus environments.

Firstly the focus was on understanding the thermal reactions that took place between the metal precursor $IrCl(DMSO)_3$ (**III**) and the phosphine ligands (**44**-**51**) and dihydrogen prior to exploring their PHIP activities. The phosphine ligands **44**-**51** include aromatic and non-aromatic systems which differ in size and electronegativity to ensure a wide reaction landscape was explored. The phosphines proved able to displace DMSO from **III**. The aromatic phosphine tri(o-tolyl)phosphine **47**, tris-benzyl phosphine **49** and triphenyl phosphite **50** proved slow substitution and the unwanted two isomers of $IrCl(H)_2(DMSO)_3$ were prevalent whilst the others phosphines showed a fast DMSO substitution.

As expected, an array of 16 electron *mono* and *bis* phosphine substitution products were identified by NMR. In addition, many C-H bond activation (orthometallation) products were observed that proved to be in equilibrium with these 16-electron complexes. This was most prevalent with the aromatic phosphines. This diversion of product identity proved beneficial, as when H_2 was added, the slow formation of an array of dihydrides species was achieved. The conclusion from these results is that the eight phosphines react differently with **III** and H_2. These differences and similarities are linked to the electronic and steric properties of the phosphines. For example, the bulky phosphines tend to favour *mono*-substitution whereas the smaller phosphines *tris*-substitute DMSO. The more electron rich complexes are also favoured. After successfully identifying the thermal reactivity of these species, then moving forward on to exploring their hyperpolarisation reaction with *p*-H_2 in the next chapter.

In the fourth results chapter the hyperpolarisation reactions of the previous iridium – phosphine complexes were studied at high field to select the optimum conditions for hyperpolarisation. These products proved to react with *p*-H_2 to produce hyperpolarised hydride ligand signals for many minutes. Specifically, a number of species of the form $IrCl(H)_2(DMSO)(P_X)_2$ and $IrCl(H_2)(DMSO)_2(P_X)$ (where x = **45**-**50**) were produced with PHIP enhanced hydride ligand signals.

The *mono*-phosphine complexes $IrCl(H_2)(DMSO)_2(P_X)$ routinely yielded lower PHIP hydride ligand signal gains than their *bis*-phosphine $IrCl(H)_2(DMSO)(P_X)_2$ counterparts. However, the opposite behaviour was observed for partially aromatic phosphine **46** and the non-aromatic phosphine **44** where the mono-phosphine $IrCl(H_2)(DMSO)_2(P_X)$ lead to a stronger PHIP response. In fact, hydride hyperpolarisation efficiency and the hydride dissociation rate proved to be correlated, with a

dissociation rate in the range 3 – 5 s^{-1} providing the best hydride signal enhancement. In addition, the mechanism of H_2 loss was shown to be preceded by dissociative loss of DMSO. In total, due to the degree of PHIP signal gains, 3 out of 12 complexes, namely the *mono*-phosphine **92**, the *bis*-phosphine **62** and the *mono*-phosphine **79** were seen as potential Earth's field NMR candidates for detection at 298 K. The complexes formed with phosphines PBn_3 (**49**) and $POPh_3$ (**50**) also provided huge hyperpolarised hydride signals at 313 K and 333 K respectively rather than 298 K. They both therefore offer promise for being detected using an atomic magnetometer that typically operates above room temperature.

Finally, the last results chapter demonstrated the Earth's field NMR detection of these three phosphine complexes through their hydride ligand PHIP enhancements. The optimisation of the hyperpolarisation conditions with the phosphine ligands therefore led to the identification of three suitable systems. In these reactions of **III**, with the phosphines PCy_3 (**44**), PPh_3 (**45**) and PCy_2Ph (**46**) dihydride *mono*-phosphine **92**, *bis*-phosphine **62** and *bis*-phosphine **80** form which provided large hyperpolarised hydride signals that are detectable in the Earth's field NMR spectrometer. These species have hydride ligands that experience asymmetric phosphorus couplings and undergo continuous repolarisation with fresh *p*-H_2 under exchange. I therefore demonstrate and report for the first time, that signals emanating from metal complexes themselves can be seen in the ultra-low field regime. Furthermore, with the phosphine **45**, the simultaneous detection of both PHIP and SABRE in the hydride and DMSO ligands was achieved. Density matrix simulations of the hydrides spin systems were used to validate the EF NMR results. This provided an insight on the hyperpolarised spin states created in the ultra-low field regime and good agreement between experimental and simulated data was observed for all three species.

8.1.2 How this work fit in the broad picture

The overall aims of this PhD project was to use *p*-H_2 hyperpolarisation methods to harness the zero and ultra-low field (ZULF) NMR detection. It has to be noted that this thesis only contains EF NMR (micro-Tesla) results because it is the spectrometer available here in York. A placement in Krakow, Poland was planned in order to carry out studies on an atomic magnetometer in truly zero field (nano-Tesla) but was not possible due to COVID-19 travel restrictions.

The results discussed in this thesis shows some advancements in the field of EF NMR. Previously, SABRE at EF NMR was reported where the reversible exchange of the substrates accumulate hyperpolarisation in the free pool of ligands and allow detection of hyperpolarised free substrates. One of the significant outcomes of this thesis was the hyperpolarisation and detection of metal complexes through the hydrides in the Earth's field NMR. Indeed, it is here demonstrated and reported for the first time the hyperpolarisation and detection of metal complexes in the Earth's field regime. In addition, simultaneous detection of the hydrides and the free ligand DMSO in the $IrCl(H)_2(DMSO)(PPh_3)_2$ was also achieved. This is a remarkable improvement since it allows signal differentiation at EF NMR where the chemical shift information is non-existent. Other phosphine ligands such PCy_3 and PCy_2Ph prove to react with the iridium catalyst to form dihydride species that provide a unique fingerprint in the Earth's magnetic field. Because the hydride ligands can be hyperpolarised at any PTF and do not need a polarisation build-up time, the ^1H NMR acquisition was shorter and signal averaging was possible. These outstanding results open-up new possibilities and further investigations of dihydrides metal complexes. Indeed, further studies on the evolution of the hydrides hyperpolarised states in the ultra-low field will be now possible using the starting model presented in this thesis.

8.2 Future work

The results in this thesis reveal a number of opportunities and limitations for the detection of *p*-H_2-enhanced species in the Earth's magnetic field.

The co-ligand approach with *in situ* detection is demonstrated as a versatile tool to screen reactivity. This could be expanded to further improve the hyperpolarisation of a range of substrates and observe them in the ultra-low field regime. It was seen at high field that pyruvate hyperpolarisation using SABRE was demonstrated with the employment of a co-ligand dimethyl sulfoxide[206, 218]. Several other examples were shown where the co-ligand strategy was beneficial for SABRE improvement. This includes the case of a range of weakly binding and sterically encumbered N-heterocycles[259]. Other molecules employed as co-ligands including acetonitrile[260], 1-methyl-1,2,3-triazole[261] and methyl-nicotinate[262]. This approach therefore has the potential to open up a wider range of substrates that can be analysed in the ZULF regime.

Isotope enriched nuclei like ^{13}C and ^{15}N in conjunction with the co-ligand strategy might enable the detection of heteronuclear couplings emanating from ^{1}H-^{13}C and ^{1}H-^{15}N of some compounds. In fact, examples of labelled compounds such as $^{13}C^{15}N$-urea yielded reliable thermally polarised *J*-coupling spectra detected with an atomic magnetometer in the ultra-low field regime[98]. pH dependant chemical exchange rates of ^{1}H nuclei by varying the composition of the D_2O/H_2O was also demonstrated in this study. This type of experiment can be further optimised using p-H_2 hyperpolarisation techniques where only the hyperpolarised state would be observed.

Furthermore, I was able to detect a range of systems using EF NMR but the SNR remained a challenge. Using a bigger glass cell, that allows larger sample volumes, will maximise the filling factor and hence increase signal intensity thereby enabling some of the poorer polarisation systems to be studied. However, using a bigger sample volume is not compatible with the use of expensive labelled compounds. It is also important to remember that deuterated solvents are not needed.

Implementation of temperature control within the EF NMR system is desirable if studies are to extend to chemical species with differing reactivity. Consequently, the phosphines PBn_3 (**49**) and $POPh_3$ (**50**) could be studied as used in this work. Monitoring chemical exchange at the Earth's magnetic field where variable temperature control exists will therefore be possible. In addition, the SABRE hyperpolarisation of some ligands that have optimal ligands exchange at different temperatures will then become feasible.

There are many classes of two electron donor ligands besides phosphines and hence a much wider range of complexes could be targeted. A review by Duckett details some of this diversity[223]. Ligands such as IMes that harness the two electron donor, carbene, could be ^{13}C labelled thus providing access to two-bonds ^{1}H-^{13}C couplings that might be studied in the ultra-low field regime. Besides these two examples of phosphine and carbene ligands, other nitrogen donor ligands such as $N(CH_3)_3$, oxazoline and pyridine also proved their stability and application in inorganic chemistry[263].

Another high abundance nucleus that is spin ½ is fluorine (^{19}F). Utilisation of fluorinated ligands to break the hydride symmetry may reflect another alterative. However, these types of substrate are much harder to work with that ^{31}P. Materials like PF_3 may be an option where the ^{31}P-^{19}F coupling could be harnessed and no isotope enrichment would be needed. Another widely encountered molecule in inorganic chemistry is the anion hexafluoro-phosphate PF_6^- and its utilisation through an ion-pair interaction might be possible. A review of the 1970s details the NMR data of compounds such materials possessing both ^{31}P and ^{19}F nuclei[264] which might be adapted for this work.

In chapter 6, it was seen that hyperpolarisation was transferred to the ^{31}P atom in PPh_3 ligand at a PTF of near 0 Tesla. The detection of a hyperpolarisation of ^{31}P signal in the EF NMR by adding an extra-capacitance that allows to tune to the phosphorus resonance frequency in the Earth's magnetic field which is ~ 900 Hz was attempted. Unfortunately, these experiments were unsuccessful due to high noise levels at these frequencies. This may require more formal studies on the effect of ^{31}P enhancement on complex lifetime.

Finally, Tessari[203] have shown chemical quantification at high magnetic field using SABRE. In that study, linear dependence of the SABRE signal integrals on the concentration was obtained for dilute substrates (referred to as analytes) in the presence of a large excess of a second ligand. They show that such conditions can also be realized in far more complex mixtures, provided that the total substrate concentration largely exceeds the concentration of the analytes and of the metal complex. The same approach of quantification might be possible at ultra-low field where have already been shown that the co-ligands strategy is beneficial.

Chapter 9: Experimental

9.1 General Earth's field NMR procedure

Earth's field NMR experiments were carried out using a Terranova MRI Earth's field (EF) spectrometer (Magritek, Aachen, Germany). The EF NMR spectrometer and associated NMR experiments were controlled via a PC running the Terranova-Expert software package within Prospa (Magritek, Germany). The local Earth's magnetic field for these experiments was approximately B_E = 47.7 µT, with a corresponding ^{1}H Larmor frequency of 2030 Hz. An offset coil using a small current was added to shift the peak frequency into a less noisy region. The weak Earth's magnetic field often slightly shift due to environmental perturbation, which is the reason why the value of the offset current used was not constant throughout experiments.

9.1.1 Water reference calibration

Prior to any Earth's field NMR experiment, a 500 mL bottle of water was used to calibrate the NMR signal. The shimming and the relative orientation of the apparatus with respect to the Earth's magnetic field are important. Shimming, to improve the inhomogeneity of the static field B_0 is done with a 500 mL water bottle in conjunction with the 'autoshim' routine. At the end, an improvement of the water peak linewidth of 0.6 Hz was achieved.

9.1.2 Pulse calibration

Thermally polarised ^{1}H NMR spectra on a 500 mL water sample are recorded to calibrate the pulse power over a full rotation cycle. For example, the first 360° rotation is examined in 22 steps starting with a voltage of 0.1 V and increasing it to 5.1 V. These data were then exported from Prospa for analysis in Matlab using the curve fitting tool to obtain the curve as plotted in Figure 9.1.a. The experimental points were fit to Equation 9.1. A typical goodness of the fit is given by R-squared, which in this case was 0.9952. A 90° pulse of 1.40 V was indicated for a duration of 3.68 ms. The pulse length was set to the period, which is one over the Larmor frequency; 1/2720 Hz = 3.68 ms^{-1}.

Figure 9.1.b shows an example of a 1 scan ^{1}H EF NMR spectrum of 500 mL of water centred at the protons Larmor frequency at 2720 Hz. The NMR spectrum has a linewidth of 0.6 Hz at half and an amplitude of 40 mV/Hz.

a = -1.13 ± 0.08, b = 76.66 ± 2.18, c = -2.52 ± 0.05 and d = -0.08 ± 0.07

$$a * \sin d\big(b * (x + c)\big) * e^{x*d} \quad (9.1)$$

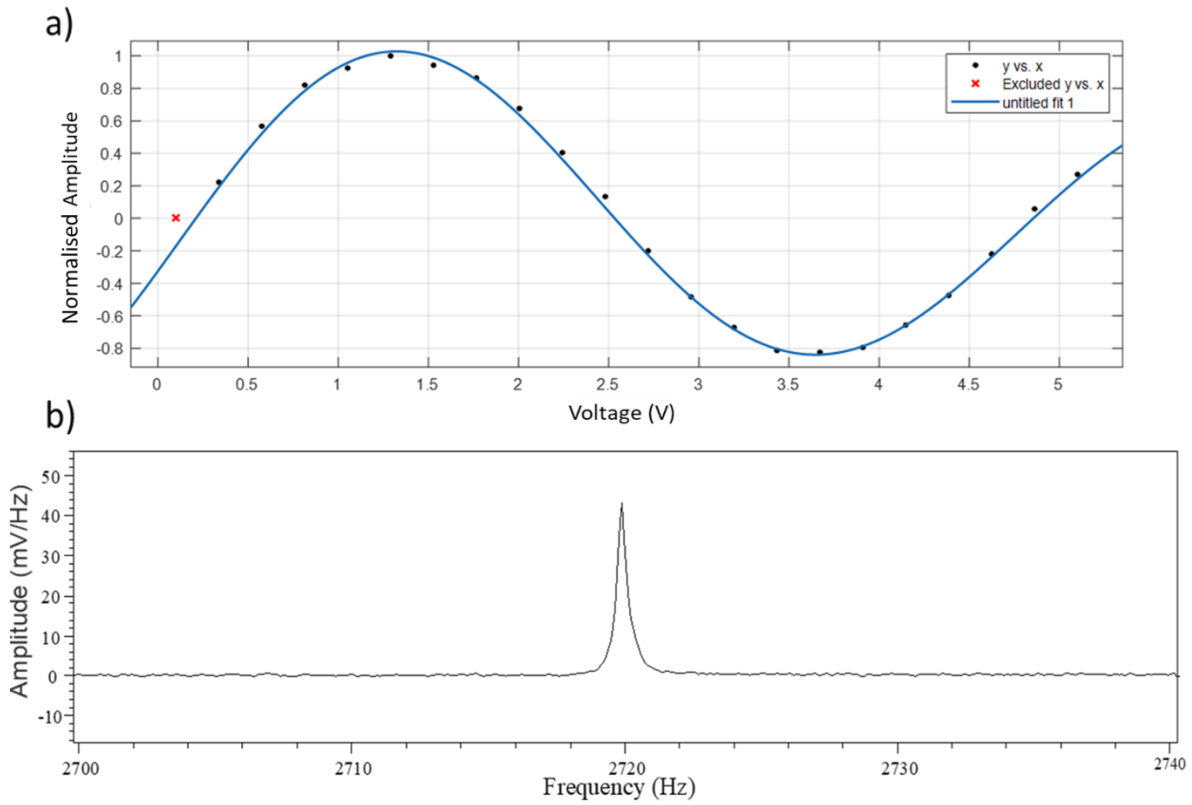

Figure 9.1: a) Nutation curve recorded with a 500 mL bottle of water at the Earth's magnetic field. b) One scan ^{1}H EF NMR spectrum of a sample of 500 mL of water sample acquired with a 90° pulse. A pre-polarising field of 18.8 mG was used for a duration of 4 s. The red x in (a) indicates a point that was excluded from the fit.

9.1.3 *In-situ* Earth's field NMR set-up

The EF NMR system[207] was integrated with a commercial Bruker *p*-H_2 generator for these studies, see Figure 9.2.a. The experiments took place inside a glass reaction chamber located in the middle of the NMR probe. The chamber consists of inlet and outlet ports, and a frit for bubbling *p*-H_2 into a SABRE solution. The outlet acts as a vent to allow *p*-H_2 gas to flow through the apparatus as a rate controlled by a back pressure regulator. By fixing the pressure difference the pressure in maintained under a slowly exchanging 3 bar *p*-H_2 gas purge.

The pulse sequence for a standard *in-situ* SABRE-PHIP hyperpolarisation experiment using EF NMR detection is presented in Figure 9.2.b. During the whole experiment, *p*-H_2 is bubbled through the sample. In the first additional step, the polarisation transfer field (PTF) is turned on by passing a fixed current through the polarising coil B_p. The duration, τ_{PTF}, and the amplitude of the PTF, is varied according to the experimental need and limited by resistive heating of the coil to a maximum duration of 5 s for the maximum current of 6 A. In the presence of the PTF, polarisation builds up on the substrate in solution according to SABRE, which results in a net magnetisation along x, the same direction as the PTF field. After build-up, the PTF current is turned off adiabatically over ~150 ms (d_2). This allows the hyperpolarised magnetisation to re-orientate to the Earth's magnetic field direction, the z-axis. In order to detect the hyperpolarised magnetisation within the Earth's field, an *r.f* pulse, angle θ, is applied with the B_1 coil, which tilts the magnetisation vector towards x-y. The resulting

vector precession induces a current in a coil to create the signal. An acquisition delay of 25 ms (d_3) is needed for coil ring-down. An optional delay (d_4) can be set after the release of the p-H_2 pressure. This is usually followed by another delay of 3 s (d_5) which allows time for the switching-off of the p-H_2 bubbling and subsequent out-gassing of H_2 from the solution.

This is essentially the same pulse sequence used to perform non-SABRE-PHIP EF NMR experiments except that in a standard thermally polarised experiment there is no bubbling of p-H_2 and the polarisation transfer field is used to pre-polarise the sample and is typically a field of 18.8 mT (6 A) and that is applied for 4 s.

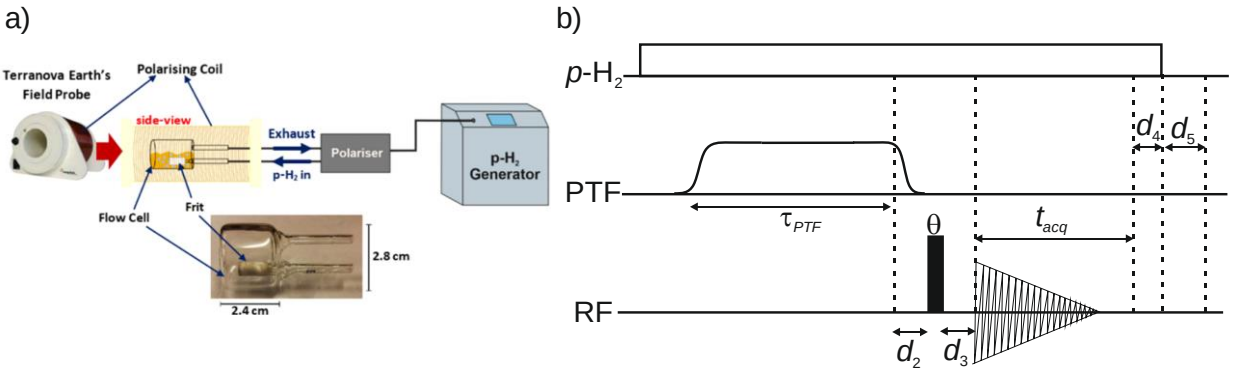

Figure 9.2: a) Reproduced from [207]. Schema of the *in situ* SABRE hyperpolarisation set-up. The reaction chamber containing the SABRE solution sits inside the EF NMR probe. p-H_2 from the generator is bubbled through the solution by passing through the frit within the chamber. The pressure difference across the p-H_2 inlet and the exhaust is set by the user and controlled by the polariser unit. b) Pulse sequence for *in situ* SABRE hyperpolarisation with EF NMR detection which is described in detail above.

9.2 General methods using the Spinsolve instrument (1 T)

The 1 T experiments were carried out at 28 °C, in the 43 MHz Spinsolve-Carbon by running the Prospa V3.40 software package (Magritek, Germany). The sample for SABRE hyperpolarisation were prepared as follows. In a typical experiment **I**, was mixed with an excess of the selected substrate and dissolved in a specified solvent. The resulting mixture was transferred to a NMR tube fitted with a Young's Tap and degassed by 3 freeze-thaw-pump cycles. The shake & drop method was employed to hyperpolarise the sample prior to the recoding of SABRE NMR spectra.

9.2.1 Shake and Drop

First, the SABRE catalyst was activated by adding 3 bar of p-H_2 into the headspace of the NMR tube which was then shaken vigorously for ten seconds before quickly transferring it into the probe for NMR signal acquisition. This procedure was repeated several times (typically 5 repeats) until hydride signals in the region -13 and -18 ppm disappeared, which indicated full sample activation.

Once activated, single-scan thermal ^{1}H NMR spectra were acquired to provide the reference needed for SABRE enhancement factor quantification and percentage polarisation calculations. For each

subsequent SABRE experiment, the head-space of the NMR tube was evacuated and charged with 3 bar of fresh *p*-H_2 and shaken vigorously again for 10 seconds, unless specified otherwise.

A 6.5 mT home-made hand-held magnet "shaker" was often used to set the PTF accurately. The sample was placed inside the shaker that produce the required magnetic field for polarisation transfer before being transferred into the NMR for detection. Devices were available for fields between 3.0 mT and 13.0 mT in steps if 10 mT[213].

9.2.2 Quantifications

For the 1T, 9.4 T and 11.7 T measurements, ^{1}H NMR signal enhancements were calculated by dividing the hyperpolarised integral intensity by the corresponding intensity from a 1 scan thermal spectrum recorded and processed under the same conditions.

The percentage polarisation values in the Earth magnetic field were obtained by comparison to a calibration plot derived for water. This reference plot demonstrated that the signal increases linearly with increase in volume of H_2O and hence number of ^{1}H nuclei. This is true for a volume of H_2O up to 250 mL approximately. Above that volume the linearity does not hold anymore. The resulting P_{SABRE} is given by Equation 9.2 and 9.3 where C_{REF} comes from the water calibration.

$$\frac{P_{SABRE}}{P_{REF}} = \frac{S_{SABRE}}{S_{REF}} \qquad (9.2)$$

$$P_{SABRE} = \frac{S_{SABRE}}{S_{REF}} \times P_{REF} = C_{REF} \times S_{SABRE} \qquad (9.3)$$

S_{SABRE} is the signal per mol of ^{1}H for the SABRE spectrum, S_{REF} is the signal per mol of ^{1}H for a reference, P_{REF} is the polarisation level of the reference, and C_{REF} is the calibration constant that relates the SABRE signal to the polarisation level. Further information relating to this calibration methodology is found in Hill-Casey *et al.*[207] .

9.2.2.1 Relaxation quantification

Hyperpolarised T_1 relaxation times were measured at 1 Tesla using a single shot approach. A series of 15 ^{1}H NMR acquisitions were carried out with the increasing pulse angle θ_n (see section 3.3.2.2 Figure 3.12.d) set to use an equal fraction of the available magnetisation each time. A variable delay δt_n was allowed between each acquisition to sample a full T_1 decay curve[207].

Hyperpolarised longitudinal relaxation times T_1 in the Earth's magnetic field were measured as follows (see section 3.3.2.2 Figure 3.12.c). During the whole experiment, *p*-H_2 was bubbled. Then a PTF of 6.5 mT was then turned on for ~10 s to enable polarisation build-up. This field is then turned off adiabatically to allow the created magnetisation to reorient with Earth's magnetic field. Subsequently, a variable delay τ is sampled, followed by a 90° pulse. This sequence is repeated several times whilst incrementing the delay τ.

9.3 General High field NMR methods

High-field NMR experiments were conducted on Bruker Advance III 400 and 500 MHz spectrometers. The ^{1}H NMR frequencies were 400.1 and 500.1 MHz, respectively. The ^{13}C NMR frequencies were 100.6 and 125.8 MHz; ^{15}N data was recorded at 50.7 MHz, ^{31}P data was recorded at 162.0 and 200.5 MHz. Bruker Topspin software, version 3.6.2, was used for data acquisition and processing. Chemical shifts are quoted as parts per million (ppm) and referenced to tetra-methyl silane (TMS).

The phosphine ligands **A**-**Q**, dimethyl-sulfoxide, the amines **1**, **2** and **3**, DMSO, acetonitrile, pyridine and the solvents were all purchased from Sigma Aldrich, Fluorochem or Alfa-Aesar and used as supplied without further purification.

IrCl(COD)(IMes) (**I**) (where IMes = 1,3-bis(2,4,6-trimethyl-phenyl)imidazole-2-ylidene and COD = cis,cis-1,5-cyclooctadiene) and $[Rh(COD)(PPh_3)_2]$ (**II**) (where PPh_3 = triphenyl phosphine) were synthesized in our laboratory according to literature procedures[265].

9.3.1 *para*-Hydrogen generation

p-H_2 is prepared by flowing H_2 gas over a silica/$FeCl_3$ catalyst at 28 K which is 99 % pure. This was used for hyperpolarisation for the 1 T, 9.4 T and 11.7 T measurements. The EF data used a Bruker parahydrogen generator, which operates at 38 K, and delivers 89 % *p*-H_2.

9.4 Samples preparation procedures

9.4.1 Amine samples preparation For EF NMR study

The samples used in the amine studies were prepared by dissolving 5.1 mM (15 mg) of **I** in 4.6 mL of solvent (chloroform or chlroform-d_3). The specified amines was added as indicated in the text, and the co-ligand DMSO-d_6 as needed (see Tables 9.1 and 9.2). In the case of substrate **3**, the DMSO-d_6 mixture involved a 127.5 mM solution (25 eq.) of **3** and a similar 125.5 mM of DMSO-d_6 relative to **I**. 4 mL of each solution was utilised in the EF NMR analysis and the remainder placed in an NMR tube for 1T studies. At the start of each experimental session, the solution of EF work was injected into the reaction chamber through the *p*-H_2 inlet using a syringe.

Table 9.1: Sample compositions for amines **1** hyperpolarisation in the Earth's magnetic field

	25 **1**/ 25DMSO	20 **1**/ 20DMSO	15 **1**/ 15DMSO	10 **1**/ 10DMSO	5**1**/ 5DMSO
I (mM)	15 mg, 5.1 mM	15 mg, 5.1 mM	15 mg, 5.1 mM	15 mg, 5.1 mM	15 mg, 5.1 mM
1 volume	63.9 µL	51.2 µL	38.4 µL	25.6 µL	12.8 µL
1 Concentration	127.5 mM	102 mM	76.5 mM	51 mM	25.5 mM
DMSO-d_6 volume	41.4 µL	33.16 µL	24.9 µL	16.6 µL	8.3 µL
DMSO-d_6 concentration	127.5 mM	102 mM	76.5 mM	51 mM	25.5 mM
$CDCl_3$	4.6 mL	4.6 mL	4.6 mL	4.6 mL	4.6 mL

Table 9.2: Sample compositions for amines **2** hyperpolarisation in the Earth's magnetic field

	50 **2**/ 50 DMSO	50 **2**/ 40DMSO	50 **2**/ 30DMSO	50 **2** / 20DMSO	50 **2** / 10 DMSO
I (mM)	15 mg, 5.1 mM	15 mg, 5.1 mM	15 mg, 5.1 mM	15 mg, 5.1 mM	15 mg, 5.1 mM
2 Volume, Concentration	153.4 µL, 255 mM	153.4 µL, 255 mM	153.4 µL, 255 mM	153.4 µL, 255 mM	153.4 µL, 255 mM
DMSO-d_6 volume, conc.	71.8 µL, 255 mM	66.3 µL, 204 mM	49.7 µL, 153 mM	33,15 µL, 102 mM	16.57 µL, 51 mM
$CDCl_3$	4.6 mL	4.6 mL	4.6 mL	4.6 mL	4.6 mL

9.4.2 Preparation of $[IrCl(COE)]_2$

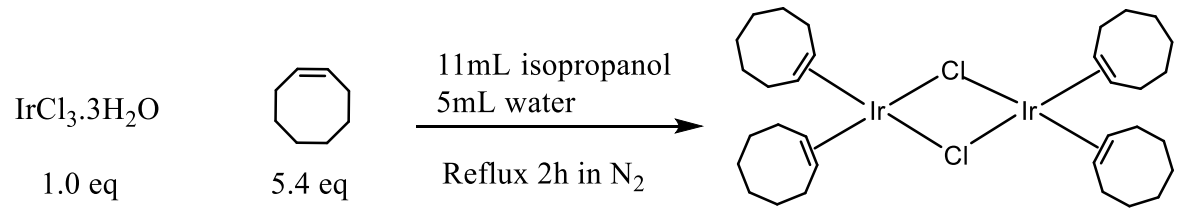

$IrCl_3.3H_2O$ (1.0 g 2.83 mmol 1.0 eq.) and *cis*-cyclooctene (2.0 mL 15.35 mmol 5.4 eq) were refluxed in a mixture of isopropanol (11 mL) and water (5 mL) under a steady stream of nitrogen. After 2 hours, the dark red coloured solution changes to orange yellow and $[IrCl(COE)]_2$ precipitates out from the solution. The precipitate was collected by filtration under nitrogen and washed with ice-cold methanol

to remove the traces of unreacted cyclooctene. Finally, the orange yellow powder was dried under vacuum and stored in nitrogen atmosphere in the freezer. (Yield 89%)

9.4.3 Preparation of $[IrCl(DMSO)_3]$ (**III**)

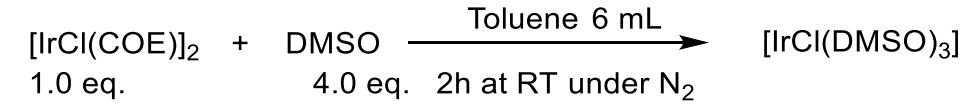

Drop wise addition of DMSO (0.9 mL $1.26.10^{-5}$ mol) to a bright suspension of $[IrCl(COE)]_2$ (0.265 g, 0.39 mmol) in toluene (6 mL) produced a limpid yellow solution. Stirring at room temperature for *ca*. 3 hours resulted in a formation of yellow lemon precipitates, which were filtered off, washed with diethyl ether and dried under vacuum. The same procedure was used to synthesise deuterated **III-*d*$_{18}$**. 1H NMR in toluene at 3.15, 3.91 ppm confirm (Yield 81%)

9.4.4 Preparation of $IrCl(COD)(PCy_3)$ (**IV**)

In a ampoule, 500 mg of $[Ir(COD)Cl]_2$ was dissolved in 12 mL of toluene which was degassed beforehand. The reaction is carried out in a Glovebox under nitrogen atmosphere. A solution of 371.6 mg (1.8 equivalence) of PCy_3 was separately dissolved in 7 mL toluene. Then, the PCy_3 toluene solution was added dropwise into the solution of $[Ir(COD)Cl]_2$. The final mixture was stirred for 2 hrs at room temperature, which yielded a yellow precipitate. This latter was collected and dried under vacuum. The ^{31}P NMR spectrum yielded a single resonance at 14.78 ppm for the pure product.

9.5 Hyperpolarisation reaction of phosphine 10-18 and 44-51

For phosphorus containing **10**-**18** hyperpolarisation reactions, 5 mM of **I** was reacted with (1, 2 or 5 equivalences) of phosphine in dichloromethane or methanol with the specified co-ligand as stated in Table 9.3. For the samples of **III** and phosphines **44**-**51** were used in toluene-d_8 as stated in table 9.4. The corresponding sample composition data for the samples used with EF NMR detection are given in Table 9.5. The phosphines were treated as air sensitive.

Table 9.3: Sample composition of for the hyperpolarisation reaction of phosphine **10-18**. In some case, a co-ligand was used.

	10	**11**	**12**	**13**	**14**	**15**	**16**	**17**	**18**
I	5 mM 2 mg	5 mM 2 mg	5 mM 2 mg	5 mM 2 mg	5 mM 2 mg	5 mM 2 mg		5mM 2mg	5mM 2mg
II (mM)							1 mg		
Phosphine	2 eq. =1.09 µL; 5 eq. = 2.72 µL	5 eq. =3.16 mg; 1eq. =0.70mg	2 eq. =1.01 mg	2 eq. =1.26 µL; 5 eq. =3.16 µL	1 eq. =0.58 µL	2 eq. =0.89 µL	10 eq. =7.13 µL	2 eq. =1.84 mg; 3eq. =2.76 mg	4 eq. =1.35 mg
DMSO	1 eq. = 0.22 µL	1 eq. 1.1 µL						2eq. =0.5 µL	1eq.=0.2 µL
Pyridine	1 eq. = 0.25µL							3 eq. =0.75 µL	
Acetonitrile							2 eq.=0.32 µL		
Benzylamine		5 eq. =1.7 µL; 4 eq.=1.36 µL			3 eq. =1.02 µL	3 eq. =1.02 µL			
Solvent (mL)	0.6	0.6	0.6	0.6	0.6	0.6	0.6	0.6	0.6

Table 9.4: samples composition for hyperpolarisation reaction of phosphine **44-51**.

	44	**45**	**46**	**47**	**48**	**49**	**50**	**51**
III (mM)	3 mg 12.mM	2.5mg 9.0 mM	5 mg18.0mM	2.6 mg 8.8 mM	5 mg 18.0 mM	5 mg 18.0mM	2.5 mg 9.0 mM	2.5 mg 9.0 mM
Phosphine (mM)	2 eq. 2.5 mg	1 eq. 1.1 mg	1 eq. 2.8 mg	1 eq. 1.1 mg	1 eq. 3.60 mg	1 eq. 3.0 mg	3 eq. 2.9 mg	2 eq. 1.4 µL
Toluene-d_8 mL	0.6	0.6	0.6	0.6	0.6	0.6	0.6	0.6

IV (mM)	6.76 mM 2.5 mg
DMSO	1.4 µL (5 eq.)
Toluene-d_8 or dichloromethane- d_2 (mL)	0.6

9.5.1 EXSY measurements using *p*-H_2

Due to the weak thermally polarised hydride signals for the *bis*-phosphine **62**, recording normal EXSY measurements was impractical. The pulse sequence of Figure 9.3 described in 1995[266] was therefore used in conjunction with *p*-H_2[267]. It refocuses the antiphase magnetisation created by the initial $\pi/4$ pulse a with a τ-π-τ sandwich where τ is set to $1/4J_{HH}$. X refers to ^{31}P. However, as the sample is filled with fresh *p*-H_2 and shaken each time, a temperature fluctuation results which increases the error in the rate data.

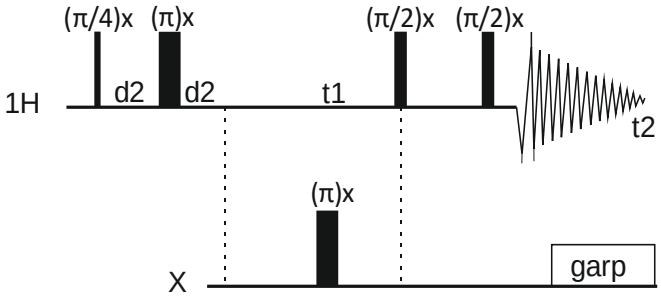

Figure 9.3: Pulse sequence used with *p*-H_2 EXSY.

9.5.2 2D correlation NMR using *p*-H_2

The 2D correlation NMR using *p*-H_2 was also used extensively in this thesis. Compared to a traditional COSY experiment[268], COSY-PHIP experiment includes *p*-H_2 starting magnetisation in the product operators. As explained by Dr Chris Sleigh[269], the initial $(\pi/2)_x$ pulse is then replaced by a $(\pi/4)_x$ pulse. Therefore, the cross-peaks and diagonals arise from the hyperpolarised singlet state magnetisation, leading to large increases of the signal recorded. The resonances that are coupled are identified by a significant gain of NMR time whilst keeping the same information as the traditional COSY. COSY-PHIP was developed in 1995[266] along with other two-dimensional NMR pulse sequences such as HMQC-PHIP, HSQC-PHIP and EXSY/NOESY-PHIP[266, 267, 270]. In addition, a ^1H-X HMQC-PHIP experiment, ^1H coupling to the heteronuclei X, for example ^{31}P must be first evaluated in order to optimise the delay for magnetisation transfer. The standard experimental method for these types of experiment is to pressurise the sample with *p*-H_2 before a rapid transfer in the NMR probe for an acquisition of usually 2~3 minutes, depending of number of data point (TD) and number of scan (NS) selected.

9.5.3 Detection of hyperpolarised phosphine complexes at EF NMR

Table 9.5: samples composition for hyperpolarisation reaction at the EF NMR of phosphine **44**, **45** and **46**.

Phosphine	**44**	**45**	**46**
III (mM)	(26mg) 13.5mM	(26mg) 13.5mM	(26mg) 13.5mM
Phosphine (mM)	(0.7 eq.) mg	(1.8 eq.) 1.1 mg	(1 eq.) 2.8 mg
Toluene mL	4	4	4

Signal detected in the EF NMR system.

The Loop pulse sequence (Figure 9.5) was designed for the detection of the hyperpolarised hydride signals at the EF NMR. Instead of the pulse sequence of Figure 9.4, there is no need for a PTF and a time for build-up because the hyperpolarised complexes itself is being observed. *p*-H_2 is bubbled continuously during the whole NMR experiment at the Earth's magnetic field, which is the field experienced by the spins. Firstly, an internal loop, consisting of the pulse Θ, the delay for coil ring down and the NMR acquisition is repeated *n* time. The repetition time has to be lower than the maximum bubbling time. Then, an external loop, which consist of repeating the whole experiment *m* time with the additional 60 s delay (d_3) for the *p*-H_2 generator pressure recovery. Hence, EF NMR signal is an accumulation of *n*m* experiments. This pulse sequence is therefore suitable for hyperpolarised hydride signals detection at the Earth's field due to its very weak signal.

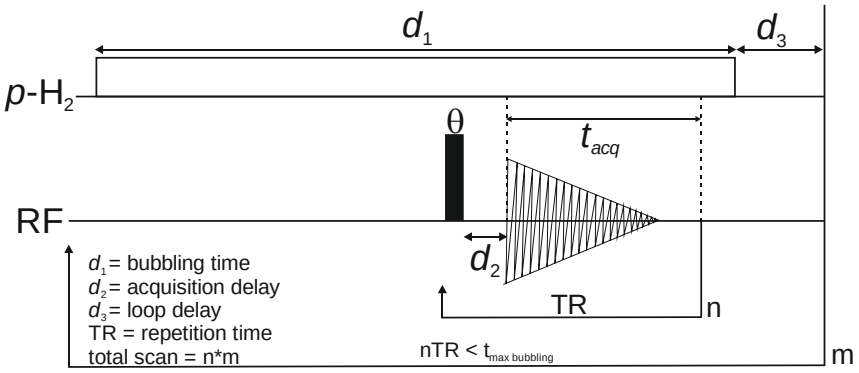

Figure 9.4: Pulse sequence loop for phosphine complexes

9.6 Chapter 5: NMR Characterisation data for phosphine complexes

9.6.1 Characterisation of 13.5 mM Ir(COD)(PCy_3)Cl with 5 eq. DMSO in 0.6 mL of dichloromethane-d_2 at 253 K: 92

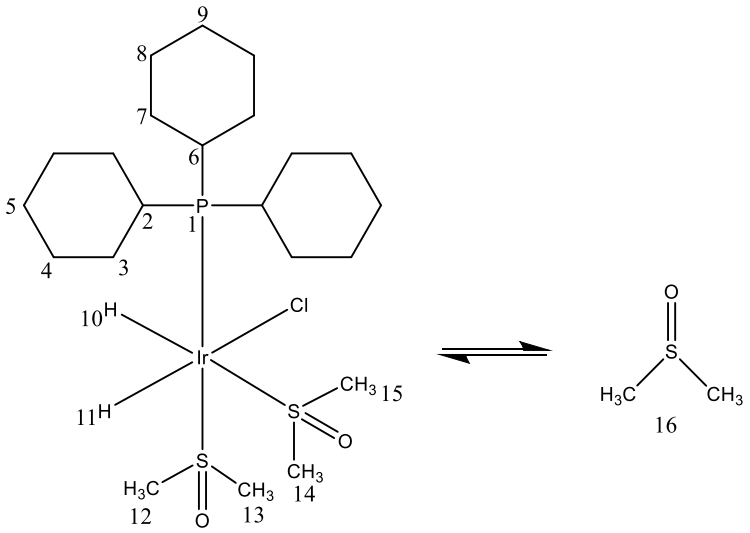

Resonance number	^{1}H (ppm)	^{13}C (ppm)	^{31}P{^{1}H} (ppm)
1			21.6, s
2	2.30, q, J(HH) = 10.7 Hz, J(PH) = 10.7	60.17, d, J(CP) = 33 Hz	
3	1.96, t, J = 10.7 Hz	55.84, J(CP) = 95 Hz	
4	1.79, m	53.45, J(CP) = 33 Hz	
5	1.40, m	56.14	
6	1.26, dd, J(HH) = 5.6 Hz, J(PH) = 19.2 Hz	53.58	
7	2.13, m	51.44	
8	1.48, m	52.16	
9	1.67, m	52.60	
10	-16.89, dd, J(HP) = 19.8 Hz, J(HH) = 5.9 Hz		
11	-21.69, dd, J(PH) = 17.8 Hz, J(HH) = 5.9 Hz		
12	3.47, s	58.07	
13	3.45, s	46.94	
14	3.35, s	50.96	
15	3.25, s	42.15	
16	2.59, s	41.11	

9.6.2 Characterisation of 18.0 mM $Ir(DMSO)_3Cl$ 5mg with 1 eq. (3.1mg) $P(Ph\text{-}CH_3)_3$ (M) in 0.6 mL of toluene-d_8 at 263 K: 88and 47

A toluene solution of 30 mg of **III** was reacted *in-situ* with 1 eq. of **47** for two hrs allowing the formation of phosphine *mono*-substitution. Then the solution was dried under vacuum and the excess of DMSO washed off with hexane. The resulting yellow crude obtained is the 16 electron complex $IrCl(DMSO)_2(P_{47})$ which after reaction with H_2 yields a total conversion of **88** complex. Then **88** was characterised at 263 K.

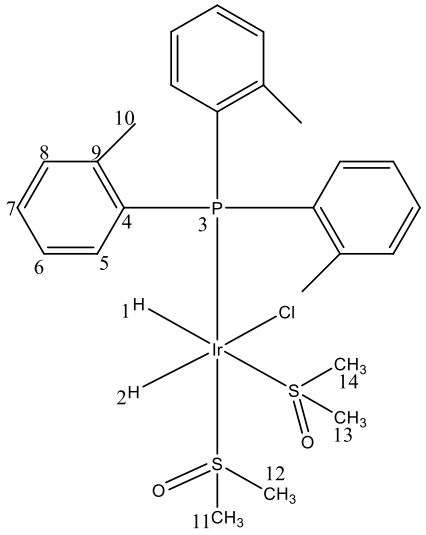

Resonance number	^{1}H (ppm)	^{13}C (ppm)	^{31}P (ppm)
1	-16.23, dd, J(HH) = 5.8 Hz J(HP) = 22 Hz		
2	-20.60, dd, J(HH) = 5.8 Hz J(HP) = 22 Hz		
3			-7.9
4		137.17	
5	7.00	133.04	
6	6.90, m, J(HH) = 8.0 Hz	126.34	
7	7.09, m, J(HH) = 7.8 Hz	128.82	
8	7.03, m, J(HH) = 7.1 Hz	130.25	
9		124.89	
10	2.45, s	57.46	
11	2.97, s	44.42	
12	3.28, s	41.46	
13	2.19, s	48.95	
14	1.61, s	40.62	

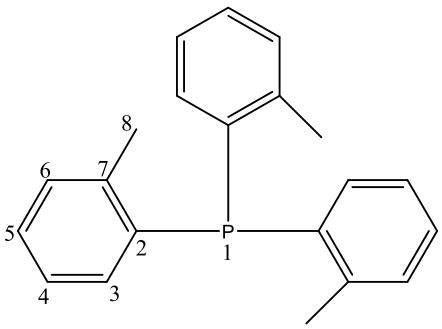

Resonance number	^{1}H (ppm)	^{13}C (ppm)	^{31}P (ppm)
1			-29.8
2		134.14	
3	7.02	128.86	
4	7.15	128.02	
5	7.08	125.15	
6			
7			
8	2.44	21.05	

9.6.3 Characterisation of 18.0 mM $Ir(DMSO)_3Cl$ with 2 eq. $P(Ph\text{-}O\text{-}CH_3)_3$ (47) in 0.6ml of toluene-d_8 at 253 K: 75 and 76

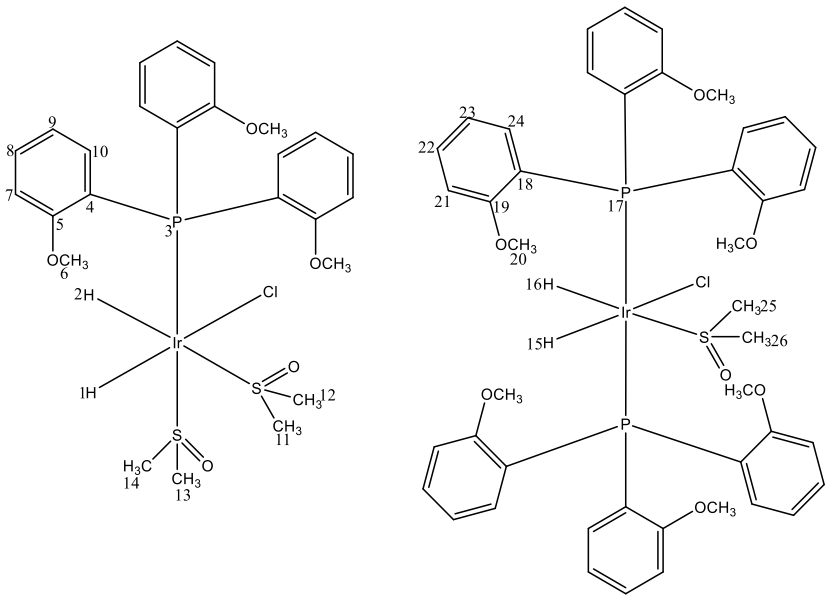

Resonance number	^{1}H (ppm)	^{13}C (ppm)	^{31}P (ppm)
1	-15.42, dd, J(HH) = 6 Hz J(HP) = 19.42 Hz		
2	-19.4, dd, J(HH) = 6 Hz J(HP) =18 Hz		
3			0.46
4		126.47 J(CP) = 63 Hz	
5		162.0 J(HC) = 14.5 Hz	
6	3.25	54.21	
7	6.76	113.12 J(HC) = 13 Hz	
8	6.69		
9	6.75	113.20 J(HC) = 12 Hz	
10	7.97	136.15 J(HC) = 13 Hz	
11	3.18	46.25	
12	2.80	56.88	
13	3.07	41.67	
14	3.03	49.18	
15	-13.87, dt, J(HH) = 6.3 Hz J(HP) = 19.9 Hz		
16	-20.28, dt, J(HH) = 6.3 Hz J(HP) = 15.4 Hz		
17			3.85
18		127.96 J(CP) = 29.0 Hz	
19		160.90 J(CH) = 14 Hz	
20	3.27	54.23	
21	8.06	136.30	
22	6.76	113.12 J(CH) = 13 Hz	
23	6.69		
24	6.79	113.20 J(CH) = 12 Hz	
25	3.22	42.24	
26	3.48	47.58	
27	-11.35, dd, J(HH) = 4.7 Hz J(HP) = 148.6 Hz		

28	-19.47, dd J(HH) = 4.7 Hz J(HP) = 10.4 Hz		
29	2.89	54.25	
30	3.11	44.89	
31	2.65	43.52	
32	3.08	59.22	
33			-5.05
34		126.25 J(CP) = 49 Hz	
35	3.28	54.19	
36		160.85 J(CH) = 13.5 Hz	
37	8.17	136.45 J(CH) = 13.3 Hz	
38	6.80	113.18 J(CP) = 12.2 Hz	
	6.74		
	7.74		

9.6.4 Characterisation of 18.0 mM $Ir(DMSO)_3Cl$ with 1 eq. of $PPh(Cy)_2$ (46) in 0.6 mL of toluene-d_8 at 263 K: 75

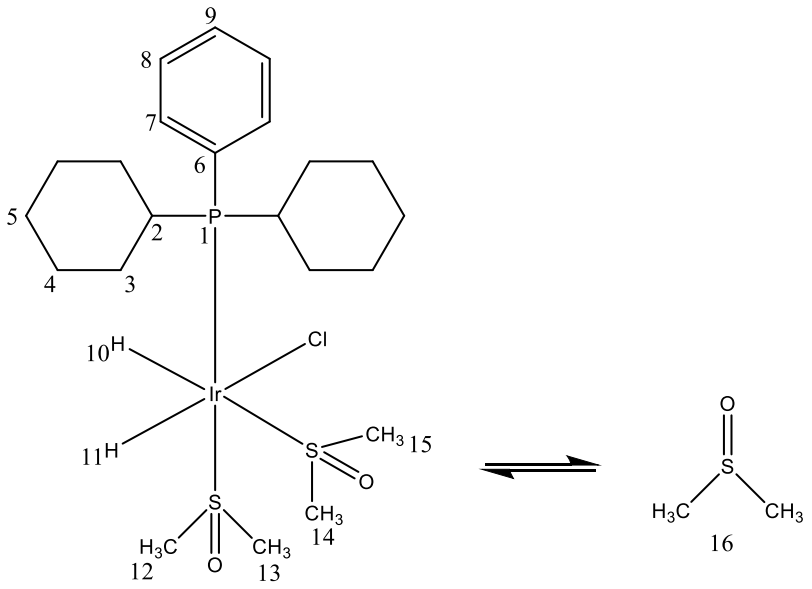

Resonance number	^{1}H (ppm)	^{13}C (ppm)	^{31}P (ppm)
1			1.08
2	2.48	33.62	
3	1.80	26.86	
4	1.72	28.28	

5	1.57	26.29	
6		131.88, J(PC) = 52 Hz	
7	8.31	135.07	
8	7.29	127.36	
9	7.15	129.64	
10	-16.71, dd, J(HP) = 21 Hz J(HH) = 6.1 Hz		
11	-20.90, dd, J(HP) = 19.3 Hz J(HH) = 6.1 Hz		
12	3.26, s	41.77	
13	3.12, s	50.09	
14	2.71, s	57.24	
15	3.04, s	45.23	
16	1.72, s	40.28	

9.6.5 Characterisation of 18.0 mM $Ir(DMSO)_3Cl$ with 2 eq. of $P(Ph)_2Me$ (50) in 0.6 mL of toluene-d_8 at 273 K: 91 and 50

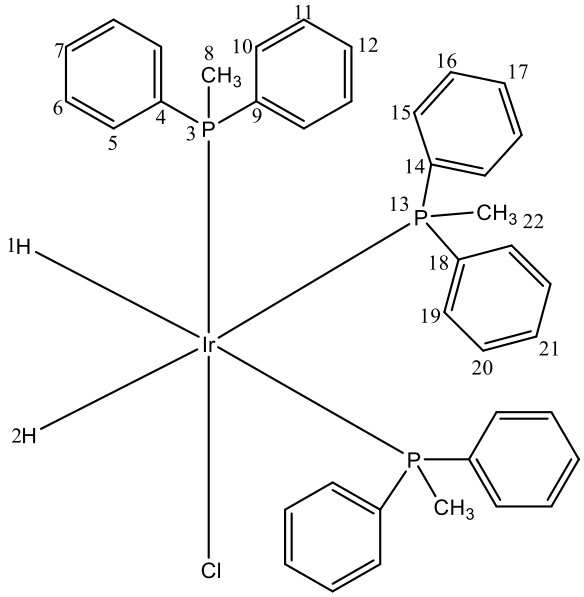

Resonance number	^{1}H (ppm)	^{13}C (ppm)	^{31}P (ppm)
1	-10.33, second order multiplet*		
2=1			
3			-10.65, t, J(PP) = 5 Hz

4		139.69 J(PC) = 60 Hz	
5	7.33, m, J(PH) = 11 Hz	132.32	
6	6.84	127.67	
7	6.89	132.35	
8	1.55, d, J(PH) = 10 Hz	D, 22.1 J(8-3) = 45.7 Hz	
9		137.60 J(PC) = 36 Hz	
10	7.90	134.5	
11	7.05	128.8	
12	6.99	127.81	
13			-18.9, d, J(PP) = 5 Hz
14		138.90 J(PC) = 46.7 Hz	
15	7.67, m, J(PH) = 8 Hz	133.22	
16	6.96	127.25	
17	7.13	128.78	
18		137.59 J(PC) = 37 Hz	
19	7.14, m, J(PH) = 8.3 Hz	133.04	
20	7.09	127.25	
21	7.00	127.82	
22	1.78, d, J(PH) = 7.5 Hz	15.1	

*The hydride *trans* ^{31}P arrangement is reflective of a second order spin system and whilst appearing with the features expected for an $[AM]_2X$ arrangement, there was insufficient information to identify specific couplings.

9.6.7 Characterisation of 18.0 mM $Ir(DMSO)_3Cl$ with 1 eq. of $P(Bn)_3$ (49) in 0.6 mL of toluene-d_8 at 273 K: 63, 79 and 80

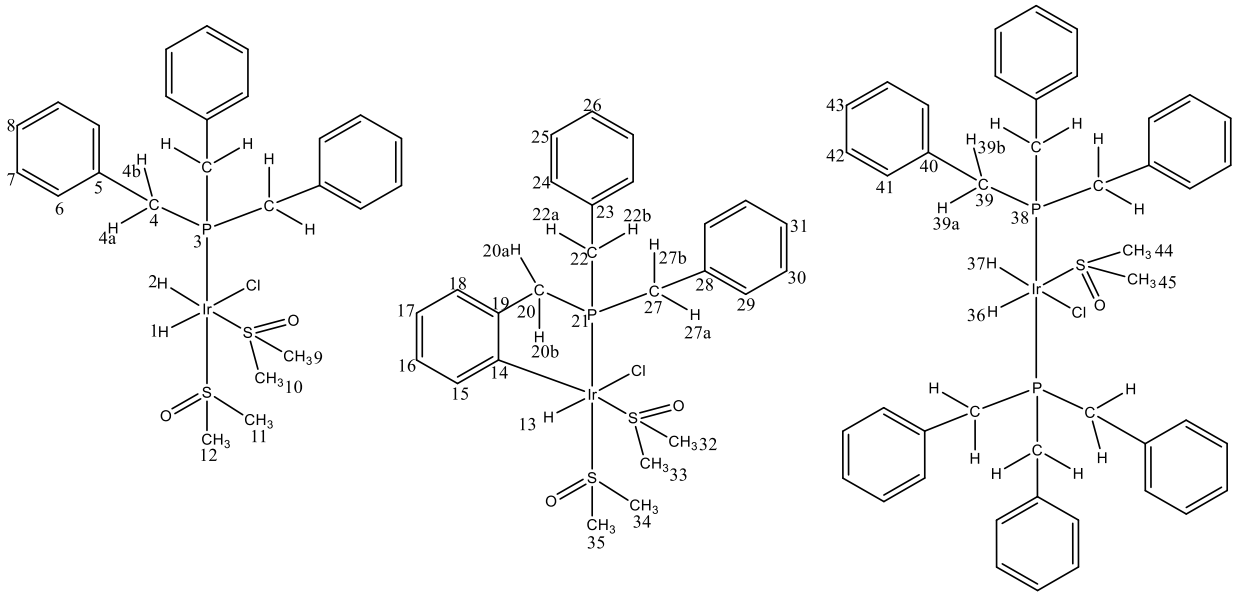

Resonance number	^{1}H (ppm)	^{13}C (ppm)	^{31}P (ppm)
1	-20.52, dd,		

	J(PH) = 15.6 Hz J(HH) = 6.1 Hz		
2	-15.96, dd, J(PH) = 19.6 Hz J(HH) = 6.1 Hz		
3			8.42
4		32.81	
4a	3.72		
4b	3.60		
5		152.76	
6	7.24	130.96	
7	7.14	128.08	
8	7.09	126.29	
9	3.04	46.15	
10	2.49	56.92	
11	3.22	41.52	
12	2.87	49.94	
13	-15.93, d, J(PH) = 17.2 Hz		
14		144.47	
15	8.66	138.20	
16	7.02	124.25	
17	7.10	128.15	
18	7.40	130.23	
19		180.81	
20		30.85	
20a	3.71		
20b	4.50		
21			30.45
22		38.61	
22a	3.84		
22b	2.64		
23			
24	7.39		
25	6.96		
26	6.84		
27		34.94	
27a	2.62		
27b	3.24		
28		154.87	
29	6.97	124.32	
30	7.10overlap		
31	7.02overlap		
32	2.90	44.31	
33	2.29	51.47	
34	2.03	39.8	
35	2.79	40.42	

36	-21.54, dt, J(PH) = 13.5 Hz J(HH) = 6.7 Hz		
37	-15.31, dt, J(PH) = 20.4 Hz J(HH) = 6.7 Hz		
38			4.15
39		33.54	
39a	3.39		
39b	3.53		
40		134.66	
41	7.16	128.69	
42	7.13	128 overlap	
43	7.11	126.72	
44	2.67	35.11	
45	2.66	35.6	

9.6.8 Characterisation of 9.0 mM $Ir(DMSO)_3Cl$ (2.5 mg) with 3 eq. of $P(OPh_3)$ (50) in 0.6 mL of toluene-d_8 before H_2 addition at 273 K: 69

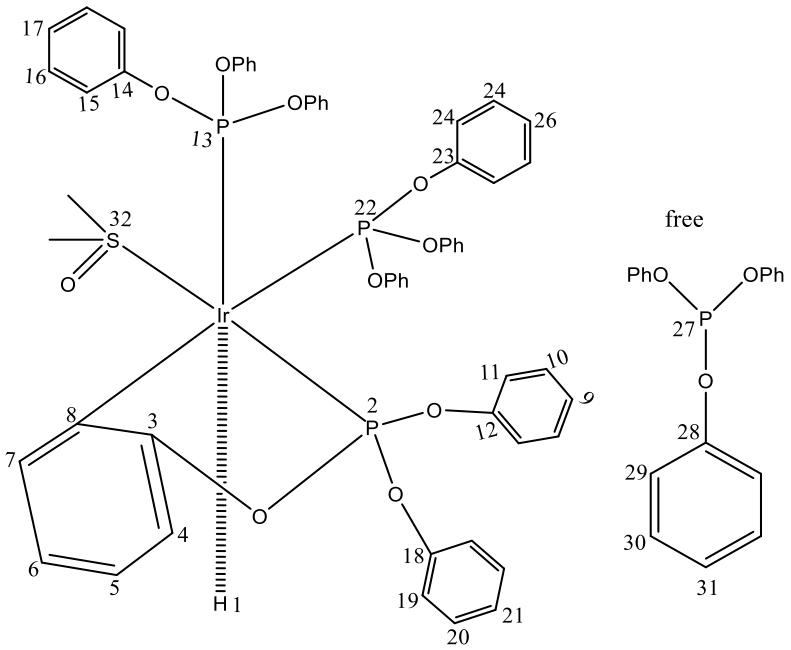

Characterisation data of $Ir(DMSO)_3Cl$ 2.5 mg 3 eq. $P(OPh)_3$ (2.90 µL) in toluene-d_8 before p-H_2 298 K

Resonance number	^{1}H (ppm)	^{13}C (ppm)	^{31}P (ppm)
1	-9.31, td, *cis* J(HP) = 19.1 Hz *trans* J(HP) = 276.3 Hz		
2			96.74, q, J(PP) = 19.4 Hz
3		151.9	
4	7.50 J(HH) = 7.8 Hz	121.77	
5	6.90	129.13	
6	6.97		
7	8.77, t, J(HH) = 7.8 Hz	137.21	
8		125.09	
9	6.97	129.08	
10	6.88	129.17	
11	7.03	129.55	
12		110.04	
13			87.48, m, J(PP) = 19.4 Hz
14		152.06	
15	7.36	121.99	
16	6.94	129.29	
17	6.84	124.55	
18		overlap	
19	6.88	125.23	
20	7.15	120.79	
21	7.02	122.90	
22			72.25, q, J(PP) = 31 Hz J(PP) = 18 Hz
23		151.31	
24	6.99	121.33	
25	6.87	124.05	
26	6.78	124.19	
27			127.5, s
28		137.19	
29	7.14	127.95	
30	7.17	128.87	
31	7.06	128.09	
32	2.14	46.39	

9.6.9 Characterisation data of 9.0 mM $Ir(DMSO)_3Cl$ with 1 eq. $P(OPh)_3$ (50) in toluene-d_8 after H_2 addition and the sample warmed in hot water 298 K: 85 and 86

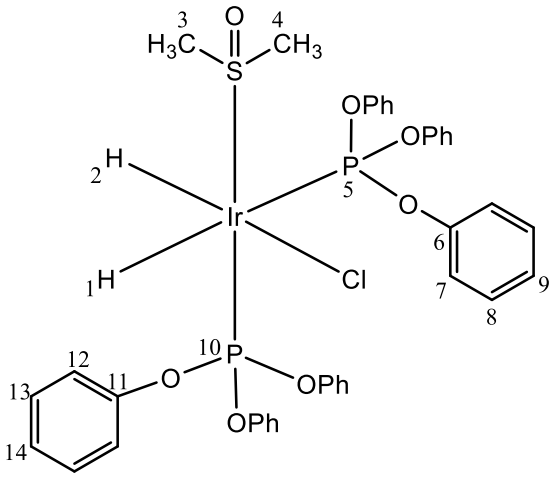

Resonance number	^{1}H (ppm)	^{13}C (ppm)	^{31}P (ppm)
1	-10.15, dd, *trans* J(HP) = 237.3 Hz *cis* J(HP) = 20.0 Hz J(HH) = 6 Hz		
2	-19.06, dd, *cis* J(HP) = 13.6 Hz, J(HH) = 6 Hz		
3	2.64		
4	3.11		
5			Broad 98.4
6	overlap		
7	overlap		
8	overlap		
9	overlap		
10			80.12 J(PP) = 32 Hz
11	overlap		
12	overlap		
13	overlap		
14	overlap		

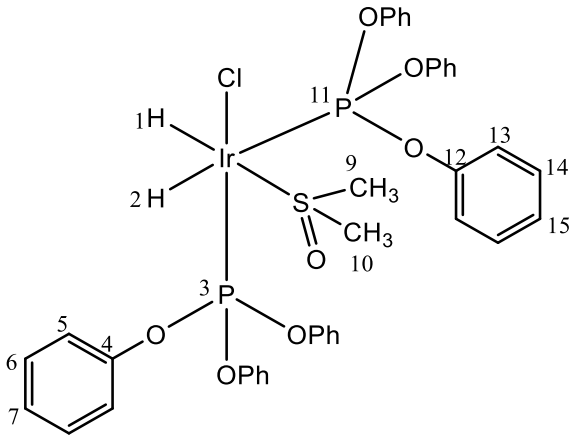

Resonance number	^{1}H (ppm)	^{13}C (ppm)	$^{1\ 31}$P (ppm)
1	-15.22, dd, *cis* J(HP) = 17.8 Hz J(HH) = 3.5 Hz		
2	-8.8, dd, *trans* J(HP) = 276 Hz *cis* J(HP) = 20.8 Hz J(HH) = 3.5 Hz		
3			94.03 J(PP) = 26 Hz
4	overlap		
5	overlap		
6	overlap		
7	overlap		
8	overlap		
9	overlap		
10	overlap		
11			Broad 72.40
12	overlap		
13	overlap		
14	overlap		
15	overlap		

9.6.10 Characterisation of 14.4 mM $Ir(DMSO)_3Cl$ with 1.78 eq. of PPh_3 (45) in 0.6 mL toluene-d_8 at 273 K: 53, 54, 55 and 56

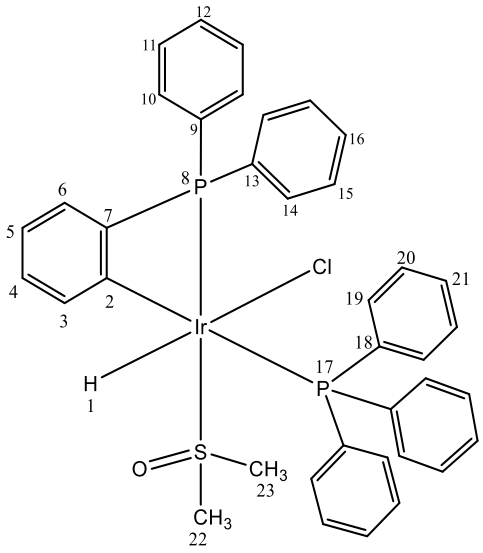

Resonance number	^{1}H (ppm)	^{13}C (ppm)	$^{1\ 31}P$ (ppm)
1	-18.02, dd, J(HP) = 18.2 Hz J(HP) = 11.0 Hz		
2		129.28	
3	7.90	134.89	
4	7.06	125.12	
5	7.02	128.89	
6	8.02		
7		129.28	
8			-92.96, d, J(PP) = 14 Hz
9		129.36	
10	7.07		
11	7.96	134.96	
12	6.98		
13		148.89	
14	6.89		
15	7.21	124.81	
16	~6.98		
17			-3.18, d, J(PP) = 14 Hz
18		137.2	
19	7.16	127.95	
20	7.01	127.79	
21			
22	2.78	39.34	
23	3.20	43.86	

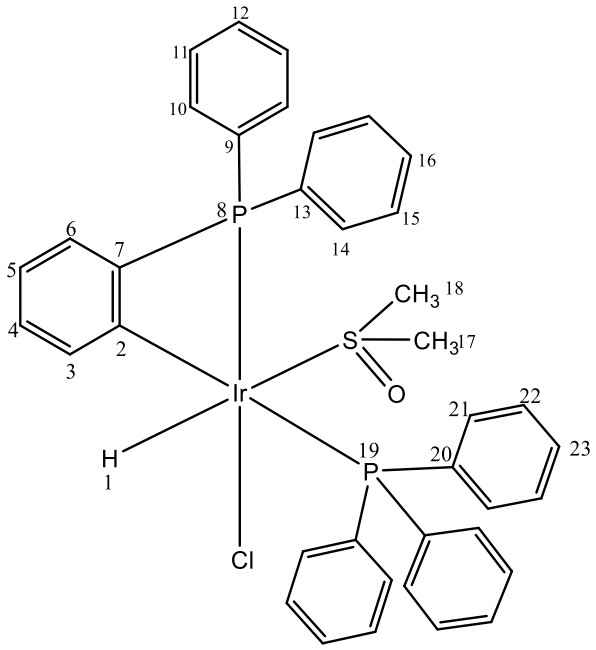

Resonance number	^{1}H (ppm)	^{13}C (ppm)	^{31}P (ppm)
1	-13.28, dd, J(HP) = 21.7 Hz J(HP) = 14.3 Hz		
2			
3	7.89	134.86	
4	6.91		
5	7.03		
6	7.80	134.36	
7			
8			-78.02 J(PP) = 5 Hz
9			
10	8.09	135.53	
11	6.72		
12	6.92		
13			
14	7.80	134.94	
15	7.78		
16	~6.92		
17	3.45	39.06	
18	2.13	43.52	
19			-2.75 J(PP) = 5 Hz
20			

21	7.91		
22	6.99		
23	6.72		

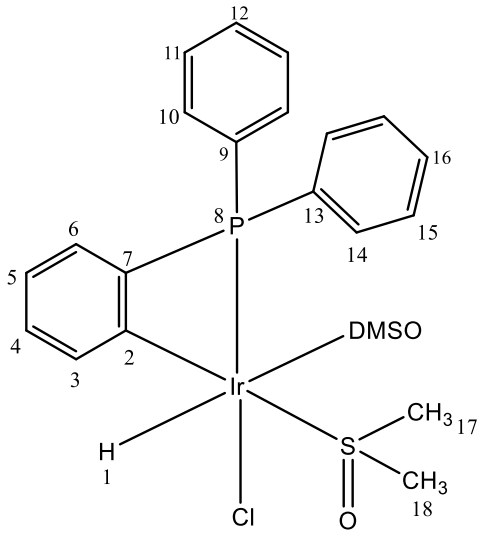

Resonance number	^{1}H (ppm)	^{13}C (ppm)	$^{1\ 31}$P (ppm)
1	-13.6, d J(HP) = 21.1 Hz		
2	overlap		
3	7.75		
4	6.98		
5	overlap		
6	7.66		
7	overlap		
8			-70.88
9	overlap		
10	6.89		
11	overlap		
12	overlap		
13	overlap		
14	8.41		
15	overlap		
16	overlap		
17	overlap		
18	overlap		

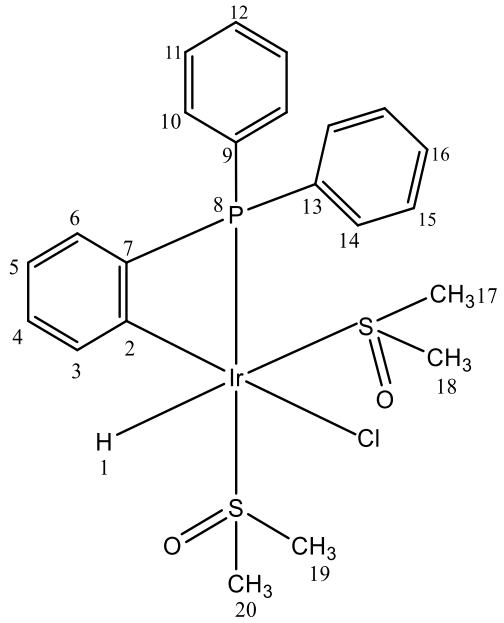

Resonance number	^{1}H (ppm)	^{13}C (ppm)	^{31}P (ppm)
1	-17.08, d J(HP) = 16.6 Hz		
2	overlap		
3	overlap		
4	7.00		
5	7.22		
6	6.89		
7	overlap		
8	overlap		-73.36
9	overlap		
10	8.10		
11	overlap		
12	overlap		
13	overlap		
14	6.81		
15	overlap		
16	overlap		
17	2.81, s	39.35	
18	3.15, s	49.56	
19	3.16, s	43.11	
20	2.83, s	~55	

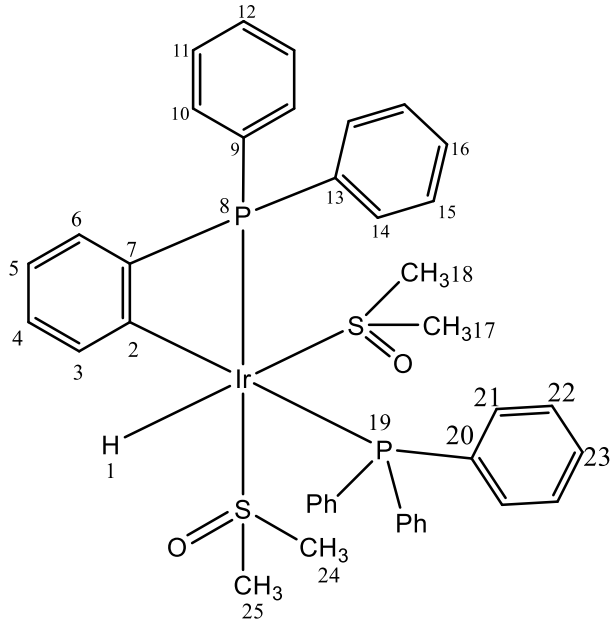

Resonance number	^{1}H (ppm)	^{13}C (ppm)	$^{1\ 31}$P (ppm)
1	-17.57, dd, J(HP) = 17.7 Hz J(HP) = 12.1 Hz		
2	overlap		
3	6.86	131.78	
4	6.77	127.71	
5	7.04	132.69	
6	6.95		
7	overlap		
8			broad, -92.37
9	overlap		
10	8.41	133.68	
11	overlap		
12	overlap		
13	overlap		
14	7.70	132.69	
15	overlap		
16	overlap		
17	overlap		
18	overlap		
19			broad, 2.75
20	overlap		
21	overlap		
22	overlap		
23	overlap		
24	2.78	39.35	
25			

9.6.11 Characterisation of 18.0 mM $Ir(DMSO)_3Cl$ with 1 eq. of $P(Ph)_3$ (45) in H_2 and 0.6 mL of toluene-d_8 at 263 K: 62, 58 and 60

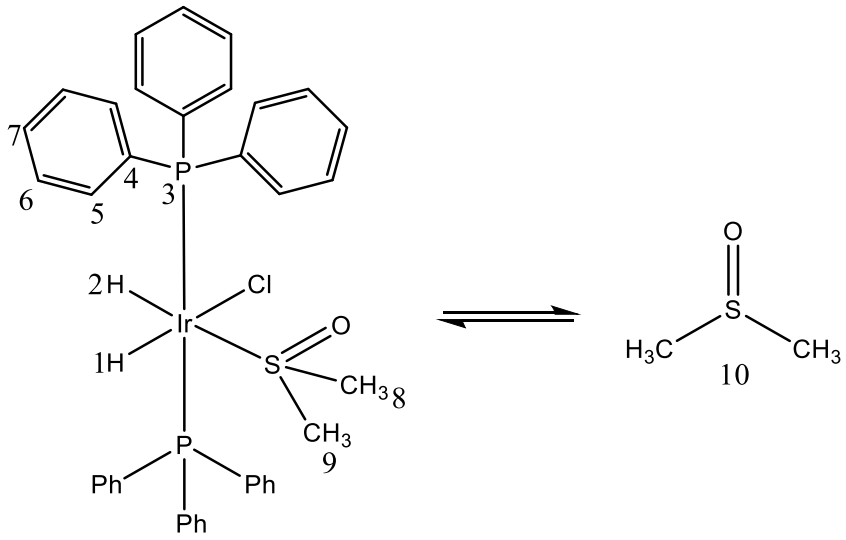

Resonance number	^{1}H (ppm)	^{13}C (ppm)	^{31}P (ppm)
1	-14.04, dt, *cis* J(PH) = 14.7 Hz J(HH) = 6.4 Hz		
2	-20.28, dt, *cis* J (PH) = 19.5 Hz J(HH) = 6.4 Hz		
3			9.20
4		129.83	
5	8.02	134.83	
6	7.09	127.77	
7	7.73	132.4	
8	2.35	45.13, J(CH) = 66 Hz	
9	2.13	20.49	
10	1.70	40.23, J(CH) = 70.0 Hz	

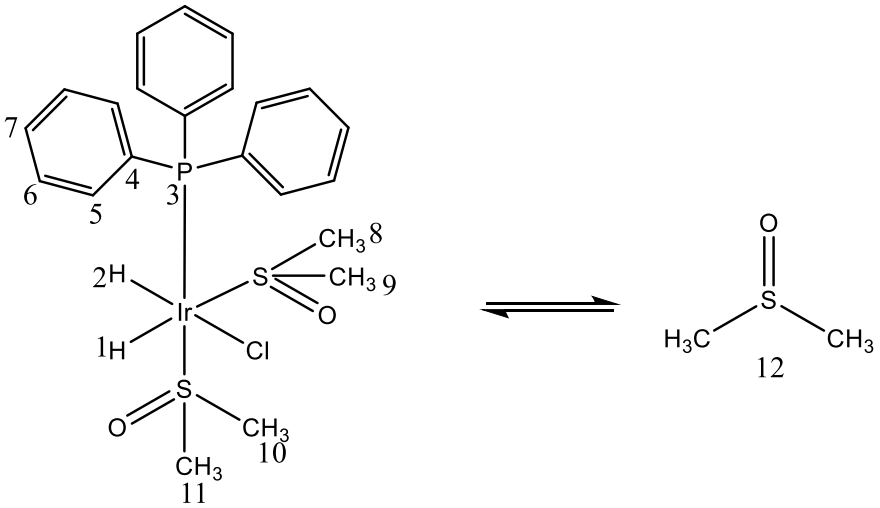

Resonance number	^{1}H (ppm)	^{13}C (ppm)	^{31}P (ppm)
1	-15.30, dd, *cis* J(PH) = 19.2 Hz J(HH) = 5.9 Hz		
2	-19.62, dd *cis* J(PH) = 17.77 Hz J(HH) = 5.9 Hz		
3			4.96
4		129.72	
5	8.4	134.74	
6	7.04	129.76	
7	7.72	132.08	
8	3.10	46.05, J(CH) = 69.5 Hz	
9	2.66	56.60, J(CH) = 70.1 Hz	
10	3.02	41.03, J(CH) = 68.7 Hz	
11	2.94	49.12, J(CH) = 68.1 Hz	
12	1.70	40.23	

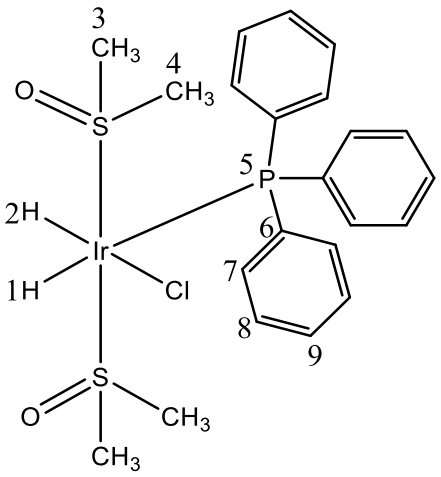

Resonance number	^{1}H (ppm)	^{13}C (ppm)	^{31}P (ppm)
1	-11.44, dd, *trans* J(PH) = 147.9 Hz J(HH) = 3.4 Hz		
2	-19.25,dd, *cis* J(PH) = 19.5 Hz J(HH) = 3.4 Hz		
3	2.97	59.18, J(CH) = 70.3 Hz	
4	2.60	43.38, J(CH) = 66 Hz	
5			-1.30
6		129.50	
7	8.23	134.88	
8	7.14	128.1	
9	7.06	129.7	

9.7 Chapter 4: NMR characterisation data for phosphine phosphate and phosphonate complexes

9.7.1 Characterisation of 10.4 mM IrCl(COD)(IMes) with 2 eq. of diphenylphosphine (20) in 0.6mL of dichloromethane-d_2 at 250 K: 20

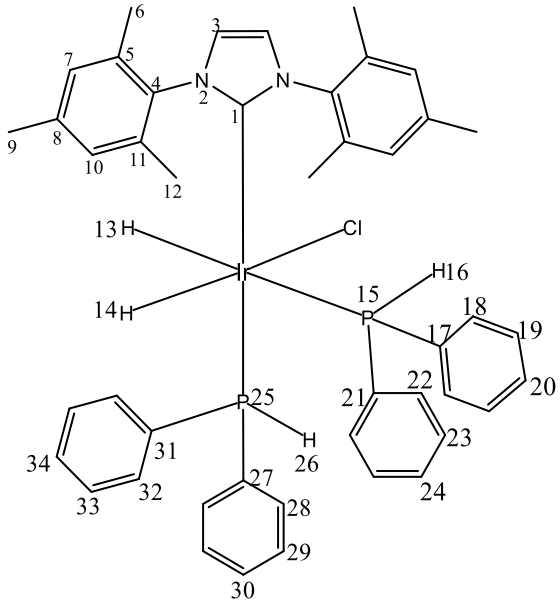

Resonance number	^{1}H (ppm)	^{13}C (ppm)	^{31}P (ppm)
1		133.55	
2			
3	7.00	122.44	
4		136.54	
5		139.06	
6	2.30	18.81	
7	7.08	128.62	
8		128.59	
9	2.35	21.18	
10	6.71,d, J(HH) = 4.1 Hz	129.28	
11		139.06	
12	1.92	18.26	
13	-9.16, ddd, J(HP) = 152 Hz, J(HH) = 6.2 Hz, J(HP) = 18.2 Hz		
14	-23.14, dtt, J(HP) = 9.5 Hz, J(HP) = 15.6 Hz J(HH) = 6.2 Hz		
15			Broad, -29.2
16	4.67, dd, J(HP) = 351 Hz J(HH) = 8.4 Hz		

17		137.60?	
18	6.96	132.58	
19	7.18	128.14	
20	7.19	132.99	
21		overlap	
22	7.13	135.75	
23	7.29	127.21	
24		overlap	
25			Broad, 5.33
26	4.94, dd, J(HP) = 342 Hz J(HH) = 9.1 Hz		
27		overlap	
28	7.12	139.26	
29	7.18	overlap	
30	overlap	overlap	
31		overlap	
32	7.16	133.0	
33	7.07	127.55	
34	7.24	129.19	

9.7.2 Characterisation data of complex 23 at 250 K:

The sample used for the characterisation of complex **20** in section 9.7.1 was added in 3 eq. of diphenyl phosphine **10**. This yielded to the formation of the unique complex **23**, which characterisation data is presented here in this section.

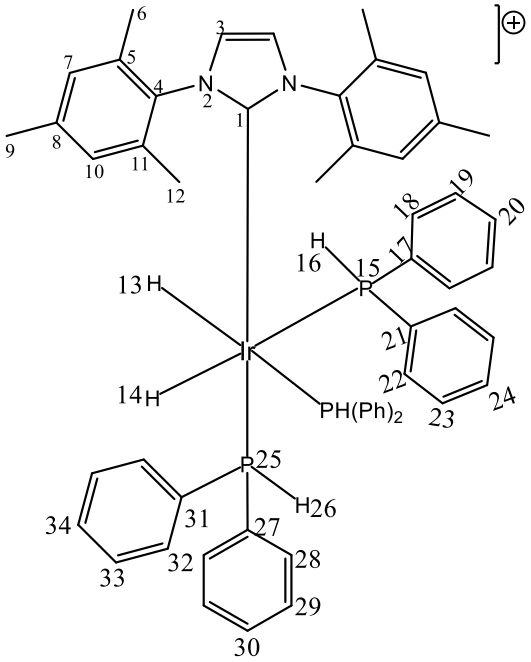

Resonance number	^{1}H (ppm)	^{13}C (ppm)	^{15}N (ppm)	^{31}P (ppm)
1		Not resolved		
2			Not resolved	
3	7.13	129.70		
4				
5		136.80		
6	2.22	19.14		
7	6.80	129.33		
8		121.36		
9	2.18	21.15		
10				
11				
12				
13 = 14	-11.03, dd, |*trans* J(HP) + *cis* J(HP)| = 128 Hz			
15				-37.3
16	5.60-6.32, dt, J(PH) = 360 Hz J(HH) = 5 Hz			
17		Not resolved		
18	6.68, m, J(HP) = 17.3 Hz	132.56		
19	7.26	128.52		
20	7.41	130.29		
21		Not resolved		
22	6.03, m, J(HP) = 16.2 Hz	133.44		

23	7.04	129.79		
24	6.70	127.68		
25				1.95
26	4.82, dt, J(PH) = 365 Hz, J(HH) = 4.7 Hz			
27		Not resolved		
28	7.50	133.86		
29	7.35	128.58		
30	7.18	128.66		
31	Not resolved			
32	Not resolved			
33	Not resolved			
34	Not resolved			

9.7.3 Characterisation of 5 mM IrCl(COD)(IMes) with 2 eq. of di-methyl phenyl phosphine 15 and 3 eq. of benzylamine in 0.6 mL of dichloromethane-d_2 at 263 K

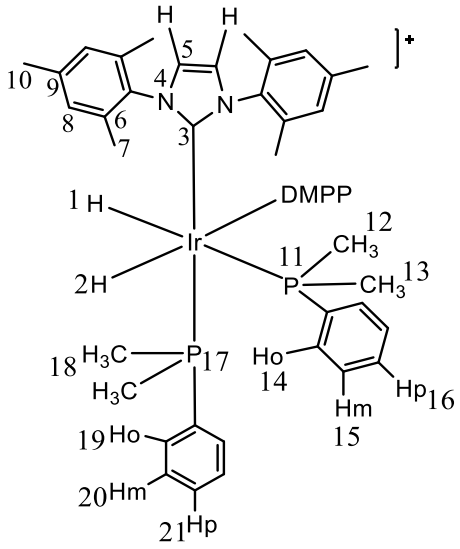

Resonance number	^{1}H (ppm)	^{31}P (ppm)	^{13}C (ppm)	^{15}N (ppm)
1 = 2	-11.79, |*cis* J(HP) +*trans* J(PH)| = 160 Hz			
3			153.8	
4				201.08
5	6.88		124.5	
6			135.25	
7	1.93		19.38	
8	6.58		129.71	

9			138.64	
10	2.26		20.86	
11		-37.8		
12	1.53 J(HP) = 7 Hz, J(HC) = 28 Hz		21.1	
13	1.48, J(HP) = 6.5 Hz, J(HC) = 32 Hz		23.37	
14	7.37		131.2	
15	7.35			
16	7.3			
17		-37.2		
18	1.63, J(HP) = 8.4 Hz, J(HC) = 36.5 Hz		22.64	
19	7.42		129.7	
20				
21				

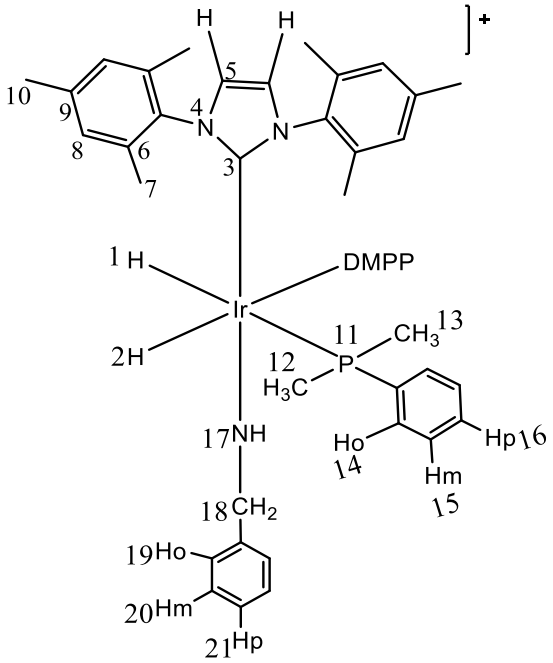

Resonance number	^{1}H (ppm)	^{31}P (ppm)	^{13}C (ppm)	^{15}N (ppm)
1 = 2	-11.73, |*trans* J(HP) + *cis* J(HP)| = 140 Hz			
3			153.8	
4				201.08
5	6.88		124.5	
6			135.25	

7	2.15		19.70	
8	6.90		129.29	
9			138.64	
10	2.21		20.78	
11		-37.66, t, J(PC) = 11 Hz		
12	1.8, J(HP) = 6.4 Hz		19.43	
13	1.4, J(HP) = 6.7 Hz		17.77 J(PC) = 28 Hz	
14	7.30		129.29	
15				
16				
17	1.27			-20.17, J(HN) = 30 Hz
18	3.03		21.58, J = 22Hz	
19	6.26		126.9, J = 9 Hz	
20	7.10 overlap		128.4	
21	7.28 overlap			

9.7.4 Characterisation of 26 mM IrCl(COD)(IMes), with 1 eq. of diphenyl phosphine oxide 11 and 3 eq. of benzylamine in 0.6 mL dichloromethane-d_2 at 273 K: 27 and 28

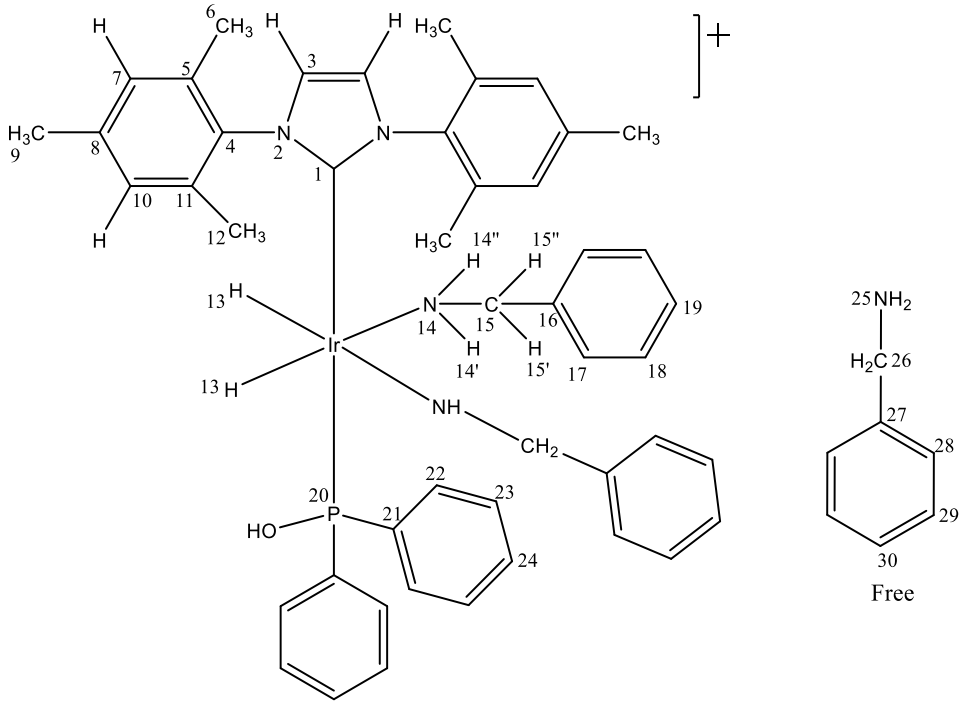

Resonance number	^{1}H (ppm)	^{31}P (ppm)	^{13}C (ppm)	^{15}N (ppm)
1			169.59	
2				197.27
3	6.91		123.33	
4			136.02	
5			138.46	
6	1.78		18.62	
7	6.25		129.66	
8			137.60	
9	2.33		21.05	
10	7.05		128.36	
11			138.99	
12	2.46		19.6	
13	-21.47, d, J(HN) = 18.2 Hz			
14				15.13
14'	3.26			
14''	2.18			
15			55.5	
15'	4.08			
15''	3.76			
16				
17	7.09		127.6	
18				
19				
20		27.8		
21			143.0, d, J(PC) = 67 Hz	
22	7.43, J(HP) = 12.5 Hz		131.79	
23	7.15		126.94	
24	7.29		128.96	
25	2.62 1.45			
26	3.82		46.07	
27				
28	7.31		127.20	
29	7.10		143.06	
30	~7			

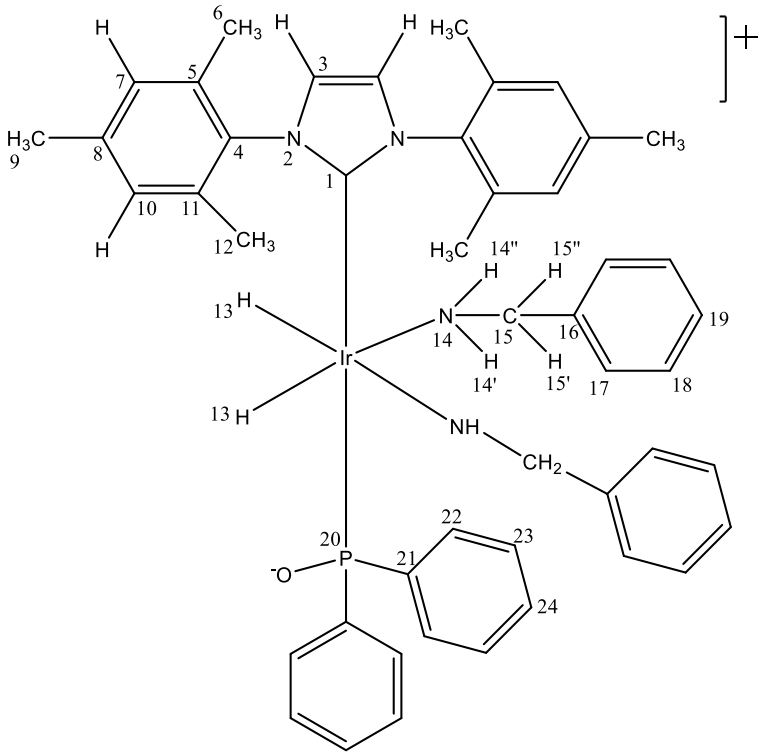

Resonance number	^{1}H (ppm)	^{31}P (ppm)	^{13}C (ppm)	^{15}N (ppm)
1				
2				195.4 dd, J(NC) = 93 Hz, J(NP) = 389 Hz
3	7.09		122.85	
4			135.07	
5			137.53	
6	2.15		18.19	
7	7.05		129.36	
8			139.31	
9	2.18		20.87	
10	7.05		129.36	
11			137.53	
12	2.15		18.19	
13	-22.63, d, J(HN) = 19.65 Hz			
14				14.97
14'	2.09			
14''	4.99			
15			55.74	
15'	3.43			
15''	2.94			
16	overlap			
17	overlap			
18	overlap			

19	overlap			
20		76.01		
21				
22	7.59, d, J(HP) = 6.65 Hz		130.04	
23	7.20		128.67	
	7.24		126.84	

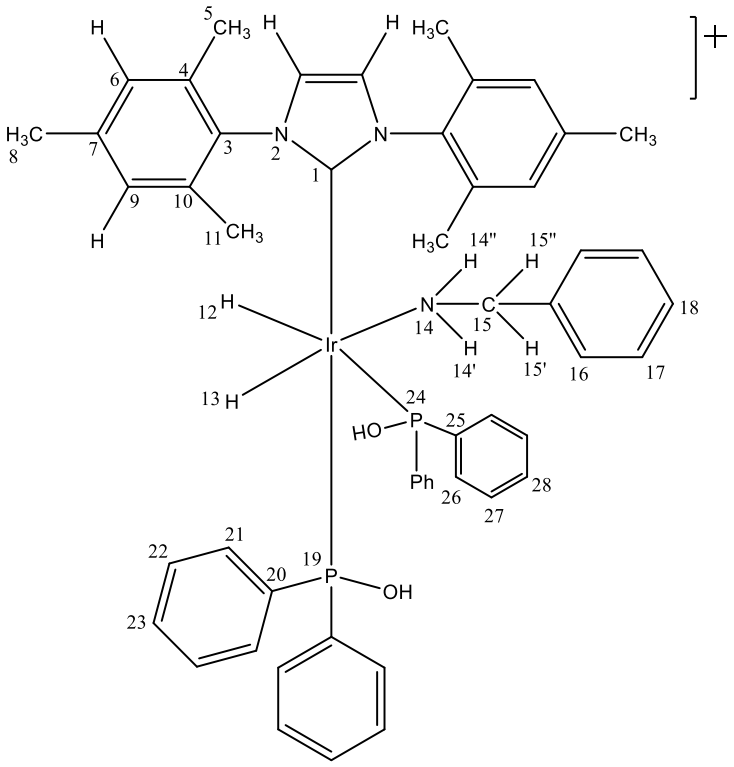

Resonance number	^{1}H (ppm)	^{31}P (ppm)	^{13}C (ppm)	^{15}N (ppm)
12	-9.89, dd, J(HP) = 130 Hz, J(HP) = 19 Hz			
13	-21.96, t, J(HP) = 16 Hz			
19		81.2		
24		63.4		

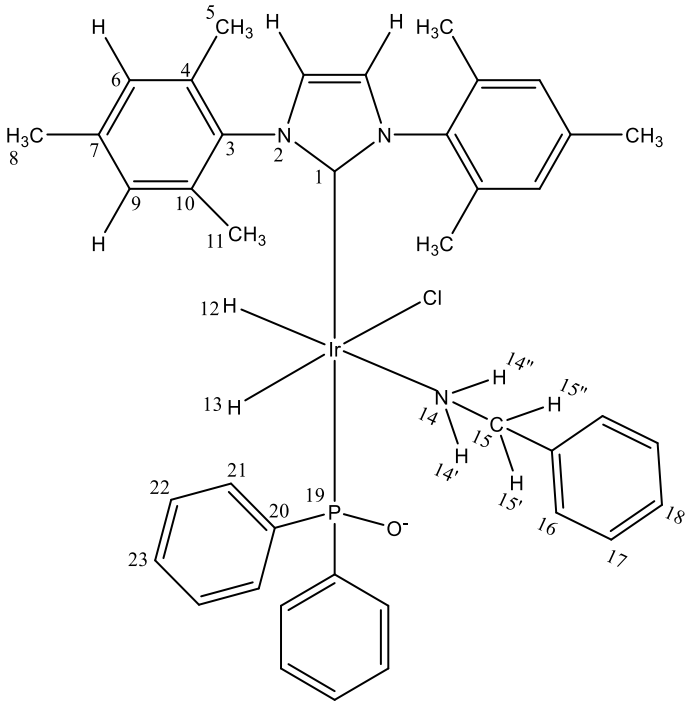

Resonance number	^{1}H (ppm)	^{31}P (ppm)	^{13}C (ppm)	^{15}N (ppm)
12	-23.2, dd, J(HP) = 10.0 Hz, J(HN)= 22.9 Hz			
13	-24.96,d, J(HP) = 10.6 Hz, J(HN) = 29.4 Hz			
19		83.3		

9.8 Chapter 3: NMR Characterisation data for amine complexes

9.8.1 Characterisation of 10.4 mM IrCl(COD)(IMes) with 5 eq. benzylamine 1 in 0.6 mL chlroform-d_3 at 263 K

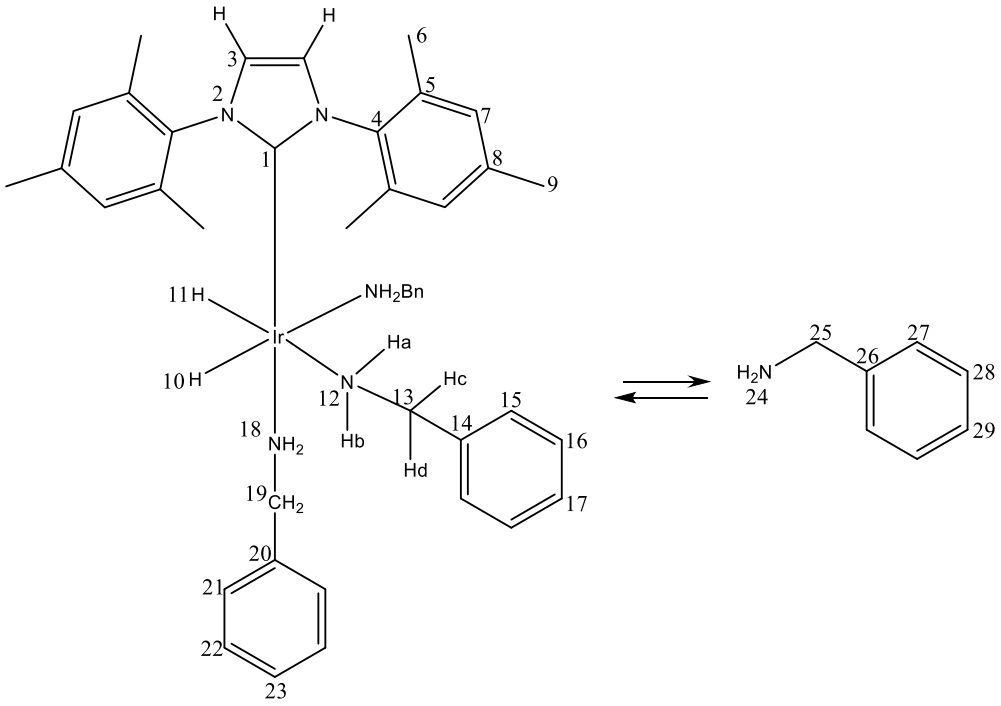

Resonance number	^{1}H (ppm)	^{13}C (ppm)	^{15}N (ppm)
1		154.74	
2			193.08
3	6.76	121.71	
4		138.39	
5		137.97	
6	2.12	18.54	
7	6.85	129.53	
8		140.92	
9	2.16	21.03	
10	-23.85, s		
11	-23.85, s		
12			-5.94 J(NN) = 72.2 Hz J(NH) = 41.2 Hz
12a	2.20		
12b	4.94		
13		53.50	
13c	3.63		
13d	3.23		
14		141.51	

15	7.29	127.30	
16	7.23	overlap	
17	7.19	overlap	
18	4.29		Broad, -13.78
19	3.85	57.39	
20		140.48	
21	7.30	128.35	
22	7.22	128.53	
23	7.17	127.33	
24	1.46		overlap
25	3.90	46.55	
26		143.33	
27	7.35	127.05	
28	7.29	128.45	
29	7.38	overlap	

9.8.2 Characterisation of 5 mM IrCl(COD)(IMes) with 20 eq. DMSO and 20 eq. of phenoxyethylamine 2 in 0.6 mL of chloroform-d_3 at 263 K

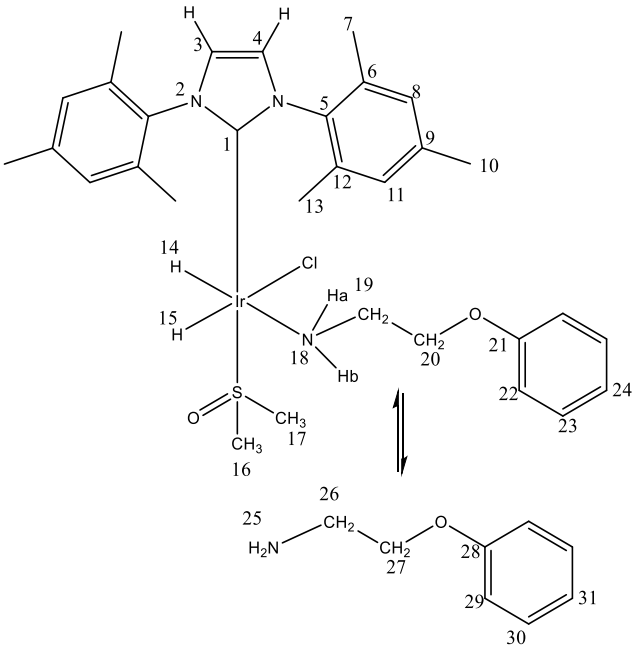

Resonance number	^{1}H (ppm)	^{13}C (ppm)	^{15}N (ppm)
1	-	120.8	
2	-	-	194.9
3	6.82	114.0	
4	6.82		
5	-	137.63	

6	-	136.27	
7	2.25	129.21	
8	6.97	128.91	
9	-	138.96	
10	2.20	129	
11	7.01	129.18	
12	-	136.01	
13	2.26		
14	-23.99, d, J(HH) = 7.6 Hz		
15	-22.99, d, J(HH) = 7.6 Hz		
16	3.18	58.66	
17	3.15	44.67	
18	Ha = 2.33, J(HN) = 20 Hz Hb = 1.95, J(HN) =70 Hz	-	-13.13
19	3.03, 2.57	46.8	
20	3.45	67.8	
21			
22			
23			
24			
25	1.34	-	
26	3.12, t, J = 5.1 Hz	41.55	
27	4.00, t, J = 5.2 Hz	69.77	
28	-		
29	7.3	124.51	
30	6.96	120.77	
31	6.93	122.22	

9.8.3 Characterisation of 5 mM IrCl(COD)(IMes) with 20 eq. DMSO and 20 eq. of benzylamine 1 in 0.6 mL of chloroform-d_3 at 263 K

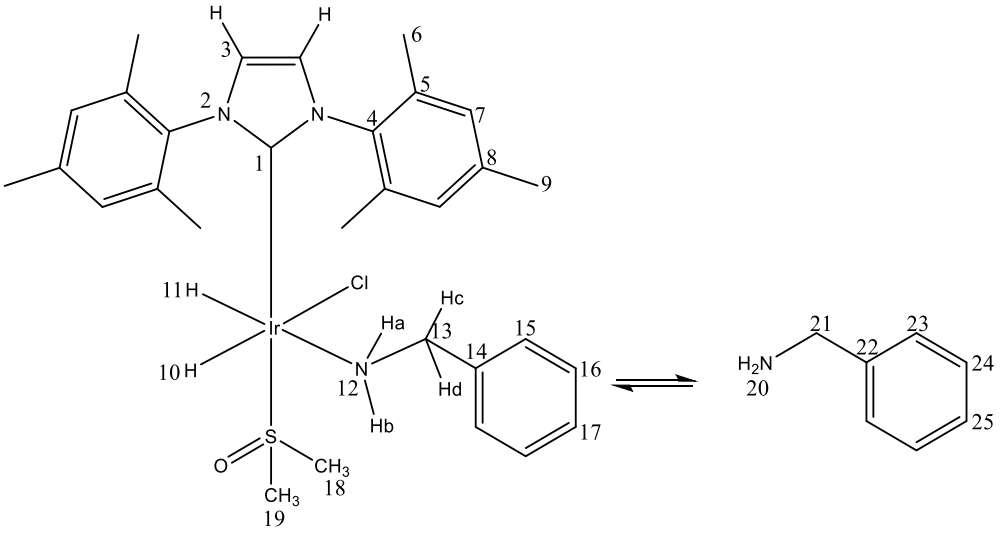

Resonance number	^{1}H (ppm)	^{13}C (ppm)	^{15}N (ppm)
1			
2			194.95
3	6.90	122.12	
4		136.43	
5		137.43	
6	1.51	26.7	
7	6.93	129.16	
8		137.	
9	2.20	18.32	
10	-23.88, d, J(HH) = 7.6 Hz		
11	-23.12, d, J(HH) = 7.6 Hz		
12			-2.52
12a	2.34		
12b	2.03		
13		51.7	
13c	3.74		
13d	3.34		
14		142.14	
15	7.25	128.33	
16	7.03	127.17	
17	6.98	128.17	
18	3.19	58.92	
19	3.16	45.68	
20	1.42		26.52
21	3.88	46.69	
22		143.49	

23	7.35	128.63	
24	7.33	127.15	
25	7.26	126.86	

Appendix: Matlab simulation

```
function [outI,t2,spec,fAxis] = fullSim_ABXY_Hz_PHIP_AS()

    % Define spins system

    % Number of spins
      N = 3;
      dim = 2^N;

    % J coupling network
      JH1X = 19.53;
      JH2X = 14.7;
      JH1Y = 19.53;
      JH2Y = 14.7;
      JHH = 5.8;
      JPP = 0;
      J = zeros(N);
      J(1,2) = JHH;
      J(1,3) = JH1X;
      J(2,3) = JH2X;
      J(1,4) = JH1Y;
      J(2,4) = JH2Y;
      J(3,4) = JPP;

    % Chemical shift / Larmor frequencies
      B0 = 51.95;
      gamma1H = 42.577;
      gamma31P = 17.235;
      freqs = [gamma1H,gamma1H,gamma31P,gamma31P]*B0;    % Chemical shift
values / ppm

    % Define experimental parameters
      expType = 1;          % 0 - thermal; 1 - pH2; 2 - PASADENA; 3 -
ALTADENA
      f0 = 0;               % centre frequency / Hz
      swh = 1/100e-6;       % spectral width / Hz
      tacq = 1.6384*2;      % acquisition time / s
      nZF = 16384*2;        % number pints in t2 (zero-filled)
      T2 = 0.5;             % T2 relaxation time in s
      flipAngle = 45;       % excitation pulse angle
      deadTime = 20e-3;     % deadtime between excitation and detection / s
      evolTime = 80e-3;     % Polarisation build-up time / s

    % Calculate Acquisition parameters
      frel = freqs-f0;      % Offset relative to centre of spectrum (Hz)
      delt2 = 1/swh;        % dwell time
      nt2 = tacq/delt2+1;   % number of simulation points

    % Ensure nZF is a power of 2
      test = log2(nZF);
      if abs(test-floor(test))>0
         nZF = 2^(round(test));         % Set to nearest power of 2
      end

    % Check that nZF > nt2 (increase if not, maintaining it as a power of
    % 2)
      while (nZF < nt2)                 % make sure nZF>nt2
```

```
        nZF = nZF*2;
    end
    fAxis = linspace(f0-swh/2,f0+swh/2,nZF);
    t2 = (0:nt2-1)*delt2;           % time axis for simulated points

% Rotation pulse properties
    spins = [1,1,0,0];
    theta = flipAngle*pi/180;     % rad
    phase = 90*pi/180;            % rad

% Output matrix
    outI = zeros(nZF,1);

%%%%%%%%%%%%%%%%%%%%%% Set up product operators

% Set-up product operators
    Iz = 0.5*[1 0;0 -1];
    Ix = 0.5*[0 1;1 0];
    Iy = 0.5*1i*[0 -1;1 0];
    E  = eye(2);

% Intermediate operators
    Iza = kron(Iz,E);
    Izb = kron(E,Iz);
    Ixa = kron(Ix,E);
    Ixb = kron(E,Ix);
    Iya = kron(Iy,E);
    Iyb = kron(E,Iy);

% Hydrides
    dimP31 = 2^(N-2);
    I1z = kron(Iza,eye(dimP31));
    I1x = kron(Ixa,eye(dimP31));
    I1y = kron(Iya,eye(dimP31));
    I2z = kron(Izb,eye(dimP31));
    I2x = kron(Ixb,eye(dimP31));
    I2y = kron(Iyb,eye(dimP31));
    I1zI2z = kron(kron(Iz,Iz),eye(dimP31));
    I1yI2y = kron(kron(Iy,Iy),eye(dimP31));
    I1xI2x = kron(kron(Ix,Ix),eye(dimP31));

%31P
    S1z = kron(kron(eye(4),Iz),eye(2^(N-3)));
    S1x = kron(kron(eye(4),Ix),eye(2^(N-3)));
    S1y = kron(kron(eye(4),Iy),eye(2^(N-3)));
    S2z = kron(eye(8),Iz);
    S2x = kron(eye(8),Ix);
    S2y = kron(eye(8),Iy);

% Cross term (PH)
    I1zS1z = kron(kron(Iza,Iz),eye(2));
    I2zS1z = kron(kron(Izb,Iz),eye(2));
    I1zS2z = kron(kron(Iza,eye(2)),Iz);
    I2zS2z = kron(kron(Izb,eye(2)),Iz);
    I1xS1x = kron(kron(Ixa,Ix),eye(2));
    I2xS1x = kron(kron(Ixb,Ix),eye(2));
    I1xS2x = kron(kron(Ixa,eye(2)),Ix);
    I2xS2x = kron(kron(Ixb,eye(2)),Ix);
    I1yS1y = kron(kron(Iya,Iy),eye(2));
    I2yS1y = kron(kron(Iyb,Iy),eye(2));
```

```
    I1yS2y = kron(kron(Iya,eye(2)),Iy);
    I2yS2y = kron(kron(Iyb,eye(2)),Iy);

  % PP terms
    S1zS2z = kron(eye(4),kron(Iz,Iz));
    S1xS2x = kron(eye(4),kron(Ix,Ix));
    S1yS2y = kron(eye(4),kron(Iy,Iy));

%%%%%%%%%%% Define system operators %%%%%%%%%%%%%%%%%%%%%%%%%%%%%%%%%%%%


  % Initial density matrix
    if expType == 0       % Thermal
        rho0 = I1z+I2z;
    elseif expType == 1   % pH2
        rho0 = I1zI2z+I1yI2y+I1xI2x;
    elseif expType == 2   % PASADENA
        rho0 = I1zI2z;
    elseif expType == 3   % ALTADENA
        rho0 = I1z-I2z;
    end
    norm0 = norm(rho0);

  % Observation operator  (hydrides only)
    Iobs = ((I1x+I2x)+1i*(I1y+I2y))';   % Observe 1H

  % Evolution Hamiltonian

  % 1H chemical shift
    H1 = -2*pi*frel(1)*I1z-2*pi*frel(2)*I2z-2*pi*frel(3)*S1z-
2*pi*frel(4)*S2z;

  % J coupling (HH) - full coupling (strong or weak)
    H1 = H1+2*pi*J(1,2)*(I1zI2z+I1xI2x+I1yI2y);
    H1 = H1+2*pi*J(1,3)*(I1zS1z+I1xS1x+I1yS1y);
    H1 = H1+2*pi*J(1,4)*(I1zS2z+I1xS2x+I1yS2y);
    H1 = H1+2*pi*J(2,3)*(I2zS1z+I2xS1x+I2yS1y);
    H1 = H1+2*pi*J(2,4)*(I2zS2z+I2xS2x+I2yS2y);
    H1 = H1+2*pi*J(3,4)*(S1zS2z+S1xS2x+S1yS2y);

  % Rotation operator (for hydrides)
    Rop = eye(dim);

  % Spin 1
    if spins(1) == 1
        Rop = Rop + I1x*cos(phase)+I1y*sin(phase);
    end
  % Spin 2
    if spins(2) == 1
        Rop = Rop + I2x*cos(phase)+I2y*sin(phase);
    end
  % Spin 3
    if spins(3) == 1
        Rop = Rop + S1x*cos(phase)+S1y*sin(phase);
    end
  % Spin 4
    if spins(4) == 1
        Rop = Rop + S2x*cos(phase)+S2y*sin(phase);
    end
```

```
    Urot = expm(-1i*theta*Rop);
    UrotT =expm(+1i*theta*Rop);

  % Pre-pulse evolution (evolTime)
    U1 = expm(-1i*H1*evolTime);
    U1t= expm(+1i*H1*evolTime);

  % Evolution operators for t2 (detection)
    U2 = expm(-1i*H1*delt2);
    U2t= expm(+1i*H1*delt2);

  % Evolution operators for the dead time
    Udt = expm(-1i*H1*deadTime);
    Udtt= expm(+1i*H1*deadTime);

  % Simulation pulse sequence

  % Step 1 - evolution before pulse
    rho1 = U1*rho0*U1t;

  % Step 2 - RF pulse
    rho2 = Urot*rho1*UrotT;

  % Step 3 - Evolve during deadTime
    rho2 = Udt*rho2*Udtt;

  % Step 4 - Acuire signal as a function of t2
    for mm = 1:nt2
      outI(mm) = real(trace(Iobs*rho2)/norm0*exp(-delt2*(mm-1)/T2));
      rho2 = U2*rho2*U2t;
    end

  % Fourier transform in t2
    spec = fftshift(fft(outI));

end
```

References:

1. A. N. Matlachov, P. L. Volegov, M. A. Espy, J. S. George and R. H. Kraus, *Journal of Magnetic Resonance*, 2004, **170**, 1-7.
2. M. Grootveld, B. Percival, M. Gibson, Y. Osman, M. Edgar, M. Molinari, M. L. Mather, F. Casanova and P. B. Wilson, *Analytica Chimica Acta*, 2019, **1067**, 11-30.
3. S. D. Riegel and G. M. Leskowitz, *TrAC Trends in Analytical Chemistry*, 2016, **83**, 27-38.
4. K. Singh, E. Danieli and B. Blümich, *Analytical and Bioanalytical Chemistry*, 2017, **409**, 7223-7234.
5. O. Semenova, P. M. Richardson, A. J. Parrott, A. Nordon, M. E. Halse and S. B. Duckett, *Analytical Chemistry*, 2019, **91**, 6695-6701.
6. K. Singh and B. Blümich, *Analyst*, 2018, **143**, 4408-4421.
7. https://www.zulf.eu/.
8. D. A. Barskiy, M. C. D. Tayler, I. Marco-Rius, J. Kurhanewicz, D. B. Vigneron, S. Cikrikci, A. Aydogdu, M. Reh, A. N. Pravdivtsev, J.-B. Hövener, J. W. Blanchard, T. Wu, D. Budker and A. Pines, *Nature Communications*, 2019, **10**, 3002.
9. S. Alcicek, P. Put, V. Kontul and S. Pustelny, *The Journal of Physical Chemistry Letters*, 2021, **12**, 787-792.
10. J. W. Blanchard, T. Wu, J. Eills, Y. Hu and D. Budker, *Journal of Magnetic Resonance*, 2020, **314**, 106723.
11. W. Köckenberger and J. Matysik, in *Encyclopedia of Spectroscopy and Spectrometry (Third Edition)*, eds. J. C. Lindon, G. E. Tranter and D. W. Koppenaal, Academic Press, Oxford, 2017, pp. 156-162.
12. T. R. Carver and C. P. Slichter, *Physical Review*, 1953, **92**, 212-213.
13. M. Tanaka, T. Kunimatsu, M. Fujiwara, H. Kohri, T. Ohta, M. Utsuro, M. Yosoi, S. Ono, K. Fukuda, K. Takamatsu, K. Ueda, J. P. Didelez, G. Prossati and A. de Waard, *Journal of Physics: Conference Series*, 2011, **295**, 012167.
14. M. E. Halse, *TrAC Trends in Analytical Chemistry*, 2016, **83**, 76-83.
15. M. L. Hirsch, N. Kalechofsky, A. Belzer, M. Rosay and J. G. Kempf, *Journal of the American Chemical Society*, 2015, **137**, 8428-8434.
16. A. W. Overhauser, *Physical Review*, 1953, **92**, 411-415.
17. T. Maly, G. T. Debelouchina, V. S. Bajaj, K.-N. Hu, C.-G. Joo, M. L. Mak–Jurkauskas, J. R. Sirigiri, P. C. A. van der Wel, J. Herzfeld, R. J. Temkin and R. G. Griffin, *The Journal of Chemical Physics*, 2008, **128**, 052211.
18. V. Denysenkov, M. J. Prandolini, M. Gafurov, D. Sezer, B. Endeward and T. F. Prisner, *Physical Chemistry Chemical Physics*, 2010, **12**, 5786-5790.
19. M. A. Bouchiat, T. R. Carver and C. M. Varnum, *Physical Review Letters*, 1960, **5**, 373-375.
20. C. R. Bowers and D. P. Weitekamp, *Physical Review Letters*, 1986, **57**, 2645-2648.
21. C. R. Bowers and D. P. Weitekamp, *Journal of the American Chemical Society*, 1987, **109**, 5541-5542.
22. D. G. Gadian, K. S. Panesar, A. J. Perez Linde, A. J. Horsewill, W. Köckenberger and J. R. Owers-Bradley, *Physical Chemistry Chemical Physics*, 2012, **14**, 5397-5402.
23. D. T. Peat, M. L. Hirsch, D. G. Gadian, A. J. Horsewill, J. R. Owers-Bradley and J. G. Kempf, *Physical Chemistry Chemical Physics*, 2016, **18**, 19173-19182.

24. J. R. Owers-Bradley, A. J. Horsewill, D. T. Peat, K. S. K. Goh and D. G. Gadian, *Physical Chemistry Chemical Physics*, 2013, **15**, 10413-10417.
25. A. Abragam, *Proceedings of the Royal Society of London. Series A. Mathematical and Physical Sciences*, 1965, **283**, 458-458.
26. R. V. Pound, *Physical Review*, 1950, **79**, 685-702.
27. T. J. Keller and T. Maly, *Magnetic Resonance*, 2021, **2**, 117-128.
28. E. Ravera, C. Luchinat and G. Parigi, *Journal of Magnetic Resonance*, 2016, **264**, 78-87.
29. Q. Z. Ni, E. Daviso, T. V. Can, E. Markhasin, S. K. Jawla, T. M. Swager, R. J. Temkin, J. Herzfeld and R. G. Griffin, *Accounts of Chemical Research*, 2013, **46**, 1933-1941.
30. J. H. Ardenkjaer-Larsen, in *eMagRes*, 2018, **7**, 63-78.
31. H. Jóhannesson, S. Macholl and J. H. Ardenkjaer-Larsen, *Journal of Magnetic Resonance*, 2009, **197**, 167-175.
32. C. Laustsen, P. M. Nielsen, H. Qi, M. H. Løbner, J. Palmfeldt and L. B. Bertelsen, *Scientific Reports*, 2020, **10**, 9650.
33. L. Salamanca-Cardona and K. R. Keshari, *Cancer & Metabolism*, 2015, **3**, 9.
34. M. Beloueche-Babari, P. Workman and M. O. Leach, *Cell Cycle*, 2011, **10**, 2883-2893.
35. D. J. Cheney and C. J. Wedge, *Journal of Magnetic Resonance*, 2022, **337**, 107170.
36. P. Zeeman, *Nature*, 1897, **55**, 347-347.
37. A. Kastler, *Journal of Physical Radium*, 1950, **11**, 255-265.
38. K. W. Miller, N. V. Reo, A. J. Schoot Uiterkamp, D. P. Stengle, T. R. Stengle and K. L. Williamson, *Proceedings of the National Academy of Sciences*, 1981, **78**, 4946-4949.
39. G. E. Pavlovskaya, Z. I. Cleveland, K. F. Stupic, R. J. Basaraba and T. Meersmann, *Proceedings of the National Academy of Sciences*, 2005, **102**, 18275-18279.
40. K. F. Stupic, Z. I. Cleveland, G. E. Pavlovskaya and T. Meersmann, *Journal of Magnetic Resonance*, 2011, **208**, 58-69.
41. *Makulski, W. Explorations of Magnetic Properties of Noble Gases: The Past, Present, and Future. Magnetochemistry **2020**, 6, 65.*
42. P. Nikolaou, B. M. Goodson and E. Y. Chekmenev, *Chemistry – A European Journal*, 2015, **21**, 3156-3166.
43. K. Ruppert, *Report on Progress in Physic*, 2014, **77**, 116701.
44. S. Klippel, J. Döpfert, J. Jayapaul, M. Kunth, F. Rossella, M. Schnurr, C. Witte, C. Freund and L. Schröder, *Angewandte Chemie International Edition*, 2014, **53**, 493-496.
45. L. Schröder, *Physica Medica*, 2013, **29**, 3-16.
46. J. Natterer and J. Bargon, *Progress in Nuclear Magnetic Resonance Spectroscopy*, 1997, **31**, 293-315.
47. T. C. Eisenschmid, R. U. Kirss, P. P. Deutsch, S. I. Hommeltoft, R. Eisenberg, J. Bargon, R. G. Lawler and A. L. Balch, *Journal of the American Chemical Society*, 1987, **109**, 8089-8091.
48. Bowers, C.R. (2007). Sensitivity Enhancement Utilizing Parahydrogen. In eMagRes (eds R.K. Harris and R.L. Wasylishen)
49. V. V. Zhivonitko, V.-V. Telkki, K. Chernichenko, T. Repo, M. Leskelä, V. Sumerin and I. V. Koptyug, *Journal of the American Chemical Society*, 2014, **136**, 598-601.
50. V. V. Zhivonitko, K. Sorochkina, K. Chernichenko, B. Kótai, T. Földes, I. Pápai, V.-V. Telkki, T. Repo and I. Koptyug, *Physical Chemistry Chemical Physics*, 2016, **18**, 27784-27795.
51. K. Sorochkina, V. V. Zhivonitko, K. Chernichenko, V.-V. Telkki, T. Repo and I. V. Koptyug, *The Journal of Physical Chemistry Letters*, 2018, **9**, 903-907.

52. K. Golman, O. Axelsson, H. Jóhannesson, S. Månsson, C. Olofsson and J. S. Petersson, *Magnetic Resonance in Medicine*, 2001, **46**, 1-5.
53. K. Golman, L. E. Olsson, O. Axelsson, S. Månsson, M. Karlsson and J. S. Petersson, *The British Journal of Radiology*, 2003, **76**, S118-S127.
54. L. T. Kuhn and J. Bargon, in *In situ NMR Methods in Catalysis*, eds. J. Bargon and L. T. Kuhn, Springer Berlin Heidelberg, Berlin, Heidelberg, 2007.
55. M. Haake, J. Barkemeyer and J. Bargon, *The Journal of Physical Chemistry*, 1995, **99**, 17539-17543.
56. M. J. Cowley, R. W. Adams, K. D. Atkinson, M. C. R. Cockett, S. B. Duckett, G. G. R. Green, J. A. B. Lohman, R. Kerssebaum, D. Kilgour and R. E. Mewis, *Journal of the American Chemical Society*, 2011, **133**, 6134-6137.
57. S. Korchak, S. Mamone and S. Glöggler, *ChemistryOpen*, 2018, **7**, 672-676.
58. R. V. M. Packard, *Physical Review* , 1954, **93**, 941.
59. D. F. Elliott and R. T. Schumacher, *The Journal of Chemical Physics*, 1957, **26**, 1350-1350.
60. P. T. Callaghan and M. Le Gros, *American Journal of Physics*, 1982, **50**, 709-713.
61. G. J. Béné, *Physics Reports*, 1980, **58**, 213-267.
62. J. Stepišnik, V. Eržen and M. Kos, *Magnetic Resonance in Medicine*, 1990, **15**, 386-391.
63. J. Stepisnik, M. Kos, G. Planinsic and V. Erzen, *Journal of Magnetic Resonance, Series A*, 1994, **107**, 167-172.
64. G. Planinsic, J. Stepisink and M. Kos, *Journal of Magnetic Resonance, Series A*, 1994, **110**, 170-174.
65. P. T. Callaghan, C. D. Eccles and J. D. Seymour, *Review of Scientific Instruments*, 1997, **68**, 4263-4270.
66. P. T. Callaghan, C. D. Eccles, T. G. Haskell, P. J. Langhorne and J. D. Seymour, *Journal of Magnetic Resonance*, 1998, **133**, 148-154.
67. D. Palandro, T. Nedwed, S. Altobelli, E. Fukushima, M. Conradi, N. Sowko and E. DeMicco, *International Oil Spill Conference Proceedings*, 2017, **2017**, 1877-1889.
68. M. S. Conradi, S. A. Altobelli, N. J. Sowko, S. H. Conradi and E. Fukushima, *Journal of Magnetic Resonance*, 2017, **281**, 241-245.
69. E. Fukushima, S. Altobelli, A. McDowell and T. Zhang, in *Symposium on the Application of Geophysics to Engineering and Environmental Problems 2013*, Environment and Engineering Geophysical Society, 2013, pp. 694-694.
70. S. A. Altobelli, M. S. Conradi, E. Fukushima, J. Hodgson, T. J. Nedwed, D. A. Palandro, A. Peach, N. J. Sowko and H. Thomann, *Marine Pollution Bulletin*, 2019, **144**, 160-166.
71. M. E. Halse and P. T. Callaghan, in *eMagRes*, John Wiley & Sons, 2009, 7952.
72. P. T. Callaghan, A. Coy, R. Dykstra, C. D. Eccles, M. E. Halse, M. W. Hunter, O. R. Mercier and J. N. Robinson, *Applied Magnetic Resonance*, 2007, **32**, 63-74.
73. D. C. Kaseman, M. T. Janicke, R. K. Frankle, T. Nelson, G. Angles-Tamayo, R. J. Batrice, P. E. Magnelind, M. A. Espy and R. F. Williams, *Applied sciences*, 2020, **10**, 3836.
74. V. S. Zotev, T. Owens, A. N. Matlashov, I. M. Savukov, J. J. Gomez and M. A. Espy, *Journal of Magnetic Resonance*, 2010, **207**, 78-88.
75. V. S. Zotev, P. L. Volegov, A. N. Matlashov, M. A. Espy, J. C. Mosher and R. H. Kraus, *Journal of Magnetic Resonance*, 2008, **192**, 197-208.
76. M. Espy, M. Flynn, J. Gomez, C. Hanson, R. Kraus, P. Magnelind, K. Maskaly, A. Matlashov, S. Newman, T. Owens, M. Peters, H. Sandin, I. Savukov, L. Schultz, A. Urbaitis, P. Volegov and V. Zotev, *Superconductor Science and Technology*, 2010, **23**, 034023.

77. S. Appelt, H. Kühn, F. W. Häsing and B. Blümich, *Nature Physics*, 2006, **2**, 105-109.
78. S. Appelt, F. W. Häsing, H. Kühn, J. Perlo and B. Blümich, *Physical Review Letters*, 2005, **94**, 197602.
79. S. Appelt, F. W. Häsing, U. Sieling, A. Gordji-Nejad, S. Glöggler and B. Blümich, *Physical Review A*, 2010, **81**, 023420.
80. M. E. Halse and P. T. Callaghan, *Journal of Magnetic Resonance*, 2008, **195**, 162-168.
81. B. C. Hamans, A. Andreychenko, A. Heerschap, S. S. Wijmenga and M. Tessari, *Journal of Magnetic Resonance*, 2011, **212**, 224-228.
82. R. L. Fagaly, *Review of Scientific Instruments*, 2006, **77**, 101101.
83. P. D. D. Schwindt, S. Knappe, V. Shah, L. Hollberg, J. Kitching, L.-A. Liew and J. Moreland, *Applied Physics Letters*, 2004, **85**, 6409-6411.
84. J. Li, W. Quan, B. Zhou, Z. Wang, J. Lu, Z. Hu, G. Liu and J. Fang, *IEEE Sensors Journal*, 2018, **18**, 8198-8207.
85. I. Savukov and S. J. Seltzer, in *Optical Magnetometry*, eds. D. F. Jackson Kimball and D. Budker, Cambridge University Press, Cambridge, 2013.
86. M. P. Ledbetter, I. M. Savukov, V. M. Acosta, D. Budker and M. V. Romalis, *Physical Review A*, 2008, **77**, 033408.
87. J. C. Allred, R. N. Lyman, T. W. Kornack and M. V. Romalis, *Physical Review Letters*, 2002, **89**, 130801.
88. H. B. Dang, A. C. Maloof and M. V. Romalis, *Applied Physics Letters*, 2010, **97**, 151110.
89. D. P. Weitekamp, A. Bielecki, D. Zax, K. Zilm and A. Pines, *Physical Review Letters*, 1983, **50**, 1807-1810.
90. D. B. Zax, A. Bielecki, K. W. Zilm, A. Pines and D. P. Weitekamp, *The Journal of Chemical Physics*, 1985, **83**, 4877-4905.
91. M. P. Ledbetter, T. Theis, J. W. Blanchard, H. Ring, P. Ganssle, S. Appelt, B. Blümich, A. Pines and D. Budker, *Physical Review Letters*, 2011, **107**, 107601.
92. M. Emondts, M. P. Ledbetter, S. Pustelny, T. Theis, B. Patton, J. W. Blanchard, M. C. Butler, D. Budker and A. Pines, *Physcal Review Letters*, 2014, **112**, 077601.
93. C. J. Lee, D. Suter and A. Pines, *Journal of Magnetic Resonance (1969)*, 1987, **75**, 110-124.
94. A. M. Thayer and A. Pines, *Journal of Magnetic Resonance (1969)*, 1986, **70**, 518-522.
95. J. W. Blanchard and D. Budker, in *eMagRes*, 2016, pp. 1395-1410.
96. G. Bevilacqua, V. Biancalana, A. B.-A. Baranga, Y. Dancheva and C. Rossi, *Journal of Magnetic Resonance*, 2016, **263**, 65-70.
97. M. C. D. Tayler, T. Theis, T. F. Sjolander, J. W. Blanchard, A. Kentner, S. Pustelny, A. Pines and D. Budker, *Review of Scientific Instruments*, 2017, **88**, 091101.
98. S. Alcicek, P. Put, D. Barskiy, V. Kontul and S. Pustelny, *The Journal of Physical Chemistry Letters*, 2021, **12**, 10671-10676.
99. T. Theis, J. W. Blanchard, M. C. Butler, M. P. Ledbetter, D. Budker and A. Pines, *Chemical Physics Letters*, 2013, **580**, 160-165.
100. G. Bevilacqua, V. Biancalana, A. B. Baranga, Y. Dancheva and C. Rossi, *Journal of Magnetic Resonance*, 2016, **263**, 65-70.
101. J. W. Blanchard, M. P. Ledbetter, T. Theis, M. C. Butler, D. Budker and A. Pines, *Journal of the American Chemical Society*, 2013, **135**, 3607-3612.
102. M. P. Ledbetter, C. W. Crawford, A. Pines, D. E. Wemmer, S. Knappe, J. Kitching and D. Budker, *Journal of Magnetic Resonance*, 2009, **199**, 25-29.

103. T. Theis, P. Ganssle, G. Kervern, S. Knappe, J. Kitching, M. P. Ledbetter, D. Budker and A. Pines, *Nature Physics*, 2011, **7**, 571-575.
104. T. Theis, M. P. Ledbetter, G. Kervern, J. W. Blanchard, P. J. Ganssle, M. C. Butler, H. D. Shin, D. Budker and A. Pines, *Journal of the American Chemical Society*, 2012, **134**, 3987-3990.
105. M. H. Levitt, *Malcolm H. Spin Dynamics: Basics of Nuclear Magnetic Resonance.* , John Wiley & Sons Ltd,, 2nd ed. edn., 2008.
106. J. Keeler, *Understanding NMR Spectroscopy, Apollo - University of Cambridge Repository; 2002.*
107. I. Alkorta and J. Elguero, *Structural Chemistry*, 1998, **9**, 187-202.
108. J. A. Pople, W. G. Schneider and H. J. Bernstein, *Canadian Journal of Chemistry*, 1957, **35**, 1060-1072.
109. H. J. Hogben, M. Krzystyniak, G. T. P. Charnock, P. J. Hore and I. Kuprov, *Journal of Magnetic Resonance*, 2011, **208**, 179-194.
110. C. R. Bowers, Sensitivity Enhancement Utilizing Parahydrogen. (eds R.K. Harris and R.L. Wasylishen) in *eMagRes*, 2007.
111. R. A. Green, R. W. Adams, S. B. Duckett, R. E. Mewis, D. C. Williamson and G. G. R. Green, *Progress in Nuclear Magnetic Resonance Spectroscopy*, 2012, **67**, 1-48.
112. M. E. Halse, B. Procacci, S.-L. Henshaw, R. N. Perutz and S. B. Duckett, *Journal of Magnetic Resonance*, 2017, **278**, 25-38.
113. R. W. Adams, S. B. Duckett, R. A. Green, D. C. Williamson and G. G. R. Green, *The Journal of Chemical Physics*, 2009, **131**, 194505.
114. K. L. Ivanov, A. N. Pravdivtsev, A. V. Yurkovskaya, H.-M. Vieth and R. Kaptein, *Progress in Nuclear Magnetic Resonance Spectroscopy*, 2014, **81**, 1-36.
115. D. A. Barskiy, S. Knecht, A. V. Yurkovskaya and K. L. Ivanov, *Progress in Nuclear Magnetic Resonance Spectroscopy*, 2019, **114-115**, 33-70.
116. A. N. Pravdivtsev, K. L. Ivanov, A. V. Yurkovskaya, P. A. Petrov, H.-H. Limbach, R. Kaptein and H.-M. Vieth, *Journal of Magnetic Resonance*, 2015, **261**, 73-82.
117. A. N. Pravdivtsev, A. V. Yurkovskaya, H.-M. Vieth, K. L. Ivanov and R. Kaptein, *ChemPhysChem*, 2013, **14**, 3327-3331.
118. S. L. Eriksson, J. R. Lindale, X. Li and W. S. Warren, *Science Advances*, **8**, eabl3708.
119. J. Clayden, et al., *Organic Chemistry*, Oxford University Press, 2nd ed., edn., 2012.
120. I. Ojima, in *Fundamental Research in Homogeneous Catalysis: Volume 2*, eds. Y. Ishii and M. Tsutsui, Springer US, Boston, MA, 1978, pp. 181-206.
121. S. I. Hommeltoft, D. H. Berry and R. Eisenberg, *Journal of the American Chemical Society*, 1986, **108**, 5345-5347.
122. J. Bargon, H. Fischer and U. Johnsen, *I. Aufnahmeverfahren und Beispiele*, 1967, **22**, 1551-1555.
123. S. B. Duckett, R. Eisenberg and A. S. Goldman, *Journal of the Chemical Society*1993, **15**, 1185-1187.
124. M. Carravetta, O. G. Johannessen and M. H. Levitt, *Physical Review Letters*, 2004, **92**, 153003.
125. M. Carravetta, O. G. Johannessen and M. H. Levitt, *Physical Review Letters*, 2004, **92**, 153003.
126. K. V. Kovtunov, V. V. Zhivonitko, L. Kiwi-Minsker and I. V. Koptyug, *Chemical Communications*, 2010, **46**, 5764-5766.

127. I. V. Koptyug, K. V. Kovtunov, S. R. Burt, M. S. Anwar, C. Hilty, S.-I. Han, A. Pines and R. Z. Sagdeev, *Journal of the American Chemical Society*, 2007, **129**, 5580-5586.
128. S. B. Duckett, in *Encyclopedia of Spectroscopy and Spectrometry (Third Edition)*, eds. J. C. Lindon, G. E. Tranter and D. W. Koppenaal, Academic Press, Oxford, 2017, pp. 527-534.
129. J.-B. Hövener, A. N. Pravdivtsev, B. Kidd, C. R. Bowers, S. Glöggler, K. V. Kovtunov, M. Plaumann, R. Katz-Brull, K. Buckenmaier, A. Jerschow, F. Reineri, T. Theis, R. V. Shchepin, S. Wagner, P. Bhattacharya, N. M. Zacharias and E. Y. Chekmenev, *Angewandte Chemie International Edition*, 2018, **57**, 11140-11162.
130. H. D. Kaesz and R. B. Saillant, *Chemical Reviews*, 1972, **72**, 231-281.
131. L. Malatesta, G. Caglio and M. Angoletta, *Journal of the Chemical Society*, 1965, **0**, 6974-6983.
132. R. H. Crabtree, *The Organometallic Chemistry of the Transition Metals. Hoboken,*, N.J: John Wiley, , 2005.
133. R. U. Kirss and R. Eisenberg, *Journal of Organometallic Chemistry*, 1989, **359**, C22-C26.
134. R. Eisenberg, *Accounts of Chemical Research*, 1991, **24**, 110-116.
135. K. D. Atkinson, M. J. Cowley, P. I. P. Elliott, S. B. Duckett, G. G. R. Green, J. López-Serrano and A. C. Whitwood, *Journal of the American Chemical Society*, 2009, **131**, 13362-13368.
136. R. H. Crabtree, H. Felkin and G. E. Morris, *Journal of Organometallic Chemistry*, 1977, **141**, 205-215.
137. S. H. Cho, J. Y. Kim, J. Kwak and S. Chang, *Chemical Society Reviews*, 2011, **40**, 5068-5083.
138. F. Roudesly, J. Oble and G. Poli, *Journal of Molecular Catalysis A: Chemical*, 2017, **426**, 275-296.
139. J. Chatt and J. M. Davidson, *Journal of the Chemical Society*, 1965, **10**, 843-855.
140. J. A. Labinger and J. E. Bercaw, *Nature*, 2002, **417**, 507-514.
141. R. H. Crabtree and M. Lavin, *Journal of the Chemical Society, Chemical Communications*, 1985, 794-795.
142. C. Y. Tang, W. Smith, D. Vidovic, A. L. Thompson, A. B. Chaplin and S. Aldridge, *Organometallics*, 2009, **28**, 3059-3066.
143. M. Prinz, M. Grosche, E. Herdtweck and W. A. Herrmann, *Organometallics*, 2000, **19**, 1692-1694.
144. N. Phillips, J. Rowles, M. J. Kelly, I. Riddlestone, N. H. Rees, A. Dervisi, I. A. Fallis and S. Aldridge, *Organometallics*, 2012, **31**, 8075-8078.
145. S. Rej, A. Das and N. Chatani, *Coordination Chemistry Reviews*, 2021, **431**, 213683.
146. R. Manoharan and M. Jeganmohan, *Asian Journal of Organic Chemistry*, 2019, **8**, 1949-1969.
147. A. H. Janowicz and R. G. Bergman, *Journal of the American Chemical Society*, 1982, **104**, 352-354.
148. J. K. Hoyano and W. A. G. Graham, *Journal of the American Chemical Society*, 1982, **104**, 3723-3725.
149. W. D. Jones and F. J. Feher, *Organometallics*, 1983, **2**, 562-563.
150. B. A. Arndtsen, R. G. Bergman, T. A. Mobley and T. H. Peterson, *Accounts of Chemical Research*, 1995, **28**, 154-162.
151. S. Niu and M. B. Hall, *Chemical Reviews*, 2000, **100**, 353-406.
152. M. Albrecht, *Chemical Reviews*, 2010, **110**, 576-623.

153. I. Omae, *Coordination Chemistry Reviews*, 1980, **32**, 235-271.
154. T. Rogge, N. Kaplaneris, N. Chatani, J. Kim, S. Chang, B. Punji, L. L. Schafer, D. G. Musaev, J. Wencel-Delord, C. A. Roberts, R. Sarpong, Z. E. Wilson, M. A. Brimble, M. J. Johansson and L. Ackermann, *Nature Reviews Methods Primers*, 2021, **1**, 43.
155. I. Hussain and T. Singh, *Advanced Synthesis & Catalysis*, 2014, **356**, 1661-1696.
156. S.-F. Ni, G. Huang, Y. Chen, J. S. Wright, M. Li and L. Dang, *Coordination Chemistry Reviews*, 2022, **455**, 214255.
157. J. Wencel-Delord and F. Glorius, *Nature Chemistry*, 2013, **5**, 369-375.
158. T. Dalton, T. Faber and F. Glorius, *ACS Central Science*, 2021, **7**, 245-261.
159. M. A. Bennett and D. L. Milner, *Journal of the American Chemical Society*, 1969, **91**, 6983-6994.
160. J. P. Kleiman and M. Dubeck, *Journal of the American Chemical Society*, 1963, **85**, 1544-1545.
161. A. C. Cope and R. W. Siekman, *Journal of the American Chemical Society*, 1965, **87**, 3272-3273.
162. M. M. Bagga, W. T. Flannigan, G. R. Knox and P. L. Pauson, *Journal of the Chemical Society C: Organic*, 1969, 1534-1537.
163. P. Gandeepan and C.-H. Cheng, *Chemistry – An Asian Journal*, 2015, **10**, 824-838.
164. I. Omae, *Journal of Organometallic Chemistry*, 2011, **696**, 1128-1145.
165. P. Sutra and A. Igau, *Coordination Chemistry Reviews*, 2016, **308**, 97-116.
166. Y. Chauvin, *Angewandte Chemie International Edition*, 2006, **45**, 3740-3747.
167. E. O. Fischer and A. Maasböl, *Angewandte Chemie International Edition in English*, 1964, **3**, 580-581.
168. H. W. Wanzlick and H. J. Schönherr, *Angewandte Chemie International Edition in English*, 1968, **7**, 141-142.
169. H. W. Wanzlick, *Angewandte Chemie International Edition in English*, 1962, **1**, 75-80.
170. D. J. D. Wilson, S. A. Couchman and J. L. Dutton, *Inorganic Chemistry*, 2012, **51**, 7657-7668.
171. O. Torres, M. Martín and E. Sola, *Organometallics*, 2009, **28**, 863-870.
172. A. J. Arduengo, R. L. Harlow and M. Kline, *Journal of the American Chemical Society*, 1991, **113**, 361-363.
173. M. Fekete, O. Bayfield, S. B. Duckett, S. Hart, R. E. Mewis, N. Pridmore, P. J. Rayner and A. Whitwood, *Inorganic Chemistry*, 2013, **52**, 13453-13461.
174. P. J. Rayner, P. Norcott, K. M. Appleby, W. Iali, R. O. John, S. J. Hart, A. C. Whitwood and S. B. Duckett, *Nature Communications*, 2018, **9**, 4251.
175. P. Spannring, I. Reile, M. Emondts, P. P. M. Schleker, N. K. J. Hermkens, N. G. J. van der Zwaluw, B. J. A. van Weerdenburg, P. Tinnemans, M. Tessari, B. Blümich, F. P. J. T. Rutjes and M. C. Feiters, *Chemistry – A European Journal*, 2016, **22**, 9277-9282.
176. D. B. Burueva, S. V. Sviyazov, F. Huang, I. P. Prosvirin, A. V. Bukhtiyarov, V. I. Bukhtiyarov, H. Liu and I. V. Koptyug, *The Journal of Physical Chemistry C*, 2021, **125**, 27221-27229.
177. A. M. Balu, S. B. Duckett and R. Luque, *Dalton Transactions*, 2009, 5074-5076.
178. R. Zhou, E. W. Zhao, W. Cheng, L. M. Neal, H. Zheng, R. E. Quiñones, H. E. Hagelin-Weaver and C. R. Bowers, *Journal of the American Chemical Society*, 2015, **137**, 1938-1946.
179. K. D. Atkinson, M. J. Cowley, S. B. Duckett, P. I. P. Elliott, G. G. R. Green, J. López-Serrano, I. G. Khazal and A. C. Whitwood, *Inorganic Chemistry*, 2009, **48**, 663-670.

180. W. Adams Ralph, A. Aguilar Juan, D. Atkinson Kevin, J. Cowley Michael, I. P. Elliott Paul, B. Duckett Simon, G. R. Green Gary, G. Khazal Iman, J. López-Serrano and C. Williamson David, *Science*, 2009, **323**, 1708-1711.
181. M. J. Burns, P. J. Rayner, G. G. R. Green, L. A. R. Highton, R. E. Mewis and S. B. Duckett, *The Journal of Physical Chemistry B*, 2015, **119**, 5020-5027.
182. D. A. Barskiy, R. V. Shchepin, C. P. N. Tanner, J. F. P. Colell, B. M. Goodson, T. Theis, W. S. Warren and E. Y. Chekmenev, *ChemPhysChem*, 2017, **18**, 1493-1498.
183. A. M. Olaru, T. B. R. Robertson, J. S. Lewis, A. Antony, W. Iali, R. E. Mewis and S. B. Duckett, *ChemistryOpen*, 2018, **7**, 97-105.
184. S. S. Roy, P. Norcott, P. J. Rayner, G. G. R. Green and S. B. Duckett, *Chemistry – A European Journal*, 2017, **23**, 10496-10500.
185. A. M. Olaru, A. Burt, P. J. Rayner, S. J. Hart, A. C. Whitwood, G. G. R. Green and S. B. Duckett, *Chemical Communications*, 2016, **52**, 14482-14485.
186. T. Theis, M. L. Truong, A. M. Coffey, R. V. Shchepin, K. W. Waddell, F. Shi, B. M. Goodson, W. S. Warren and E. Y. Chekmenev, *Journal of the American Chemical Society*, 2015, **137**, 1404-1407.
187. M. L. Truong, T. Theis, A. M. Coffey, R. V. Shchepin, K. W. Waddell, F. Shi, B. M. Goodson, W. S. Warren and E. Y. Chekmenev, *The Journal of Physical Chemistry C*, 2015, **119**, 8786-8797.
188. T. Theis, M. Truong, A. M. Coffey, E. Y. Chekmenev and W. S. Warren, *Journal of Magnetic Resonance*, 2014, **248**, 23-26.
189. K. M. Appleby, R. E. Mewis, A. M. Olaru, G. G. R. Green, I. J. S. Fairlamb and S. B. Duckett, *Chemical Science*, 2015, **6**, 3981-3993.
190. M. Fekete, P. J. Rayner, G. G. R. Green and S. B. Duckett, *Magnetic Resonance in Chemistry*, 2017, **55**, 944-957.
191. W. Iali, P. J. Rayner, A. Alshehri, A. J. Holmes, A. J. Ruddlesden and S. B. Duckett, *Chemical Science*, 2018, **9**, 3677-3684.
192. S. S. Roy, K. M. Appleby, E. J. Fear and S. B. Duckett, *The Journal of Physical Chemistry Letters*, 2018, **9**, 1112-1117.
193. S. Knecht, D. A. Barskiy, G. Buntkowsky and K. L. Ivanov, *The Journal of Chemical Physics*, 2020, **153**, 164106.
194. P. J. Rayner, B. J. Tickner, W. Iali, M. Fekete, A. D. Robinson and S. B. Duckett, *Chemical Science*, 2019, **10**, 7709-7717.
195. R. E. Ruscoe, J. I. Ramsden and N. J. Turner, *Current Opinion in Chemical Engineering*, 2020, **30**, 60-68.
196. K. N. Gusak, Z. V. Ignatovich and E. V. Koroleva, *Russian Chemical Reviews*, 2015, **84**, 288-309.
197. F. Piazzolla and A. Temperini, *Tetrahedron Letters*, 2018, **59**, 2615-2621.
198. R. A. Al-Horani and U. R. Desai, *Tetrahedron*, 2010, **66**, 2907-2918.
199. G. Golub, I. Zilbermann, H. Cohen and D. Meyerstein, *Supramolecular Chemistry*, 1996, **6**, 275-279.
200. W. Iali, J. Rayner Peter and B. Duckett Simon, *Science Advances*, **4**, eaao6250.
201. P. J. Rayner and S. B. Duckett, *Angewandte Chemie International Edition*, 2018, **57**, 6742-6753.
202. I. Reile, N. Eshuis, N. K. J. Hermkens, B. J. A. van Weerdenburg, M. C. Feiters, F. P. J. T. Rutjes and M. Tessari, *Analyst*, 2016, **141**, 4001-4005.

203. N. Eshuis, B. J. A. van Weerdenburg, M. C. Feiters, F. P. J. T. Rutjes, S. S. Wijmenga and M. Tessari, *Angewandte Chemie International Edition*, 2015, **54**, 1481-1484.
204. J. Rayner Peter, J. Burns Michael, M. Olaru Alexandra, P. Norcott, M. Fekete, G. R. Green Gary, A. R. Highton Louise, E. Mewis Ryan and B. Duckett Simon, *Proceedings of the National Academy of Sciences*, 2017, **114**, E3188-E3194.
205. B. J. Tickner, R. O. John, S. S. Roy, S. J. Hart, A. C. Whitwood and S. B. Duckett, *Chemical Science*, 2019, **10**, 5235-5245.
206. W. Iali, S. S. Roy, B. J. Tickner, F. Ahwal, A. J. Kennerley and S. B. Duckett, *Angewandte Chemie International Edition*, 2019, **58**, 10271-10275.
207. F. Hill-Casey, A. Sakho, A. Mohammed, M. Rossetto, F. Ahwal, S. B. Duckett, R. O. John, P. M. Richardson, R. Virgo and M. E. Halse, *Molecules*, 2019, **24**, 4126.
208. W. Iali, A. M. Olaru, G. G. R. Green and S. B. Duckett, *Chemistry – A European Journal*, 2017, **23**, 10491-10495.
209. F. Hill-Casey, A. Sakho, A. Mohammed, M. Rossetto, F. Ahwal, S. B. Duckett, R. O. John, P. M. Richardson, R. Virgo and M. E. Halse, *Molecules*, 2019, **24**.
210. M. Fekete, F. Ahwal and S. B. Duckett, *The Journal of Physical Chemistry B*, 2020, **124**, 4573-4580.
211. P. M. Richardson, A. J. Parrott, O. Semenova, A. Nordon, S. B. Duckett and M. E. Halse, *Analyst*, 2018, **143**, 3442-3450.
212. L. S. Lloyd, A. Asghar, M. J. Burns, A. Charlton, S. Coombes, M. J. Cowley, G. J. Dear, S. B. Duckett, G. R. Genov, G. G. R. Green, L. A. R. Highton, A. J. J. Hooper, M. Khan, I. G. Khazal, R. J. Lewis, R. E. Mewis, A. D. Roberts and A. J. Ruddlesden, *Catalysis Science & Technology*, 2014, **4**, 3544-3554.
213. P. M. Richardson, S. Jackson, A. J. Parrott, A. Nordon, S. B. Duckett and M. E. Halse, *Magnetic Resonance in Chemistry*, 2018, **56**, 641-650.
214. P. Norcott, P. J. Rayner, G. G. R. Green and S. B. Duckett, *Chemistry – A European Journal*, 2017, **23**, 16990-16997.
215. P. Norcott, M. J. Burns, P. J. Rayner, R. E. Mewis and S. B. Duckett, *Magnetic Resonance in Chemistry*, 2018, **56**, 663-671.
216. W. Iali, P. J. Rayner and S. B. Duckett, *Science Advances*, **4**, eaao6250, 2018.
217. R. V. Shchepin, B. M. Goodson, T. Theis, W. S. Warren and E. Y. Chekmenev, *ChemPhysChem*, 2017, **18**, 1961-1965.
218. B. J. Tickner, O. Semenova, W. Iali, P. J. Rayner, A. C. Whitwood and S. B. Duckett, *Catalysis Science & Technology*, 2020, **10**, 1343-1355.
219. D. S. Glueck, *Coordination Chemistry Reviews*, 2008, **252**, 2171-2179.
220. E. C. Cagle, T. R. Totsch, M. A. Erdmann and G. M. Gray, *Journal of Chemical Education*, 2018, **95**, 1054-1059.
221. K. Moedritzer, *Synthesis and Reactivity in Inorganic and Metal-Organic Chemistry*, 1985, **15**, 551-552.
222. M. L. H. Green and D. J. Jones, in *Advances in Inorganic Chemistry and Radiochemistry*, eds. H. J. Emeléus and A. G. Sharpe, Academic Press, 1965, vol. 7, pp. 115-183.
223. S. B. Duckett and N. J. Wood, *Coordination Chemistry Reviews*, 2008, **252**, 2278-2291.
224. C. D. Swor and D. R. Tyler, *Coordination Chemistry Reviews*, 2011, **255**, 2860-2881.
225. L. H. Pignolet, *Modern Inorganic Chemistry*, 1983, **202**, 211-223.
226. N. Fey, A. G. Orpen and J. N. Harvey, *Coordination Chemistry Reviews*, 2009, **253**, 704-722.
227. G. Bodenhausen and D. J. Ruben, *Chemical Physics Letters*, 1980, **69**, 185-189.

228. S. B. Duckett and C. J. Sleigh, *Progress in Nuclear Magnetic Resonance Spectroscopy*, 1999, **34**, 71-92.
229. V. V. Zhivonitko, I. V. Skovpin and I. V. Koptyug, *Chemical Communications*, 2015, **51**, 2506-2509.
230. M. L. Truong, F. Shi, P. He, B. Yuan, K. N. Plunkett, A. M. Coffey, R. V. Shchepin, D. A. Barskiy, K. V. Kovtunov, I. V. Koptyug, K. W. Waddell, B. M. Goodson and E. Y. Chekmenev, *The Journal of Physical Chemistry B*, 2014, **118**, 13882-13889.
231. J.-L. Montchamp, *Accounts of Chemical Research*, 2014, **47**, 77-87.
232. B. J. Tickner, Y. Borozdina, S. B. Duckett and G. Angelovski, *Dalton Transactions*, 2021, **50**, 2448-2461.
233. Y. Ou, Y. Huang, Z. He, G. Yu, Y. Huo, X. Li, Y. Gao and Q. Chen, *Chemical Communications*, 2020, **56**, 1357-1360.
234. A. C. Cooper, W. E. Streib, O. Eisenstein and K. G. Caulton, *Journal of the American Chemical Society*, 1997, **119**, 9069-9070.
235. S. Cauwberghs, P. J. De Clercq, B. Tinant and J. P. Declercq, *Tetrahedron Letters*, 1988, **29**, 2493-2496.
236. S. H. Hunter, R. S. Nyholm and G. A. Rodley, *Inorganica Chimica Acta*, 1969, **3**, 631-634.
237. R. R. Schrock and J. A. Osborn, *Journal of the American Chemical Society*, 1976, **98**, 2143-2147.
238. P. W. Codding and K. A. Kerr, *Acta Crystallographica Section B*, 1978, **34**, 3785-3787.
239. R. Dorta, H. Rozenberg, L. J. W. Shimon and D. Milstein, *Chemistry – A European Journal*, 2003, **9**, 5237-5249.
240. M. Khan, PhD, University of York, 2013.
241. N. C. Payne and D. W. Stephan, *Canadian Journal of Chemistry*, 1980, **58**, 15-21.
242. T. Allman and R. G. Goel, *Canadian Journal of Chemistry*, 1982, **60**, 716-722.
243. M. A. Bennett, S. K. Bhargava, M. Ke and A. C. Willis, *Journal of the Chemical Society, Dalton Transactions*, 2000, **20**, 3537-3545.
244. A. Comas-Vives, G. Ujaque and A. Lledós, in *Advances in Inorganic Chemistry*, eds. R. van Eldik and J. Harvey, Academic Press, 2010, **62**, 231-260.
245. O. Eisenstein and R. H. Crabtree, *New Journal of Chemistry*, 2013, **37**, 21-27.
246. G. E. Dobereiner, A. Nova, N. D. Schley, N. Hazari, S. J. Miller, O. Eisenstein and R. H. Crabtree, *Journal of the American Chemical Society*, 2011, **133**, 7547-7562.
247. G. P. Rosini, F. Liu, K. Krogh-Jespersen, A. S. Goldman, C. Li and S. P. Nolan, *Journal of the American Chemical Society*, 1998, **120**, 9256-9266.
248. C. A. Tolman, *Chemical Reviews*, 1977, **77**, 313-348.
249. R. Acharyya, S.-M. Peng, G.-H. Lee and S. Bhattacharya, *Journal of Chemical Sciences*, 2009, **121**, 387-395.
250. D. G. Gusev, V. I. Bakhmutov, V. V. Grushin and M. E. Vol'pin, *Inorganica Chimica Acta*, 1990, **177**, 115-120.
251. S. Hietkamp, D. J. Stufkens and K. Vrieze, *Journal of Organometallic Chemistry*, 1978, **152**, 347-357.
252. M. Grellier and S. Sabo-Etienne, *Chemical Communications*, 2012, **48**, 34-42.
253. P. D. Morran, S. B. Duckett, P. R. Howe, J. E. McGrady, S. A. Colebrooke, R. Eisenberg, M. G. Partridge and J. A. B. Lohman, *Journal of the Chemical Society, Dalton Transactions*, 1999, **22**, 3949-3960.
254. S. A. Colebrooke, S. B. Duckett, J. A. B. Lohman and R. Eisenberg, *Chemistry – A European Journal*, 2004, **10**, 2459-2474.

255. D. Schott, C. J. Sleigh, J. P. Lowe, S. B. Duckett, R. J. Mawby and M. G. Partridge, *Inorganic Chemistry*, 2002, **41**, 2960-2970.
256. N. K. J. Hermkens, M. C. Feiters, F. P. J. T. Rutjes, S. S. Wijmenga and M. Tessari, *Journal of Magnetic Resonance*, 2017, **276**, 122-127.
257. L. Sellies, R. L. E. G. Aspers and M. Tessari, *Magnetic Resonance*, 2021, **2**, 331-340.
258. R. E. Mewis, *Magnetic Resonance in Chemistry*, 2015, **53**, 789-800.
259. P. J. Rayner, J. P. Gillions, V. D. Hannibal, R. O. John and S. B. Duckett, *Chemical Science*, 2021, **12**, 5910-5917.
260. R. E. Mewis, R. A. Green, M. C. R. Cockett, M. J. Cowley, S. B. Duckett, G. G. R. Green, R. O. John, P. J. Rayner and D. C. Williamson, *The Journal of Physical Chemistry B*, 2015, **119**, 1416-1424.
261. N. Eshuis, N. Hermkens, B. J. A. van Weerdenburg, M. C. Feiters, F. P. J. T. Rutjes, S. S. Wijmenga and M. Tessari, *Journal of the American Chemical Society*, 2014, **136**, 2695-2698.
262. P. J. Rayner, M. J. Burns, A. M. Olaru, P. Norcott, M. Fekete, G. G. R. Green, L. A. R. Highton, R. E. Mewis and S. B. Duckett, *Proceedings of the National Academy of Sciences*, 2017, **114**, E3188-E3194.
263. D. G. Gusev, *Organometallics*, 2009, **28**, 763-770.
264. G. S. Reddy and R. Schmutzler, *Zeitschrift für Naturforschung B*, 1970, **25**, 1199-1214.
265. L. D. Vazquez-Serrano, B. T. Owens and J. M. Buriak, *Inorganica Chimica Acta*, 2006, **359**, 2786-2797.
266. S. B. Duckett, G. K. Barlow, M. G. Partridge and B. A. Messerle, *Journal of the Chemical Society, Dalton Transactions*, 1995, **20**, 3427-3429.
267. D. Blazina, S. B. Duckett, J. P. Dunne and C. Godard, *Dalton Transactions*, 2004, **17**, 2601-2609.
268. W. P. Aue, E. Bartholdi and R. R. Ernst, *The Journal of Chemical Physics*, 1976, **64**, 2229-2246.
269. C. J. SLEIGH, 1999, Parahydrogen Induced Polarisation: An NMR Based Investigation of Metal Hydrides, Thesis, Doctor of Philosophy (PhD), Chemistry, University of York, UK
270. L. S. Lloyd, R. W. Adams, M. Bernstein, S. Coombes, S. B. Duckett, G. G. R. Green, R. J. Lewis, R. E. Mewis and C. J. Sleigh, *Journal of the American Chemical Society*, 2012, **134**, 12904-12907.